NASA-CR-144866

(NASA-CR-144866) F-15 INLET/ENGINE TEST TECHNIQUES AND DISTORTION METHODOLOGIES STUDIES. VOLUME 1: TECHNICAL DISCUSSION Final Report (McDonnell Aircraft Co.) 248 p HC A11/MF A01 CSCL 21E G3/07 N78-30123 Unclas 30400

F-15 Inlet/Engine Test Techniques and Distortion Methodologies Studies

Volume I - Technical Discussion

Contract Number NAS4-2364

NASA Contractor Report 144866

F-15 Inlet/Engine Test Techniques and Distortion Methodologies Studies

Volume I - Technical Discussion

C.H. Stevens
E.D. Spong
M.S. Hammock

McDonnell Douglas Corporation
McDonnell Aircraft Company
St. Louis, Missouri

Prepared for
Dryden Flight Research Center
under Contract NAS4-2364

National Aeronautics
and Space Administration

June 1978

FOREWORD

This report was prepared by the McDonnell Aircraft Company (MCAIR), a division of the McDonnell Douglas Corporation, St. Louis, Missouri for the National Aeronautics and Space Administration, Dryden Flight Research Center, Edwards, California. The study was performed under NASA Contract NAS4-2364, "F-15 Inlet/Engine Test Techniques and Distortion Methodologies Study." The work was performed from March 1977 through February 1978 with Mr. Jack Nugent (NASA/Dryden) as Program Monitor and Mr. Harvey Neumann (NASA/Lewis) as Technical Monitor. Special acknowledgement is due Mr. T. Putnam (NASA/Dryden) for his constructive criticisms and suggestions.

The effort at McDonnell Aircraft Company was conducted under the technical leadership of the Engineering Technology Division. In addition to the authors listed on the cover, other MCAIR personnel that made significant contributions to this program were Mr. Edward Smith, Mr. Lee Weltmer and Mr. Mark Sawyer. Special acknowledgement is due Mr. Hershel Sams for his reviews and suggestions.

Significant subcontract support was provided by Mr. Wayne Walter and Mr. Lew Hayward of Pratt & Whitney Aircraft (P&WA), Government Products Division, under the direction of Mr. Frank Thompson.

This report consists of nine volumes. Technical discussions of the program, results and Appendices A and B are presented in Volume I (NASA CR 144866). Appendices C through J are presented in Volume II through IX (NASA CR 144867-144874) which present the distortion analysis plots and the associated statistical functions used for the analyses.

TABLE OF CONTENTS

TABLE OF CONTENTS (Continued)

TABLE OF CONTENTS (Concluded)

LIST OF ILLUSTRATIONS

SYMBOLS

	Description	Units
A_{BYP}	Inlet Bypass Area.	sq. meters (sq. inches)
a_o	Vortex radius	cm
alpha	Aircraft angle of attack	degrees
Alt.	Altitude	m(ft.)
"b" factor	Radial distortion weighting factor	
beta	Aircraft angle of sideslip	degrees
Bypass	Inlet Bypass Area	sq. meters (sq. inches)
CIVV	Compressor Inlet (Fan) Variable Vane . . .	
dB	Decibels	
Delta3	Inlet third ramp angle relative to the Inlet Reference Line	degrees
$D_2, \frac{\Delta P}{P}$	Spatial Distortion = $[(P_{t_2})_{max} - (P_{t_2})_{min}]/\bar{P}_{t_2}$	
$f_{c/o}$	Filter cutoff frequency	hertz
$(f_{c/o})_{engine}$	Engine filter cutoff frequency	hertz
FLT	Flight test data notation.	
FSCP	Full Scale Cold Pipe (without engine) wind tunnel test data notation	
FSE	Full Scale with Engine wind tunnel test data notation.	
HZ	Frequency.	hertz
I.D.	Identification Number	
K_{a_2}	Fan distortion descriptor = $K_\theta + b\, K_{ra_2}$ . .	
$(K_{a_2})_{S.S.}$	Steady state fan distortion descriptor . .	

SYMBOLS (Continued)

	Description	Units
Kc_2	High compressor distortion descriptor . .	
K_{ra_2}	Radial distortion descriptor	
K_θ	Circumferential distortion descriptor . .	
kPa	Killopascals	KilloPascals
Mach	Mach number.	
M_o	Free Stream Mach number	
m	Meters	Meters
P_{s_2}	Static pressure at the engine face	kPa (PSIA)
P_{t_2}, $P_{t_{ss}}$	Individual probe engine face steady state pressure	kPa (PSIA)
$\bar{P}_{t_2}$	48 probe averaged engine face steady state pressure	kPa (PSIA)
$\bar{P}_{t_{25H}}$	Fan exit (high compressor inlet) steady state total pressure	kPa (PSIA)
P_{t_i}, PT2I	Individual probe time variant engine face pressure	kPa (PSIA)
PT2I, P_{t_i}	Individual probe time variant engine face pressure	kPa (PSIA)
$\overline{PT2I}$	48 probe averaged time variant engine face pressure	kPa (PSIA)
ΔP_{t_2}, ΔP_{t_i}	Fluctuating component of individual probe pressure at the engine face = $P_{t_i} - P_{t_{ss}}$	kPa (PSIA)
$\frac{\Delta P}{P}$, D2	Spatial Distortion = $[(P_{t_2})_{max} - (P_{t_2})_{min}]/\bar{P}_{t_2}$	
P_{t_o}	Freestream total pressure	kPa (PSIA)
PSIA	Pounds per Square Inch Absolute	PSIA

SYMBOLS (Continued)

	Description	Units
$\overline{P}_{t_2}/P_{t_o}$	Inlet total pressure recovery.	
$(P_{t_{2.5\ c}})$	Time variant fan exit (high compressor inlet) total pressure/fan stream	kPa (PSIA)
$(P_{t_{2.5\ H}})$	Time variant fan exit (high compressor inlet) total pressure/engine stream . . .	kPa (PSIA)
$(\Delta P_{t_{2.5\ c}})$	Fluctuating component of fan exit (high compressor inlet) total pressure/fan stream	kPa (PSIA)
$(\Delta P_{t_{2.5\ H}})$	Fluctuating component of fan exit (high compressor inlet) total pressure/engine stream	kPa (PSIA)
P2IF1	Engine face hub static pressure ratio at 338.9 degrees angular location	
P2IF2	Engine face hub static pressure ratio at 67 degrees angular location	
P2IF3	Engine face hub static pressure ratio at 157 degrees angular location.	
P2IF4	Engine face hub static pressure ratio at 247 degrees angular location.	
P2W1	Engine face tip static pressure ratio at 30.2 degrees angular location	
P2W2	Engine face tip static pressure ratio at 329.4 degrees angular location.	
P2W3	Engine face tip static pressure ratio at 236.1 degrees angular location.	
P2W4	Engine face tip static pressure ratio at 160.2 degrees angular location.	
r_i	Engine face rake ring radius/i denotes the ring	cm (inches)
r_{HUB}	Engine hub radius at engine face	cm (inches)
r_{TIP}	Engine tip radius at engine face	cm (inches)
R_{yx}	Cross-correlation coefficient.	

SYMBOLS (Continued)

	Description	Units
R_{yy}	Autocorrelation coefficient.	
Re No.	Reynolds Number.	
RHO	Inlet first ramp angle relative to the Inlet Reference Line	Degrees
RMS, rms	Root mean square pressure.	kPa (PSIA)
RPM	Revolutions Per Minute	RPM
$\overline{RS}$	Ratio of filtered to unfiltered mean square pressure	
Series VII	1/6th scale inlet wind tunnel test series data notation.	
Series VIII	1/6th scale inlet wind tunnel test series data notation.	
T_{T_0}	Freestream total temperature	°K
T_{t_2}	Engine face total temperature.	°K
$T_{t_{25H}}$	High compressor (Fan Exit) Total Temperature	°K
Tu	Individual probe engine face turbulence. .	
Tu, average	48 probe average engine face turbulence. .	
$\overline{Tu}$	48 probe average engine face turbulence. .	
W2	Engine airflow	kg/sec (LB/sec)
WAT2	Corrected engine airflow $W2\sqrt{\theta}_{t_2}/\delta_{t_2}$	kg/sec (LB/sec)
WAT2 Design	Design corrected engine airflow.	98.43 kg/sec (217 LB/sec)
WAT2 Percent	WAT2 divided by WAT2 Design x 100	
W25H	High Compressor Airflow	kg/sec (LB/sec)

SYMBOLS (Concluded)

	Description	Units
WAT25H	Corrected high compressor airflow $W_{25H}\sqrt{\theta}_{t_{25H}}/\delta_{t_{25H}}$	kg/sec (LB/sec)
WAT25H Design	Design corrected high compressor airflow .	24.69 kg/sec (54.44 LB/sec)
WAT25H Percent	WAT25H divided by WAT25H Design x 100 . .	
α	Aircraft angle of attack	degrees
β	Aircraft angle of sideslip	degrees
δ_{t_2}	Corrected average engine face total pressure $\overline{P}_{t_2}/101$	
$\delta_{t_{25H}}$	Corrected average high compressor face total pressure $\overline{P}_{t_{25H}}/101$.	
Δ_3	Inlet third ramp angle relative to the Inlet Reference Line	degrees
ρ	Inlet first ramp angle relative to the Inlet Reference Line	degrees
θ	Engine face rake leg angles.	degrees
θ_{t_2}	Corrected average engine face total temperature $T_{t_2}/288.15$	
$\theta_{t_{25H}}$	Corrected average high compressor face total temperature $T_{t_{25H}}/288.15$	
τ	Lag time for cross-correlations and auto-correlations.	seconds

SUMMARY

Recent emphasis on increased maneuverability requirements for fighter aircraft has necessitated an extensive engineering development effort be directed towards inlet/engine compatibility. Inlet/engine compatibility must be assessed early in the aircraft development program to allow necessary inlet and engine design modifications to be defined and implemented at minimum cost impact. This early assessment of inlet/engine compatibility is determined by engine stability audits computed using inlet distortion levels from subscale inlet model data and engine sensitivities to inlet distortion. Therefore, the accuracy with which subscale inlet model distortion levels predict flight test vehicle distortion levels is a crucial element in assessing inlet/engine compatibility.

The primary goal of this distortion methodologies study was to determine if time variant distortion data taken from a subscale inlet model can predict peak distortion levels for a full scale flight test vehicle. The data base used to accomplish this goal was collected in separate programs by MCAIR and NASA/Dryden. Subscale and full scale wind tunnel data were collected by MCAIR during the F-15 development program, and flight test data were collected by NASA/Dryden during the NASA F-15 inlet/engine compatibility flight test program. This data base has a Mach number range of 0.4 to 2.5 and an angle of attack range from -10 degrees to +12 degrees.

The primary objectives accomplished in meeting the overall program goal were to determine the effects on peak distortion of: (1) Reynolds Number/scale, (2) engine presence and (3) frequency content. In addition, the capability of the P&WA stability audit system to predict engine stalls was evaluated, and the capability of Melick's procedure, Reference (1), to predict peak time variant distortion levels was evaluated. Using the Pratt and Whitney Aircraft distortion descriptor, K_{a_2}, the data indicate the following significant results for the F-15/F100 inlet/engine propulsion system.

- Peak time variant distortion from subscale inlet model wind tunnel tests are representative of full scale flight test distortion.
- The time variant pressure data of this study are random stationary data, thereby allowing valid statistical analyses to be conducted.
- The effect of the engine presence on total pressure recovery, peak time variant distortion and turbulence level is small but favorable.
- The Reynolds number/scale evaluation indicates a general trend of increasing total pressure recovery, decreasing peak time variant fan distortion and decreasing turbulence with increasing Reynolds number/scale.
- The frequency content evaluation indicates that peak time variant fan distortion and turbulence increase with increasing filter cutoff frequency for all of the data evaluated in this study.
- The capability of the Pratt & Whitney Aircraft stability audit system to predict engine stalls has been verified for both stall and non-stall flight test conditions.

- Predictions of peak distortion values using Melick's procedure are accurate to 11.3 percent average error for fourteen data points having nominal turbulence levels and are accurate to 20 percent average error (the maximum error approaches 40 percent) for eight data points having high turbulence levels.

INTRODUCTION

Recent emphasis on increased maneuverability requirements for fighter aircraft has necessitated an extensive engineering development effort be directed towards inlet/engine compatibility. Inlet/engine compatibility must be assessed early in the aircraft development program to allow necessary inlet and engine design modifications to be defined and implemented at minimum cost impact. This early assessment of inlet/engine compatibility is determined by engine stability audits computed using inlet distortion levels from subscale inlet model data and engine sensitivities to inlet distortion. Therefore, the accuracy with which subscale inlet model distortion levels predict flight test vehicle distortion levels is a crucial element in assessing inlet/engine compatibility.

During the development program of the F-15 air superiority fighter aircraft, the time variant pressure data were analyzed as required to ensure the F-15/F100 to be a compatible inlet/engine system prior to fleet introduction, but no in-depth analyses were conducted to investigate distortion methodologies and test techniques. This distortion methodologies and test techniques study utilizes the extensive MCAIR F-15 development test data base and the data base collected during the NASA/Dryden F-15 inlet/engine compatibility flight test program. The wind tunnel data base was collected during the period of March 1970 through March 1972 using a subscale inlet model (1/6th Scale), a full scale inlet model without engine (FSCP) and a full scale inlet model with engine (FSE) which were all tested at the Arnold Engineering Development Center (AEDC) at Tullahoma, Tennessee. The wind tunnel test conditions simulated both level flight and high energy maneuverability flight conditions. The flight test data base was collected in the NASA inlet/engine compatibility flight test program during the period of April 1976 through June 1976 using F-15 aircraft number 71-0281 which was tested at the NASA/Dryden Flight Research Center at Edwards Air Force Base, California. The aircraft test conditions duplicated the selected wind tunnel test conditions for both high energy maneuverability and level flight test conditions. These two data bases were integrated to provide the data matrix used in this study.

The F-15 inlet system is a two-dimensional, external compression, overhead three ramp variable capture area design with an internal diffuser ramp. This unique design is capable of rotating the entire upper cowl and compression ramp system of the inlet, thus providing a variable capture area and aligning the inlet with the approaching airflow over a wide range of Mach numbers, angles of attack, and engine airflows. The Pratt and Whitney Aircraft (P&WA) F100 turbofan engine, is a twin spool, high pressure ratio, lightweight engine with mixed flow augmentation and variable area convergent-divergent exhaust nozzle, the fan module has three stages and the compressor has ten stages. The fan and compressor are each driven by dual turbine stages and the fan and core airflows are mixed in the augmentor prior to afterburning.

The primary goal of this study was to determine if subscale inlet model peak time variant distortion data will accurately predict full scale flight test peak time variant distortion data. To achieve this goal, several specific technical objectives were established including: (1) evaluate the

quality of the time variant data, (2) determine the effect of engine presence on distortion levels, (3) establish Reynolds number/scale effects on distortion levels, and (4) investigate the effect of frequency content on distortion levels.

The first sections of this report provide descriptions of the inlet models, test programs and the associated data acquisition and data reduction systems. The following sections describe the evaluation of the time variant data quality, effect of (1) engine presence, (2) Reynolds number/scale and (3) frequency content. In addition, the capability of the P&WA stability audit system to predict engine stalls is evaluated and the capability of Melick's procedure, Reference (1), to predict most probable peak time variant distortion values are evaluated. The appendices contain a sample calculation of the distortion descriptor, K_{a_2}, the distortion analysis plots and the associated statistical functions used for the analyses.

MODEL DESCRIPTIONS

The time variant pressure data from which the peak values of time variant distortion were calculated for this study were collected using a 1/6th scale inlet wind tunnel model, a full scale inlet wind tunnel model tested with and without an engine and the full scale flight test vehicle, aircraft 71-0281. Schematics of these three test articles are shown in Figure 1. The applicable test series, test dates and test facilities are as follows:

Inlet Model	MCAIR Test Series	Test Date	Test Facility	Facility Test Series
Aircraft No. 71-0281	FLT	June 1976	NASA/DRYDEN Edwards, Calif.	NASA F-15 Inlet/ Engine Compatibility Test
Full Scale With Engine	FSE	Mar 1972	AEDC* Tullahoma, Tenn.	TF269/SF144
Full Scale Cold Pipe (Without Engine)	FSCP	Nov 1971	AEDC* Tullahoma, Tenn.	SF144
1/6th Scale	VIII	June 1971	AEDC* Tullahoma, Tenn.	SF139
1/6th Scale	VII	July 1970	AEDC* Tullahoma, Tenn.	TF242/SF130

*Arnold Engineering Development Center

The general physical characteristics of the F-15 inlet configuration, full scale flight test vehicle, full scale inlet wind tunnel model, 1/6th scale inlet wind tunnel model, and engine face total pressure rake are discussed below.

F-15 Inlet Configuration

The inlet configuration is a two-dimensional, external compression, overhead three ramp variable capture area design with an internal diffuser ramp, and the ramp and bypass system geometries are illustrated in Figure 2. The inlet consists of the three forward compression ramps and a diffuser or fourth ramp. The cowl rotation system rotates the first compression ramp assembly about a pivot point near the cowl lip. The second, third and fourth ramp systems are slaved together and are positioned simultaneously. The boundary layer bleed systems consist of the second and third ramp porous surfaces, throat slot bleed and inboard and outboard sideplate bleeds. The throat slot in conjunction with the bypass door acts as the inlet bypass system for inlet/engine matching.

Full Scale Flight Test Vehicle

The flight test data for this study was obtained using F-15 aircraft number AF 71-0281 on bail to NASA from the U.S. Air Force and is shown in Figure 3. This aircraft which is fully instrumented was used initially as the Flight Test Propulsion Subsystem Development Aircraft for the MCAIR F-15 flight test development program.

On the F-15 aircraft, the second, third and fourth (diffuser) inlet ramps are linked together and are positioned by a utility hydraulics power actuator. The variable capture area feature is accomplished by a single actuator which rotates the cowl (including the first, second and third ramps) about the lower cowl lip. The bypass door is positioned by a third hydraulic actuator.

The positioning of the three actuators is accomplished by an Air Inlet Controller (AIC) which uses freestream Mach number, inlet throat Mach number, total temperature, and angle of attack signals from the aircraft sensors. In addition, this aircraft is equipped with manual air inlet controller capability (not a production item) to allow inflight pilot control of the ramp and bypass door positions.

The F-15 aircraft is powered by two Pratt and Whitney Aircraft F100-PW-100 turbofan engines. The F100 engine is a twin spool, high pressure ratio, lightweight engine with mixed flow augmentation and a variable area convergent-divergent exhaust nozzle. The fan module has three stages and the compressor has ten stages. The fan and compressor are each driven by dual turbine stages and the fan and core airflows are mixed in the augmentor prior to afterburning. The combustor is an annular design. The F100 engines used for this study were Serial Numbers P690063 and P690081. Engine S/N 063 which is a pre-production engine and denoted as an F100(2 7/8) was retrofitted with a production fan and engine controls. This engine was installed in the left engine nacelle and instrumented with a high response engine face rake.

Full Scale Inlet Wind Tunnel Model

The full scale inlet wind tunnel model, shown in Figure 4, was tested with and without an engine installed, therefore providing the data necessary to evaluate the effect of the engine presence on peak time variant distortion levels. This full scale inlet test article includes the basic components of the inlet, inlet controls, engine and transonic and supersonic partial forebodies.

The full scale inlet model, including the entire diffuser section, represents the true aerodynamic configuration of the aircraft. This inlet model is fabricated of flightweight hardware and the aircraft inlet description of the previous section is an accurate description of this inlet model.

The inlet ramps, variable cowl and bypass door were positioned using the same model AIC as on the flight test aircraft. The AIC used the freestream Mach number, inlet throat Mach number, total temperature and angle of attack signals from either the model or wind tunnel sensors to position the ramps, variable cowl and bypass door. This AIC also had a manual mode (same as the flight test AIC) which allowed the test operator to vary the inlet ramps, variable cowl and bypass door while the tunnel was operating.

For the full scale inlet testing with engine, Pratt and Whitney Aircraft (P&WA) furnished the XF100-PW-100 ground test engine designated as XD-13. This engine is of the same basic design as the prototype and production F100 engines with minor differences in the aerodynamic gas path. For the full scale inlet testing without engine, a flow control/measurement system, denoted as the cold pipe, was used in place of the engine, i.e. full scale cold pipe. The size, mounting and face geometry duplicated the P&WA engine.

The complete aircraft forebody could not be simulated at full scale because of tunnel size limitations. Therefore, transonic and supersonic partial forebodies were designed to simulate the local flowfield at the inlet. Previous inlet development testing using the 1/6th scale model indicated that transonically over the range of angle of attack and zero sideslip covered in the full scale wind tunnel testing, the inlet performance and distortion characteristics were not significantly affected by the presence of the forward fuselage. Therefore, a small partial forebody was designed, which was primarily required to function as a fairing forward of the fuselage. The supersonic partial forebody shape was defined during the F-15 Forebody Flowfield Development Test. Flowfield comparisons between the full forebody and the partial forebody showed that the full forebody generated more downwash at the inlet plane. This downwash was duplicated during the full scale inlet testing with the partial forebody by rotating the entire model negatively, with the amount of rotation as a function of fuselage angle of attack. The full scale test article and supersonic partial forebody are shown in Figure 4.

The boundary layer bleed system was identical to that on aircraft 71-0281. However, a test peculiar auxiliary bypass door was built into the test article forward of the engine face. The auxiliary door eliminated inlet instabilities during engine startup and windmilling. During normal engine operation, the auxiliary door closed to make a smooth diffuser line. All bleed systems on the full scale model were individually calibrated prior to testing.

1/6th Scale Inlet Wind Tunnel Model

The 1/6th inlet wind tunnel model was used during the F-15 inlet development program. The model consisted of a fuselage forebody assembly, a remotely controlled left inlet and an inlet to engine duct that is internally simulated to the engine compressor face station. The main duct aft of the engine face station is equipped with a remotely actuated mass flow plug. The tunnel installation of this model is shown in Figure 5.

The 1/6th scale inlet model, including the entire diffuser section, represents the true aerodynamic configuration of the aircraft. The cowl rotation system, which includes the first ramp assembly, and the second, third and fourth ramp system is identical to the full scale ramp system and can be remotely positioned using two independent drive systems. The inlet assembly can be tested isolated or with the forebody.

The aerodynamic configuration of the boundary layer bleed system is identical to the full scale test articles, however, bleed flow ducts were attached to the bleed exits and these ducts were fitted with remotely actuated mass flow plugs. The ducts could be removed if desired.

Engine Face Total Pressure Rake

The engine face rake configuration has eight legs and six rings equal area weighted with the high response and steady state pressure probes located side by side. The 1/6th scale configuration is an exact scale version of full scale engine face rakes as shown in Figure 6. The full scale engine face rake was used for the full scale inlet wind tunnel testing and also on the flight test vehicle.

TEST DESCRIPTIONS

Valid comparisons of peak time variant distortion data from flight test and wind tunnel test require that the inlet configurations, test conditions, analysis times and inlet airflows, be equivalent. The inlet configurations, described above, are identical for each of the test articles. The techniques used to obtain comparable test conditions, analysis times and inlet airflows of flight and wind tunnel test articles are discussed below.

Flight Test Procedure

The data base for the 1/6th scale inlet and the full scale inlet wind tunnel models existed prior to the NASA F-15 Inlet/Engine Compatibility Test Program. Test conditions were selected from these data that would provide a high level of turbulence and steady state distortion. Some of these selected test conditions have extreme aircraft attitudes such as -10 degrees angle of attack and +10 degrees angle of sideslip at 0.9 Mach number and -4 degrees angle of attack at 1.6 Mach number. While wind tunnel models can be positioned in these extreme attitudes for indefinite periods of time, the aircraft cannot fly at these flight conditions indefinitely and still maintain Mach number and altitude. To achieve these extreme attitudes, the aircraft had to be maneuvered into the desired test condition. For the -10 degree angle of attack and +10 degree angle of sideslip at 0.9 Mach number, Figure 7, the aircraft was first inverted and then sideslipped. For the 1.6 Mach number at -4 degrees angle of attack, the aircraft was accelerated to the desired Mach number, then "pulled-up" to positive angle of attack (increasing altitude and decreasing Mach number) and then "pushed over" (decreasing altitude, increasing Mach number) to achieve -4 degrees angle of attack, 1.6 Mach number at the correct altitude as shown in Figure 8.

Analysis Time

The available analysis times (time at desired flight condition) for the extreme flight maneuvers are relatively short since simultaneous matching of the first ramp, variable cowl position, second, third and fourth ramp position, bypass door position, angle of attack, angle of sideslip while maintaining constant Mach number, airflow level and altitude are required to properly assess the data comparisons between flight and wind tunnel data.

The analysis times for the flight data ranged from .600 to 2.8 seconds depending on the desired test condition. Using the acoustic scaling criteria of Reference (2), the respective analysis times for the 1/6th scale inlet wind tunnel model are .100 to .467 seconds.

Engine Airflow Level

An engine power setting of intermediate power or afterburning power was required for most of the flight maneuvers to achieve or sustain the flight maneuver. These two power settings both have maximum corrected engine airflow. Therefore, most of the data comparisons for flight test conditions are limited to one corrected engine airflow. However, for the wind tunnel test articles, the engine power setting was varied or the mass flow plug was translated to provide a range of corrected engine airflow levels for both supercritical

(without engine only) and subcritical inlet operation for each test condition. Therefore, data points for two engine corrected airflow levels were selected from the wind tunnel data to bracket the airflow from the flight test data point. This allowed interpolation to match the flight test airflow levels.

DATA ACQUISITION AND REDUCTION

Two similar procedures were used to acquire and reduce the time variant pressure data, one for the wind tunnel tests and one for the flight tests. The primary difference between the two procedures is that the Analog Distortion Calculator was used in reducing the flight test data but not the wind tunnel test data.

The Analog Distortion Calculator (ADC) was used during the NASA F-15 inlet/engine compatibility flight test program. Analog values of distortion data were computed as a function of time, and electronic flags were placed on the wide band FM pressure data tapes corresponding to peak distortion values. The analog pressure data were then digitized $\pm$300 milliseconds about this peak flag, and the digital time variant distortion data were calculated. This procedure which was also used during the F-15 inlet development wind tunnel program represented a substantial cost savings since it eliminated digitizing lengthy data segments (thirty seconds for the F-15 inlet development program). However, for this study, the ADC was not used for the wind tunnel data reduction procedure since the maximum analysis time was only 2.8 seconds. The analog pressure data were digitized, and peak distortion values were calculated for the entire analysis time. The data segment to be digitized was randomly selected from within the thirty second data record. Approximately 35 million pressure values were digitized and used to compute the time variant distortion data and the required statistical functions for this study. The data reduction paths for the flight test data and wind tunnel test data, the filter characteristics, the pressure probe substitution technique, the distortion data accuracy and the time history comparisons of analog and digital distortion data are described below.

MCAIR Flight Test Data Processing System

The system consists of a network of equipment located at MCAIR/Edwards and at MCAIR/St. Louis linked together by a high-speed digital transmission system utilizing a leased telephone line. The heart of the system is a high speed digital computer located at the MCAIR/St. Louis facility. The total system is composed of the preprocessor subsystem, digital transmission subsystem, high speed digital computer subsystem and the formal data display subsystem. A flow diagram depicting the data processing system is shown in Figure 9.

Preprocessor Subsystem - The purpose of the preprocessor subsystem is to accept the onboard tape recorded signals, perform the necessary processing controls, convert the analog signals into a digital form, merge the analog and pulse coded modulation (PCM) data, provide time synchronization of the data and produce a computer compatible tape. Header information on this preprocessed tape provides the necessary instructions to the high speed digital computer to allow it to perform all the requested computations and plots on the test runs preprocessed. The preprocessor has a mini-computer central processing unit (CPU) and a special purpose digital computer. Set-up of the preprocessor is accomplished through the use of process control cards that include the job definition cards and measurand definition cards. These cards are denoted as the Instrumentation Ground Equipment (IGE) cards and are also used for pre-flight instrumentation checkout and set-up of the programmable airborne data acquisition system. In addition, the preprocessor subsystem

uses a data compression algorithm that reduces data transmission time by removing redundant data points during transmission.

Digital Transmission Subsystem - Low- and high-speed digital transmission subsystems utilizing voice-grade telephone lines interconnect the MCAIR/St. Louis and the MCAIR/Edwards facilities. The low speed system is used for computer file updates and the high-speed system is used as a tape-to-tape system managed on both ends by identical controllers. The high speed transmission system transmits synchronously (constant bit rate) and operates in a full duplex mode which allows simultaneous transmission of data and error signals. Effective transmission rates of approximately 6700 bits per second are being obtained. The low-speed transmission systems at the MCAIR/Edwards facility consists of a mini-computer interface subsystem configured with a keyboard and printer, card reader, and card punch. It is connected to the high speed digital computer in St. Louis. Transmission is asynchronous at rates up to 14.8 characters per second in a half-duplex mode.

High Speed Computer Subsystem - This high speed digital computer subsystem provides storage space for the information files and the computational capability to rapidly process and display the required data in support of the MCAIR flight test activities. To handle this task, the system is configured with a 512 thousand byte memory, a 400 million byte disk storage, four nine-track dual-density (800/1600 BPI) tape units, a line printer (1100 LPM) and a combination card reader/punch (1100 CPM read and 300 CPM punch). The subsystem is operated in a Virtual Storage (VS-1) environment which is currently configured to allow four multiprogrammed partitions of 512 thousand bytes. If necessary, any partition size can be increased to 4 million bytes of virtual memory. This arrangement provides many features of a very large computing system without the large scale costs.

Formal Data Display Subsystems - The Formal Data Display subsystem consists of line printers and electrostatic plotter/printers. The MCAIR/St. Louis facility has an electrostatic plotter/printer interfaced (on-line) to the high speed digital computer. This plotter/printer is capable of producing a completely annotated hard copy plot in approximately 4 seconds and a tabular printout at approximately 2500 lines per minute. A printer (1100 lines per minute) is also interfaced to the high speed digital computer. The MCAIR/Edwards facility has an electrostatic plotter/printer which operates as a "stand alone" system controlled by a mini-computer. In this configuration, a magnetic tape is the input to the subsystem.

MCAIR Wind Tunnel Test Data Processing System

The data processing system consists of a network of equipment located at MCAIR/St. Louis. The total system is composed of a data recording subsystem, data digitizing subsystem, a high speed digital computer subsystem and a formal data display system.

Data Recording and Playback Subsystem - The high response wind tunnel pressure data is recorded on one inch wide band magnetic tape using constant bandwidth (CBW) techniques. The subscale data were recorded with six data channels per track and the full scale data were recorded with seven data channels per track. In addition, two tracks were allocated to record the IRIG time code and a reference oscillator signal, and two tracks were left blank for use during the digitizing process.

Data Digitizing Subsystem - To identify the data segment for digitization, the magnetic tapes are replayed on the tape recorder as shown in Figure 10a. During playback, the IRIG time code is electronically processed by the time code reader and associated electronics and a D.C. level digitizing pulse is recorded on one of the blank tracks to identify the data segment selected for digitization.

The tapes were then replayed again as shown in Figure 10b, and the data were discriminated (two tracks for each pass), filtered with the desired four pole Bessel filters and digitized using sample and hold modules and an analog-to-digital converter. Since the data were digitized during multiple passes of the tape, it was necessary to time correlate these data. This was accomplished by gating the D.C. level digitizing pulse with the IRIG time code and then gating the reference oscillator signal to the analog-to-digital converter. The digitized data were then buffered into a core memory and recorded on a nine track, eight hundred bits per inch digital tape.

High Speed Digital Computer Subsystem - Using the digital data tape generated during the digitizing process as the primary input, the multiple pass digitized data segments were merged into a single pass data segment which was output to magnetic tape (merged high response data) having a blocked format with one data file per data segment, as shown in Figure 10b. The merging process was controlled by a high speed digital computer which used a 80 megabyte disc for working files. The output data format was a 24 bit binary integer which corresponded numerically to the 16 bit input data.

The merged high response pressure data were then read from the magnetic tape by a high speed digital computer and calibration scaling was applied to obtain high response pressure data in engineering units. These data were used to compute the time variant fan distortion data. The time variant pressure and distortion data were then output to magnetic tape.

Formal Data Display Subsystem - Using the time variant pressure and distortion data magnetic output tape and the appropriate software packages, high quality time history traces of distortion data, total pressure contour, power spectral density plots, cross spectral density plots, autocorrelation plots and cross correlation plots were produced using a high speed electrostatic printer/plotter.

Filter Characteristics

Low band pass, 4 pole adjustable Bessel filters were used for this study, the frequency response characteristics of which are shown in Figure 11. The filter cutoff frequency could be adjusted, thus allowing the entire set of data used for the study (wind tunnel and flight test) to be reduced using this one set (48) of filters, thereby, eliminating inconsistencies in frequency response characteristics for the model and flight data. High response pressure data used to compute time variant distortion data for the F100 engine stability audits are filtered at 170 Hertz cutoff frequency as specified by P&WA which corresponds to design rotor speed.

Pressure Probe Substitution Technique

During the computation of digital distortion and generation of engine face pressure profile plots, it was sometimes necessary to substitute for inoperative probes on the rake to obtain values at all 48 probe locations.

A probe was considered to be out of tolerance when the total pressure recovery for that probe location was greater than 1.1 and less than 0.2. The output from each probe of the rake was examined prior to data reduction, and probes were deleted if the probe output was suspect. In addition, data reduction was halted if more than six probes were inoperative on two adjacent legs or more than twelve probes were inoperative on the forty eight probe rake.

A set of probe substitution criteria which were developed during the F-15 inlet development program were used for the study are are presented in Figure 12. If these criteria failed to determine a forty-eight probe set, the adjacent most radial and circumferential three probes were averaged and used to obtain a probe location valu Probes were obtained by proceeding in a radial direction first and in a rcumferential direction second.

Distortion Data Accuracy

An error assessment was made in Reference (3) for the F-15 flight test/ full scale inlet wind tunnel model engine face rake configuration. Typical error in the fan distortion factor as a function of pressure error is shown in Figure 13.

Analog and Digital Distortion Data Comparisons

The Analog Distortion Calculator was used during the NASA F-15 inlet/ engine flight test program to flag peak values, therefore identifying the data time segment to be digitized. It is important that the ADC calculate peak time variant distortion accurately so that the correct time segment is selected for digitization. To illustrate the accuracy of the ADC, time history traces of analog distortion data and of digital distortion data for the flight test program are compared in Figure 14 and additional comparisons are made in Appendix A. As can be seen from the figures, the ADC computes peak distortion values to within ± 5 percent of the digitally computed peak distortion values.

DATA BASE SELECTION

The data base for this study was established by assembling data from four distinct inlet test series: (1) the NASA inlet/engine compatibility flight test program, (2) the MCAIR full scale inlet development test without engine (FSCP), (3) the MCAIR full scale inlet development test with engine (FSE), and (4) the MCAIR 1/6th scale inlet development test. To meet the objectives of the study, test conditions were selected which encompassed wide ranges of Mach number, angle of attack, angle of sideslip and corrected engine airflow and had high levels of peak distortion.

The inlet configuration, as previously described, was identical for all the wind tunnel models and the flight test vehicle. The programmed inlet ramp and bypass door schedules were also identical. The inlet ramp angles, as defined in Figure 2, were identical to within ± 0.5 degrees for each selected data point and test article for a given test condition. The bypass door areas were either fully open or fully closed for each test condition with the exception of three data points which had partially opened bypass positions. The test conditions for each data point, model scale, Mach number, angle of attack, angle of sideslip, inlet cowl rotation angle, inlet third ramp angle, bypass door position, percent corrected engine airflow, Reynolds number, analysis time and part-point number for this study are summarized in Figure 15.

DISTORTION DESCRIPTOR

One of the objectives of this study was to evaluate the capability of the Pratt & Whitney stability audit procedure to predict engine stalls. Since current state of the art distortion descriptors are dependent upon the engine configuration, evaluation of the Pratt & Whitney stability audit procedure necessitates using the Pratt & Whitney distortion descriptor, K_{a_2}, since it is the distortion descriptor for the F-15 powerplant, the F100 engine.

During the development phase of the F-15 inlet/engine propulsion system, the distortion descriptor was repeatedly improved as the experimental data base increased to better define the relationship between the distortion descriptor and the engine stall margin. As a result of the repeated improvement of the distortion descriptor, the wind tunnel distortion data and flight test distortion data were not comparable on a direct basis. To make valid comparisons of distortion levels, the distortion data for all the test conditions of Figure 15 were computed using the current distortion descriptor per Reference (4). The mathematical formulae of the distortion descriptor used to reduce the data for this study and previous F-15 development data are presented in Figure 16. The parameters that have been changed throughout the development phase of the F100 engine are the reference radial profile and the radial distortion weighting factor. A sample calculation of the distortion descriptor is shown in Appendix B, and the reference radial profiles and radial distortion weighting factors for the F100 (2 7/8) engine are also presented.

Distortion descriptor values are derived to have a linear relationship with remaining engine stall margin, and the distortion limit is defined as the distortion level for which no remaining stall margin exists (engine stall). Therefore, the significance of a distortion level is its relative magnitude to the distortion limit level for which an engine stall may occur. The levels of distortion values for which a stall may occur for the F100 (2 7/8) engine are shown in Figure 17. This curve is a screening curve which is conservative relative to predicting engine stalls since it uses the lowest level of distortion for a given airflow that could possibly stall an engine for any given Mach number and altitude. It is termed a screening curve since values from this curve are not to be used as distortion limits for engine stall; instead when an inlet distortion level for a particular airflow exceeds the value from this curve, additional analysis should be conducted to determine if there is any remaining engine stall margin for the particular test condition. It should be noted from Figure 17 that the variation in engine tolerance to distortion level from high to low airflow is significant since the respective ranges of distortion level from the screening curve range from 0.75 (high airflow) to 16.75 (low airflow).

The range in distortion level from high to low airflow is primarily a result of significant changes in the radial distortion weighting factor, b. This factor is shown in Figure 18 to range from 0.93 (high airflow) to 29.29 (low airflow) as a function of airflow. Since fan distortion is the sum of circumferential distortion and radial distortion multiplied by the radial distortion weighting factor ($K_{a_2} = K_\theta + b \cdot K_{r_a}$), and since the levels of

circumferential and radia distortion generally have values between 0.25 to 1.0 for the engine airflows of interest in this study, radial weighting factors corresponding to low engine airflows (b = 25) can easily result in fan distortion values of 16 or greater. The radial distortion weighting factor implies that at reduced engine airflows, the fan is more sensitive to radial distortion than to circumferential distortion. As a result of discontinuities in the radial distortion weighting factor, Figure 18, at approximately 82 percent corrected engine airflow, an interpolation procedure was required for distortion data comparisons at constant corrected engine airflows. This is discussed in the Interpolation Procedure section.

The irregularity in the radial distortion weighting factor is directly related to the subtle aspects of the P&WA F100 stability audit system. The decreasing sensitivity of the F100 fan to circumferential distortion and the increasing sensitivity to radial distortion, as corrected engine airflow is reduced, results in the irregularity at approximately 82 percent corrected engine airflow as shown in Figure 18.

TIME VARIANT DATA QUALITY

The data comparisons necessary to satisfy the primary objectives of this study require that the samples of time variant distortion data be stationary random data. This implies that the statistical properties of each data sample are constant with time and are repeatable. With constant statistical properties and identical test conditions, reduced data from the various inlet test programs can be meaningfully investigated for the effects of Reynolds/scale effects, frequency content and engine presence. Detailed investigation into the data classification, description and characterization were made and samples of wind tunnel and flight data were evaluated in detail for stationary random data verification. In addition, comparisons of stationary random data and periodic data were made for two samples of flight data. The test conditions selected from the complete data matrix, Figure 15, for evaluation of stationary random characteristics are shown in Figure 19.

Data Classification

Data from observed phenomena are generally categorized as either deterministic or random, and the various classifications of data for both deterministic and random data are shown in the schematic of Figure 20. Deterministic data can be categorized as being either periodic or non-periodic. Periodic data can be further categorized as being either sinusoidal or non-sinusoidal (complex periodic). Non-periodic data can be further categorized as being either "almost periodic" or transient. In addition, combinations of these deterministic forms may also occur.

Data representing random physical phenomenon cannot be described by an explicit mathematical relationship since each observation of the phenomenon is unique. Any given observation will represent only one of many possible results that could have occurred. A single time history representing a random phenomenon is called a sample record, and the collection of all possible sample records which the random phenomenon could have produced is called a random process. Therefore, a sample record can be thought of as one physical occurrence of the random process. Random processes can be categorized as either non-stationary or stationary. Non-stationary random processes can be further categorized into specific types of non-stationary phenomenon. More detailed discussions of non-stationary data can be found in Reference (6). Stationary random processes can be further categorized as either ergodic or nonergodic.

Data Description

Examples of each data classification are as follows:

- o Deterministic Data
  - Sinusoidal Periodic - Described mathematically by the periodic function: $x(t) = X \sin (2\pi fo + \theta)$
  - Complex Periodic - With few exceptions can be described mathematically by the Fourier series:

$$x(t) = \frac{a_o}{2} + \sum_{n=1}^{\infty} [a_n \cos (2\pi n f_1 t) + b_n \sin (2\pi n f_1 t)]$$

- Almost Periodic - Has an infinitely long fundamental period and does not satisfy: $x(t) = [x(t) \pm NT_p]$ relationships,

  Example: $x(t) = X_1 \sin (2t + \theta_1) + X_2 \sin (3t + \theta_2) + X_3 \sin (\sqrt{50}t + \theta_3)$

o Random Data

- Non-Stationary - includes all random processes which do not meet the requirements for stationarity. Example: $x(t) = X(t) \cdot A(t)$ where $X(t)$ is random and $A(t)$ is deterministic.

- Weakly Stationary - Mean Value (first moment) invariant with time

  - Autocorrelation (joint moment) invariant with time

- Strongly Stationary - All possible moments and joint moments invariant with time.

- Ergodic Stationary - Mean value (first moment) invariant with time for all sample records

  - Autocorrelation (joint moment) invariant with time for all sample records

For deterministic data in general, explicit mathematical functions will describe the dependent variable as a function of time for a particular category of data. In contrast, there are no explicit mathematical functions that will describe the random data observation since it is unique. However, time averages of stationary random data will be constant over the sample record of interest, and if the data is ergodic stationary random, the time averages will be constant for all sample records for a given ensemble of data. In actual practice, if random data exhibit stationary physical phenomena, the data are generally said to be ergodic and random stationarity can be measured properly from a single sample record rather than an ensemble of simple records.

Data Characterization

Since no explicit mathematical functions exist for stationary random data, four main types of statistical functions are used to characterize the basic properties of stationary random data. These statistical functions are (a) mean square values, (b) probability density functions, (c) autocorrelation functions, and (d) power spectral density functions.

The mean square value furnishes a description of the intensity of the data. The probability density function (PDF) furnishes information about the

data in the amplitude domain. The autocorrelation function and the power spectral density function furnish information about the data in the time domain and the frequency domain respectively. For stationary random data, the power spectral density function furnishes no new information relative to the autocorrelation function since the autocorrelation function and the power spectral density function are transform pairs of one another.

For most stationary random data, it is unnecessary to derive all of the statistical functions discussed above. Using four basic assumptions, which are listed below, stationary random data can be verified using the time varying mean and time varying mean square values. These statistical parameters must have a constant value for the sample record. It should be noted that the mean square of the fluctuating pressure component is equal to the variance of the instantaneous pressure (steady state pressure component plus the fluctuating pressure component) and is referred to as the instantaneous pressure variance throughout the remainder of the report.

$$\text{Mean Square of Fluctuating Pressure Component} = \lim_{T\to\infty} \frac{1}{T} \int_0^T [P_{t_i}(t)]^2 \, dt = \lim_{T\to\infty} \frac{1}{T} \int_0^T [P_{t_i}(t) - P_{t_{ss}}]^2 \, dt$$

$$= \text{Variance of Instantaneous Pressure}$$

Theoretical proof of stationarity requires that all statistical properties of the random process be invariant with time. Verifications of this type are clearly not feasible since there are an infinite number of statistics that would have to be computed for an ensemble rather than a single sample record. However, four basic assumptions can be made, thereby allowing practical tests for stationarity.

The first assumption is that the statistical properties of a short time interval of data will not vary significantly from a short time interval of the next sample. This simply means that self stationarity of individual records can be accepted as stationarity of the random process from which the sample records were taken.

The second assumption is that verification of weak stationarity is sufficient. If this assumption is accepted, stationarity can be verified using only the mean value and the autocorrelation function of the sample record. Two reasons make this assumption acceptable. Power spectra and autocorrelation analysis do not require more than weak stationarity to be valid and random data will generally be strongly stationary if weakly stationary. For the case of data with a normal probability density function, weak stationary data are strong stationary data since all higher order statistical properties of normal data are determined by the mean value and autocorrelation function.

The third assumption is that the sample record to be investigated is long compared to the random fluctuations of the data time history. In effect, the sample must be lengthy enough to permit long term trends to be differentiated from the time history fluctuations.

A fourth important assumption is that if the variance of the sample data record is stationary then the autocorrelation function is also stationary. This assumption which is somewhat less dependable than the first three assumptions simplifies the testing procedures and is usually valid since it is highly unlikely that nonstationary data will have a time varying autocorrelation function for any time displacement τ without the value at $\tau = 0$ varying. Since the variance equals the autocorrelation function at $\tau = 0$, the variance rather than the entire autocorrelation function is used.

With these assumptions, the stationarity of random data can be verified using only the mean and the variance of the sample data record. These assumptions are verified in the following section by examining power spectral density functions, autocorrelation functions, probability density functions, mean values and variance values for selected flight test and wind tunnel data points.

Verification of Random Stationary Data

Statistical data analyses were made to: (1) verify the use of the pressure variance and the mean pressure values to determine if data are random stationary, (2) verify the flight test data to be stationary random for relatively short analysis times and (3) illustrate the differences between stationary random data and periodic (deterministic) data.

One of the most extreme flight test conditions, Mach number 1.6 at angle of attack of -4 degrees and sideslip angle of 0 degrees, was selected to verify the assumptions for stationarity of random data. This test condition required a transient flight maneuver, shown in Figure 8, to obtain the desired flight attitude. The test condition was obtained by a pull-push maneuver and the aircraft was on condition for approximately 0.6 seconds as noted in Figure 15. If this data point, with the underlying assumptions for stationarity exhibits the properties of stationary data, the assumptions for stationarity should also be valid for the wind tunnel data and one "g" flight conditions.

The power spectral density function (PSD) of Figure 21(a), generated using data for the flight test condition from Figure 8, exhibits the same frequency characteristics of wide band random noise typical of random stationary data, per Reference (6). In contrast, the PSD function of Figure 21(b) shows periodic data with discrete frequency spectra of approximately 9, 18, 27, 39, 45 and 54 Hertz. This contrast of the PSD functions emphasizes the pressure data randomness (no discrete frequency spectra) of the selected flight test condition.

The autocorrelation functions for the two flight test conditions are presented in Figure 22. The autocorrelation function of Figure 22(a) shows no correlation for the inlet rake pressure probe L6R3 at the engine face. This is typical of random data, and very rapidly approaches a constant value as a function of lag time which also is typical of stationary data, therefore the data again exhibits the properties of stationary random data. For the periodic data of Figure 22(b), almost perfect correlation is obtained for the same pressure probe location as used for the random data analysis. The elapsed times between the peak correlations for the pressure probe of Figure 22(b) are 0.111 seconds which correspond to the fundamental frequency of 9 Hertz obtained from the PSD function. As expected, the autocorrelation function does not approach a constant value.

The probability density functions for the random and periodic data sets for the same pressure probe used in the comparisons of the PSD and autocorrelation functions are plotted in Figure 23. Even though only a limited number of pressure data are available, the random data set are seen to approach a normal distribution and the periodic data set are seen to approach a sine wave distribution as expected. Since the random data is approximately normally distributed, the higher order statistical properties will be stationary since the autocorrelation function (variance when using the fourth assumption as described above) and the mean are stationary.

The time history values of freestream total pressure, instantaneous probe pressure L6R3 and the associated mean and variance values are presented in Figure 24 for both the random and periodic flight test data sets. The time history mean and variance values can be seen to be stationary for the random data of Figure 24(a), whereas the time history mean and variance values of Figure 24(b) are periodic as expected for the periodic data.

The statistical functions used to prove random stationarity for the flight data have also been used to verify random stationarity for the wind tunnel data. These statistical functions are presented in Figure 25 through Figure 30 for data collected using the full scale model with engine, the full scale coldpipe model (without engine) and the 1/6th scale inlet model. High frequency spikes occurred in some of the wind tunnel PSD plots as shown in Figures 25a, 27a and 29a. The cause of these spikes is unknown, however, the frequency at which they occurred is significantly above the frequency of interest for this study. The normalized autocorrelation function of Figure 27 shows a bias or offset of approximately -0.2. The cause of the offset is unknown, but the level of correlation is insignificant. These two discrepancies have no impact on this study. The time history plots of instantaneous pressure, of mean pressure and of the pressure variance for selected probes from each of the test conditions listed in Figure 19 are presented in Appendix C.

In summary, representative data from the complete data matrix have been shown to be random stationary. In addition, assumptions have been verified that allow random stationary data to be demonstrated using only the time averaged mean and variance of the pressure values.

INTERPOLATION PROCEDURE

One of the primary considerations in establishing the study base was identifying test conditions with comparable engine airflows for each test article. Since actual inflight engine airflows could not be predicted for every combination of Mach number and altitude combination during the development phase of the inlet, the data collected during the wind tunnel testing and the data collected during flight testing generally have different engine airflow values even though the geometrical configurations are identical. Significant differences in distortion level can occur not only because of the differences in the total pressure contours at the engine face, but also as a result of significant changes in the engine related weighting factors which are a function of engine airflow.

As an example, the effect of filter cutoff frequency on fan distortion and turbulence is illustrated in Figure 31 where the airflow for each data point of the test condition is different. These data are not directly comparable since each curve is for a different airflow. Therefore, to illustrate the effect of engine airflow, the data with filter cutoff frequency of 170 Hertz are plotted in Figure 32 as a function of corrected engine airflow for each of the three test articles. Since only one airflow level (78.9 percent) is available for the flight data, the full scale cold pipe data and the full scale with engine data have to be interpolated and extrapolated respectively to obtain comparable distortion and turbulence values. Note that the full scale cold pipe fan distortion levels at 78.9 percent engine airflow are significantly higher than those of the other two test articles.

In general, the circumferential and radial components of fan distortion are well behaved functions of airflow. Since fan distortion is not only dependent on these descriptors but also on the radial distortion weighting factor which is not a well behaved function of airflow (as discussed above), fan distortion is not expected to be a well behaved function of airflow. Therefore, interpolation of circumferential and radial distortion data is technically feasible whereas interpolation of fan distortion is questionable.

A technique involving linear interpolation/extrapolation of circumferential and radial distortion data was developed for this study. The interpolated values are used together with the appropriate radial distortion weighting factor as a function of engine airflow to define fan distortion values at constant engine airflow. The solid symbols of Figure 33 were computed using this technique. In the engine airflow range of 82 percent, the interpolated values of fan distortion strongly reflect the characteristic variation of the radial distortion weighting factor with airflow, as might be expected. However, comparison of the differences between the distortion levels ($\pm$0.4) at 78.9 percent for the three test articles and of the screening curve, Figure 17, distortion level (8.4) illustrates that the differences are relatively insignificant.

The results of interpolating the fan distortion and turbulence at all frequencies for 78.9 percent engine airflow is shown in Figure 34. For a constant filter cutoff frequency, increasing turbulence correlates with increasing fan distortion, and for a particular test article increasing the filter cutoff frequency increases both fan distortion and turbulence.

Interpolated/extrapolated fan distortion values with respect to airflow have been computed using this technique throughout the study to make direct data comparisons when comparisons at identical airflows are not available.

ENGINE PRESENCE EFFECT ON DISTORTION LEVELS

The data for this study are unique since there are limited sets of data where the same inlet has been tested both with and without an engine. The effect of the engine installation was evaluated for the test conditions shown in Figure 35. Sixteen data points for supersonic flight conditions were used to establish the five test conditions for evaluation.

The inlet models used to generate the data are the full scale with engine (FSE) and the full scale cold pipe (FSCP) which in effect is the same inlet model tested with and without an engine. Therefore, the inlet geometrical configurations are identical for these test conditions with the exception of bypass door areas which differ for two test conditions as noted in Figure 35.

However, the bypass area differences were only significant for the Mach 2.2, $\alpha = -2°$ test condition, therefore only this condition was eliminated from the comparisons to determine engine presence effect. In determining the effect of engine presence on distortion level, the following six items were investigated: (1) steady state and instantaneous pressure contours, (2) power spectral density functions, (3) derived turbulence level, (4) total pressure recovery, (5) fan distortion descriptor, and (6) measured turbulence level.

Contour Plots and Power Spectral Density Plots

The comparisons of steady state total pressure contours, instantaneous total pressure contours and power spectral density (PSD) plots with and without engine are shown in Figures 36 through 45. In general, the steady state total and instantaneous pressure contours compare favorably. In particular, the steady state contours of Figure 40 are almost identical. The engine airflow differences between these contours is 1.0 percent. The small differences in the steady state contours of the other comparisons may be due to small differences in the airflow levels.

Although the patterns for with and without engine are similar for both steady state and instantaneous pressure contours, one qualitative difference was observed. In Figure 40, the "islands" in the upper right quadrant for both the steady state and the instantaneous contours tend to be slightly rotated counter clockwise for the with engine contours, the same rotational direction as the engine.

The steady state pressure contours are labeled with the static pressure ratios and their locations in Figures 36 through 40. A compilation of these static pressure ratios is presented in Figure 36 for increasing engine airflow for each test condition. In addition, the average hub and average tip static pressure ratios have been computed for each data point and are plotted in Figure 47. For these five test conditions, the data indicates that the engine presence decreases the average tip static pressure ratio relative to the average hub static pressure ratio. These relative changes in hub and tip static pressure ratios reflect relative changes in hub and tip duct velocities that are conducive to improved inlet engine compatibility for these test conditions.

The power spectral density (PSD) plots, with and without engine are presented in Figures 41 through 45. Additional PSD plots for each of these data points are presented in Appendix D, and the corresponding auto-correlation functions are presented in Appendix E. The PSD functions are well behaved for all the data points and test conditions evaluated.

Turbulence, derived from these PSD plots by integration, is presented as a function of filter cutoff frequency in Figures 48 through 52 for the respective PSD plots of this section. The characteristic function of turbulence as a function of frequency is consistent and well behaved for these pressure probes. Turbulence values for every PSD plot of this study were derived and presented as a function of frequency in Appendix F. No apparent engine effect was observed for the PSD plots or for their respective integrated functions.

Pressure Recovery, Distortion and Turbulence

Total pressure recovery, peak time variant distortion and turbulence values with and without the engine present are compared in Figures 53 and 54. In these figures, favorable engine effects are indicated for total pressure recovery values above and time variant distortion values below the line of perfect agreement. For each of these three inlet parameters, the data indicated that the engine has a small but favorable effect.

In summary, a qualitative assessment of the total pressure contours and power spectral density plot comparisons indicates that the "with" and "without engine" inlet configuration result in no significant differences. However, a quantitative assessment of total pressure recovery, peak time variant distortion and turbulence level comparisons indicate a small but favorable effect of the engine installation. In addition, the data indicate that the engine presence decreases the average tip static pressure ratios relative to the average hub static pressure ratios.

REYNOLDS NUMBER/SCALE EFFECTS ON DISTORTION, PRESSURE RECOVERY AND TURBULENCE

To evaluate the effect of Reynolds number/scale on peak time variant distortion, steady state distortion, total pressure recovery, spatial distortion and turbulence, 62 data points were utilized from a total of 82 for the study. The respective test conditions for the 62 data points are shown in Figure 55. The Reynolds number/scale evaluation was conducted using time variant data filtered at 170 Hertz for full scale data and at 1040 Hertz for 1/6th scale data. The Reynolds number/scale values are computed by multiplying the Reynolds number per foot values obtained from the test conditions by one foot (unit characteristic length) for full scale data and by 1/6th foot for the 1/6th scale data.

In general, the range of Reynolds number/scale values for each of the test articles are shown in the following table. An F-15 flight envelope as a function of Reynolds number/scale and Mach number is shown in Figure 56.

Inlet Model	Reynolds Number/Scale
1/6th scale	$0.2 \times 10^6 - 0.4 \times 10^6$
Full Scale Cold Pipe (FSCP)	$1.2 \times 10^6 - 1.5 \times 10^6$
Full Scale With Engine (FSE)	$1.2 \times 10^6 - 3.6 \times 10^6$
Flight	$0.8 \times 10^6 - 3.6 \times 10^6$

Plots of total pressure recovery, turbulence levels, peak time variant distortion values and time variant spatial distortion (at peak time variant distortion) as a function of Reynolds number/scale are presented in Figures 57 through 82. In addition, steady state fan distortion data and steady state spatial distortion data are shown as solid symbols and exhibit the same trends as the corresponding time variant data. The majority of the data show the expected trends of increasing total pressure recovery and decreasing peak time variant distortion and turbulence with increasing Reynolds number/scale. Time variant spatial distortion was evaluated at the same time frame at which the peak time variant distortion level occurred and shows no consistent trend with increasing Reynolds number/scale.

The data trend of increasing pressure recovery and decreasing fan distortion and turbulence as a function of increasing Reynolds number/scale does have some inconsistencies, examples of which are shown in Figures 58 and 62. The discrepancies occur in comparing 1/6th scale inlet data at low Reynolds number/scale values ($.2 - .45 \times 10^6$) to full scale inlet data (either flight, FSE or FSCP) at low Reynolds number/scale values (approximately 1.5×10^6). These discrepancies do not occur when comparing 1/6th scale inlet data at low Reynolds number/scale to full scale data at large Reynolds number/scale values (3.5×10^6). The discrepancies noted represent only a small percentage of the data evaluated for the effect of Reynolds number/scale and may be due to several possible factors.

Peak time variant distortion is a statistical parameter since it is computed from random stationary time variant pressure data. The peak value for a given time segment may not repeat itself exactly, but may fall into a range of values for the specified time segment. Therefore as the range of Reynolds number/scale values is reduced, the variation in the peak distortion values for a given time segment may overshadow the change in peak time variant distortion for small changes in Reynolds number/scale values. Note that the discrepancies did not occur for large differences in Reynolds number/scale values. In addition, the discrepancies in the Reynolds number/scale data trend occurred for comparisons of 1/6th scale inlet data and full scale inlet data. While these two sets of data were acquired with identical rake configurations, different dynamic probes and different data acquisition systems were used.

In summary, the data exhibits a definite trend as a function of Reynolds number/scale, i.e., increasing total pressure recovery, decreasing peak time variant distortion values and decreasing turbulence levels as a function of increasing Reynolds number/scale. The time variant spatial distortion value taken at peak time variant fan distortion did not correlate with the peak time variant fan distortion value.

FREQUENCY CONTENT EFFECT ON DISTORTION AND TURBULENCE

The test conditions and the thirty two associated data points used to determine the effect of frequency content on peak time variant fan distortion, turbulence level and time variant spatial distortion values (at peak time variant fan distortion) for various values of Reynolds number/scale are shown in Figure 83. For each test condition, the data were evaluated at the engine corrected airflows listed in Figure 83.

To relate frequency content to peak time variant distortion, the analog pressure data were filtered at selected filter cutoff frequencies, and peak time variant fan distortion, turbulence and spatial distortion were calculated and plotted as a function of the filter cutoff frequency. The filters used for this study were the adjustable four pole Bessel filters described in Figure 11. The full scale filter cutoff frequencies were selected to be both greater than and less than the P&WA specified engine filtering frequency of 170 hertz. The 1/6th scale filter cutoff frequencies are scaled to match the full scale filter cutoff frequencies using the frequency scaling criteria of Reference (2). The filter cutoff frequencies used for full scale pressure data were 45, 100, 170 and 500 hertz, and the filter cutoff frequencies used for the 1/6th scale pressure data were 275, 615, 1040 and 3070 hertz. The frequency content effect on fan distortion, turbulence and spatial distortion for the 1/6th scale test is plotted as a function of the equivalent full scale filter frequencies to simplify the comparisons between the 1/6th scale and full scale data. To accurately represent these data digitally, the analog pressure signals were sampled at approximately five times (or greater) the appropriate filter cutoff frequency. The sampling rates varied from 270 samples per second to 21,000 samples per second, and these rates are listed in Figure 11 for each of the respective filter cutoff frequencies.

Filter Cutoff Frequency Effect

Increasing filter cutoff frequency is seen to increase peak time variant distortion as shown in Figure 34. This effect of filter cutoff frequency on peak time variant fan distortion and turbulence is expected if a physical understanding of the frequency content is recognized. A power spectral density plot is shown in Figure 84a, with dependent and independent parameters of $\Delta P^2/Hz$ and frequency respectively. The area beneath the curve from zero frequency to a selected "cutoff" frequency is proportional to turbulence. Since turbulence is proportional to the area beneath the PSD curve, the larger the cutoff frequency for a particular pressure probe the large the turbulence as shown in Figure 84b. This same logic follows for peak time variant fan distortion values. Since time variant distortion is calculated using time variant pressure increases in time variant pressure variance (increases in turbulence) increase the probability of larger peak time variant distortion values with increasing cutoff frequency.

Peak time variant fan distortion increases as filter cutoff frequency is increased, but the peaks do not necessarily occur at the same segment time. This effect can be seen in Figure 85 where time history traces of time variant distortion for cutoff frequencies of 45, 100, 170 and 500 Hertz are shown for data point 43. Time history traces of time variant distortion are shown in Appendix G for all of the data points in this section. The time history data traces include 100 milliseconds of 1/6th scale (600 milliseconds for full-scale data) time variant distortion data and the peak distortion level.

Peak time variant distortion, turbulence and spatial distortion data are presented as a function of full scale filter cutoff frequency in Figures 86 through 93. The curves for turbulence pass through zero turbulence at zero cutoff frequency. This simply implies that at zero frequency response the time variant pressure (with no variance) is equal to the steady state pressure. Similarly, the time variant distortion value at zero frequency response is equal to the steady state fan distortion. The steady state fan distortion levels are denoted by solid symbols in the plots.

For all test conditions, increasing filter cutoff frequency increased both the levels of peak time variant fan distortion and turbulence. For all but one test condition, the test article with the highest turbulence also has the highest distortion level for a given filter cutoff frequency. The time variant spatial distortion data at peak time variant fan distortion did not indicate any correlating properties with peak fan distortion. The plotted values of spatial distortion appear to occur randomly about the steady state level.

Combined Effect of Filter Cutoff Frequency and Reynolds Number/Scale

The effect of Reynolds number/scale on peak time variant fan distortion, turbulence level and spatial distortion is shown in Figures 94 through 101 for constant levels of filter cutoff frequency. The trend of decreasing turbulence level and decreasing peak time variant fan distortion for increasing Reynolds number/scale is similar to that shown in the section for Reynolds number/scale effects. This trend in the data appears to be consistent for all levels of filter cutoff frequency. Since much of the same data is utilized here as in the Reynolds number/scale analysis, some of the same discrepancies occur. Since they were discussed in the previous section, they are not reiterated here.

In summary, turbulence level and peak time variant fan distortion increase as filter cutoff frequency is increased. This data trend is maintained when evaluating turbulence level and peak time variant distortion as a function of Reynolds number/scale for constant filter cutoff frequency.

PEAK TIME VARIANT FAN DISTORTION PREDICTIONS

The primary objective of this analysis was to compare the predicted most probable peak distortion values as computed by Melick's procedure to the measured peak time variant distortion values. Melick's procedure was developed under NASA Contract NAS2-6901 and is described in detail in Reference (1).

The necessary inputs to Melick's procedure, an evaluation of the distortion prediction capability and an assessment of the hypothesis used in developing the procedure are described below.

Inputs to Melick's Procedure

The necessary inputs to Melick's procedure are:

- Unfiltered turbulence for each of the dynamic probes to be used in the prediction (each data point was evaluated using unfiltered turbulence levels for all 48 dynamic probes),
- Ratio of filtered mean square pressure variation to unfiltered mean square pressure variation for each of the dynamic probes to be used in the prediction (each data point was evaluated using mean square pressure ratios for all 48 dynamic probes),
- Filter cutoff frequency for the filtered mean square pressure variation,
- Airflow velocity at the engine face, normalized dynamic pressure, (q/P_{t_2}) at the engine face and engine cutoff frequency, $(f_{c/o})$ eng,
- Reference radial profile, radial distortion weighting factor, and analysis time,
- Steady state total pressure array at the engine face and the average engine face static pressure ratioed to freestream total pressure.

Measured and Predicted Peak Instantaneous Distortion Value Comparisons

The data points used to evaluate Melick's procedure are shown in Figure 102. This data set is composed of two sets of data, one with nominal average turbulence with no engine stalls and one with a high level of average turbulence such that an engine stall occurred for each data point. The comparison of measured peak time variant distortion values and the predicted most probable peak distortion values for the data with nominal turbulence levels and no engine stalls is shown in Figure 103. The average error for the predicted data is 11.3 percent. The comparisons of measured peak time variant distortion values and the predicted most probable peak distortion values for the data with high turbulence levels and engine stalls is shown in Figure 104. The average error for the predicted data is 20 percent with the maximum error approaching 40 percent. Note that the predicted distortion levels are lower than the measured distortion levels for all test conditions for the distortion data with high turbulence levels.

Vortex Diameter and Cross Correlation Coefficient Comparisons

Melick hypothesized in Reference (1) that inlet turbulence results from a random distribution of discrete vortices being convected downstream by the mean flow, and in Reference (7), that the cross correlation coefficient (at zero lag time) between two dynamic probes is a function of the probe spacing normalized by the vortex radius for these set of random vortices. To investigate these hypotheses for every pressure probe at the engine face would incur an exorbitant data reduction cost. However, Melick indicates in Reference (1) how the mean vortex position can be found, therefore allowing judicious selection of probes to be cross correlated. The procedure for finding the position of the vortex, an example of its use, and an investigation of Melick's hypothesis regarding the presence of vortices are discussed below.

Using the steady state total pressure data at the engine face, the rake legs having the minimum and maximum total pressure recovery are determined. If these two legs divide the engine face into two unequal circular segments, the vortex should be found in the smaller circular segment midway between the two legs. If the two legs with minimum and maximum total pressure recovery divide the engine face into two semi-circles, the vortex should be found midway between the two legs in the semi-circle with lowest overall pressure recovery.

An example of how the probes were selected for computing cross correlation functions uses the steady state total pressure contour shown in Figure 105. The rake legs with minimum and maximum total pressure recovery bracket the circumferential section of interest and are noted. The probes are selected on the rake leg approximately midway within the designated circumferential sector. The circumferential section and rake leg location is noted in Figure 105. Cross correlation functions for the selected probes are presented in Figures 106, 107 and 108, and the peak correlation coefficients between the probes are noted in each figure. Cross correlation functions for each of the data points evaluated (without engine stalls) are presented in Appendix H and the respective cross spectral density plots are presented in Appendix I.

Using Melick's hypotheses of References (1) and (7) as previously discussed, the values of the computed vortex radius using Melick's analysis and the Cross Correlation Coefficients (at zero lag time) derived from measured pressure data are presented in Figure 109 for selected probes located in the region of the hypothetical random vortices. Using Melick's analysis, Reference (7), the cross correlation coefficients were derived that correspond to the computed vortex radius and probe spacing for each of the test conditions of Figure 109. The derived cross correlation coefficients and the measured cross correlation coefficients for each set of probes have been tested for similarity using the Chi-Square Test. Acceptance of the null hypothesis (H_o: derived cross correlation coefficient = measured cross correlation coefficient) would confirm the existence of a random set of vortices and would confirm the fluid dynamic model (Melick's analysis) representing the random set of vortices. However, the data for the test conditions corresponding to Figure 109 indicate that the null hypothesis can be rejected with more than 99.95 percent probability, i.e., Probability (derived cross correlation coefficient $\neq$ measured cross correlation coefficient) $>$ .9995.

However, the evaluation of these statistical data is inconclusive as to the determination of the existence or non-existence of a discrete set of random vortices. It is possible for the vortices to exist and the mathematical relationship between the vortex radius and cross correlation coefficient to be inaccurate, therefore yielding low probability of similarly between the measured and derived cross correlation coefficients.

In summary, Melick's procedure predicted peak distortion values to within 11.3 percent average error for fourteen data points having an average turbulence of 0.0155 and to within 20 percent average error for eight data points where engine stalls had been induced having an average turbulence of 0.109. The procedure is inaccurate for test conditions with high levels of inlet turbulence. The derived and measured cross correlation data is inconclusive as to the determination of the existence or non-existence of a discrete set of random vortices. If the vortices are present, then the theory for mathematical modeling of the vortices is inaccurate, and if the mathematical model of the vortices is correct, then the vortices are non-existent.

ENGINE STABILITY AUDIT EVALUATION

P&WA has established a stability audit system for the F100 engine which has been successfully used throughout the F-15 development program. The capability of the P&WA stability audit procedure to predict F100 engine stalls was evaluated for the ten flight conditions of Figure 110. Engine stalls were induced during the NASA F-15 Inlet/Engine Compatibility Flight Test Programs by positioning the inlet ramps to an off-design position, thereby artificially creating high inlet distortion levels. During this test program, aircraft instrumentation was installed to accurately measure inlet distortion and pertinent engine parameters necessary to conduct stability audits.

Stability Audit Procedure

The F100 engine stability audit procedure was developed to predict fan and high compressor stability level for steady state operation from idle to maximum augmentation. In addition, it can also be used to predict fan and high compressor stability levels for normal augmentor transients within intermediate power to maximum augmentation power setting. The engine audited in this study is an F100 (2 7/8) engine with Serial Number P690063. The F100 (2 7/8) engine compression system components consist of an Improved Stability Fan (ISF) with a -25° to -5° inlet guide vane schedule and an Advanced Aerodynamic Compressor (AAC) with a Scheme VII inlet guide vane schedule.

An engine matching procedure was established which matched F100 (2 7/8) data obtained during sea level tests, flight tests and simulated ground testing at AEDC. Sufficient instrumentation was available during the NASA F-15 Inlet/Engine Compatibility Test Program to obtain complete engine match points for the stability audits by matching the following measurands with the engine matching procedure. The procedure then provided predictions for any other required parameters.

$\overline{P_{t_2}}$ ∿ Fan inlet average total pressure

$\overline{T_{t_2}}$ ∿ Fan inlet average total temperature

N_1 ∿ Low rotor speed

CIVV ∿ Fan inlet guide vane angle

$P_{t_{6_m}}/P_{t_2}$ ∿ Engine pressure ratio

RCVV ∿ High Pressure Compressor (HPC) inlet guide vane angle

The surge line destabilizing influences accounted for in the stability audit include Reynolds number, engine-to-engine variations and inlet distortion as shown in Figure 111. Operating line destabilizing influences accounted for include distortion rematch and augmentor combustion anomalies.

The surge line destablizing influences applied to the highest available surge line (Point A) are shown in Figure 111. These influences include Reynolds number (Point B), engine-to-engine variations (Point C) and inlet distortion (Point D). The operating line destablizing influences applied to

the original match Point 1 are also shown. These include distortion rematch (Point 2), augmentor blowout (Point 3) and augmentor reignition (Point 4). After accounting for all destabilizing influences, the stall margin remaining is determined by subtracting the final operating pressure ratio from the final surge pressure ratio and normalizing this with the highest available surge pressure ratio, e.g. $(PR_D - PR_4)/PR_A$.

Surge line losses due to Reynolds number effects are based on a correlation of surge line loss versus Reynolds number for various engines including the F100. These losses were applied to fan and HPC undistorted surge lines previously obtained from numerous rig and engine tests. The surge line loss attributed to engine-to-engine variation was audited at one percent for both the fan and high compressor.

The surge line loss due to inlet distortion was based on time variant distortion measured with the 48 probe engine face rake. Fan and HPC sensitivities to inlet distortion have been previously determined from F100 rig and engine tests. Peak time variant distortion values were determined using an analog distortion calculator to "flag" maximum time variant distortion levels for non-stall test conditions. For test conditions with engine stall, values occurring 8-20 milliseconds prior to the engine stall were used for the audits.

The destabilizing effect on fan and high compressor operating lines due to distortion rematch was 1% and 0% respectively as determined from data collected during previous engine testing.

For some of the test conditions where engine stalls were induced by fully extending the third ramp actuator an augmentor anomaly (blowout and reignition) would occur. The effect of this anomaly on the fan operating line has been determined from measured engine parameters and factored into the stability audits of this study.

Induced Stall Procedure

The data for the induced engine stalls were obtained on a F100(2 7/8) test engine with Serial Number P690063 which was mounted in the left hand side of Aircraft Number 71-0281. Stalls were induced by manually extending the left inlet third ramp actuator shown in Figure 2 beyond the scheduled position.

Extending the inlet third ramp actuator beyond the scheduled position results in a smaller inlet throat area which significantly reduces total pressure recovery and increases fan distortion factor, K_{a2} as shown in Figure 112. Note the reduction in total pressure recovery and increase in distortion which occurs relative to normal third ramp scheduling ($\delta 3 = 11°$). This total pressure reduction brings about an increase in the effective pressure altitude at the engine face. The "as tested" altitude and Mach number for each of the stability audit points as well as the engine face effective pressure altitude is shown in Figure 113.

Stability Audit Test Conditions

The ten test conditions of Figure 110 were selected to provide representative stability audits throughout the F-15 flight envelope. Engine stalls were induced for eight of the ten test conditions by fully extending the third ramp actuator. The Mach number range for these eight test conditions is 0.4 to 1.2. The remaining two test conditions are for Mach number 1.6 and 2.0. For flight safety reasons, engine stalls were not induced at the high supersonic Mach number flight conditions. The instrumentation pertinent to measuring time variant fan distortion and for detecting the stalling component (fan and high pressure compressor) and augmentor instabilities is shown in Figure 114.

During the process of inducing engine stalls on engine P690063, augmentor combustion anomalies occurred for three of the ten test conditions. For Data Points 3, 4 and 16, augmentor blowouts occurred and were followed by stalls induced by augmentor reignition pressure pulses. The augmentor blowouts occurred because the augmentor was operating outside the design envelope. This occurred because the repositioned inlets ramps reduced the engine face total pressure to a level corresponding to an altitude outside the design envelope, as shown in Figure 113. The stability audit can account for the effect of augmentor blowout and reignition on the fan operating point by using the fan discharge high response probe data.

Upon examining the time history traces of fan distortion, it was found that the fan would, for some test conditions, tolerate distortion levels higher than those that finally stalled the fan. As the total pressure at the engine face was reduced, due to third ramp actuator extension, the engine operating pressures were reduced and the fan would match to a lower operating fan pressure ratio, thereby allowing tolerance to higher distortion levels. As the engine control system matched the fan back up to the normal operating fan pressure ratio, a peak distortion level would be encountered of sufficient level to stall the fan, thereby explaining the engine's temporary tolerance to higher than stalling distortion levels. These fan operating point excursions are depicted on a fan map in Figure 115.

Stability Audits

Five stability audits representative of the ten audits conducted are presented in the set of Figures 116 through 120. The audits for the remaining five test conditions are presented in Appendix J. The first figure of each set presents data traces of fan discharge high response pressures, fan inlet high response pressure and inlet third ramp actuator position at the time of the stall point audited or for the time at which peak distortion occurred during a non-stall point. The second figure of each set indicates the peak distortion value selected just prior to stall or the peak value during the event for a no-stall point. The third figure of each set presents the fan inlet pattern audited for each flight point, and the fourth figure of each set presents the fan and HPC stability audit results for each test condition.

For the fan and HPC stability audits, the corrected airflows presented were converted from the engine value to an equivalent fan and HPC "rig basis".

Stability audits are conducted on this basis since the original stall margin loss and distortion correlations were established from rig data. Stability audits for five of the ten test conditions are discussed below.

Stability Audit (Mach 0.59, Altitude=7610m, WAT2=104.1%, I.D.=2) - A fan stall during steady state augmentor operation with the third ramp actuator fully extended is illustrated in Figure 116a. An audit of the peak distortion just prior to stall (see Figures 116b and 116c) indicate a negative 6.2 percent fan stall margin and a positive 18.4 percent HPC stall margin remaining as shown in Figure 116d.

Stability Audit (Mach 0.52, Altitude=10960m, WAT2=107.1%, I.D.=3) - A rumble induced augmentor blowout followed by an augmentor auto-ignition relight, which induced a fan stall with the third ramp actuator full extended is illustrated in Figure 117a. An audit of the peak distortion prior to surge from Figure 117b indicates stable fan operation after the blowout but prior to augmentor reignition. Once reignition occurs, a negative 27.4 percent fan stall margin is shown in Figure 117d along with 14.7 percent positive HPC stall margin remaining. The augmentor blowout and reignition effects on the fan operating point were determined from the fan discharge high response pressure probe traces.

Stability Audit (Mach 0.85, Altitude=1076m, WAT2=104.2%, I.D.=15) - A fan stall during steady state augmentor operation with the third ramp actuator fully extended is illustrated in Figure 118a. Fan stability audits of the highest non-stall distortion, as well as the peak stall inducing distortion, from Figure 118b are presented in Figure 118d. The non-stall case indicates +0.6 percent positive fan stall margin remaining while the stall case indicates a negative 6.4 percent fan stall margin. The HPC stability audit is shown in Figure 118e and indicates a positive 15.0 percent HPC stall margin remaining.

Stability Audit (Mach 1.2, Altitude=11220m, WAT2=98.3%, I.D.=34) -A fan stall during steady state augmentor operation with the third ramp actuator fully extended is illustrated in Figure 119a. An audit of the peak distortion prior to stall from Figure 119b indicates a negative 3.1 percent fan stall margin and a positive 16.2 percent HPC stall margin remaining as shown in Figure 119d.

Stability Audits (Mach 1.6, Altitude=18470m, WAT2=89.3, I.D.=44) - High response pressures and inlet third ramp actuator positon at the time of peak distortion are illustrated in Figure 120a for this test condition. This was a supersonic non-stall event with the engine power set at maximum augmentation, and the inlet third ramp automatically scheduled to its normal position. The peak distortion factor shown in Figure 120c was audited and the results are shown in Figure 120d. The audits indicate a positive 22.4 percent fan stall margin remaining and a positive 17.0 percent HPC stall margin remaining.

Screening Curve Verification

The levels of distortion values for which a stall may occur for the F100 (2 7/8) engine are shown in the distortion screening curve of Figure 121. It is a screening curve in the sense that the values from this curve are not to be used as distortion limits for engine stall, but when an inlet distortion level for a particular airflow exceeds the comparable value from the screening

curve, additional analysis should be conducted to determine if there is any remaining engine stall margin for the particular test condition. The fan distortion levels for the audited test conditions are plotted on the screening curve of Figure 121. For the eight test conditions where engine stalls were induced, the distortion levels lie above the line in the region of predicted stability problems and the distortion levels for the two no stall test conditions lie below the screening curve in the region where stable operation is predicted. These results lend credibility to both the stability audit system and the screening curve.

Identification of Stall Inducing Distortion Peaks

For each of the stall points audited, the peak time variant distortion value just prior to the stall was chosen as the level which induced the stall. For each test condition evaluated, the data record time at which the peak distortion and the engine stall occurred are summarized in Figure 122, and the elapsed time from the beginning of the distortion data record to the engine stall is presented. The elapsed time from the audited peak distortion to the stall point, as indicated by stall overpressure, ranged from 8 to 20 milliseconds for all events. Numerous studies have indicated that this is the time interval magnitude required for the peak distortion pressure wave to travel from the instrumentation plane to the engine stalled compression stage, for the stall to occur, and for the stall overpressure to return to the instrumentation plane.

In summary, evaluation of the stability audit system indicates that sufficient technology exists to successfully predict inlet/engine compatibility status during the early phase of the inlet/engine development programs.

CONCLUSIONS AND RECOMMENDATIONS

Conclusions

The following conclusions can be drawn from the results of this program:

- Peak time variant distortion values from subscale inlet model wind tunnel tests are representative of those from full scale flight test aircraft.

- The time variant pressure data are random stationary data, thereby allowing valid statistical analyses to be conducted.

- The effect of the engine presence on total pressure recovery, peak time variant distortion and turbulence level is small but favorable.

- The Reynolds number/scale evaluation indicates a general trend of increasing total pressure recovery, decreasing peak time variant fan distortion and decreasing turbulence level as a function of increasing Reynolds number/scale.

- The frequency content evaluation indicates that peak time variant fan distortion and turbulence level increase as a function of increasing filter cutoff frequency for all of the data evaluated in this study.

- The capability of the Pratt & Whitney Aircraft stability audit system to predict engine stalls has been verified for both stall and non-stall flight test conditions.

- Predictions of peak distortion values using Melick's procedure are accurate to 11.3 percent average error for fourteen data points having nominal turbulence levels and are accurate to 20 percent average error (the maximum error approaches 40 percent) for eight data points having high turbulence levels.

Recommendations

Based on the results of this program the following recommendation is made:

- A statistical study should be made to evaluate the properties of the time variant distortion data. Specifically the distribution and variance of the peak time variant distortion values should be investigated as a function of analysis time to further aid in the interpretation of the data for this study.

REFERENCES

1. Melick, H. C., Ybarra, A. H. and Bencze, D. P.; "Estimating Maximum Instantaneous Distortion From Inlet Total Pressure RMS and PSD Measurements"; NASA TMX-73-145, June 1976.

2. SAE Committee S-16; "Gas Turbine Engine Inlet Flow Distortion Guidelines"; SAE Report ARP 1420, 15 June 1977.

3. Farr, A. P. and Schumacher, G. A.; "System for Evaluation of F-15 Inlet Dynamic Distortion"; MCAIR 72-043, September 1972.

4. Pratt and Whitney Aircraft Customer Computer Deck 1087-1.2, dated 14 March 1975.

5. Pratt and Whitney Aircraft Customer Computer Deck 1086-1.0, dated 14 July 1974.

6. Bendat, J. S. and Piersol, A. G.; "Measurement and Analysis of Random Data", J. Wiley, New York, 1967.

7. Melick, H. C., Ybarra, A. H.; "Estimating the Loss in Compressor Stall Margin Due to Inlet Turbulent Flow", Vought Technical Report 2-57110/3R-3133, Vought Corporation, Dallas, Texas 31 October 1973.

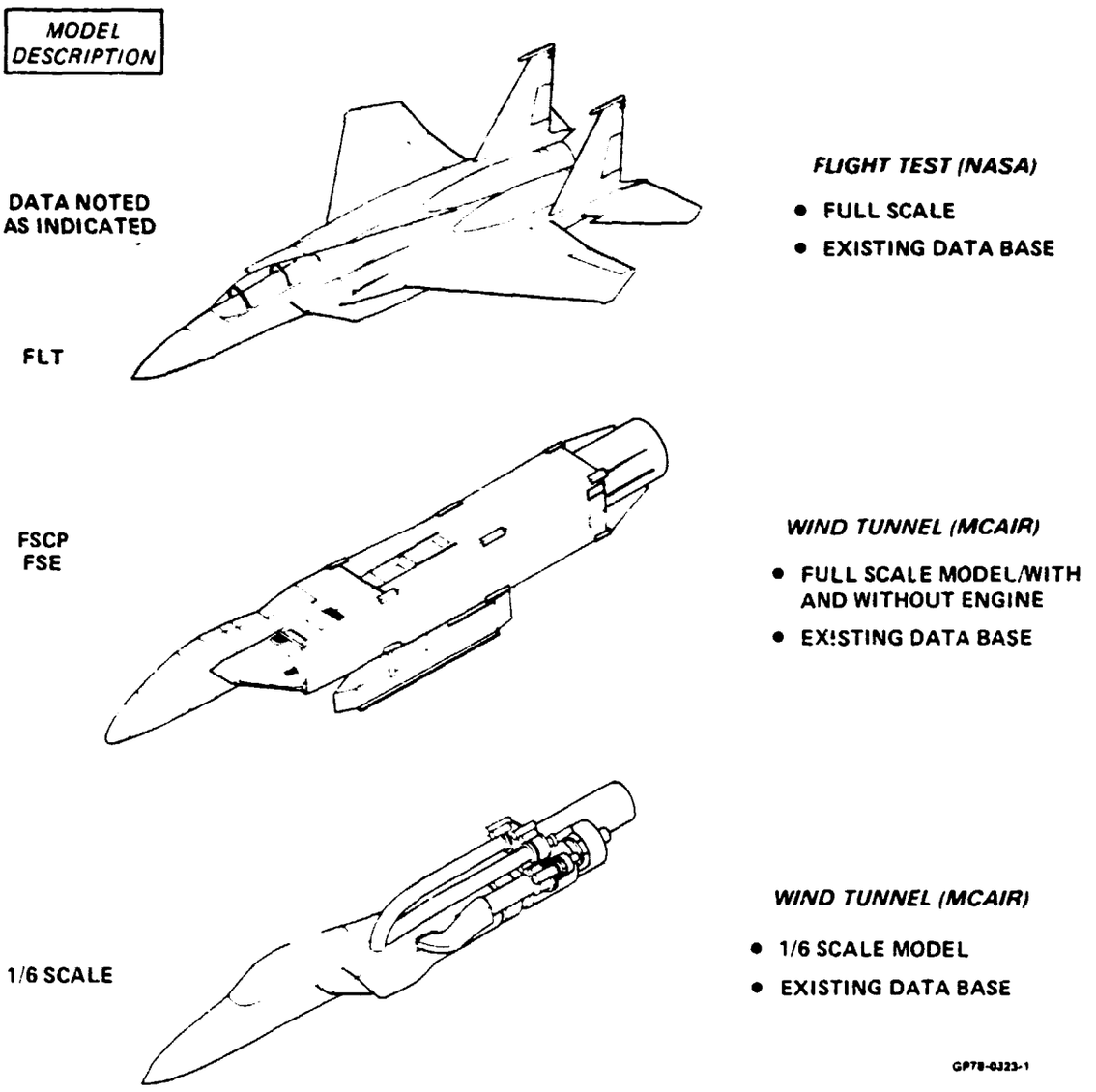

FIGURE 1
COMPARISON OF TEST ARTICLES FOR FLIGHT TEST, FULL SCALE INLET WIND TUNNEL TEST AND 1/6th SCALE INLET WIND TUNNEL TEST

MODEL DESCRIPTION

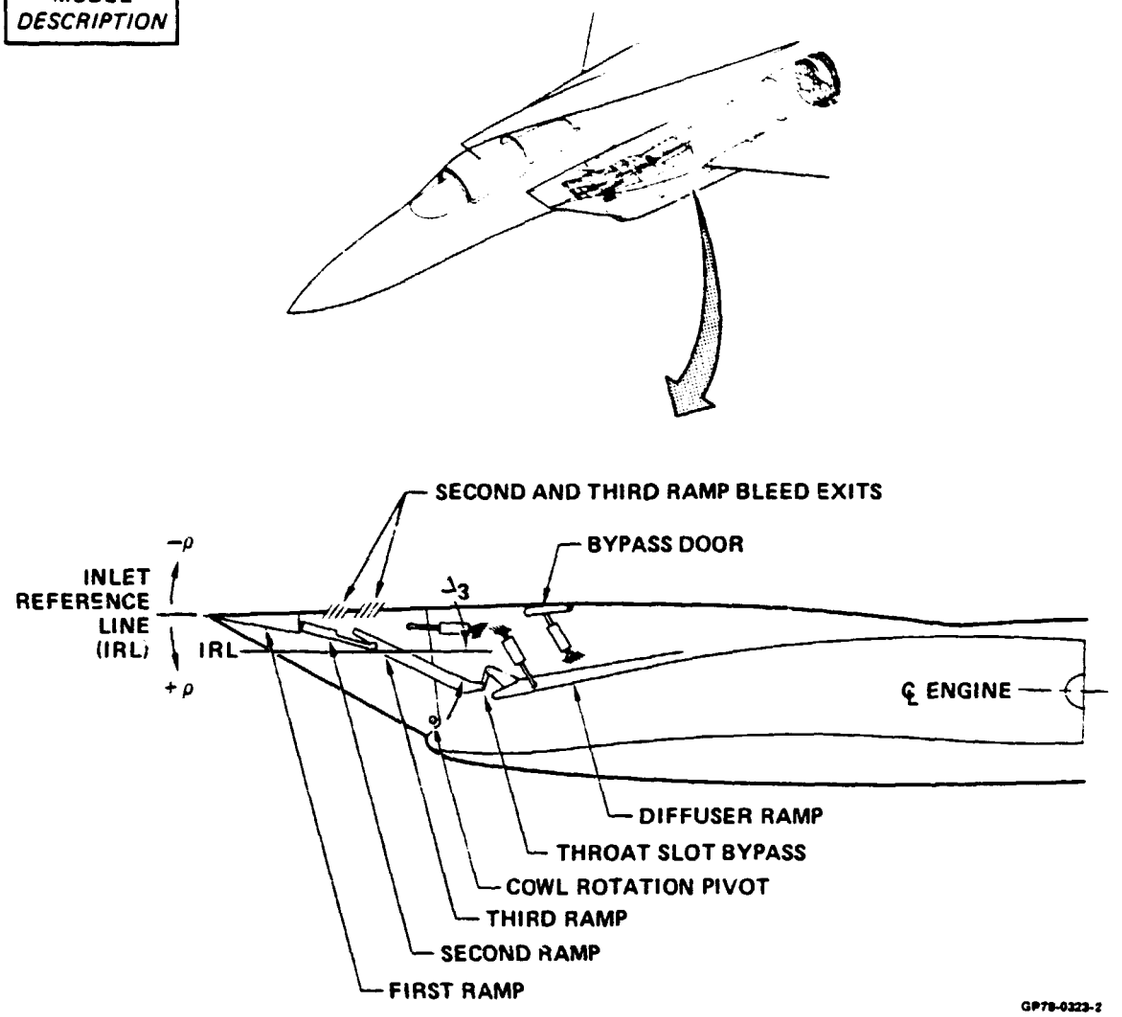

Note: Sideplate bleed not shown

FIGURE 2
F-15 ENGINE INLET

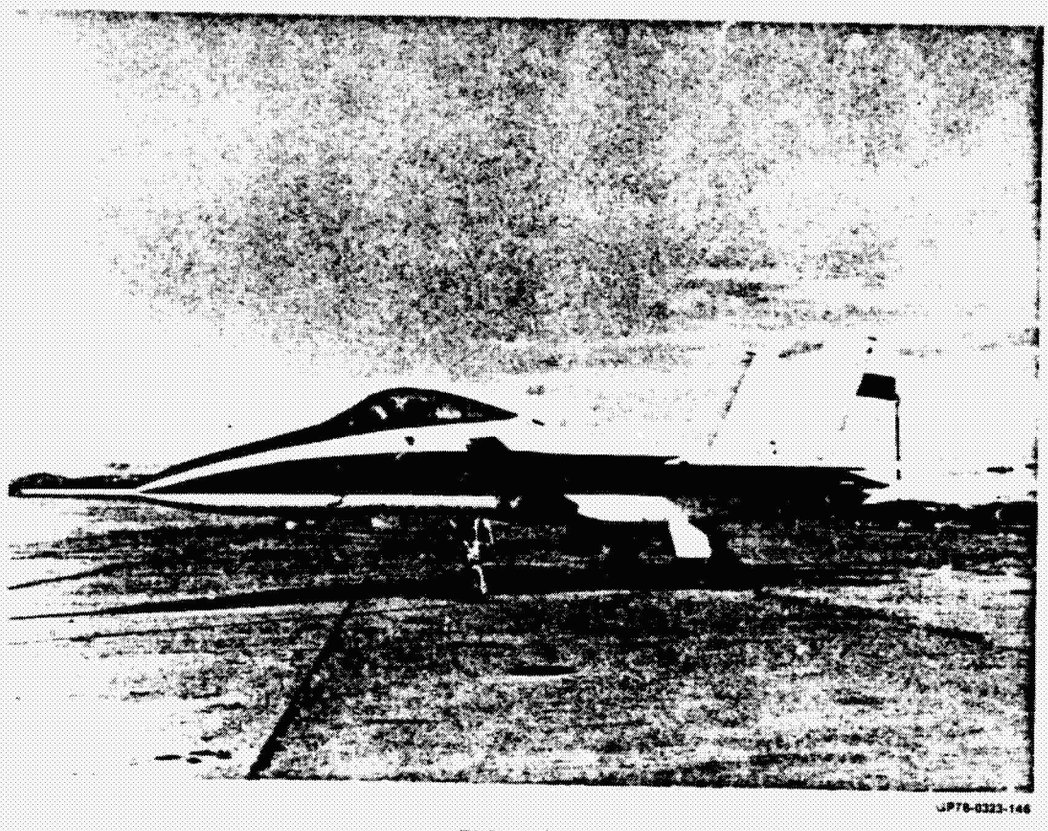

FIGURE 3
NASA F-15 FLIGHT TEST AIRCRAFT
AF 71-0281

MODEL DESCRIPTION

FIGURE 4
F-15 FULL SCALE INLET WIND TUNNEL MODEL

GP78-0323-15

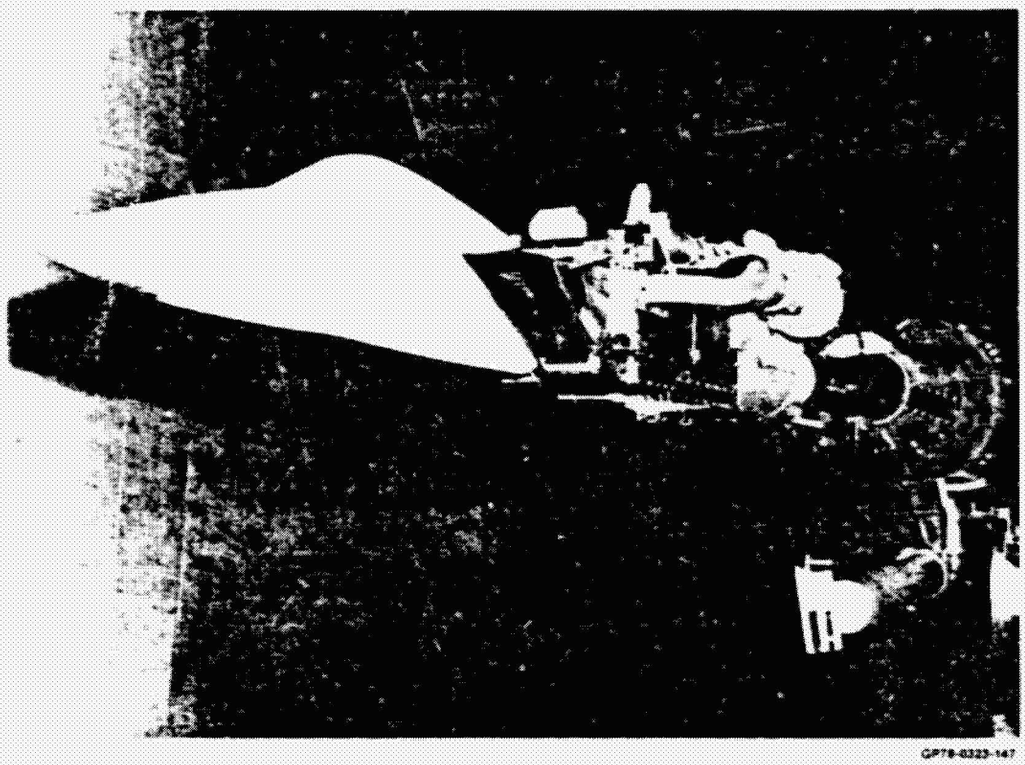

GP79-0323-147

FIGURE 5
F-15 1/6th SCALE INLET WIND TUNNEL MODEL

MODEL DESCRIPTION

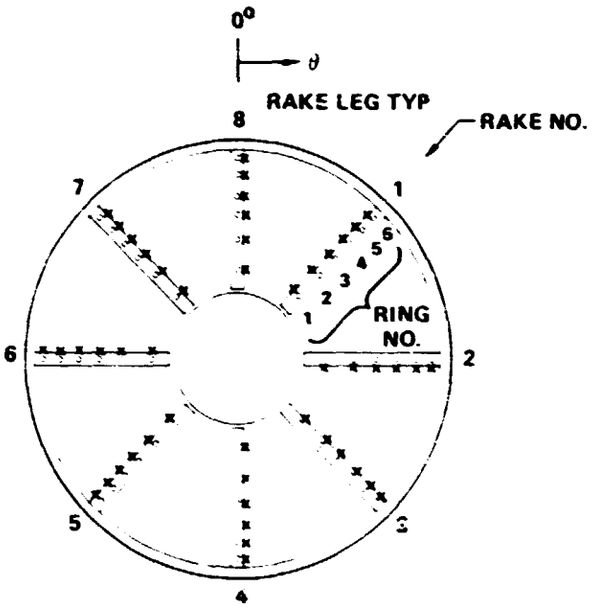

$\theta_1 = 45^\circ$ $r_{HUB} = 2.37$ cm
$\theta_2 = 90^\circ$ $r_1 = 3.11$
$\theta_3 = 135^\circ$ $r_2 = 4.22$
$\theta_4 = 180^\circ$ $r_3 = 5.09$
$\theta_5 = 225^\circ$ $r_4 = 5.83$
$\theta_6 = 270^\circ$ $r_5 = 6.49$
$\theta_7 = 315^\circ$ $r_6 = 7.09$
$\theta_8 = 360^\circ$ $r_{TIP} = 7.37$

A) 1/6 SCALE INLET MODEL

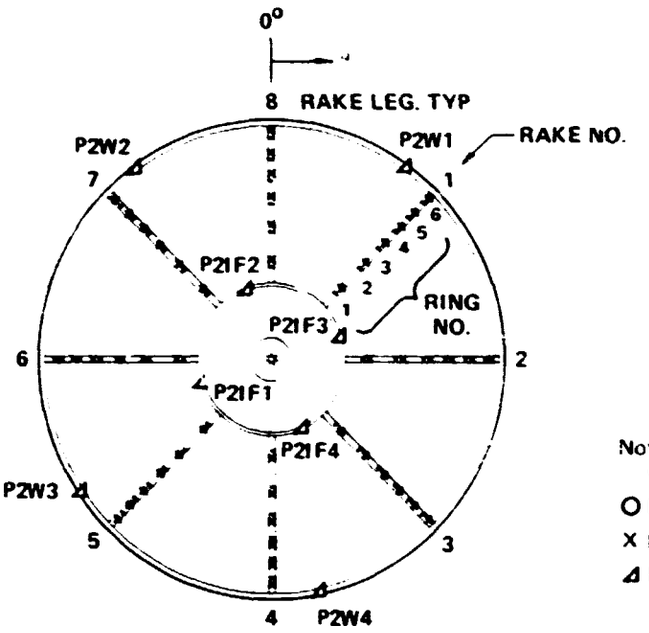

$\theta_1 = 45^\circ$ $r_{HUB} = 14.02$ cm
$\theta_2 = 90^\circ$ $r_1 = 18.48$
$\theta_3 = 135^\circ$ $r_2 = 25.19$
$\theta_4 = 180^\circ$ $r_3 = 30.46$
$\theta_5 = 225^\circ$ $r_4 = 34.94$
$\theta_6 = 270^\circ$ $r_5 = 38.91$
$\theta_7 = 315^\circ$ $r_6 = 42.51$
$\theta_8 = 360^\circ$ $r_{TIP} = 44.20$

Notes:
View looking aft at engine compressor face.
O Denotes fluctuating pressure locations
X Denotes steady state total pressure location
⊿ Denotes static pressure location

B) FULL SCALE INLET MODEL AND FLIGHT TEST AIRCRAFT GP78-0323-38

FIGURE 6
F-15 ENGINE FACE RAKES

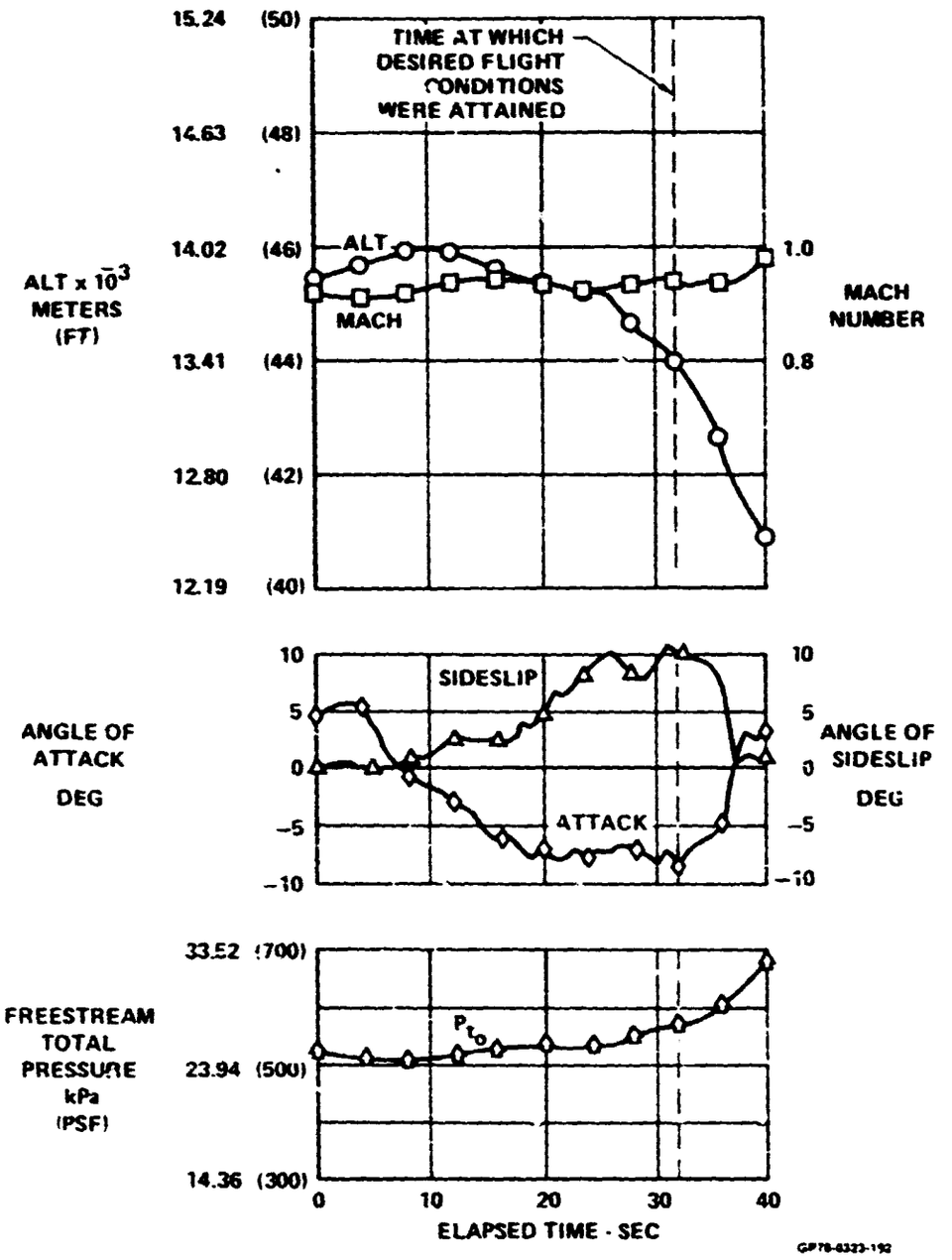

FIGURE 7

EVALUATE QUALITY OF TIME VARIANT DATA SAMPLE FLIGHT CONDITIONS

Mach 0.94 α = −8.9 β = 10.2 I.D. Number = 19 Flight 421 Run 14

TEST DESCRIPTION

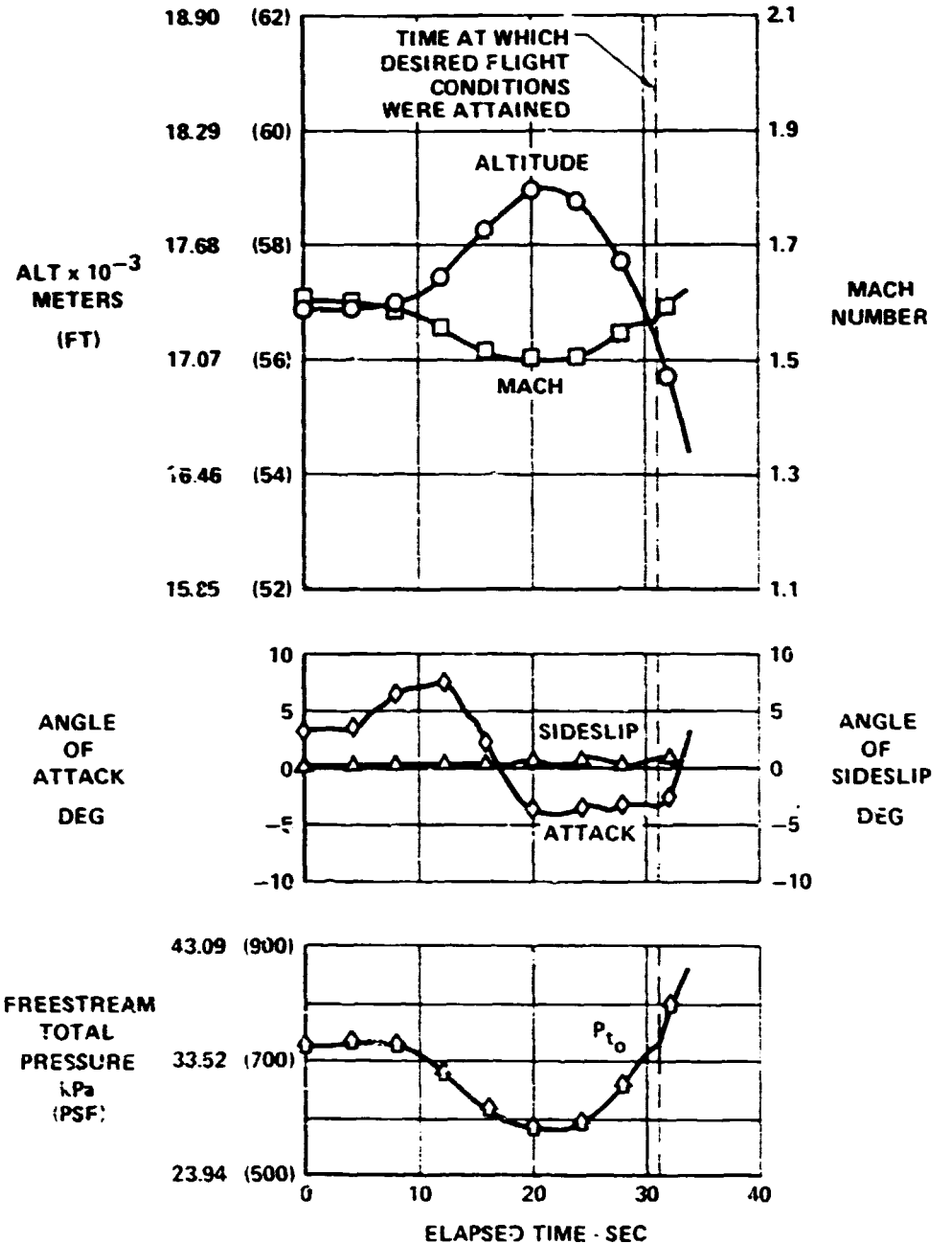

FIGURE 8
SAMPLE FLIGHT CONDITION

Mach 1.6 α = −3.6 β = 0.7 I.D. Number = 44 Flight 414 Run 2 GP78-0323 3

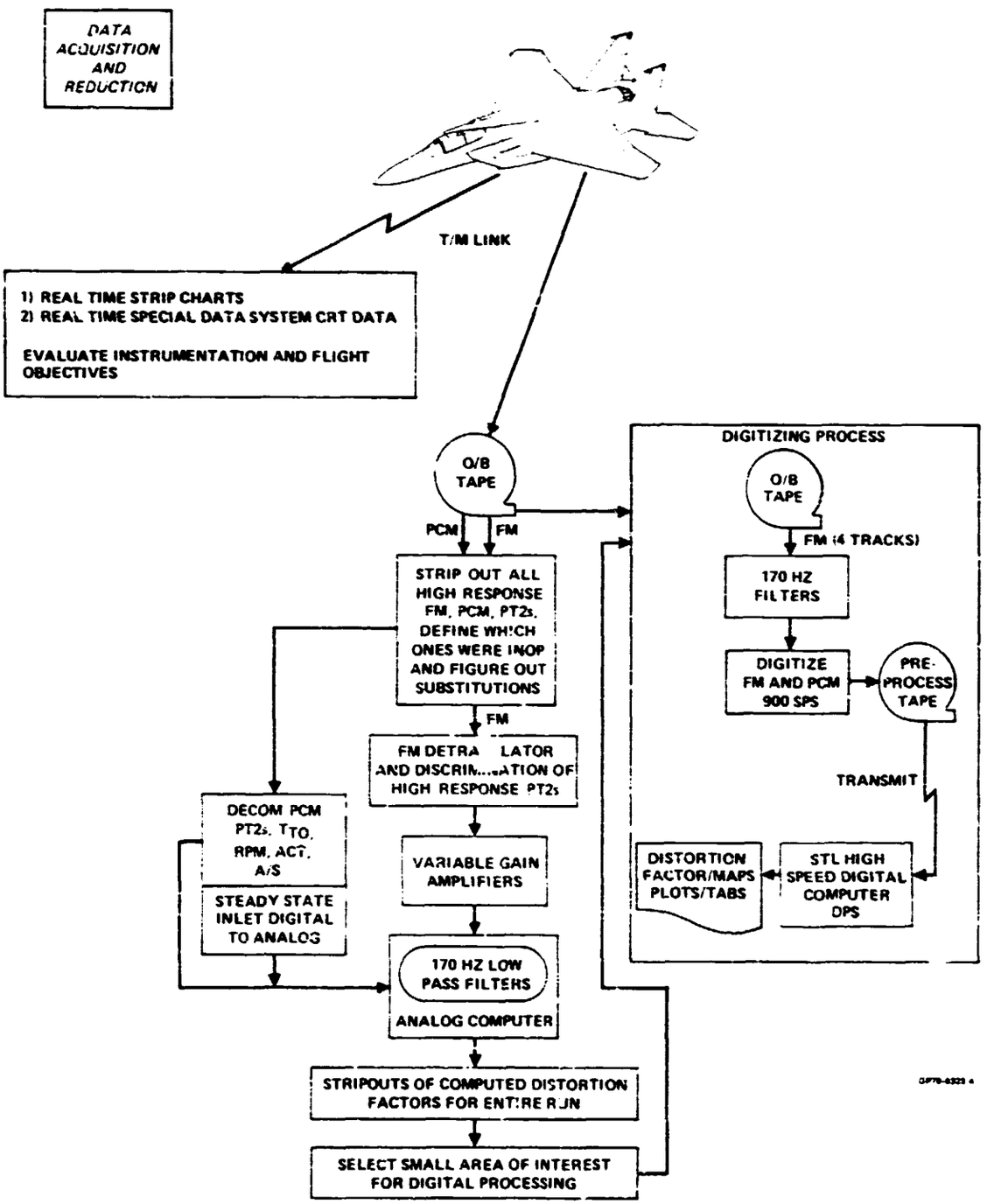

FIGURE 9
MCAIR FLIGHT TEST DATA MANAGEMENT SYSTEM

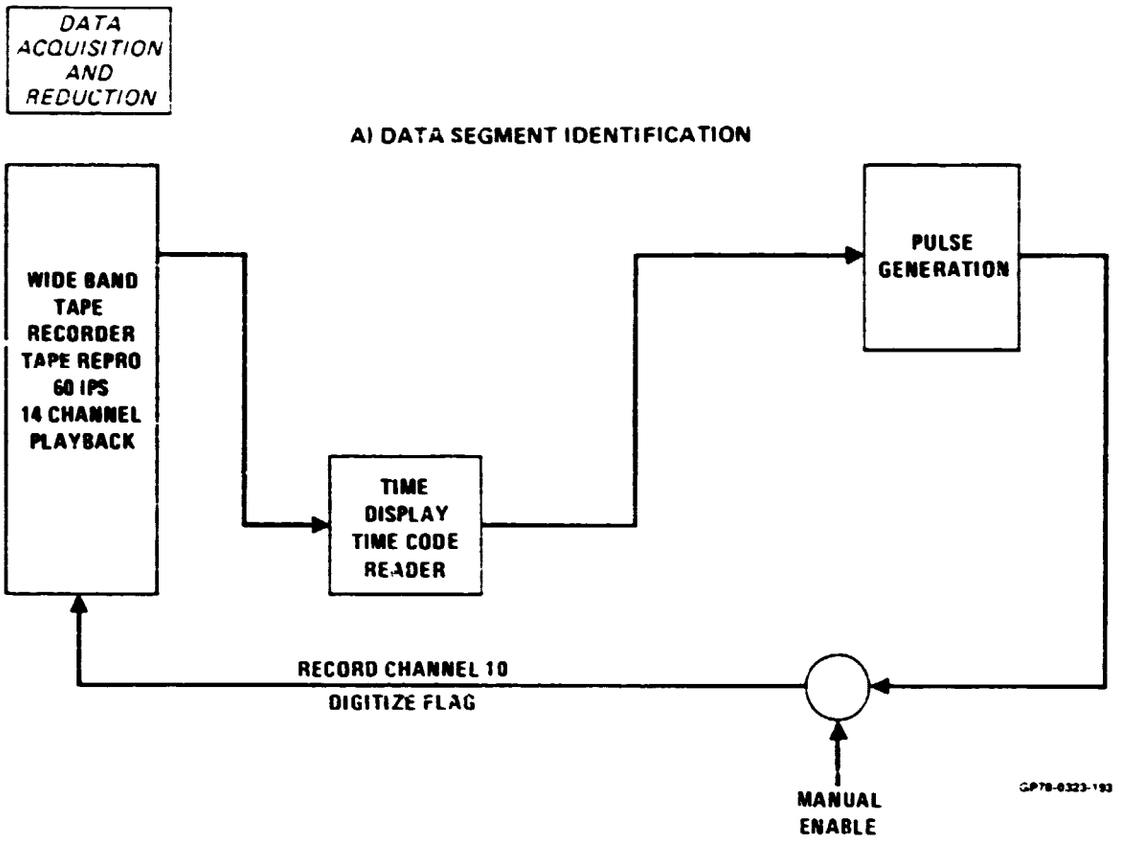

FIGURE 10
MCAIR WIND TUNNEL TEST DATA PROCESSING SYSTEM

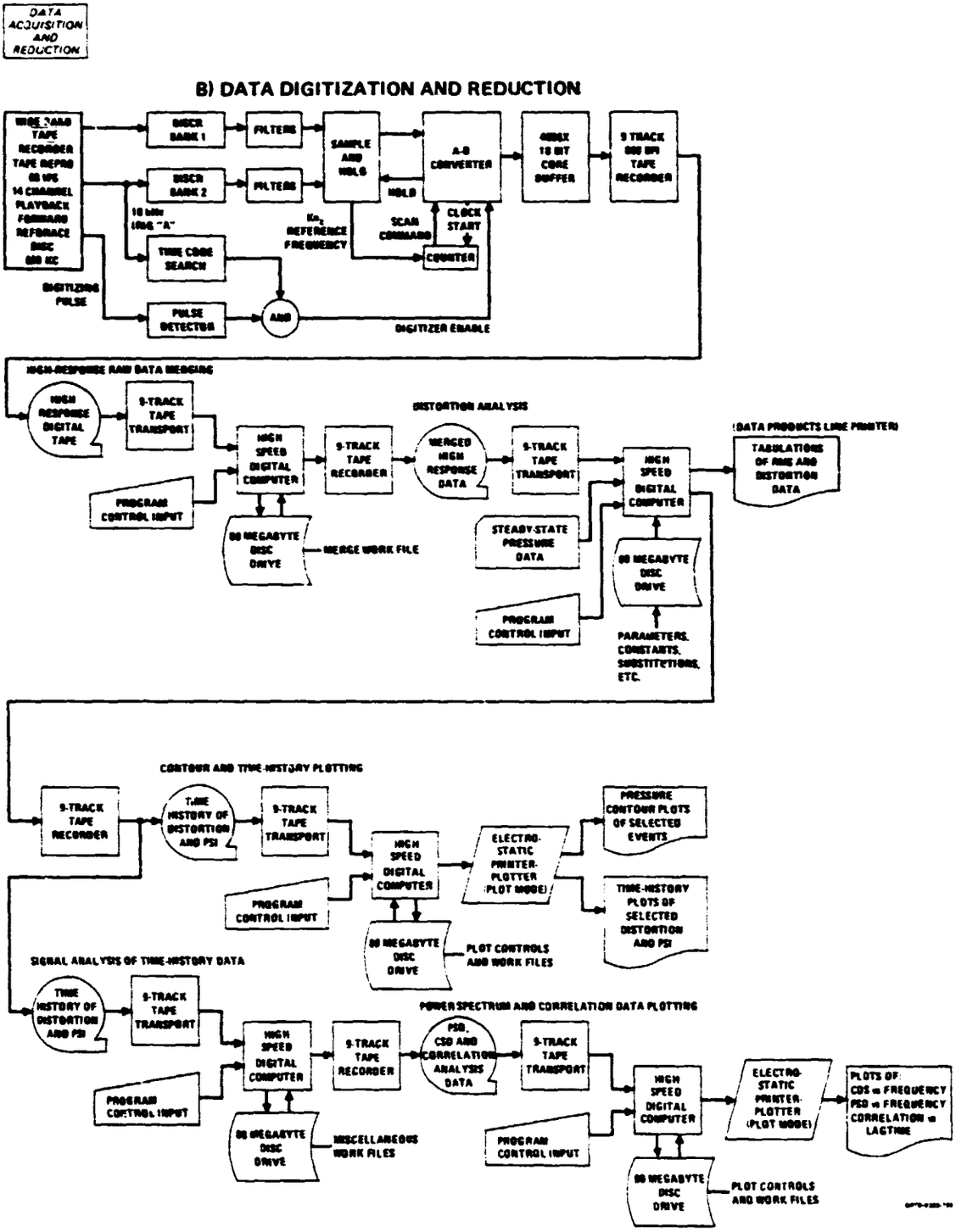

FIGURE 10 (Continued)
MCAIR WIND TUNNEL TEST DATA PROCESSING SYSTEM

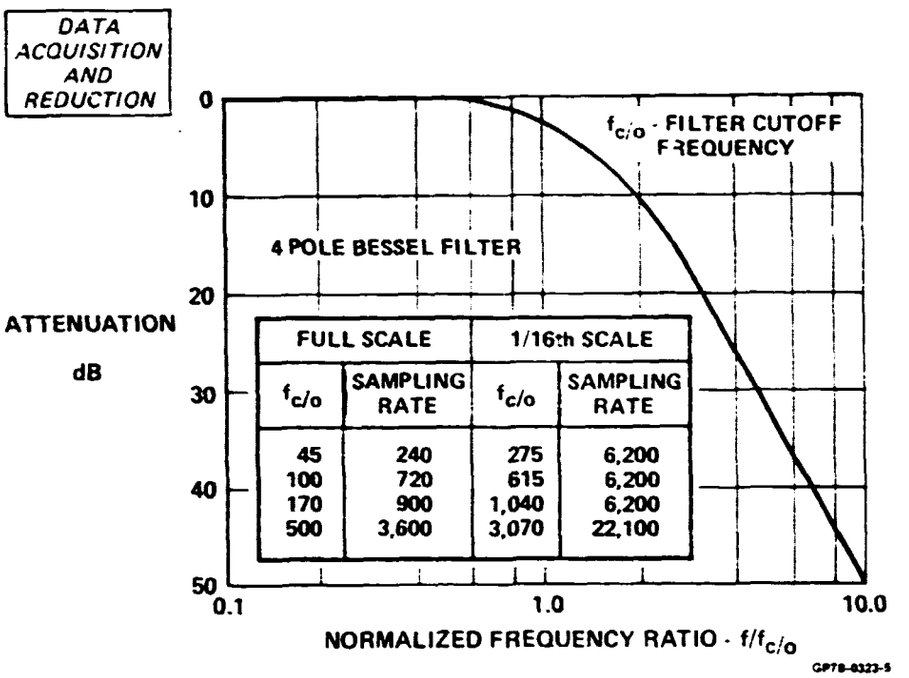

FIGURE 11
FILTER ATTENUATION CHARACTERISTICS AND CUTOFF FREQUENCIES

A) SUBSTITUTION CRITERIA

INOPERATIVE PROBES	SUBSTITUTION TECHNIQUE
SINGLE PROBES ON RING 2, 3, 4, OR 5	SUBSTITUTE AVERAGE 2 ADJACENT RADIAL PROBES
2, 3 OR 4 ADJACENT RADIAL PROBES ON RING 2, 3, 4 OR 5	SUBSTITUTE AVERAGE OF 3 ADJACENT PROBES (2 CIRCUMFERENTIAL AND 1 RADIAL)
2 ADJACENT CIRCUMFERENTIAL AND RADIAL SIMULTANEOUSLY	SUBSTITUTE AVERAGE OF ADJACENT RADIAL AND 2 ADJACENT CIRCUMFERENTIAL
SINGLE PROBES ON RINGS 1 OR 6	SUBSTITUTE AVERAGE OF 3 ADJACENT PROBES (2 CIRCUMFERENTIAL AND 1 RADIAL)
2 ADJACENT CIRCUMFERENTIAL PROBES ON RING 1 OR 6	SUBSTITUTE AVERAGE OF 3 PROBES AS INDICATED IN FIGURE 12B
GREATER THAN 2 ADJACENT CIRCUMFERENTIAL ON RING 1 OR 6	SUBSTITUTE THE OUTERMOST PROBE PER 5 ABOVE AND THEN USE SUBSTITUTION PROCEDURE
3 ADJACENT CIRCUMFERENTIAL AND 1 ADJACENT CIRCUMFERENTIAL AND 1 ADJACENT RADIAL	SUBSTITUTE AVERAGE OF 2 ADJACENT CIRCUMFERENTIAL AND 1 ADJACENT RADIAL

B) ENGINE FACE PRESSURE RAKE PROBE SUBSTITUTION

GP78-0323-2B

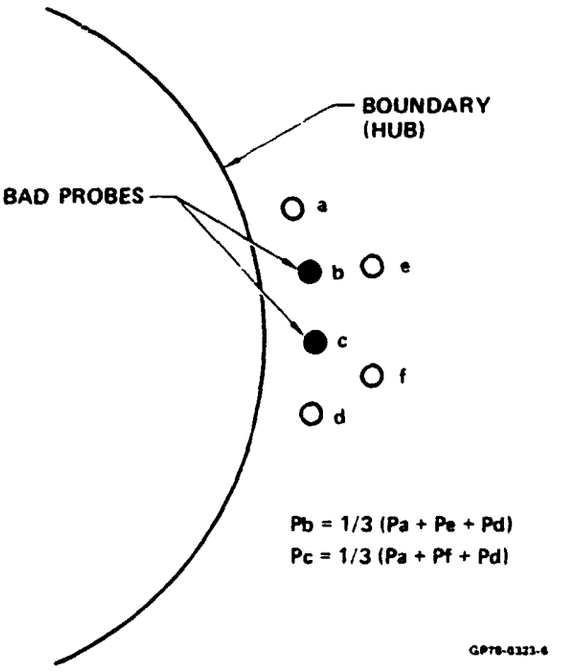

FIGURE 12
PRESSURE PROBE SUBSTITUTION TECHNIQUE
Example Diagram

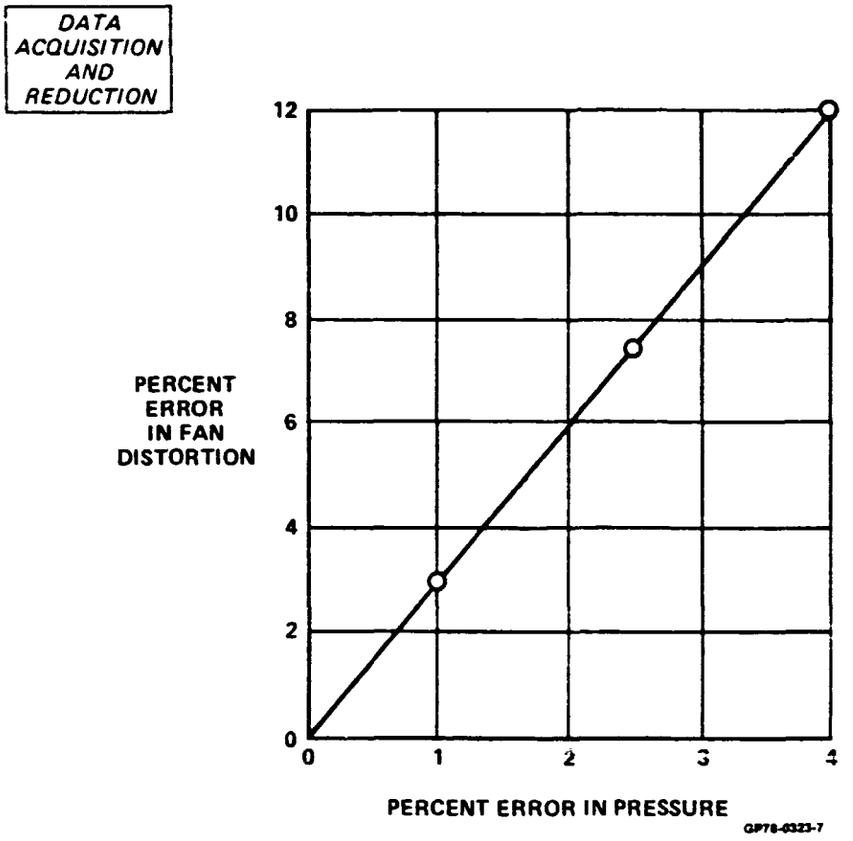

FIGURE 13
TYPICAL ERROR IN FAN DISTORTION
AS A FUNCTION OF PRESSURE ERROR

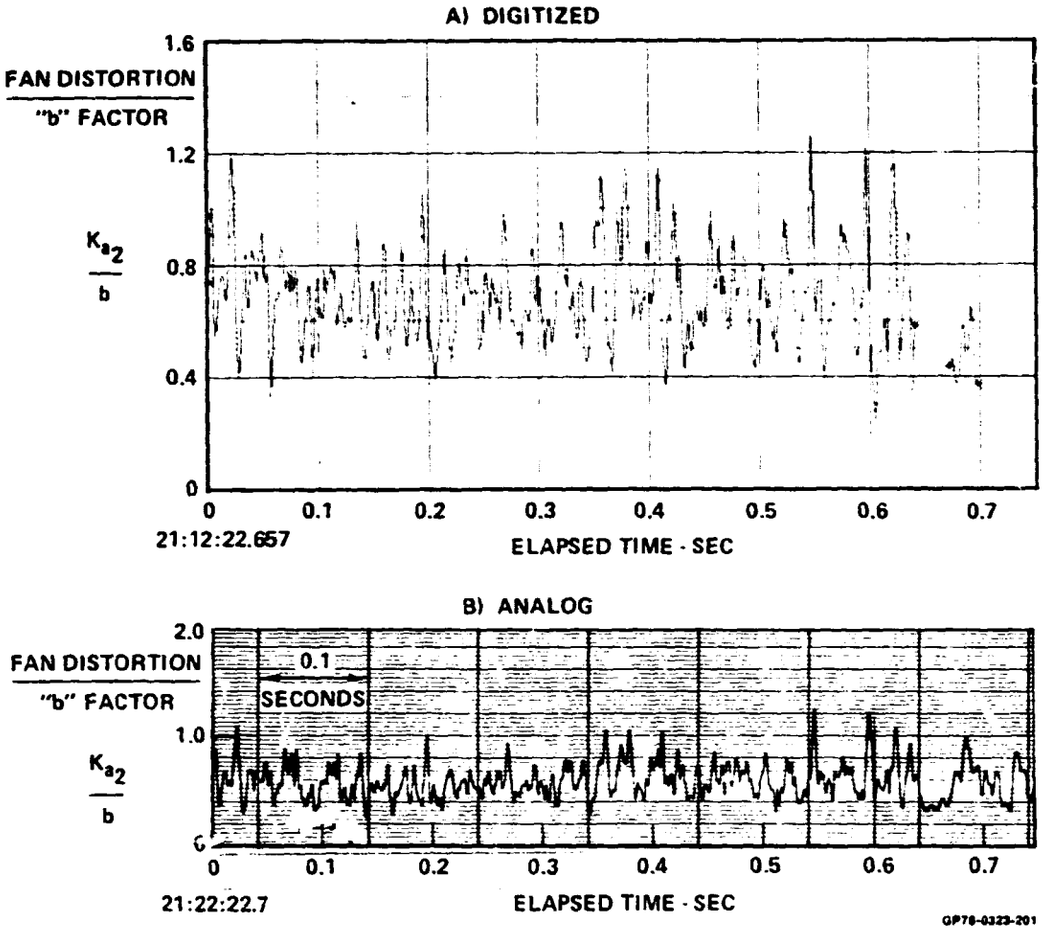

FIGURE 14
COMPARISON OF ANALOG DISTORTION CALCULATOR AND DIGITALLY COMPUTED FAN DISTORTION TIME HISTORIES
Mach 0.4 α = 16.4 β = —0.8 ρ = 6.9 Δ_3 = 27.6
WAT2 = 104.1% Bypass = 0 I.D. Number = 1

DATA BASE SELECTION

DATA POINT I.D. NO.	MODEL SCALE	M_o	α (DEG)	β (DEG)	ρ (DEG)	$\Delta\beta$ (DEG)	BYPASS*	% WAT2	RE NO. x 10^{-6}	ANALYSIS TIME (SEC)	PART–POINT**
1	FLT	0.4	16.4	−0.8	6.9	27.6	C	*	1.44	0.6	422-4
2	FLT	0.59	13.9	0.9	7.0	26.6	C	[illegible]	2.04	0.6	417-5
3	↓	0.52	10.0	0.7	↓	27.6	↓	107.1	1.33	0.6	417-4
4	↓	0.69	11.5	1.0	↓	26.5	↓	104.2	0.84	0.6	417-2
5	1/6th	0.60	−10.0	10.0	−3.0	10.6	C	97.2	0.43	0.144	164-1
6	1/6th	0.60	−10.0	10.0	−3.0	10.6	C	90.2	0.43	0.144	164-3
7	FLT	0.69	−8.4	10.6	0.6	10.5	C	101.2	1.40	0.88	421-10
8	1/6th	0.60	4.0	0	7.0	10.6	C	76.6	0.43	0.181	112-7
9	1/6th	0.60	4.0	0	7.0	10.6	C	108.6	0.43	0.181	112-5
10	FSE	0.60	4.0	0	5.2	10.0	C	97.7	3.41	1.110	116-2
11	FLT	0.67	4.3	0.7	6.9	11.1	C	94.4	3.58	0.72	424-2
12	↓	0.69	3.4	0.7	6.9	11.1	↓	74.1	3.68	0.76	425-6
13	↓	0.59	4.6	1.2	7.0	11.1	↓	107.9	1.74	0.62	412-2
14	↓	0.60	4.6	0.6	6.9	11.0	↓	76.2	1.66	1.11	424-11
15	FLT	0.85	8.8	−0.5	7.0	27.6	C	104.2	2.21	0.60	417-3
16	FLT	0.92	5.6	0.6	7.0	26.6	C	104.5	1.04	0.60	417-1
17	1/6th	0.90	−10.0	10.0	−3.0	10.6	C	70.2	0.34	0.113	157-7
18	1/6th	0.90	−10.0	10.0	−3.0	10.6	C	106.3	0.34	0.113	157-5
19	FLT	0.94	−8.9	10.2	1.0	10.5	C	107.1	1.6	0.69	421-14
20	FSE	0.90	−4.0	0	−1.0	8.2	C	97.8	3.64	1.990	102-2
21	FLT	0.90	−2.8	−0.2	−1.2	8.7	C	97.5	3.25	1.23	424-10
22	FLT	0.93	−3.3	0	−1.2	8.6	C	104.8	1.17	1.99	425-3
23	1/6th	0.90	4.0	0	7.0	10.6	C	76.8	0.34	0.369	67-9
24	1/6th	0.90	4.0	0	7.0	10.6	C	104.3	0.34	0.369	67-7
25	FSE	0.90	4.0	0	7.3	10.4	C	97.7	3.62	2.260	126-2
26	FLT	0.92	4.6	0.7	6.0	11.0	C	96.2	3.47	0.89	420-9
27	↓	0.91	5.2	0.5	6.9	11.1	↓	99.1	3.28	1.18	422-2
28	↓	0.92	4.2	0.1	7.0	11.0	↓	76.1	2.47	1.34	421-5
29	↓	0.90	4.1	0.5	6.9	11.1	↓	98.6	2.43	1.46	424-9
30	↓	0.90	5.1	0.1	7.0	11.0	↓	105.7	2.42	0.69	421-4
31	↓	0.90	3.5	0.2	7.0	11.0	↓	77.5	1.78	2.26	421-6
32	↓	0.90	5.2	−0.1	7.0	11.0	↓	100.1	1.79	0.70	421-7
33	↓	0.94	4.3	0.2	7.0	11.1	↓	105.6	1.89	1.06	421-8

*C = Closed

GP78-0323-6

**For flight test, these data are flight-run numbers

FIGURE 15
DATA MATRIX

DATA BASE SELECTION

DATA POINT I.D. NO.	MODEL SCALE	M_∞	α (DEG)	β (DEG)	ρ (DEG)	$\Lambda 3$ (DEG)	BYPASS*	% WAT2	RE NO. $\times 10^{-6}$	ANALYSIS TIME (SEC)	PART–POINT**
34	FLT	1.21	1.5	0	6.0	27.6	C	98.3	2.97	0.60	423-4
35	FLT	1.24	3.0	0	6.7	27.6	C	96.4	1.52	0.60	423-3
36	1/6th	1.2	10.0	0	7.0	10.6	C	76.6	0.45	0.198	131-7
37	1/6th	1.2	10.0	0	7.0	10.6	C	107.9	0.45	0.198	131-5
38	FLT	1.18	7.7	0.3	7.0	11.0	C	74.0	3.22	1.21	424-12
39	↓	1.2	7.4	−0.1	7.1	11.1	↓	94.4	3.35	1.19	424-13
40	↓	1.17	10.6	0.0	7.0	11.0	↓	103.4	1.40	0.60	421-17
41	FLT	1.54	1.5	0	−1.4	27.0	Auto	95.4	2.17	0.60	424-6
42	1/6th	1.6	−4.0	0	−2.0	13.5	C	87.3	0.21	0.10[illegible]	206-9
43	1/6th	1.6	−4.0	0	−2.0	13.5	C	96.9	0.21	0.10[illegible]	206-5
44	FLT	1.57	−3.6	0.7	−2.3	13.7	C	83.3	1.46	0.6[illegible]	[illegible]-2
45	1/6th	1.8	−2.0	0	−3.0	17.4	C	80.5	0.22	0.2[illegible]	[illegible]5-9
46	1/6th	1.8	−2.0	0	−3.0	17.4	C	91.0	0.22	0.20[illegible]	15-5
47	FLT	1.75	−2.6	0.4	−2.2	16.7	C	80.7	1.41	1.23	4[illegible]5-1
48	FSCP	1.8	−2.0	0	−3.0	18.7	C	75.1	1.45	0.680	353-15
49	↓	↓	−2.0	↓	−3.0	↓	↓	82.2	1.45	0.680	353-5
50	↓	↓	−2.0	↓	−3.0	↓	↓	85.4	1.44	0.680	353-12
51	FSE	1.8	−2.0	0	−2.9	18.6	C	80.6	1.46	0.680	523-2
52	FSE	1.8	−2.0	0	−2.9	18.6	C	79.8	1.46	0.680	525-4
53	FLT	1.81	−2.3	0.2	−2.9	18.2	C	78.9	1.53	0.680	416-1
54	FSCP	1.8	4.0	0	2.5	18.7	C	79.9	1.45	2.800	355-8
55	FSE	1.8	4.0	0	2.5	18.7	C	80.8	1.46	2.800	528-2
56	FSE	1.8	4.0	0	2.5	18.7	C	79.7	1.46	2.800	529-4
57	FLT	2.0	2.5	0.2	2.3	20.9	Auto	77.0	1.72	2.800	452-2

GP78-0323-9

*C = Closed

**For flight test, these data are flight-run numbers

FIGURE 15 (Continued)
DATA MATRIX

DATA BASE SELECTION

DATA POINT I.D. NO.	MODEL SCALE	M_∞	α (DEG)	β (DEG)	ρ (DEG)	$\Lambda\beta$ (DEG)	BYPASS*	% WAT2	RE NO. $\times 10^{-6}$	ANALYSIS TIME (SEC)	PART–POINT**
58	1/6th	2.2	−2.0	0	−4.0	22.5	C	68.6	0.22	0.100	258-7
59	FSCP	2.2	−2.0	0	−4.0	22.5	C	69.2	1.48	0.600	411-6
60	1/6th	2.2	−2.0	0	−4.0	25.0	O	65.0	0.22	0.100	249-5
61	1/6th	2.2	−2.0	0	−4.0	25.0	O	52.9	0.22	0.100	249-9
62	FSCP	2.2	−2.0	0	−4.0	25.0	O	61.7	1.48	0.600	385-5
63	FSCP	2.2	−2.0	0	−4.0	25.0	O	62.3	1.48	0.600	385-2
64	FSE	2.2	−2.0	0	−4.0	24.8	P	68.2	1.27	0.600	542-2
65	FSE	2.2	−2.0	0	−4.0	24.8	P	68.5	1.27	0.600	543-4
66	1/6th	2.2	0	0	−2.0	22.5	C	69.3	0.22	0.106	184-7
67	1/6th	2.2	0	0	−2.0	22.5	C	75.4	0.22	0.106	184-5
68	FSCP	2.2	0	0	−2.0	22.5	C	73.6	1.47	0.650	413-3
69	FSCP	2.2	0	0	−2.0	22.5	C	68.3	1.47	0.650	413-12
70	FLT	2.2	0.1	0.2	−2.2	22.9	C	73.8	2.34	0.650	425-1
71	FSCP	2.2	4.0	0	0.0	25.0	O	68.7	1.48	0.600	382-3
72	FSE	2.2	4.0	0	1.0	25.0	O	59.2	1.28	0.600	545-2
73	FSE	2.2	4.0	0	1.0	25.0	O	58.2	1.27	0.600	546-4
74	1/6th	2.2	12.0	0	6.0	25.0	O	47.3	0.22	0.100	252-9
75	1/6th	2.2	12.0	0	6.0	25.0	O	65.0	0.22	0.100	252-5
76	FSCP	2.2	12.0	0	6.0	25.0	O	68.8	1.48	0.600	384-2
77	FSE	2.2	11.0	0	6.0	24.8	O	59.0	1.28	0.600	548-3
78	FSE	2.2	11.0	0	6.0	24.8	P	59.0	1.27	0.600	549-8
79	1/6th	2.5	0	0	−4.0	26.0	O	63.1	0.21	0.100	227-7
80	1/6th	2.5	0	0	−4.0	26.0	O	68.2	0.21	0.100	227-5
81	FSCP	2.5	0	0	−4.0	26.0	O	62.8	1.28	0.600	465-8
82	FSCP	2.5	0	0	−4.0	26.0	O	68.9	1.28	0.600	465-5

*O = Open, C = Closed, P = Partial

**For flight test, these data are flight-run numbers

GP78-0323-10

FIGURE 15 (Concluded)
DATA MATRIX

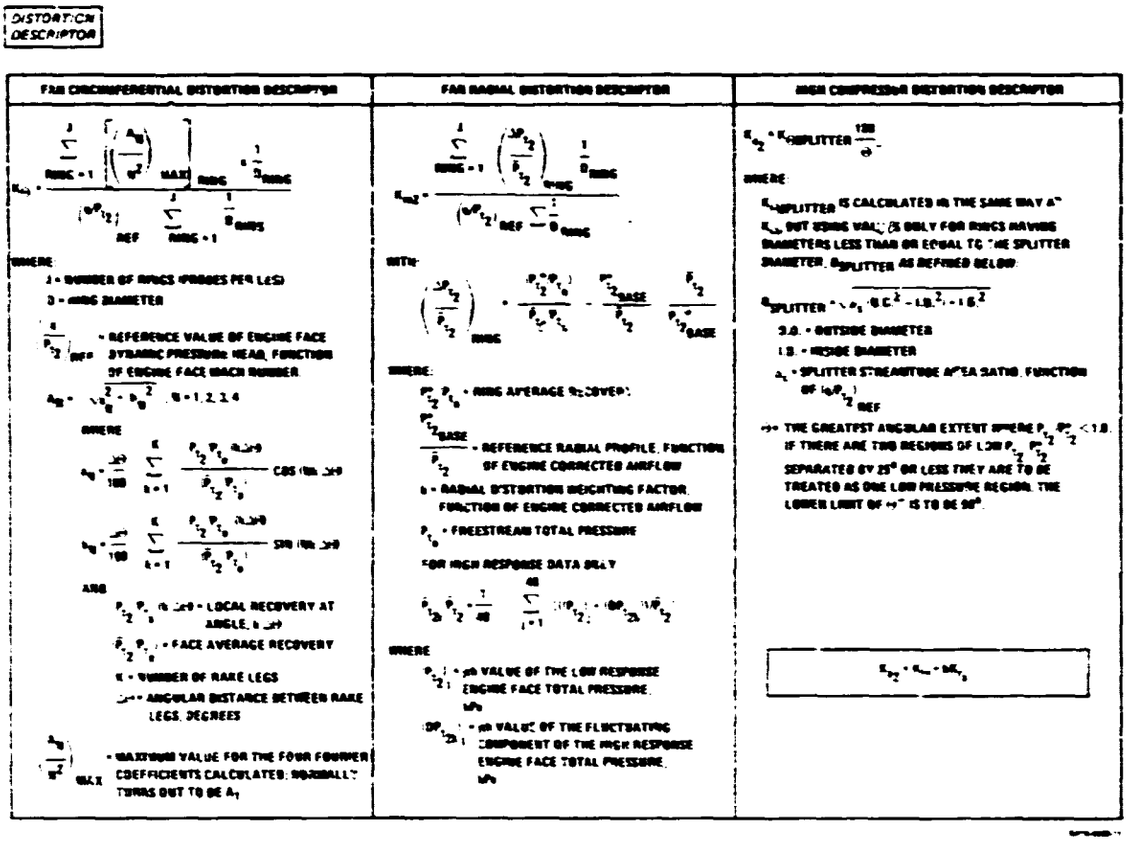

FIGURE 16

PRATT AND WHITNEY AIRCRAFT F100 ENGINE DISTORTION DESCRIPTOR

Fan Circumferential Distortion Descriptor ~ K_θ Fan Radial Distortion Descriptor ~ $b\,K_{ra_2}$

Fan Distortion Descriptor ~ $K_\theta + b\,K_{ra_2}$ High Compressor Distortion Descriptor ~ K_{c_2}

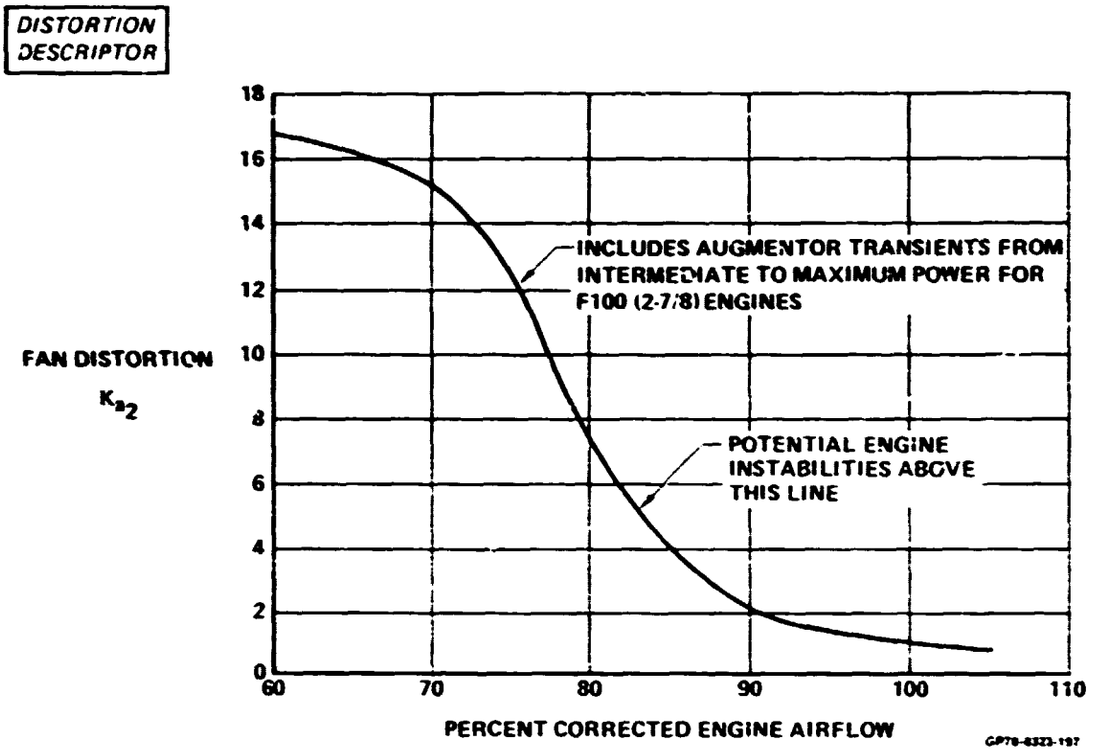

FIGURE 17
FAN DISTORTION SCREENING CURVE

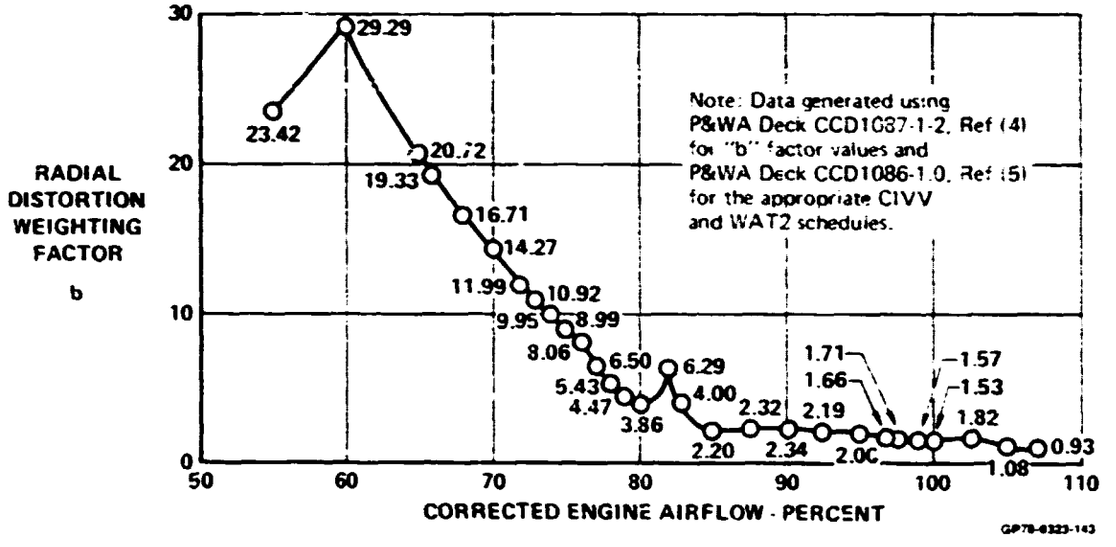

FIGURE 18
F100(2 7/8) RADIAL DISTORTION WEIGHTING FACTOR

TIME VARIANT DATA QUALITY

Data Point Identification Number										
1/6th Scale	Full Scale Cold Pipe	Full Scale With Engine	Flight Test	M_o	α (deg)	β (deg)	ω (deg)	$\Delta 3$ (deg)	Bypass*	Percent WAT2
6 5	– –	– –	7	0.6	–10	10	–3	10.6	C	90.2 - 101.2
17 18	– –	– –	19	0.9	–10	10	–3	10.6	C	70.2 - 107.1
42 43	– –	– –	44	1.6	–4	0	–2	13.5	C	87.3 - 96.9
–	48, 49, 50	51, 52	53	1.8	–2	0	–3	18.7	C	75.1 - 85.4
45 46	– –	– –	47	1.8	–2	0	–3	17.4	C	80.5 - 91.0
60 61	62 63	64 65	–	2.2	–2	0	–4	25.0	O, P	52.9 - 65.0
66 67	68 69**	–	70	2.2	0	0	–2	22.5	C	68.3 - 75.4
79 80	81 82	– –	– –	2.5	0	0	–4	26.0	O	62.8 - 68.9

*O = Open bypass, C = Closed bypass, P = Partially open bypass

GP79-0323-12

**These data exhibited harmonic characteristics and are not included in this analysis

FIGURE 19
TEST CONDITIONS FOR EVALUATING QUALITY OF TIME VARIANT DATA

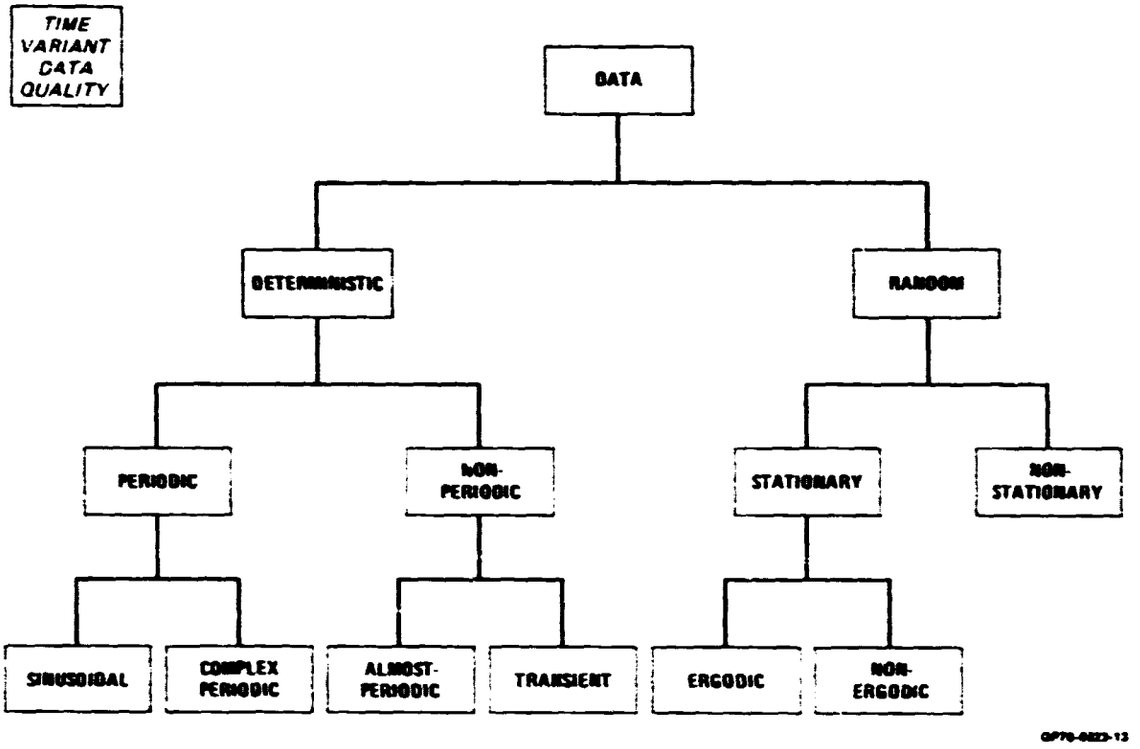

FIGURE 20
DATA CLASSIFICATION

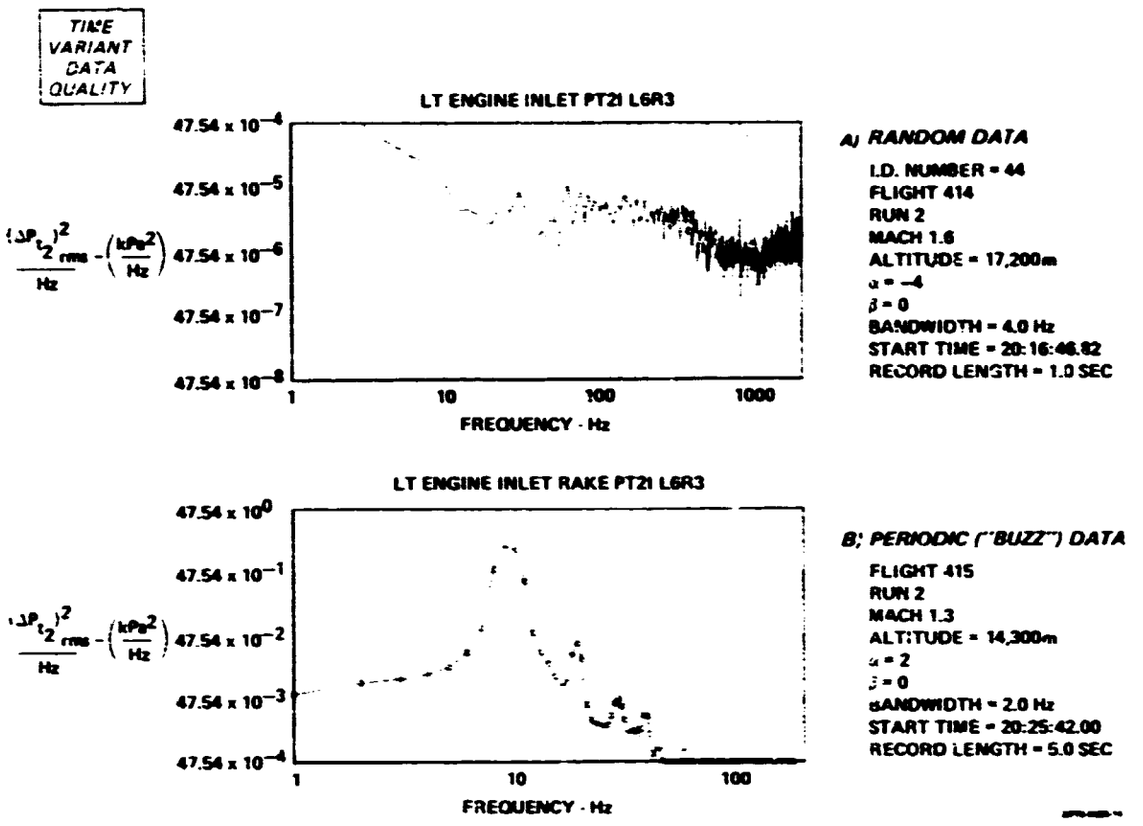

FIGURE 21
FLIGHT TEST POWER SPECTRAL DENSITY PLOTS
Random vs Periodic Data

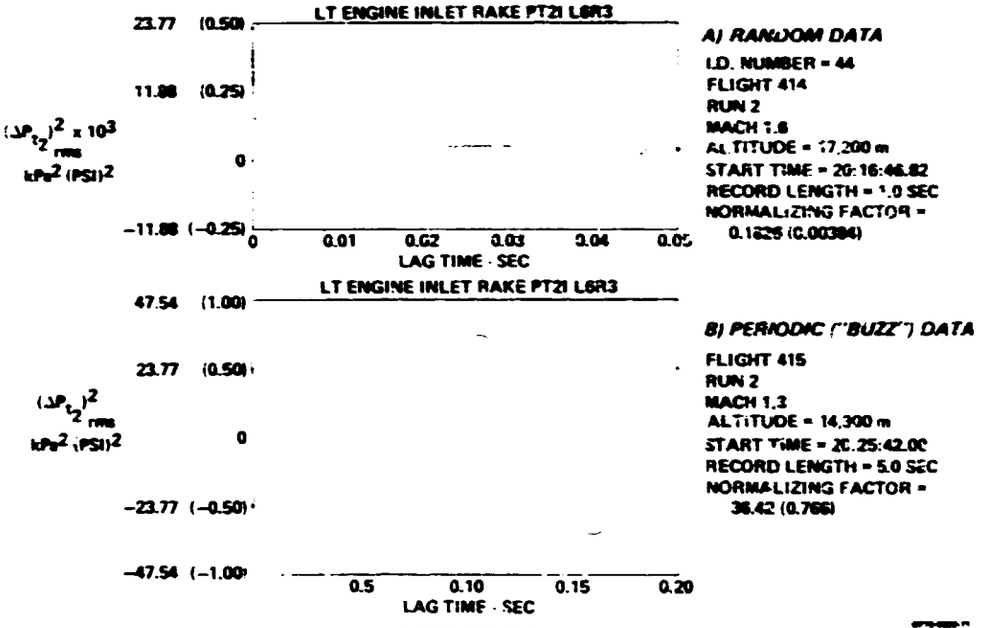

FIGURE 22
FLIGHT TEST AUTOCORRELATION FUNCTIONS
Random vs Periodic Data

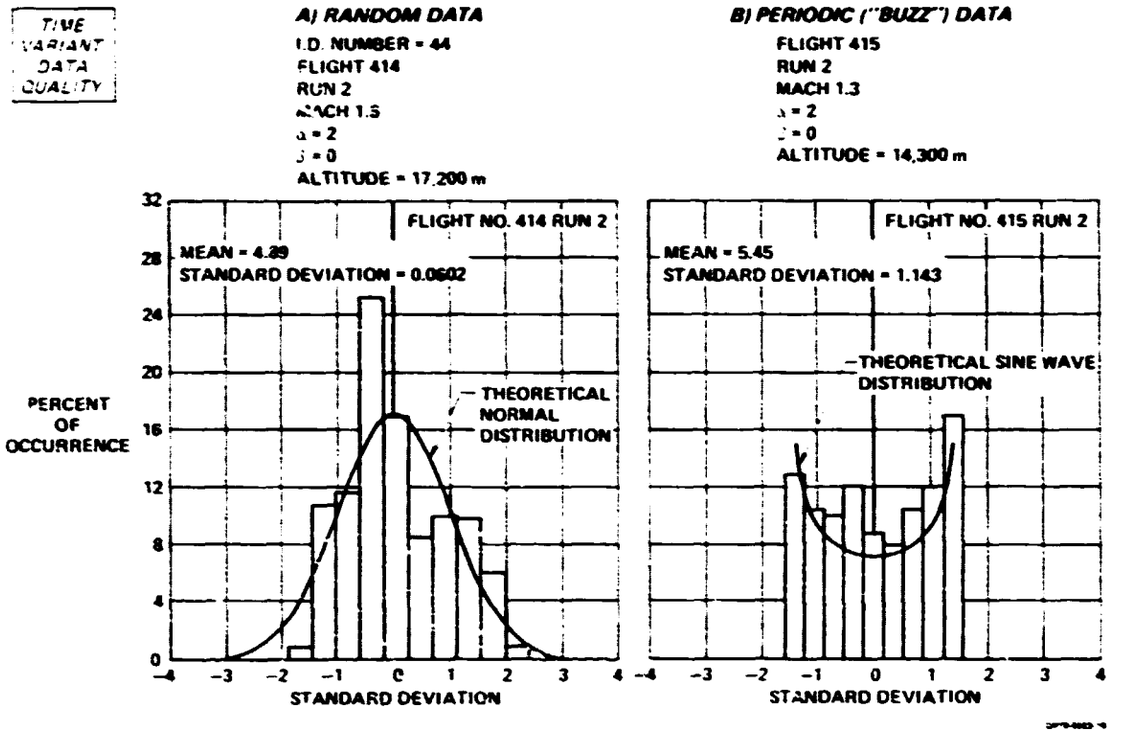

FIGURE 23
FLIGHT TEST DATA PROBABILITY DENSITY FUNCTIONS
Random vs Periodic Data

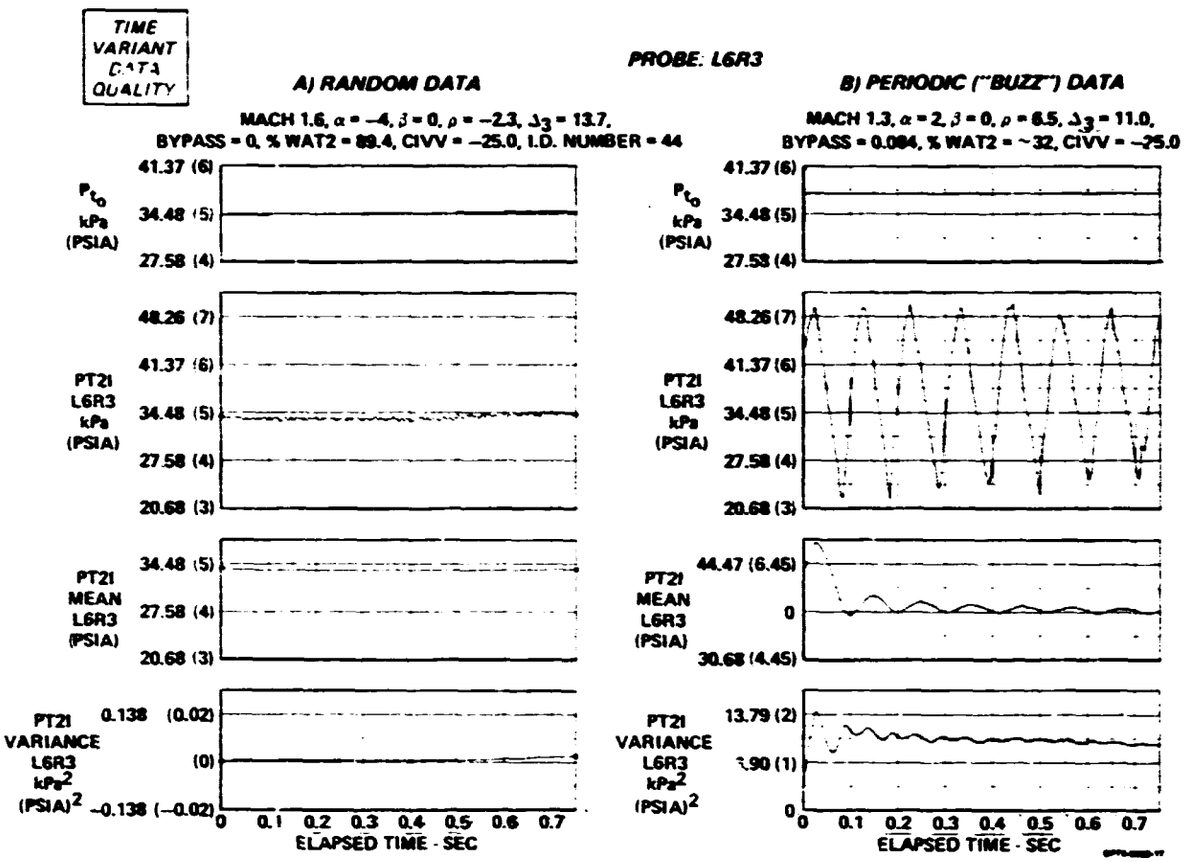

FIGURE 24

INSTANTANEOUS, MEAN AND MEAN SQUARE PRESSURE TIME HISTORY FLIGHT TEST

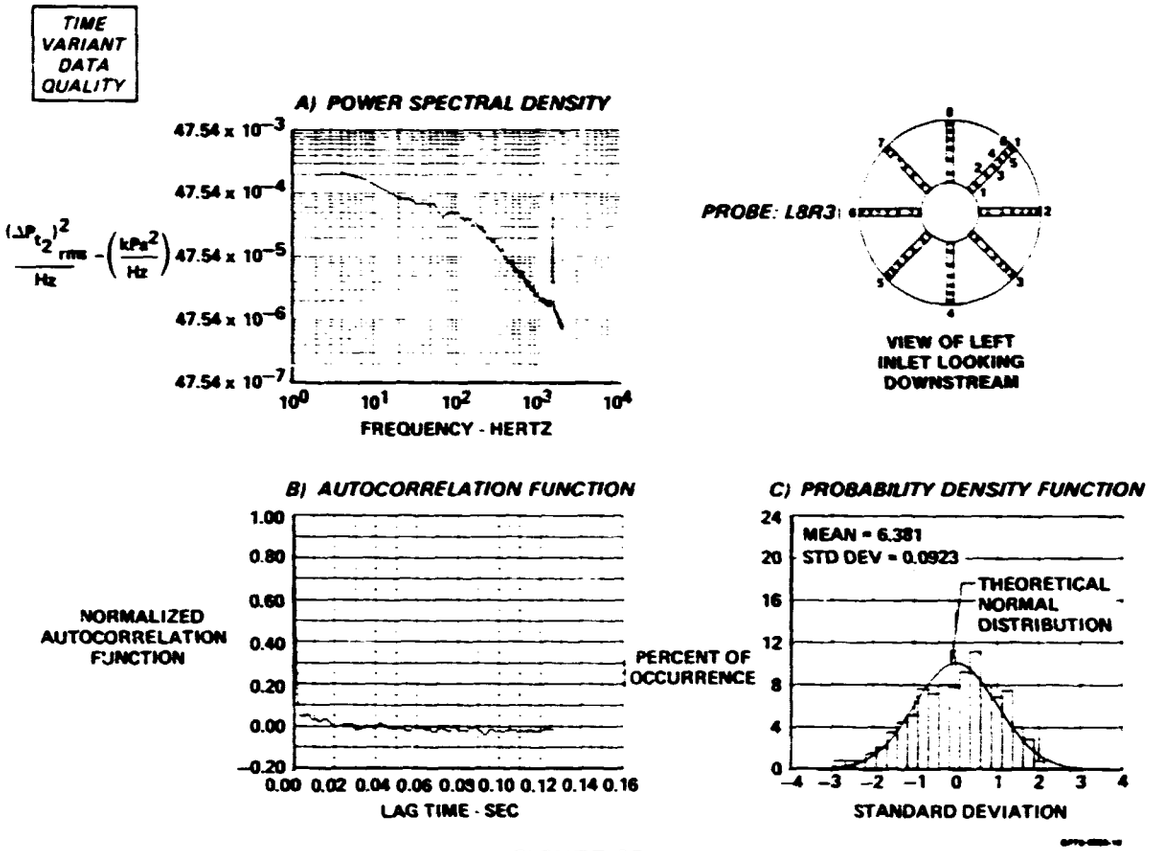

FIGURE 25
TIME VARIANT DATA QUALITY
FULL SCALE WITH ENGINE

Mach 1.8 α = —2 β = 0 ρ = 2.9 Δ_3 = 18.6
Bypass = 0 WAT2 = 79.8% CIVV = —25.0 I.D. Number = 52

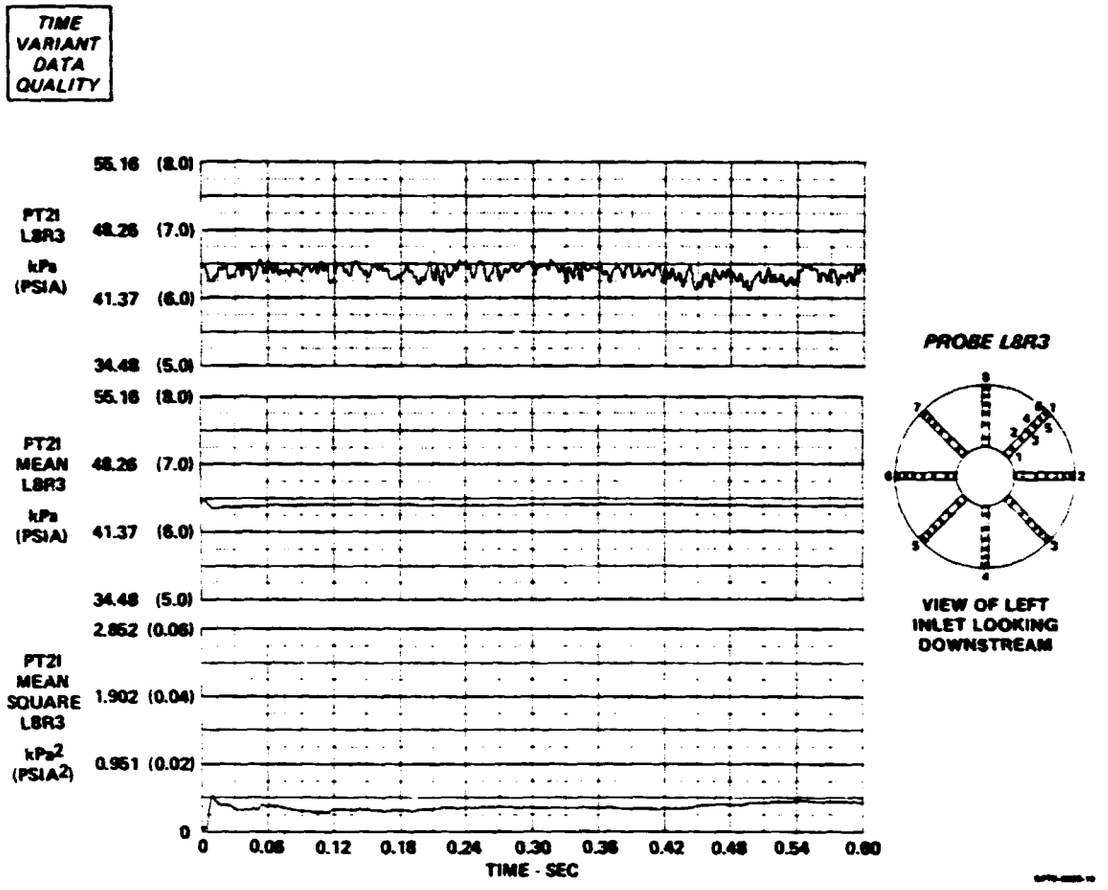

FIGURE 26
INSTANTANEOUS, MEAN AND MEAN SQUARE PRESSURE TIME HISTORY
FULL SCALE WITH ENGINE

Mach 1.8 α = —2 β = 0 ρ = —2.9 $\Delta\gamma$ = 18.6
Bypass = 0 WAT2 = 79.8% Civv = —25.0 I.D. Number = 52

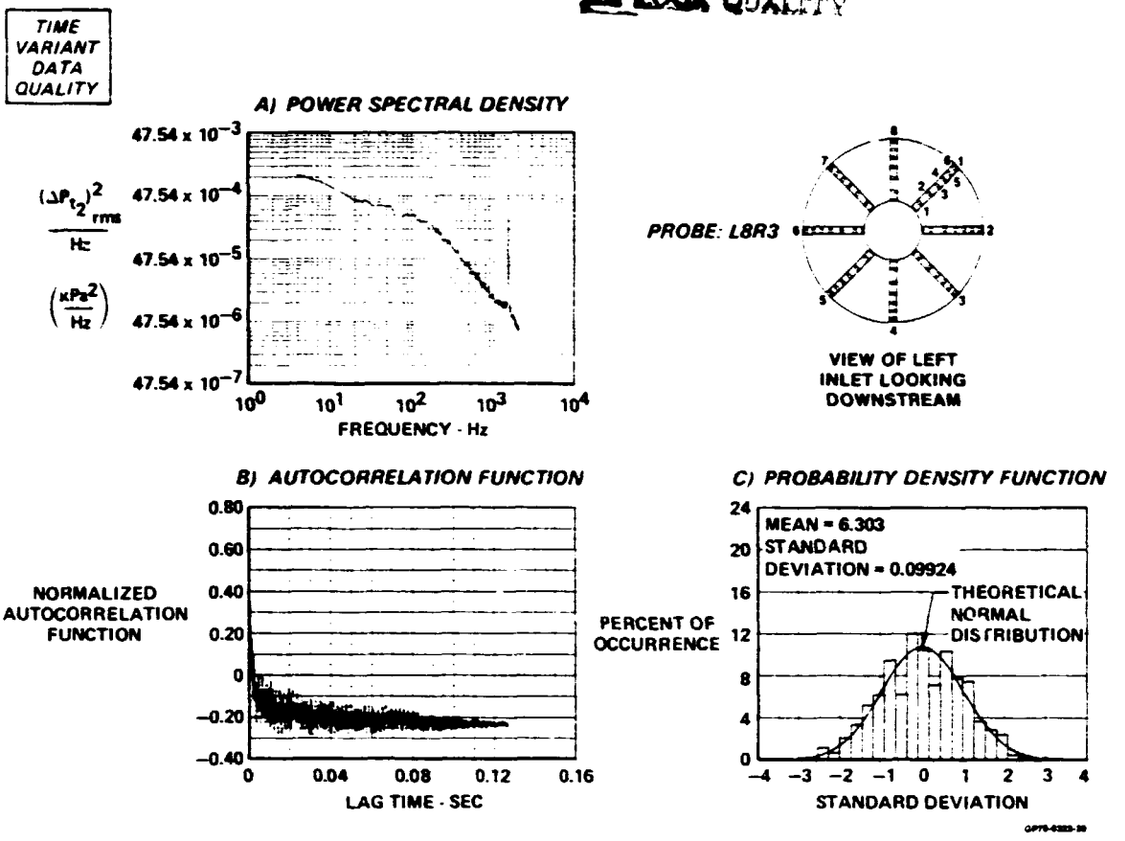

FIGURE 27
TIME VARIANT DATA QUALITY
FULL SCALE COLD PIPE

Mach 1.8 $\alpha = -2$, $\beta = 0$ $\rho = -3.0$ $\Delta_3 = 18.7$
Bypass = 0 WAT2 = 82.2% CiVV = —25.0 I.D. Number = 49

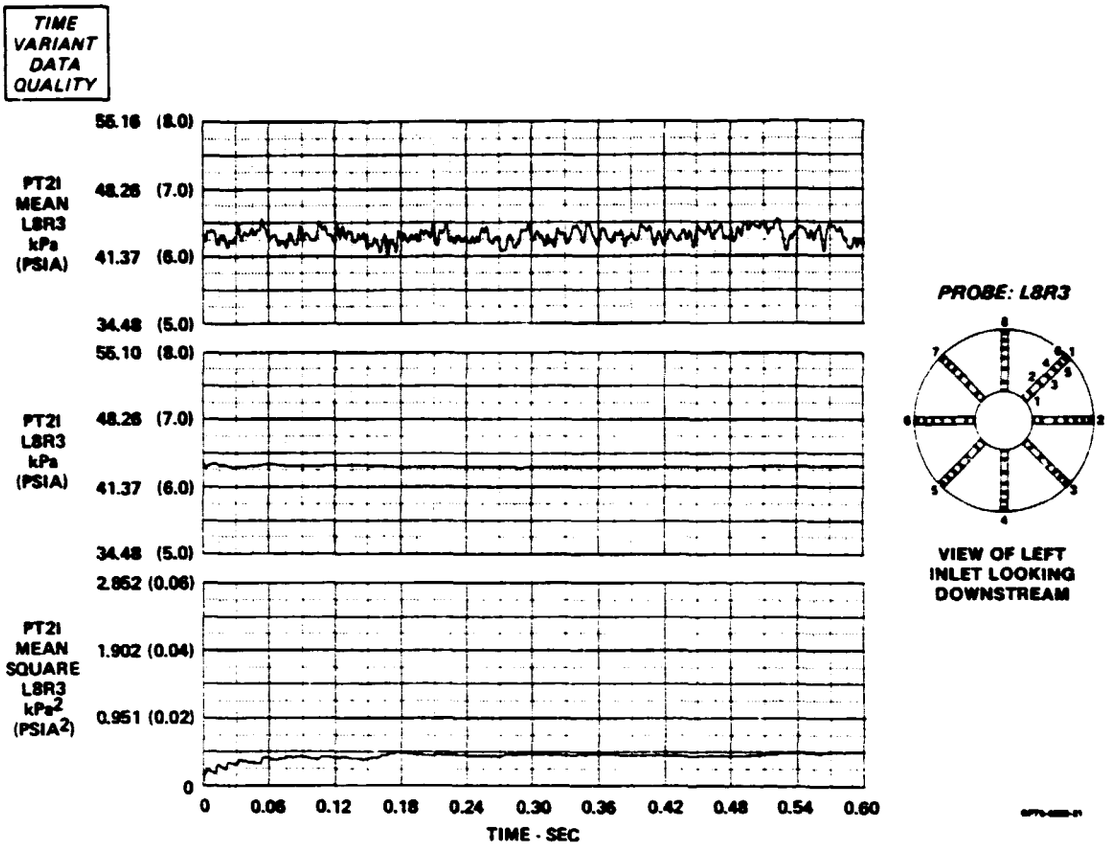

FIGURE 28
INSTANTANEOUS, MEAN AND MEAN SQUARE PRESSURE TIME HISTORY
FULL SCALE COLD PIPE MODEL

Mach 1.8 $\alpha = -2$ $\beta = 0$ $\rho = -3.0$ $\Delta_3 = 18.7$
Bypass = 0 WAT2 = 82.2% CIVV = —25.0 I.D. Number = 49

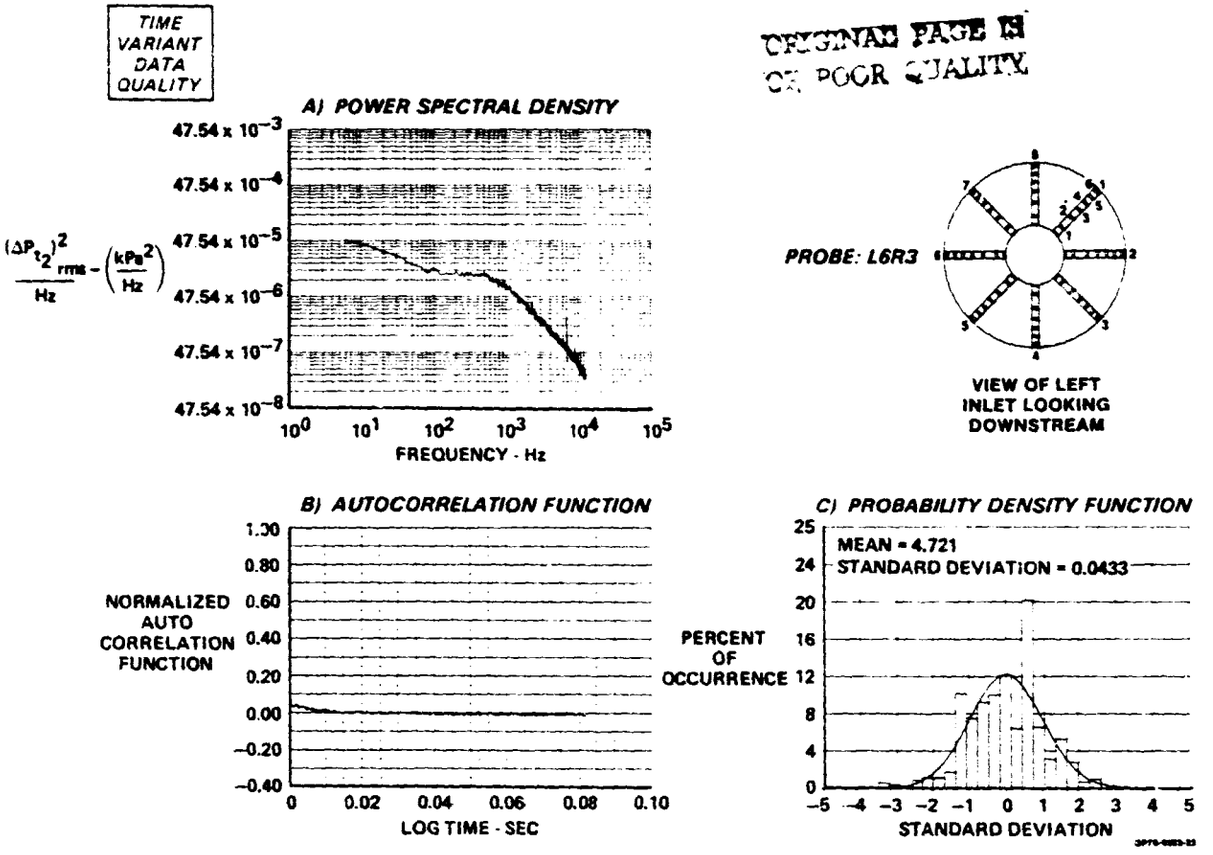

FIGURE 29
TIME VARIANT DATA QUALITY
1/6th SCALE INLET MODEL

Mach 1.6 $\alpha = -4$ $\beta = 0$ $\rho = -2$ $\lambda_3 = 13.5$
Bypass = 0.0 WAT2 = 87.3% CIVV = —21.8 I.D. Number = 42

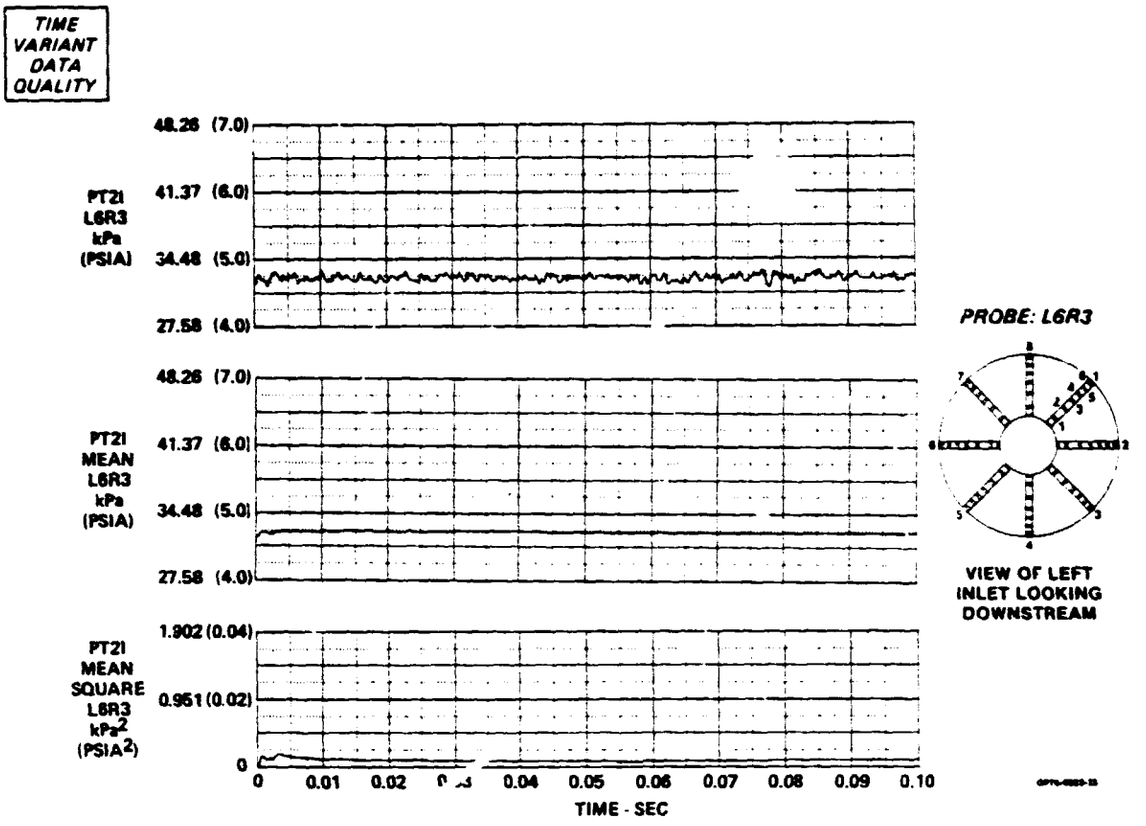

FIGURE 30
INSTANTANEOUS, MEAN AND MEAN SQUARE PRESSURE TIME HISTORY
1/6th SCALE INLET MODEL

Mach 1.6 $\alpha = -4$ $\beta = 0$ $\rho = -2.0$ $\Delta_3 = 13.6$
Bypass = 0 WAT2 = 87.3% CIVV = —21.8 I.D. Number = 42

INTERPOLATION PROCEDURE

SOLID SYMBOL - STEADY STATE
OPEN SYMBOL - CORRESPONDS TO PEAK TIME VARIANT FAN DISTORTION.

SYM	MODEL	I.D. NUMBER
○	1/6th SCALE	
□	FSCP	49, 50
◇	FSE	51, 52
△	FLT	53

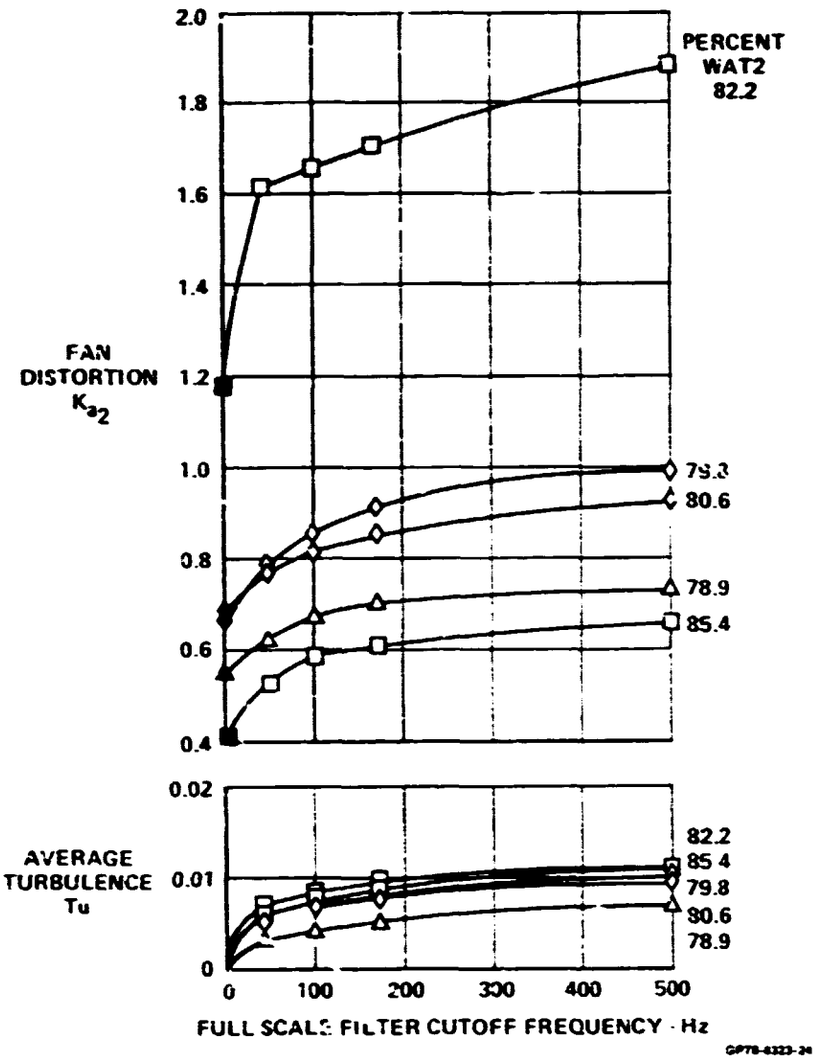

FIGURE 31
EFFECT OF FILTER CUTOFF FREQUENCY ON PEAK FAN DISTORTION PARAMETERS
Mach 1.8 $\alpha = -2$ $\beta = 0$ $\rho = -3$ $\Delta_3 = 18.7$ Bypass = 0

INTERPOLATION PROCEDURE

SYM	MODEL	I.D. NUMBER
○	1/6th SCALE	
□	FSCP	48, 49, 50
◇	FSE	51, 52
△	FLT	53

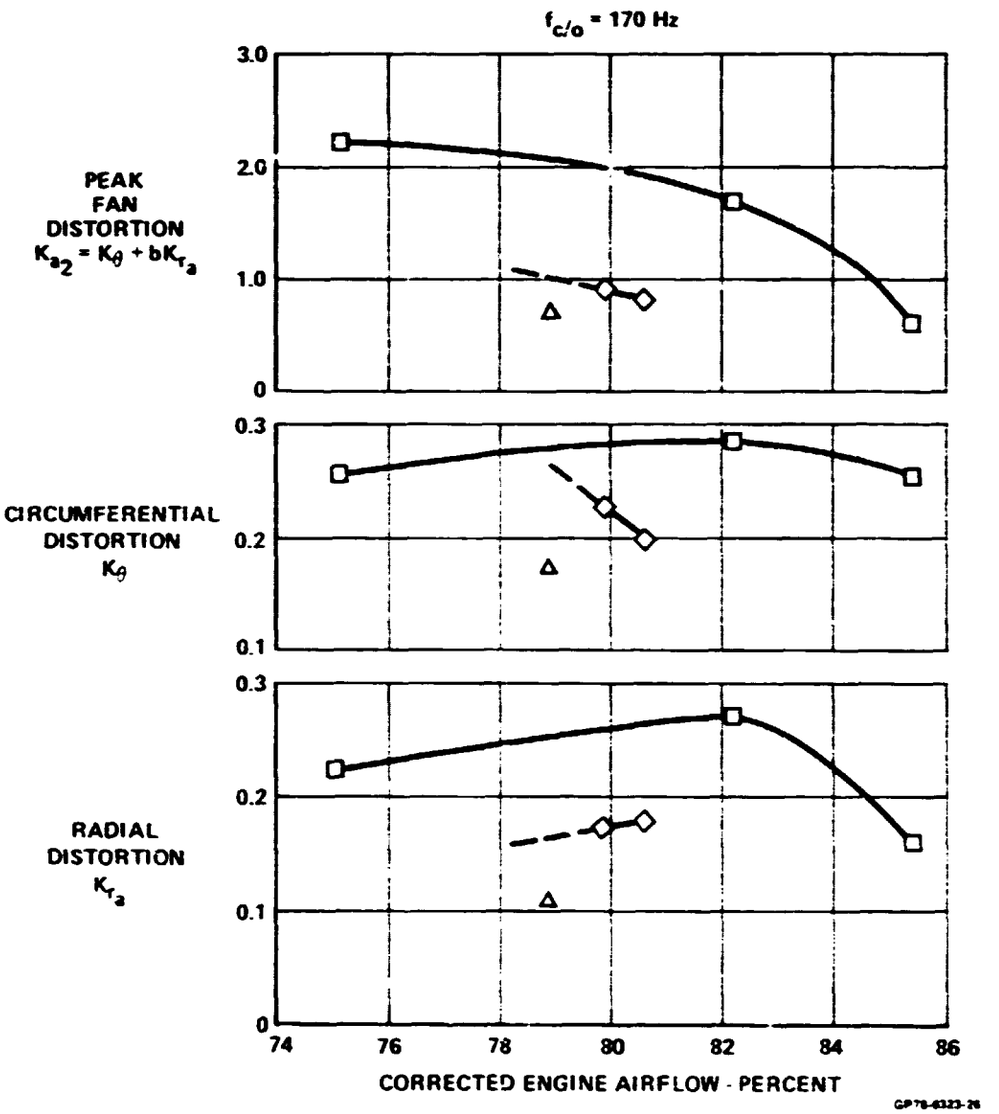

FIGURE 32
DISTORTION DESCRIPTORS vs PERCENT CORRECTED ENGINE AIRFLOW
Mach : 8 $\alpha = -2$ $\beta = 0$ $\rho = -3$ $\lambda_3 = 18.7$ Bypass 0

INTERPOLATION PROCEDURE

SYM	MODEL	I.D. NUMBER
○	1/6th SCALE	
□	FSCP	48, 49, 50
◇	FSE	51, 52
△	FLT	53

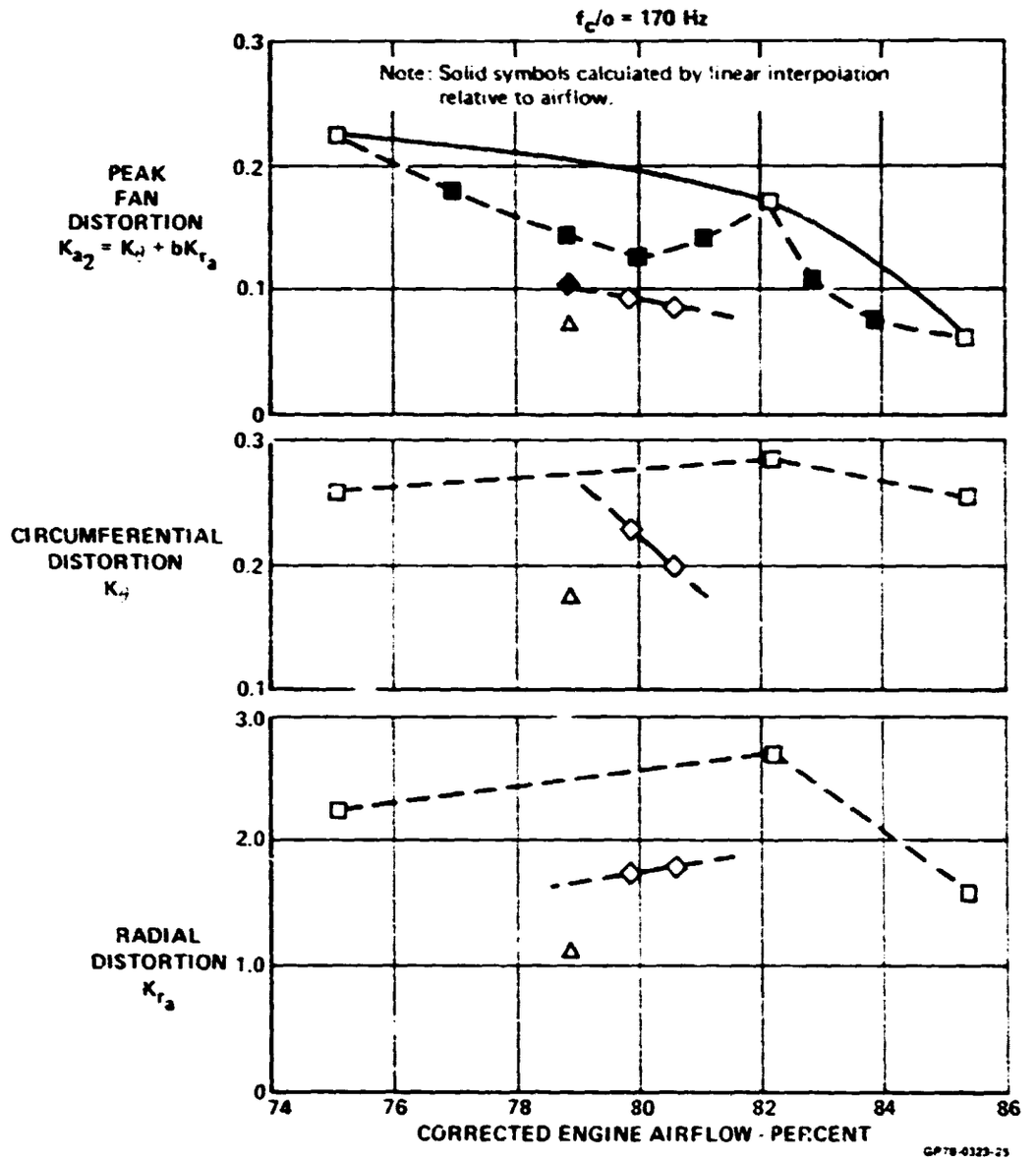

FIGURE 33
INTERPOLATION TECHNIQUE FOR FAN DISTORTION DESCRIPTORS vs PERCENT CORRECTED ENGINE AIRFLOW
Mach 1.8 $\alpha = -2$ $\beta = 0$ $\rho = -3$ $\Delta_3 = 18.7$ Bypass = C

INTERPOLATION PROCEDURE

SYM	MODEL	I.D. NUMBER
○	1/6th SCALE	
□	FSCP	48, 49, 50
◇	FSE	51, 52
△	FLT	53

Solid symbol - steady state
Open symbol - corresponds to peak time variant fan distortion
Flags indicate interpolated or extrapolated data relative to airflow

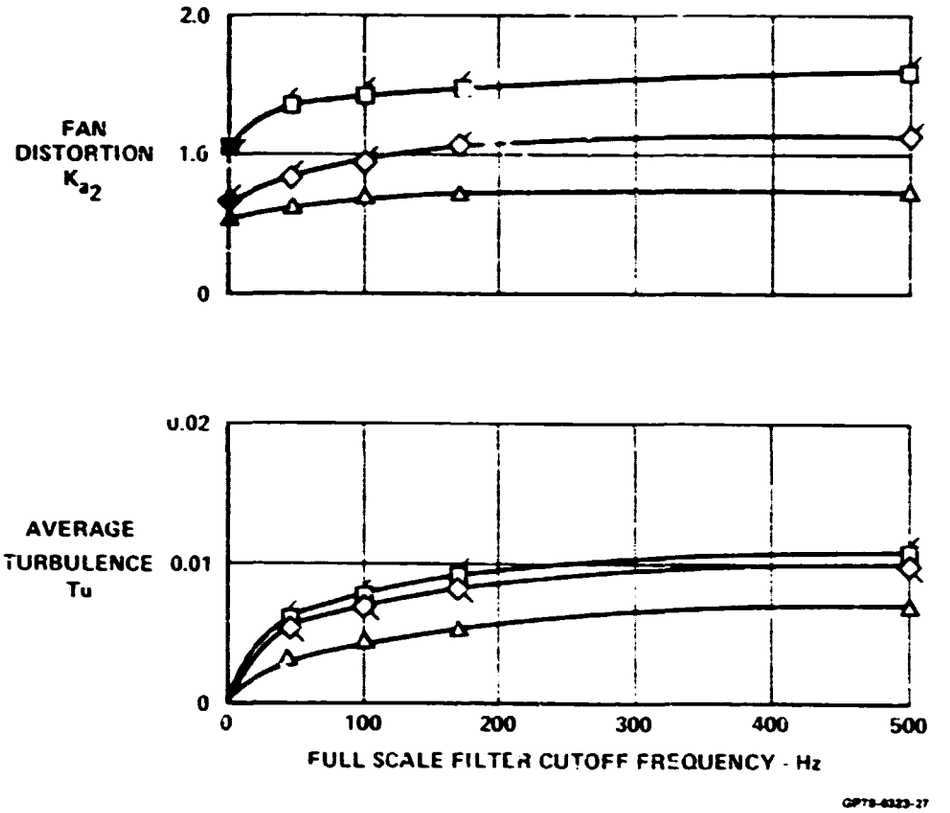

FIGURE 34
INTERPOLATION TECHNIQUE FOR FAN DISTORTION
EFFECT OF FILTER CUTOFF FREQUENCY ON INSTANTANEOUS DISTORTION PARAMETERS
Mach 1.8 $\alpha = -2$ $\beta = 0$ $\rho = -3$ $\Delta_3 = 1\&7$ Bypass = 0 WAT2 = 78.9%

ENGINE PRESENCE EFFECT

Data Point Identification Number										
1/6th Scale	Full Scale Cold Pipe	Full Scale With Engine	Flight Test	M_o	α (deg)	β (deg)	ρ (deg)	$\Delta 3$ (deg)	Bypass*	Percent WAT2
–	48, 49	51, 52	–	1.8	–2	0	–3	18.7	C	75.1-82.2
–	54	55, 56	–	1.8	4	0	2.5	18.7	C	79.7-80.8
–	62, 63	64, 65**	–	2.2	–2	0	–4	25	O,P	60.2-62.3
–	71	72, 73	–	2.2	4	0	1	25	O	58.2-60.7
–	76	77, 78	–	2.2	11	0	6.8	25	O,P	59.0-60.8

*O = Open Bypass, C = Closed Bypass, P = Partially Open Bypass

**These data have different bypass areas and are not included in the quantitative analysis.

GP78-0323-28

FIGURE 35
TEST CONDITIONS TO EVALUATE THE EFFECT ON DISTORTION PARAMETERS OF "WITH" AND "WITHOUT" AN ENGINE

ENGINE PRESENCE EFFECT

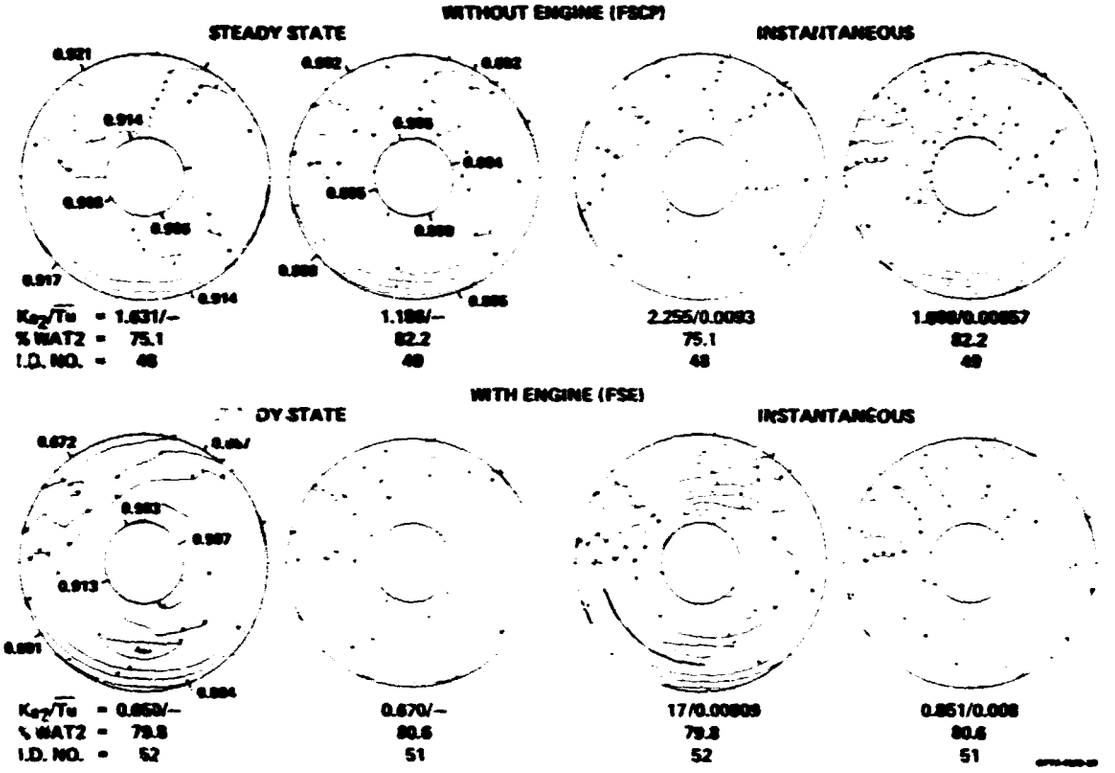

FIGURE 36
COMPARISONS OF STEADY STATE AND INSTANTANEOUS TOTAL PRESSURE CONTOURS
Mach 1.8 α = —2 β = 0 ρ = —3.0
Δ_3 = 18.7 Bypass = 0 CIVV = —25.0 Alt = 17,700

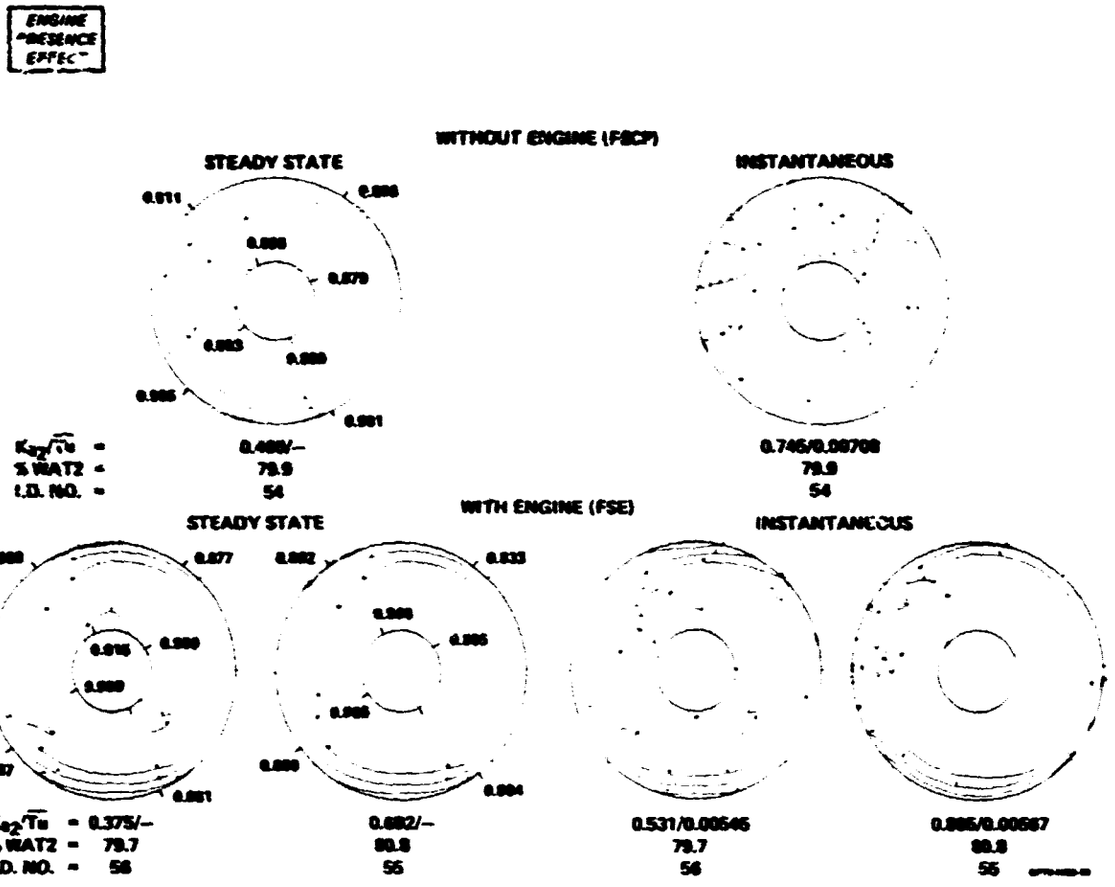

FIGURE 37
COMPARISONS OF STEADY STATE AND INSTANTANEOUS TOTAL PRESSURE CONTOURS
Mach 1.88 $\alpha = 4$ $\beta = 0$ = 2.5
$\Delta_3 = 18.7$ Bypass = 0 CIVV = —25.0 Alt = 17,700

ENGINE PRESENCE EFFECT

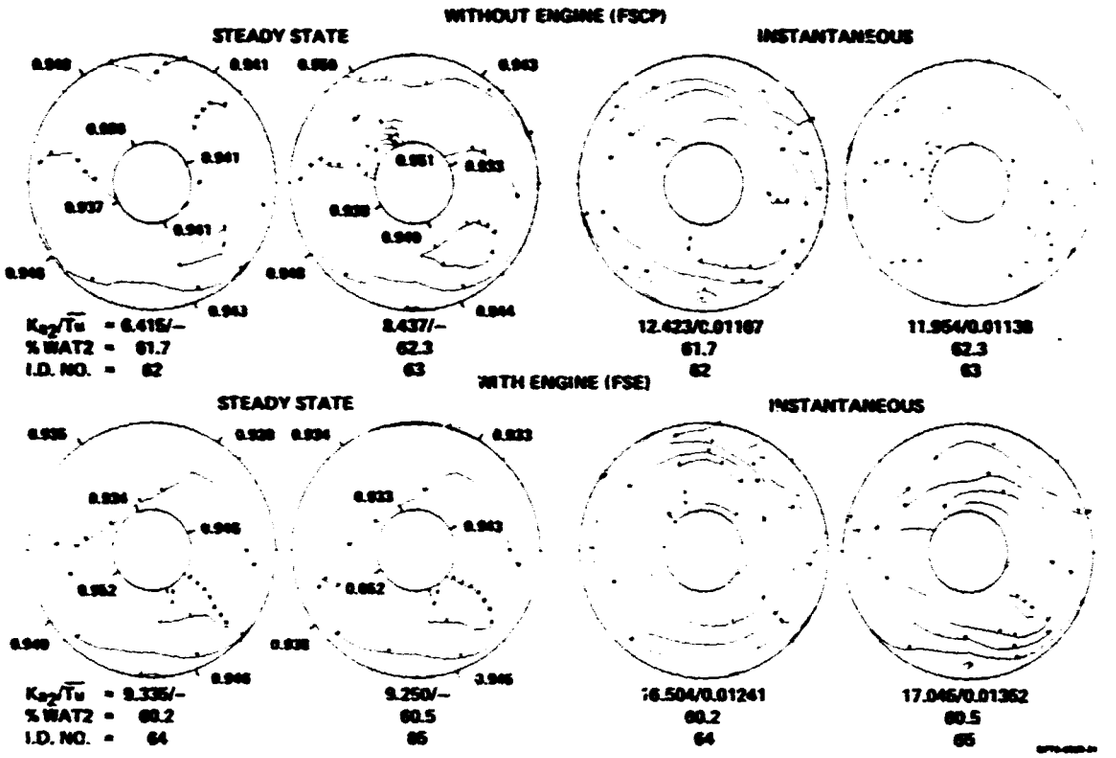

FIGURE 38
COMPARISONS OF STEADY STATE AND INSTANTANEOUS TOTAL PRESSURE CONTOURS
Mach 2.2 α = –2 β = 0 ρ = –4.0
Δ_3 = 25.0/24.8 Bypass = 0.0278 - 0.0774 CIVV = –25 0 Alt = 19,800 - 21,300

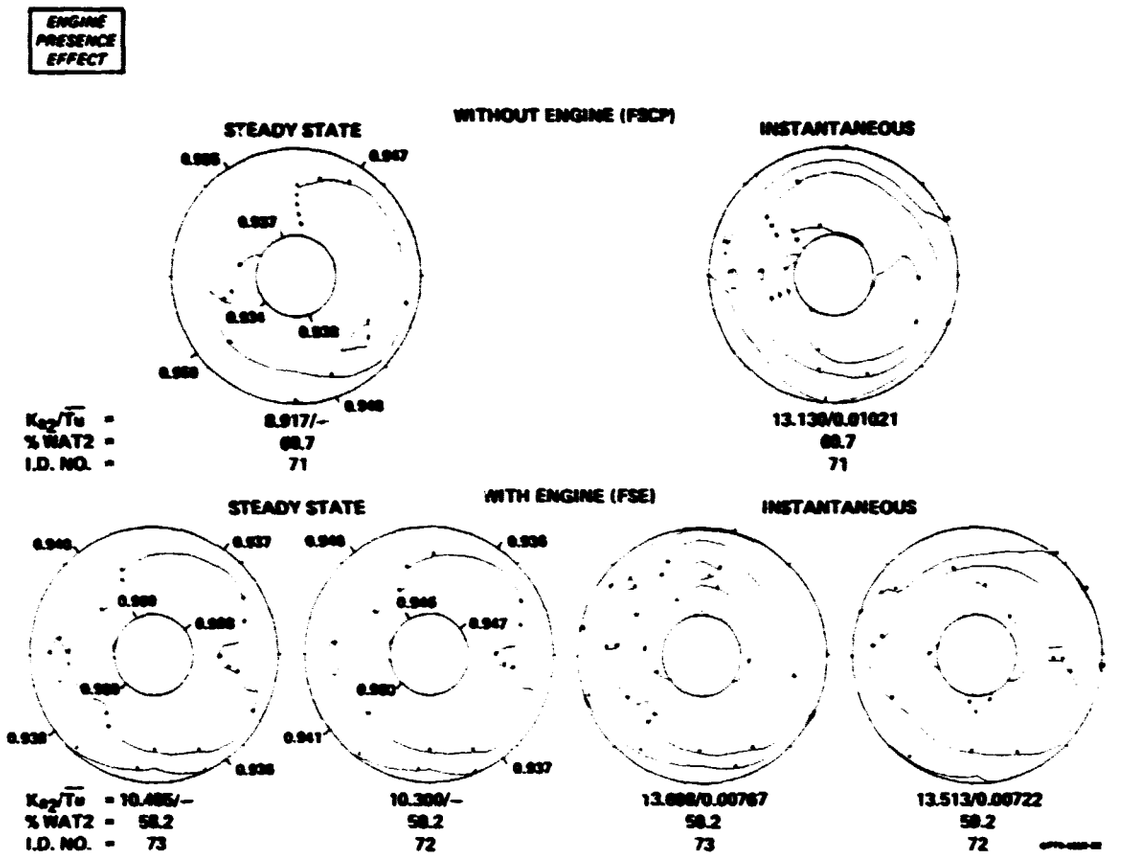

FIGURE 39
COMPARISONS OF STEADY STATE AND
INSTANTANEOUS TOTAL PRESSURE CONTOURS

γ 2.2 α = 4 β = 0 ρ = 0.0/1.0

Δ_3 = 25.0 Bypass = 0.0774 CIVV = —25.0 Alt = 19,800 - 21,300

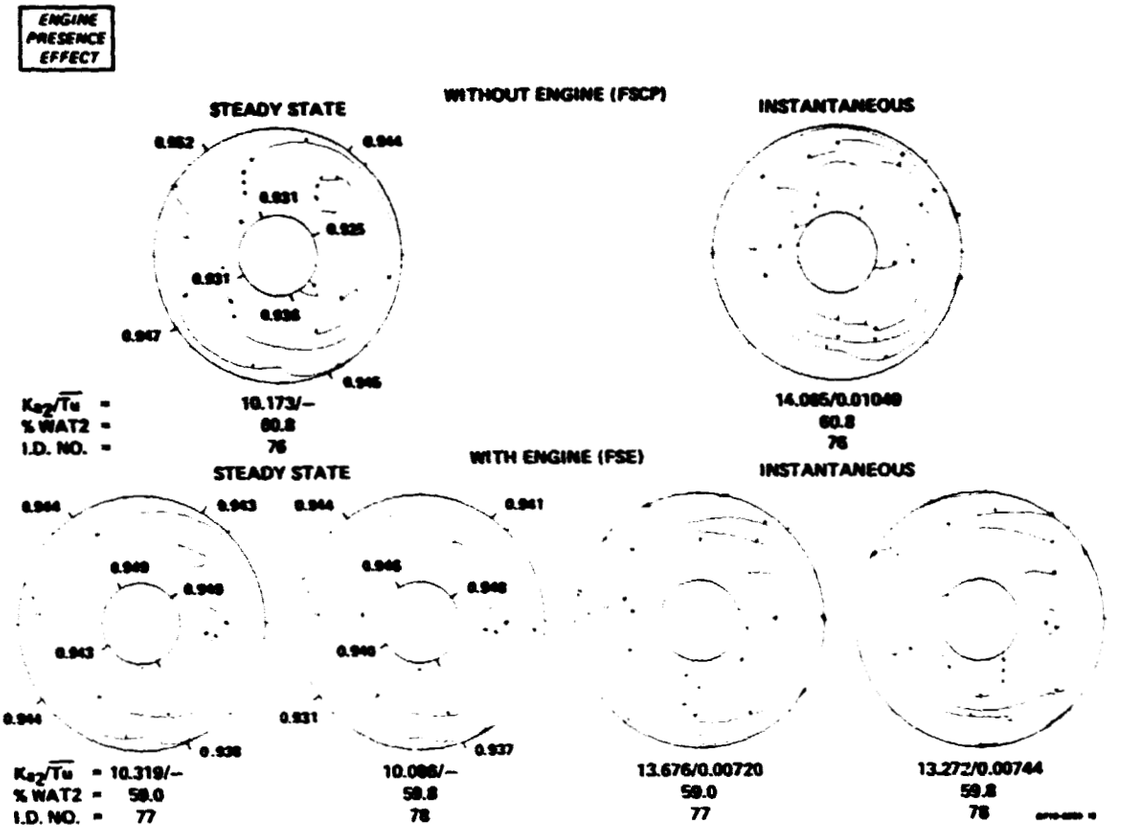

FIGURE 40
COMPARISONS OF STEADY STATE AND INSTANTANEOUS TOTAL PRESSURE CONTOURS

Mach 2.2 $\alpha = 11$ $\beta = 0$ $\rho = 6.8$

$\Delta_3 = 25.0/24.8$ Bypass = 0.0677 - 0.0774 CIVV = –25.0 Alt = 19,800 - 21,300

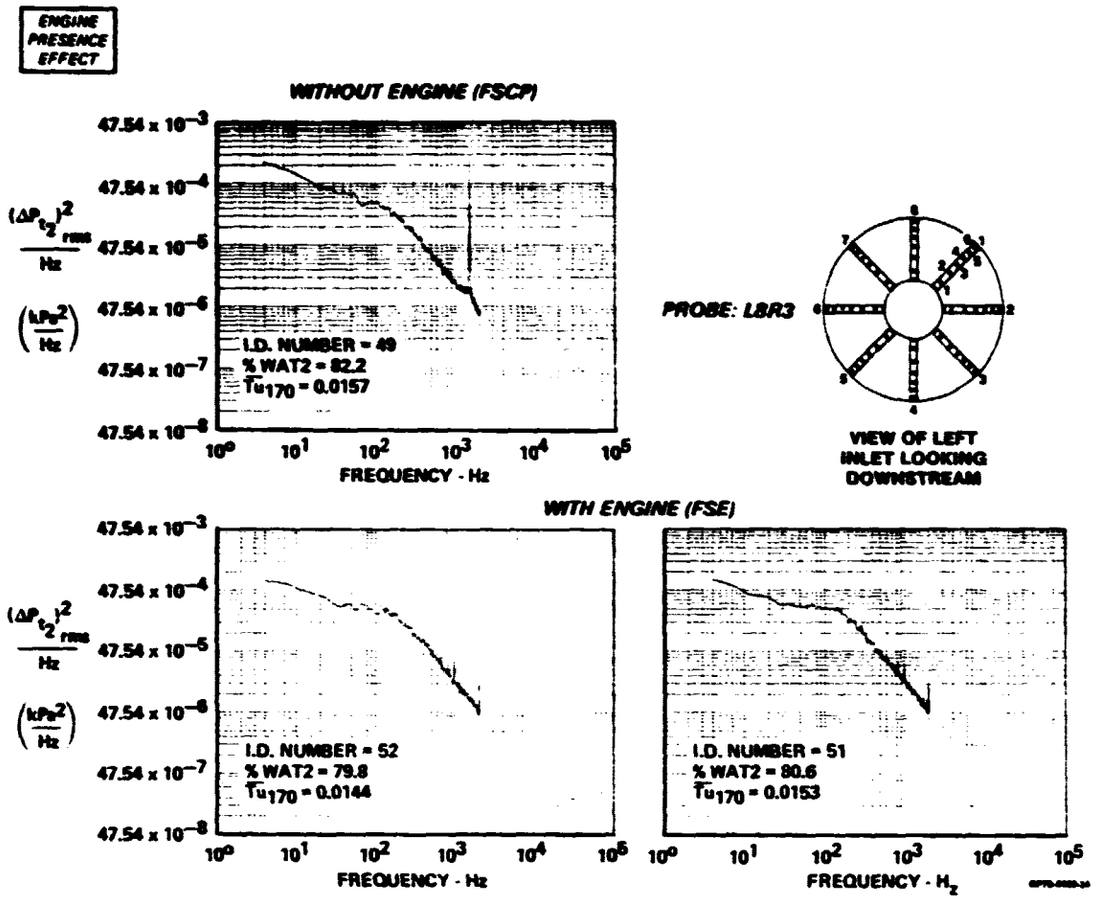

FIGURE 41
COMPARISON OF POWER SPECTRAL DENSITY PLOTS
Mach 1.8 $\alpha = -2$ $\beta = 0$ $\rho = -3.0$ $\Delta_3 = 18.7$ CIVV = −25.0

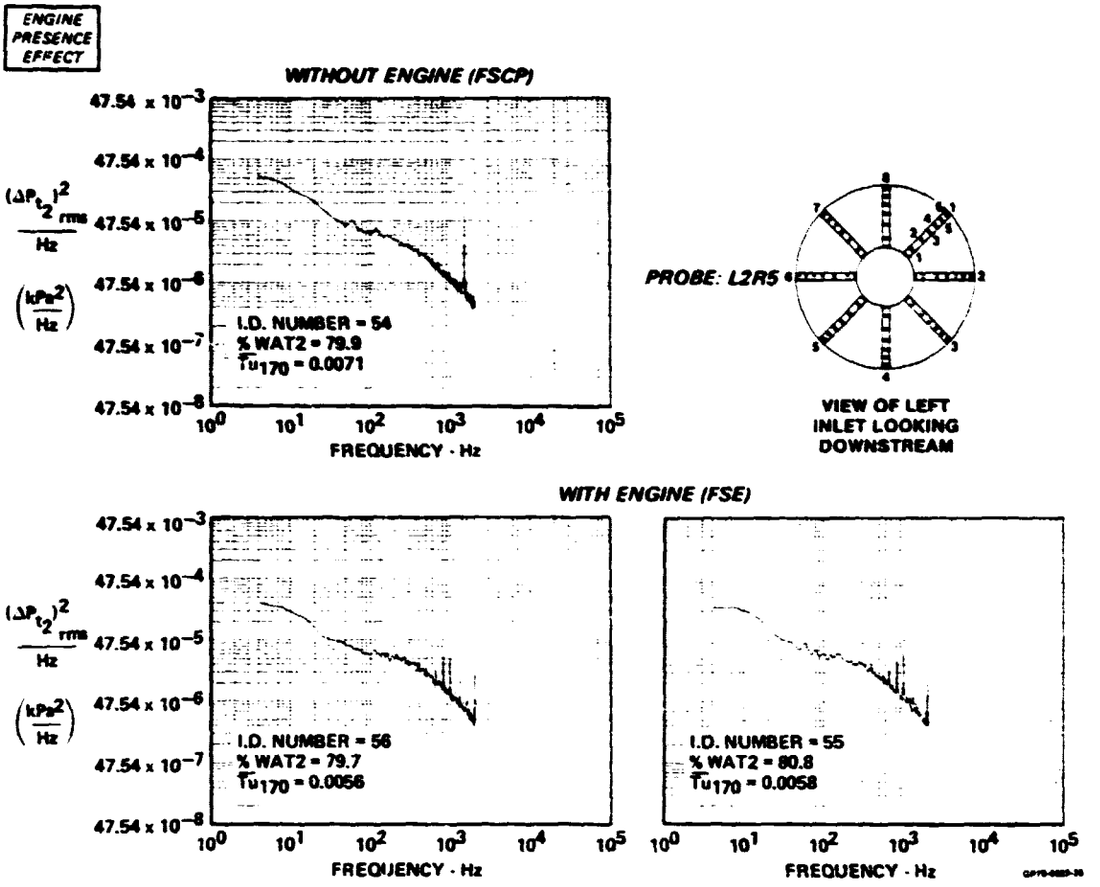

FIGURE 42
COMPARISON OF POWER SPECTRAL DENSITY PLOTS
Mach 1.8 $\alpha = 4$ $\beta = 0$ $\rho = 2.5$
$\Delta_3 = 18.7$ CIVV = —25.0

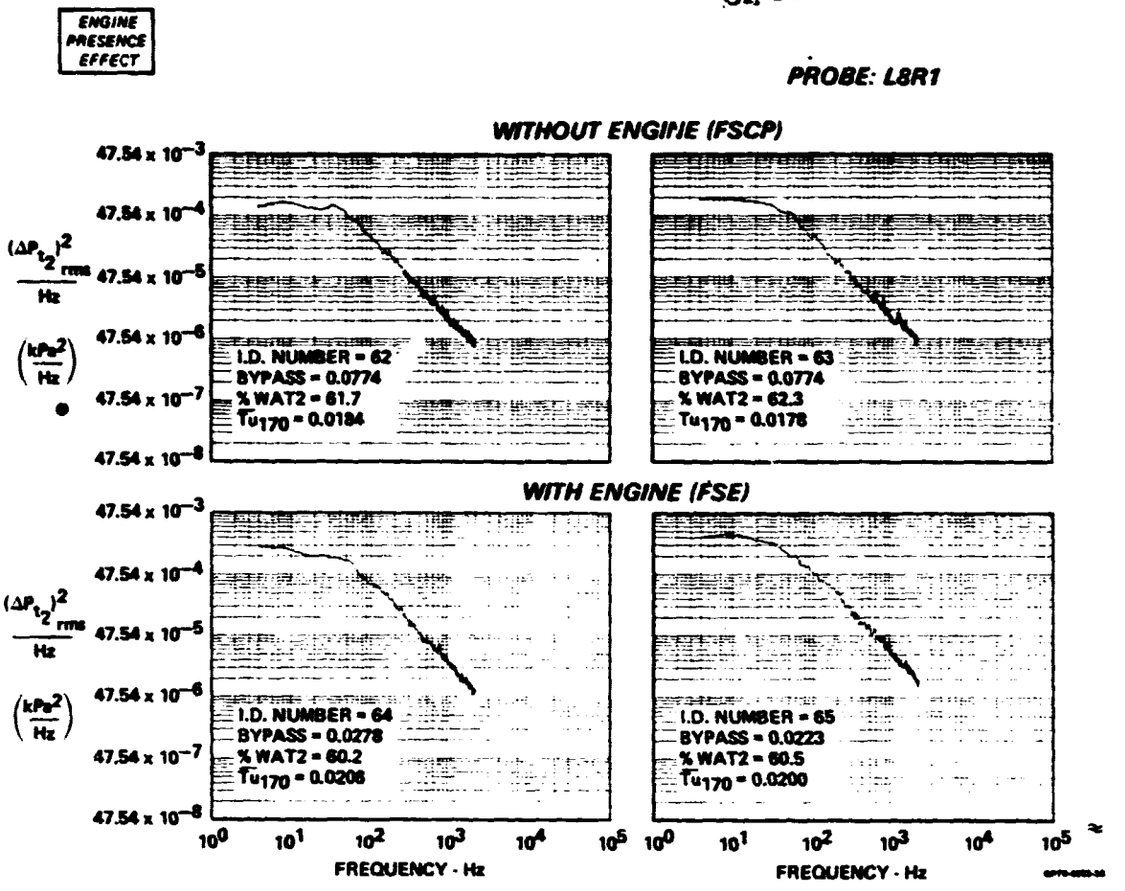

FIGURE 43
COMPARISON OF POWER SPECTRAL DENSITY PLOTS
Mach 2.2 $\alpha = -2$ β 0 $\rho = -4.0$ $\Delta_3 = 25.0$ CIVV = −25.0

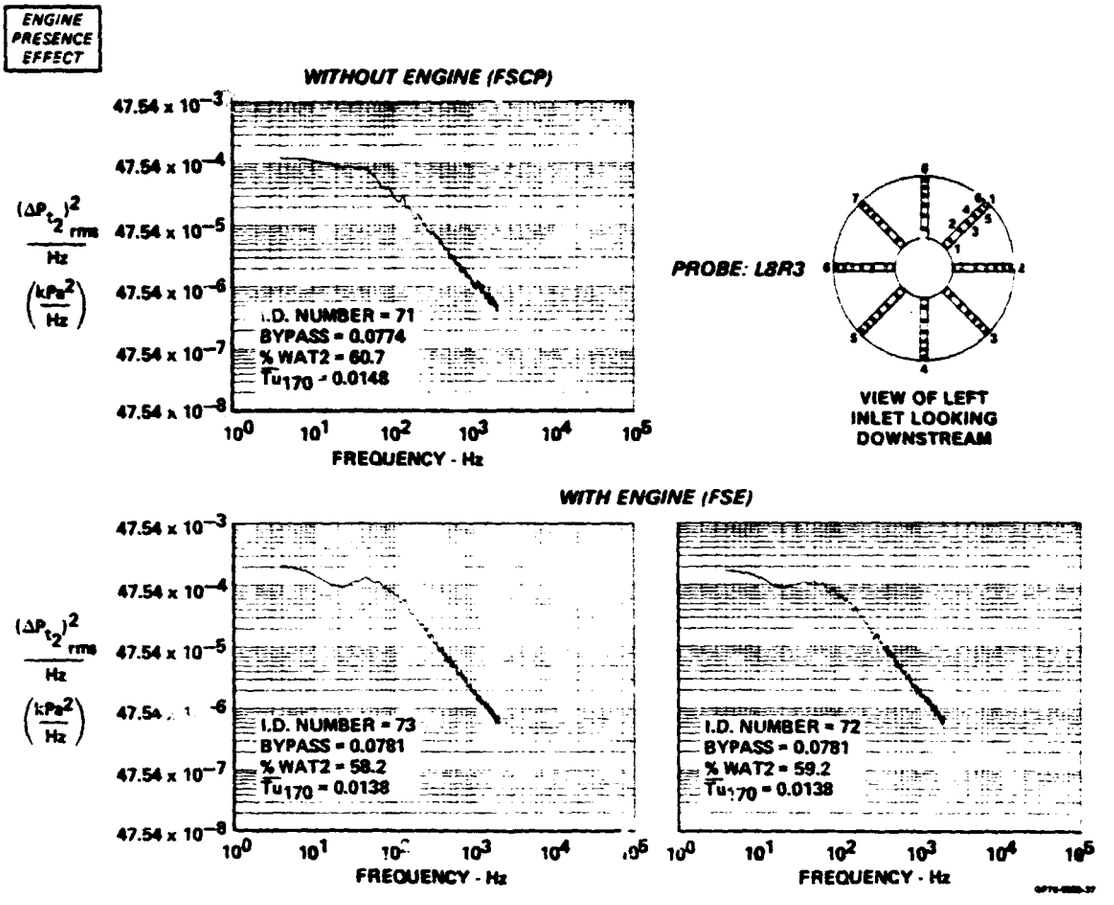

FIGURE 44

COMPARISON OF POWER SPECTRAL DENSITY PLOTS

Mach 2.2 $\alpha = 4$ $\beta = 0$ $\rho = 0$ $\Delta_3 = 25.0$ CIVV = —25.0

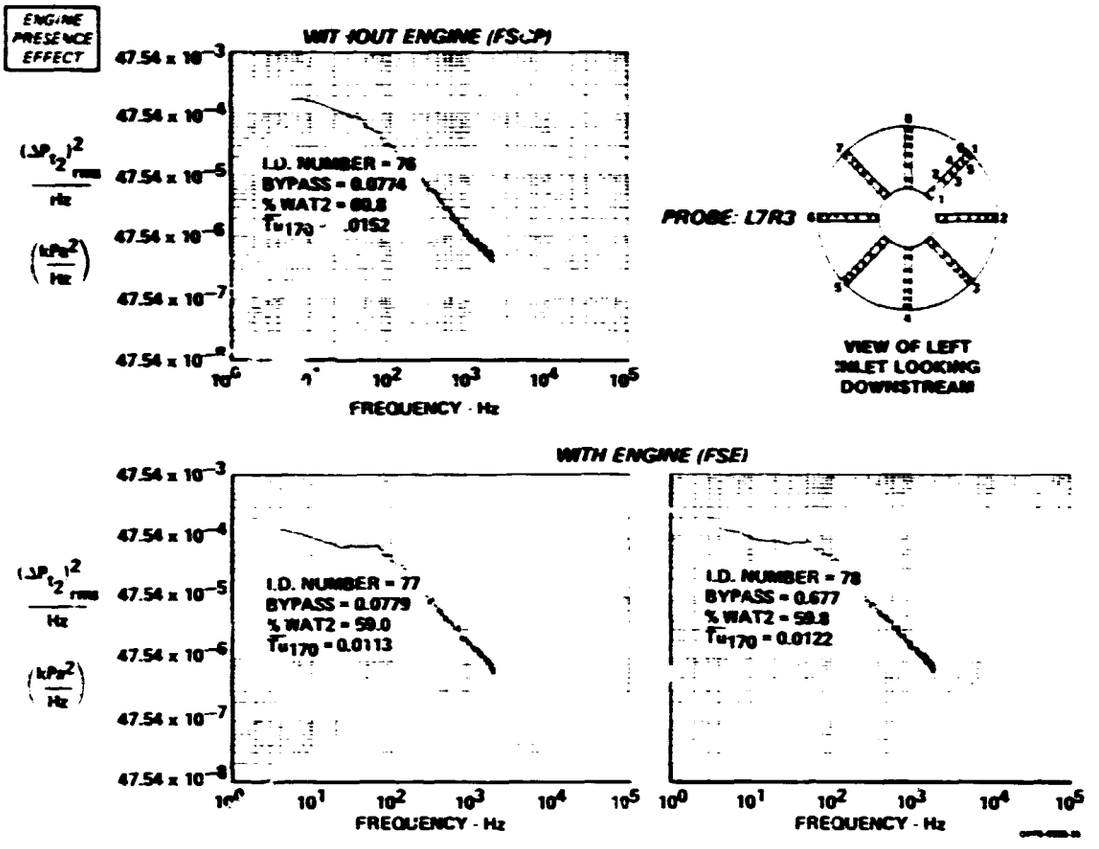

FIGURE 45
COMPARISON OF POWER SPECTRAL DENSITY PLOTS
Mach 2.2 α = 11-12 β = 0 ρ = 6.8 Δ_3 = 25.0 CIVV = —25.0

ENGINE PRESENCE EFFECT

I.D. NO.	M_o	WITH OR W/O ENGINE	WAT2	TIP*				HUB*				AVERAGES	
				PZW1	PZW4	PZW3	PZW2	PZ1F2	PZ1F3	PZ1F4	PZ1F1	TIP	HUB
48	1.8	W/O	75.1	–	0.914	0.917	0.921	–	0.906	0.906	0.914	0.917	0.909
52	1.8	WITH	79.8	0.877	0.884	0.891	–	0.907	–	0.913	0.903	0.884	0.908
49	1.8	W/O	82.2	0.892	0.895	0.898	0.902	0.884	0.890	0.895	0.906	0.897	0.894
56	1.8	WITH	79.7	0.877	0.881	0.887	0.888	0.900	–	0.909	0.915	0.883	0.908
54	1.8	W/O	79.9	0.896	0.901	0.905	0.911	0.879	0.890	0.893	0.896	0.903	0.888
55	1.8	WITH	80.8	0.883	0.884	0.890	0.892	0.898	–	0.895	0.898	0.887	0.897
64	2.2	WITH	60.2	0.928	0.946	0.948	0.935	0.946	–	0.952	0.934	0.937	0.944
65	2.2	WITH	60.5	0.933	0.945	0.938	0.934	0.943	–	0.952	0.933	0.938	0.943
62	2.2	W/O	61.7	0.941	0.943	0.946	0.948	0.941	0.941	0.937	0.950	0.944	0.942
63	2.2	W/O	62.3	0.943	0.944	0.948	0.950	0.938	0.940	0.938	0.951	0.946	0.942
73	2.2	WITH	58.2	0.937	0.936	0.938	0.940	0.948	–	0.950	0.940	0.938	0.946
72	2.2	WITH	59.2	0.936	0.937	0.941	0.940	0.947	–	0.950	0.946	0.938	0.948
71	2.2	W/O	60.7	0.947	0.948	0.950	0.955	–	0.938	0.934	0.937	0.950	0.936
77	2.2	WITH	59.0	0.943	0.938	0.944	0.944	0.949	–	0.943	0.949	0.942	0.947
78	2.2	WITH	59.8	0.941	0.937	0.931	0.944	0.948	–	0.948	0.946	0.938	0.945
76	2.2	W/O	60.8	0.944	0.945	0.947	0.952	0.925	0.936	0.931	0.931	0.947	0.931

*All Hub and Tip pressures normalized by freestream total pressure.

GP78-0323-40

FIGURE 46
TABULATED DATA COMPARISON OF AVERAGE HUB AND TIP STATIC PRESSURES FOR FULL SCALE INLET MODEL WITH AND WITHOUT ENGINE PRESENCE

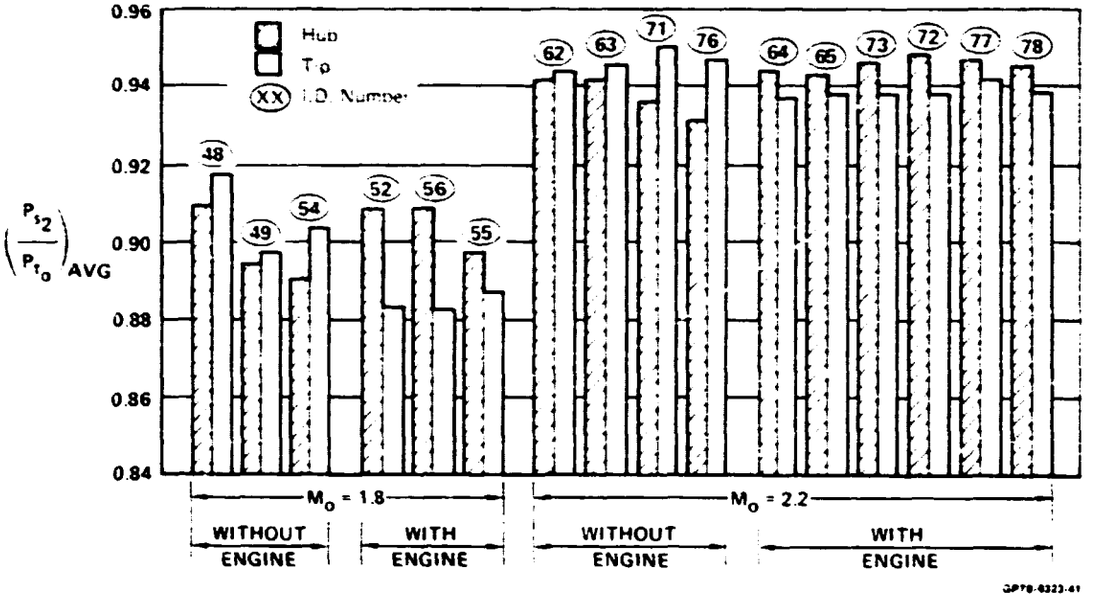

GP78-0323-41

FIGURE 47
COMPARISON OF AVERAGE HUB AND TIP STATIC PRESSURES FOR FULL SCALE INLET MODEL WITH AND WITHOUT ENGINE

ENGINE PRESENCE EFFECT

Note: These derived turbulence levels are computed by integrating the respective PSD plots.

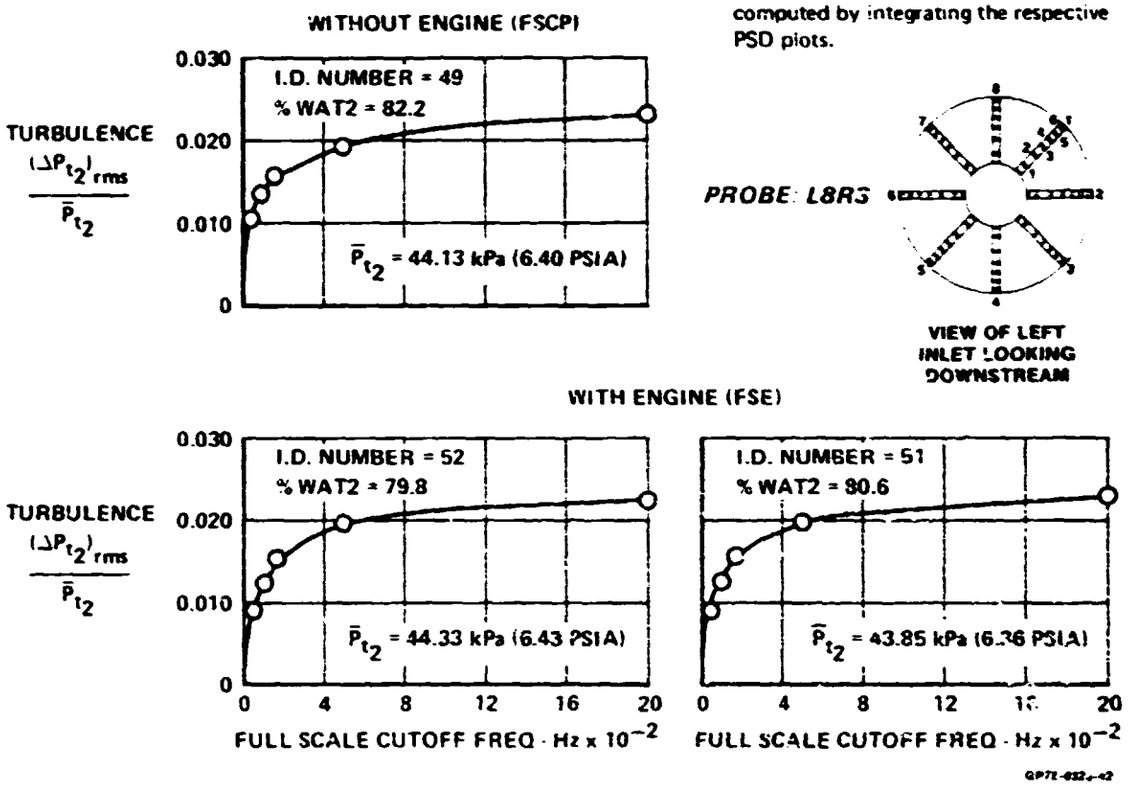

FIGURE 48
WITH AND WITHOUT ENGINE COMPARISONS OF DERIVED TURBULENCE LEVELS vs FILTER CUTOFF FREQUENCY
Mach 1.8 $\alpha = -2$ $\beta = 0$ $\rho = -3.0$ $\Delta_3 = 18.7$ CIVV = −25.0

ENGINE PRESENCE EFFECT

Note: These derived turbulence levels are computed by integrating the respective PSD plots.

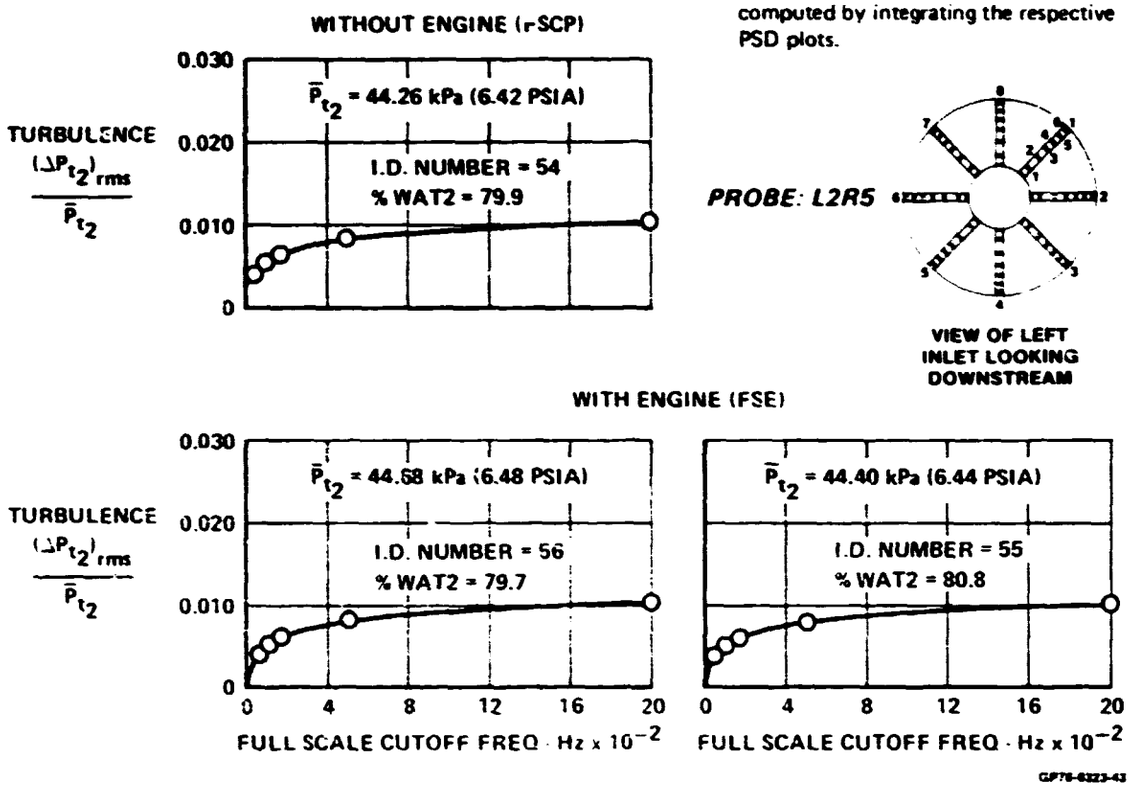

FIGURE 49
WITH AND WITHOUT ENGINE COMPARISONS OF DERIVED TURBULENCE LEVELS vs FILTER CUTOFF FREQUENCY

Mach 1.8 $\alpha = 4$ $\beta = 0$ $\rho = 2.5$ $\Delta_3 = 18.7$ CIVV = --25.0

ENGINE PRESENCE EFFECT

PROBE: L8R3

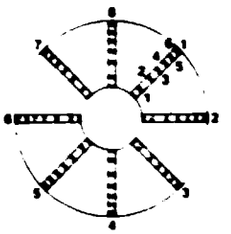

VIEW OF LEFT INLET LOOKING DOWNSTREAM

Note: These derived turbulence levels are computed by integrating the respective PSD plots.

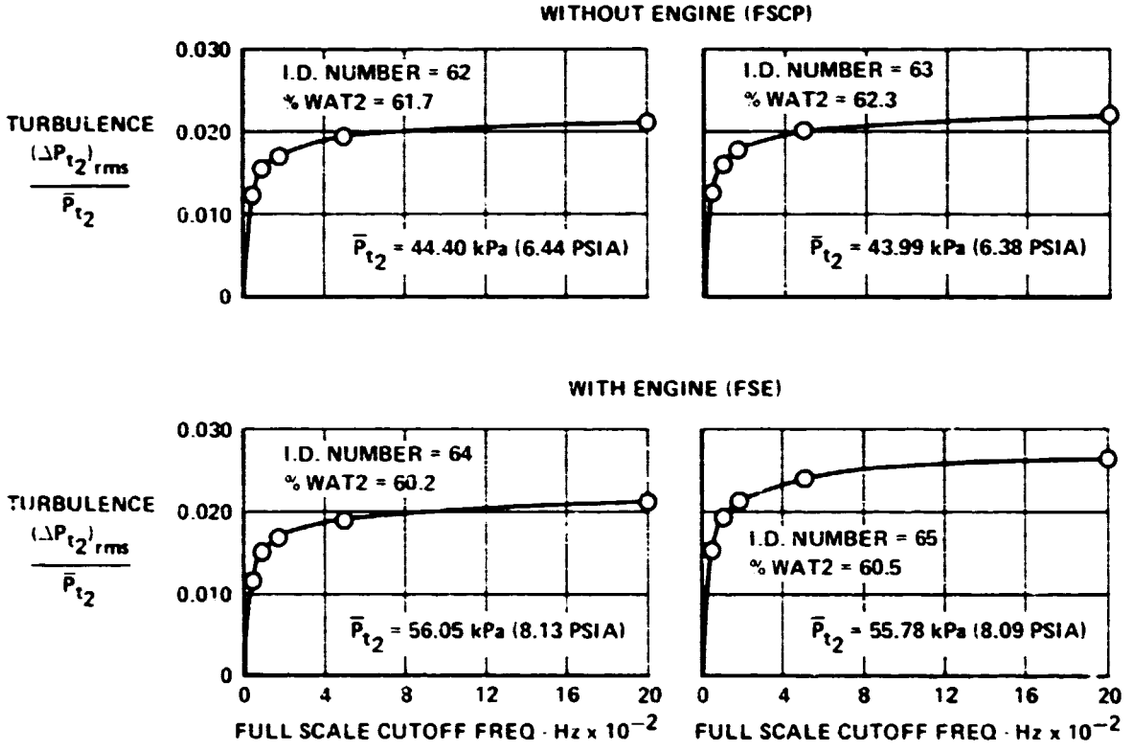

GP78-0323-44

FIGURE 50
WITH AND WITHOUT ENGINE COMPARISONS OF DERIVED TURBULENCE LEVELS vs FILTER CUTOFF FREQUENCY

Mach 2.2 $\alpha = -2$ $\beta = 0$ $\rho = -4.0$ $\Delta_3 = 25.0$ CIVV = −25.0

ENGINE PRESENCE EFFECT

Note: These derived turbulence levels are computed by integrating the respective PSD plots.

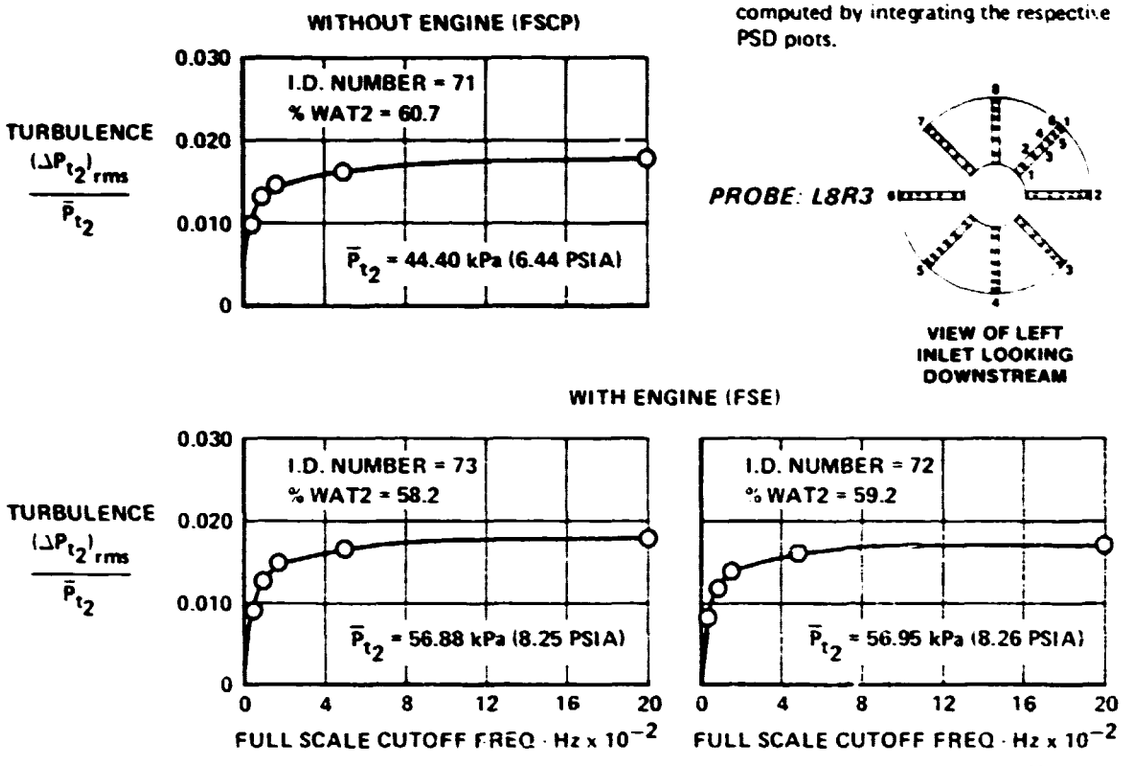

FIGURE 51
WITH AND WITHOUT ENGINE COMPARISONS OF DERIVED TURBULENCE LEVELS vs FILTER CUTOFF FREQUENCY

Mach 2.2 $\alpha = 4$ $\beta = 0$ $\rho = 0$ $\Delta_3 = 25.0$ CIVV = -25.0

SYM	I.D. NUMBER	MACH	α	A_{BYP}*	PERCENT WAT2
○	48, 52, 51, 49	1.8	−2	C	79.8
□	56, 54, 55	1.8	4	C	79.9
△	64, 65, 62, 63	2.2	−2	O,P	60.2
◇	73, 72, 71	2.2	4	O	60.7
◺	77, 78, 76	2.2	11	O,P	60.8

ENGINE PRESENCE EFFECT

FLAGS INDICATE INTERPOLATED AND EXTRAPOLATED DATA RELATIVE TO AIRFLOW.

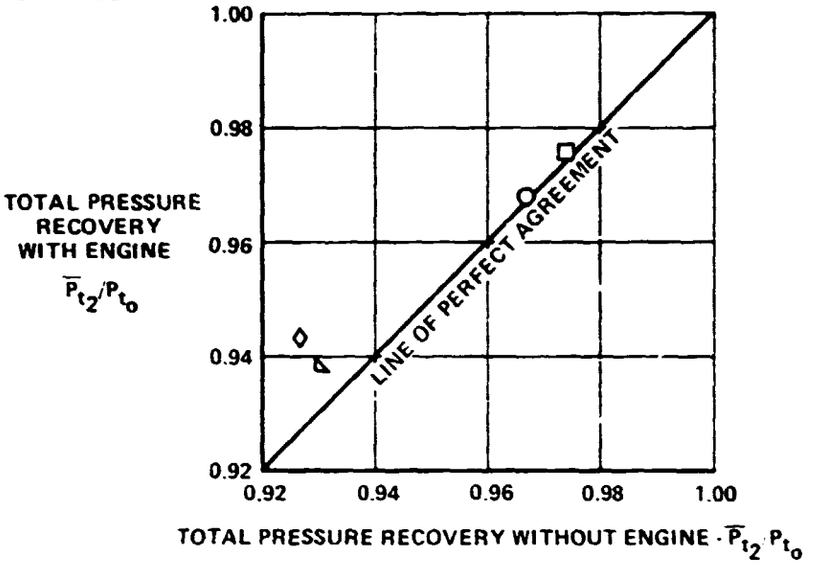

*C = Closed 0 = Open P = Partially Opened

CP78-6323-47

FIGURE 53
COMPARISON TOTAL PRESSURE RECOVERY
WITH AND WITHOUT ENGINE

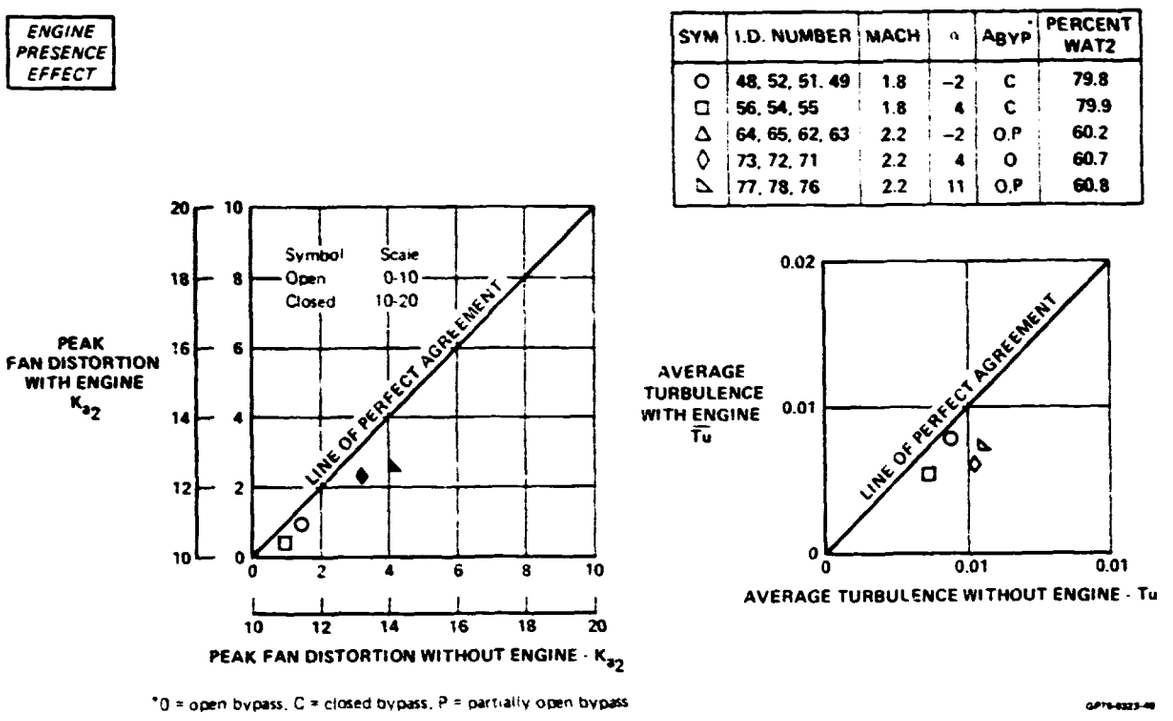

FIGURE 54
COMPARISON OF PEAK FAN DISTORTION AND TURBULENCE

REYNOLDS NUMBER, SCALE EFFECTS

DATA POINT IDENTIFICATION NUMBER										
1/6th SCALE	FULL SCALE COLD PIPE	FULL SCALE WITH ENGINE	FLIGHT TEST	M_0	α (DEG)	β (DEG)	ρ (DEG)	λ_3 (DEG)	BYPASS*	PERCENT WAT2
6	–	–	7	0.6	–10	10	–3	10.6	C	101.2
5	–	–								
8	–	–	12, 14	0.6	4	0	7	10.6	C	76.6
	–	10	11							
9	–	–	13							97.7
17	–	–	19	0.9	–10	10	–3	10.6	C	107.1
18	–	–								
–	–	20	21	0.9	–4	0	–1	8.2	C	97.6
–	–		22							
23	–	–	26, 27, 28	0.9	4	0	7	10.4	C	77.5
–	–	25	29, 30, 31							97.7
24	–	–	32, 33							
36	–	–	38, 39	1.2	10	0	7	10.6	C	76.6
37	–	–	40							103.4
42, 43	–	–	44	1.6	–4	0	–2	13.5	C	89.1
45, 46	–	–	47	1.8	–2	0	–3	17.4	C	80.7
–	48, 49	51, 52	53	1.8	–2	0	–3	18.7	C	78.9
66, 67	68, 69**	–	70	2.2	0	0	–2	22.5	C	73.0
58	59**	–	–	2.2	–2	0	–4	22.5	C	–
60, 61	62, 63	64, 65***	–	2.2	–2	0	–4	25.0	O	61.7
74, 75	76	77	–	2.2	11	0	6.8	25.0	O	60.8
73	81	–	–	2.5	0	0	–4	26.0	O	
30	82	–	–							63.1

*O = Open Bypass, C = Closed Bypass

**These data exhibited harmonic characteristics and are not included in this analysis

***These data have different bypass areas and are not included in this analysis

GP78-0323-49

FIGURE 55
TEST CONDITIONS FOR EVALUATING REYNOLDS NUMBER/SCALE EFFECTS

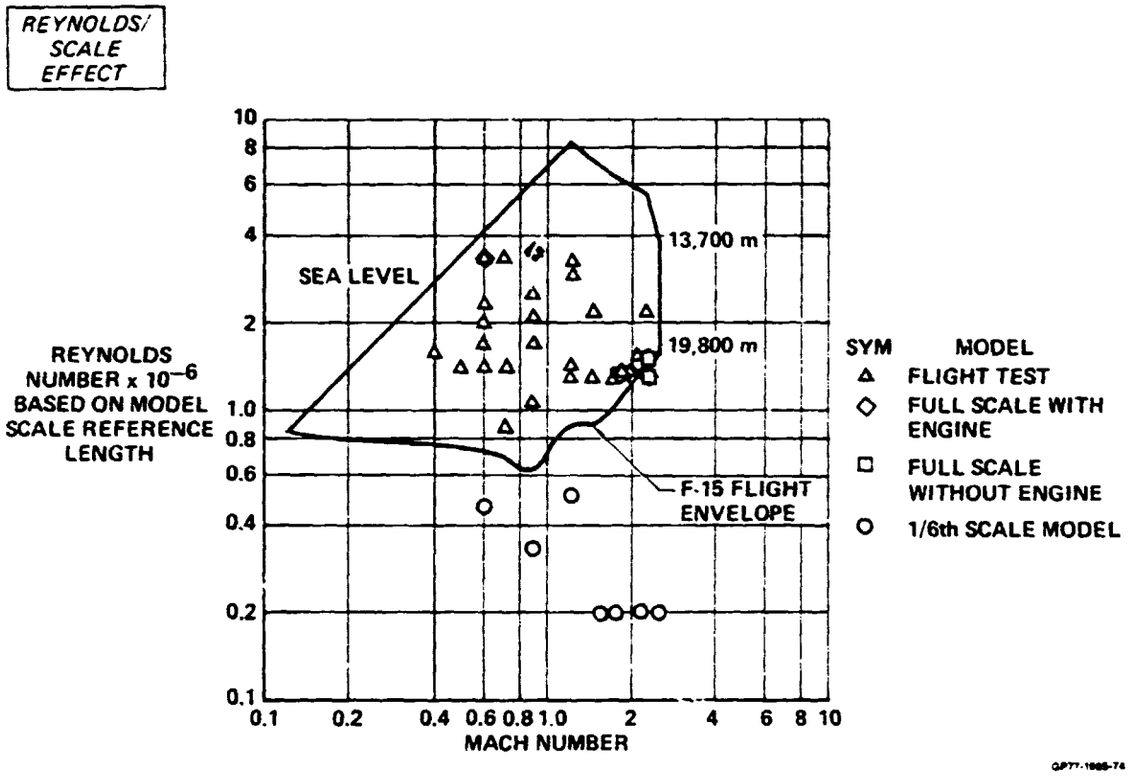

FIGURE 56
REYNOLDS NUMBER AND MACH NUMBER RANGE OF THE FLIGHT TEST FULL SCALE AND 1/6th SCALE DATA

REYNOLDS NUMBER SCALE EFFECTS

Flags indicate interpolated or extrapolated data relative to airflow

Percent WAT2 101.2

SYM	MODEL	I.D. NUMBER
○	1/6th SCALE	5, 6
□	FSCP	
◇	FSE	
△	FLT	7

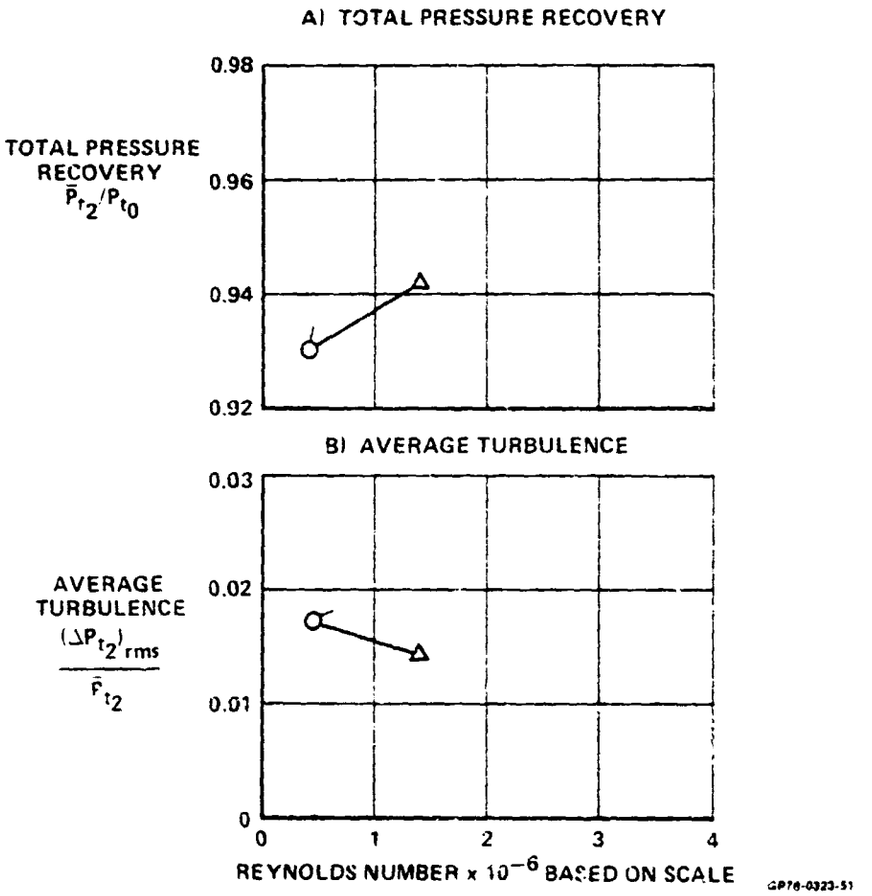

FIGURE 57
EFFECT OF REYNOLDS NUMBER/SCALE ON TOTAL PRESSURE RECOVERY AND TURBULENCE

Mach 0.6 $\alpha = -10$ $\beta = 10$ $\rho = -3$ $\Delta_3 = 10.6$ Bypass = 0.0

REYNOLDS NUMBER SCALE EFFECTS

Solid symbol - steady state
Open symbol - corresponds to peak time variant fan distortion
Flags indicate interpolated or extrapolated data relative to airflow

Percent WAT2
101.2

SYM	MODEL	I.D. NUMBER
○	1/6th SCALE	5, 6
□	FSCP	
◇	FSE	
△	FLT	7

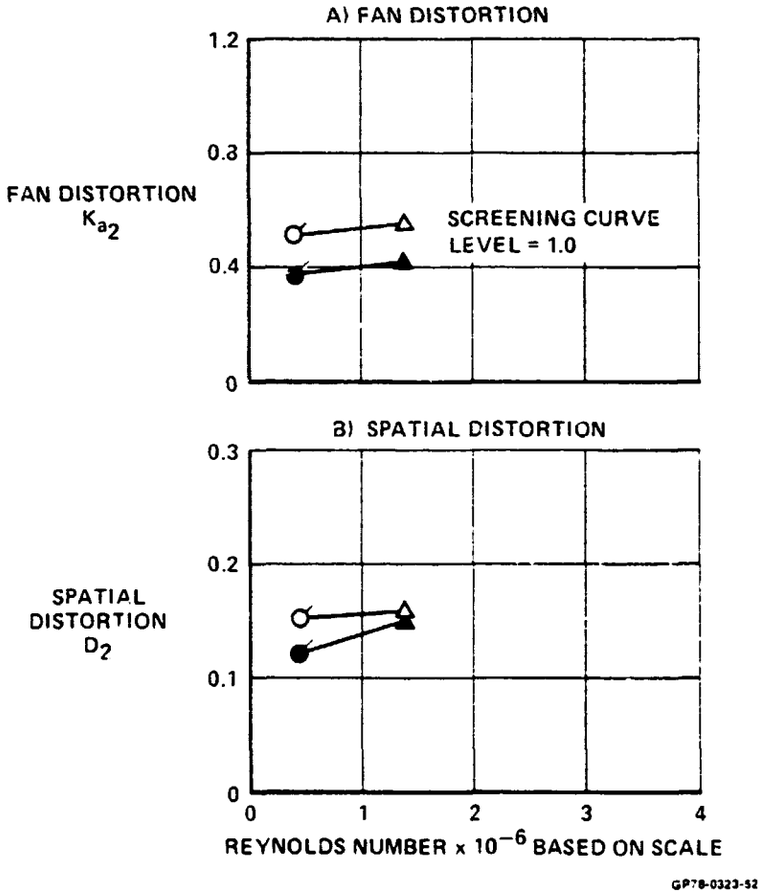

FIGURE 58
EFFECT OF REYNOLDS NUMBER/SCALE ON FAN DISTORTION AND SPATIAL DISTORTION

Mach 0.6 $\alpha = -10$ $\beta = 10$ $\rho = -3$ $\Delta_3 = 10.6$ Bypass 0.0

REYNOLDS NUMBER SCALE EFFECTS

Flags indicate interpolated or extrapolated data relative to airflow

Percent WAT2	
76.6	– – –
97.7	———

SYM	MODEL	I.D. NUMBER
○	1/6th SCALE	8, 9
□	FSCP	
◇	FSE	10
△	FLT	11,12,13,14

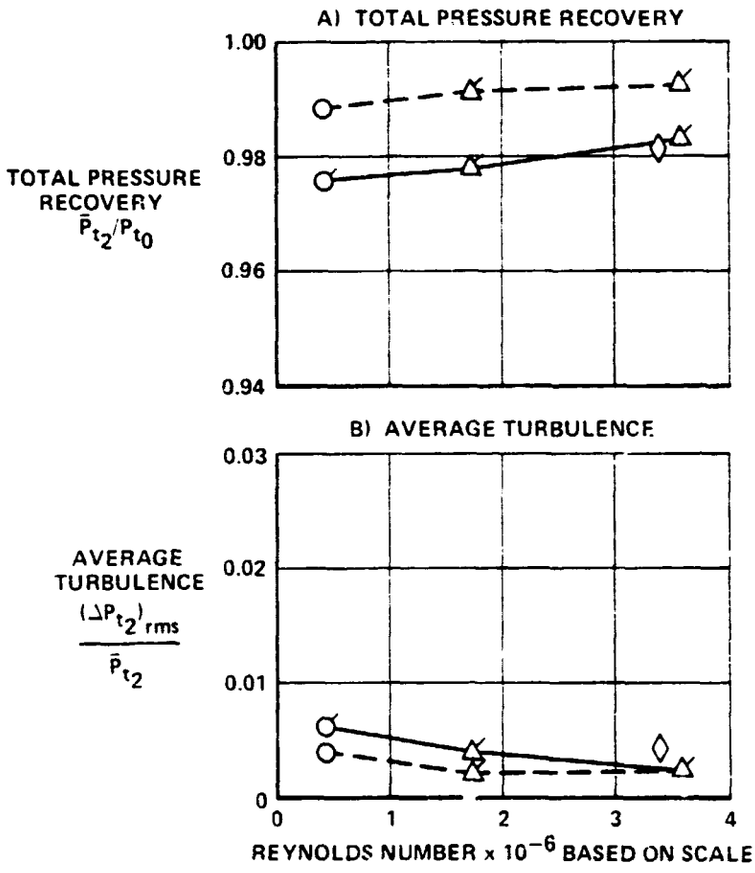

GP78-0323-53

FIGURE 59
EFFECT OF REYNOLDS NUMBER/SCALE ON TOTAL PRESSURE RECOVERY AND TURBULENCE

Mach 0.6 $\alpha = 4$ $\beta = 0$ $\rho = 7$ $\Delta_3 = 10.6$ Bypass = 0.0

REYNOLDS NUMBER SCALE EFFECTS

Solid symbol - steady state
Open symbol - corresponds to peak time variant fan distortion
Flags indicate interpolated or extrapolated data relative to airflow

Percent WAT2
76.6
97.7

SYM	MODEL	I.D. NUMBER
○	1/6th SCALE	8, 9
□	FSCP	
◇	FSE	10
△	FLT	11,12,13,14

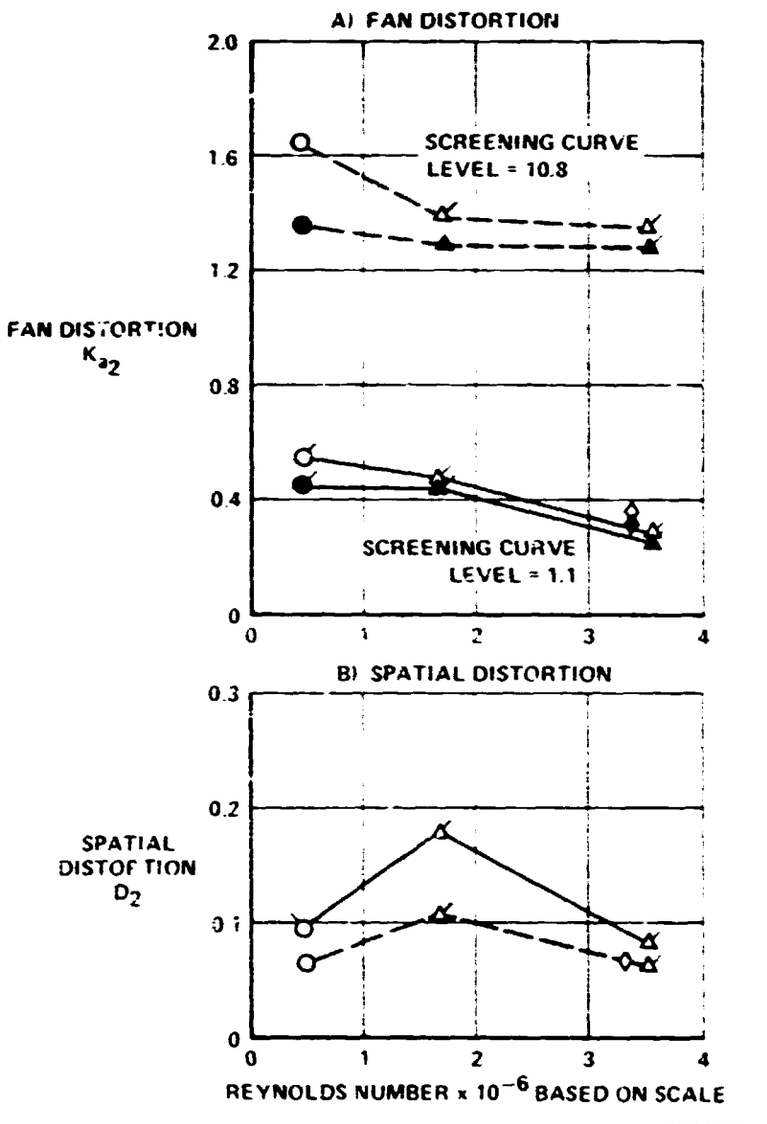

FIGURE 60
EFFECT OF REYNOLDS NUMBER SCALE ON FAN DISTORTION AND SPATIAL DISTORTION
Mach 0.6 α = 4 β = 0 ϕ = 7 Δ_3 = 10.6 Bypass = 0.0

REYNOLDS NUMBER SCALE EFFECTS

Flags indicate interpolated or extrapolated data relative to airflow

Percent WAT2
107.1

SYM	MODEL	I.D. NUMBER
○	1/6th SCALE	17, 18
□	FSCP	
◇	FSE	
△	FLT	19

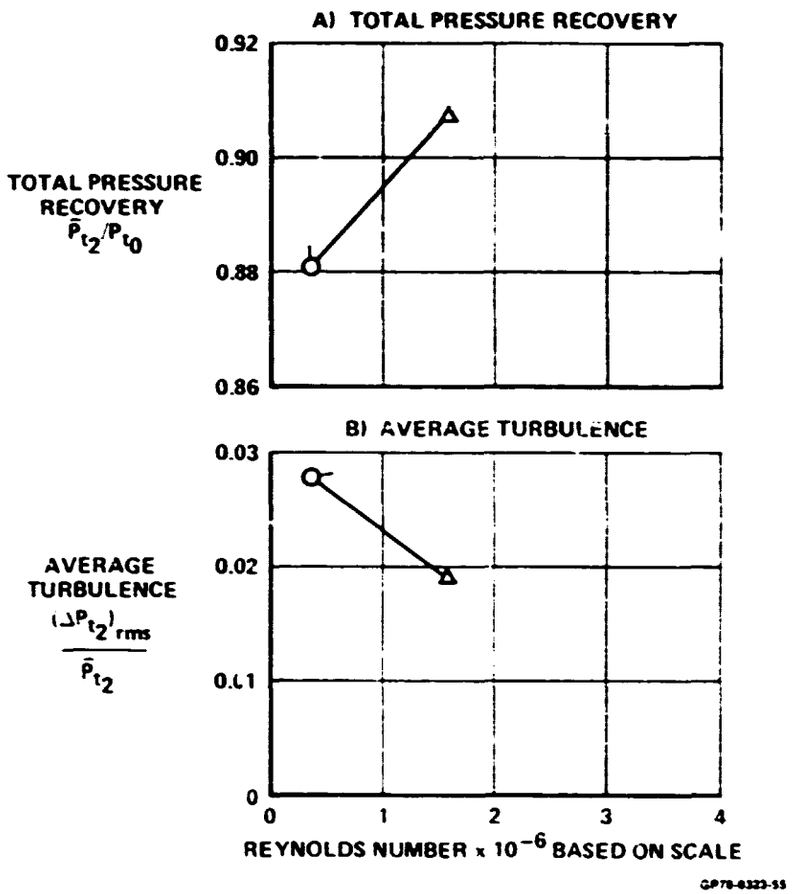

FIGURE 61
EFFECT OF REYNOLDS NUMBER/SCALE ON TOTAL PRESSURE RECOVERY AND TURBULENCE
Mach 0.9 $\alpha = -1C$ $\beta = 10$ $\rho = 3$ $\Delta_3 = 10.6$ Bypass = 0.0

REYNOLDS NUMBER/SCALE EFFECTS

Solid symbol - steady state
Open symbol - corresponds to peak time variant fan distortion
Flags indicate interpolated or extrapolated data relative to airflow

Percent WAT2
107.1

SYM	MODEL	I.D. NUMBER
○	1/6th SCALE	17, 18
□	FSCP	
◇	FSE	
△	FLT	19

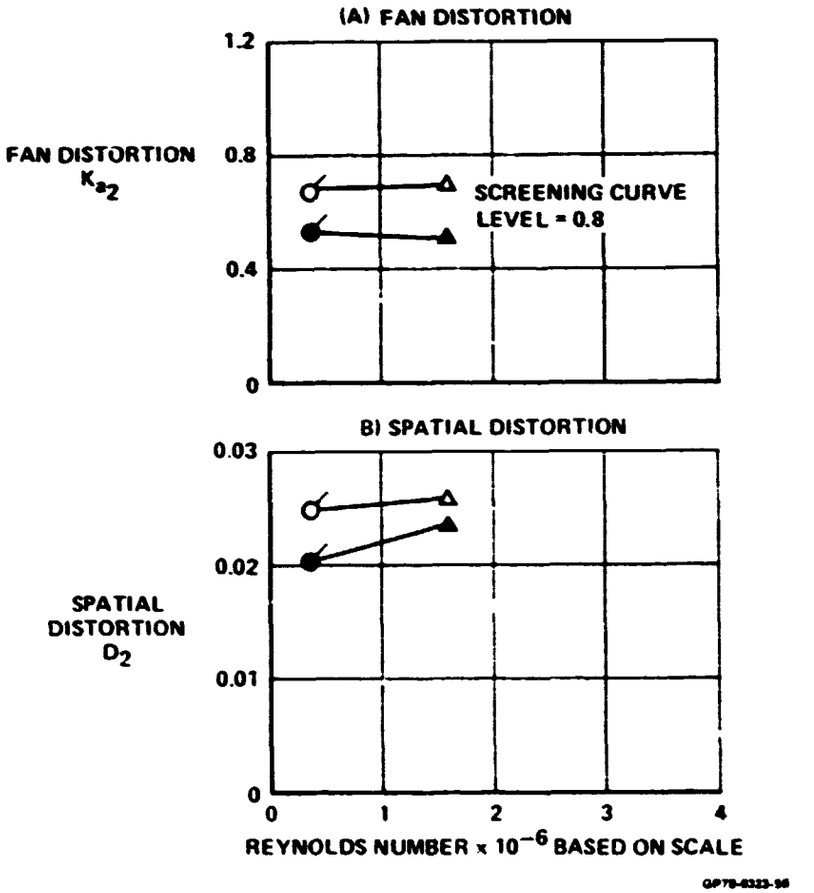

FIGURE 62
EFFECT OF REYNOLDS NUMBER/SCALE ON FAN DISTORTION AND SPATIAL DISTORTION
Mach 0.9 $\alpha = -10$ $\beta = 10$ $\rho = 3$ $\Delta_3 = 10.6$ Bypass = 0.0

REYNOLDS NUMBER/SCALE EFFECTS

Flags indicate interpolated or extrapolated data relative to airflow

Percent WAT2	
◊	97.8
△	97.5

SYM	MODEL	I.D. NUMBER
O	1/6th SCALE	
□	FSCP	
◊	FSE	20
△	FLT	21

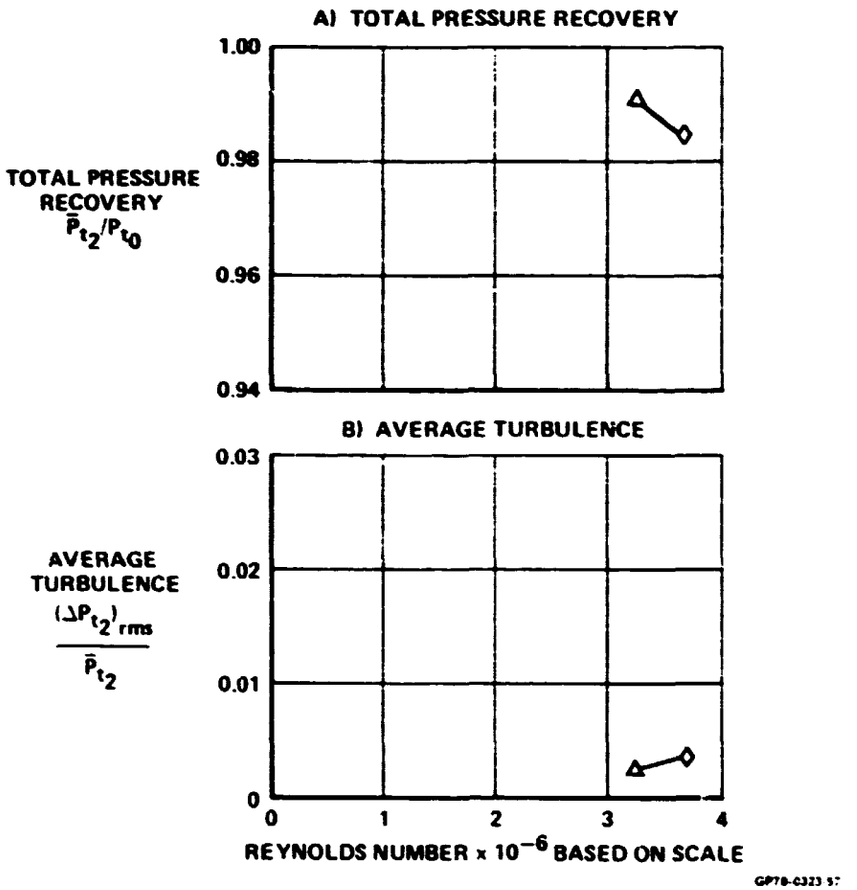

FIGURE 63
EFFECT OF REYNOLDS NUMBER/SCALE ON TOTAL PRESSURE RECOVERY AND TURBULENCE

Mach 0.9 $\alpha = -4$ $\beta = 0$ $\rho = -1$ $\Delta_3 = 8.2$ Bypass = 0.0

REYNOLDS NUMBER SCALE EFFECTS

Solid symbol - steady state
Open symbol - corresponds to peak time variant fan distortion
Flags indicate interpolated or extrapolated data relative to airflow

Percent WAT2
◊ 97.8
△ 97.5

SYM	MODEL	I.D. NUMBER
○	1/6th SCALE	
□	FSCP	
◊	FSE	20
△	FLT	21

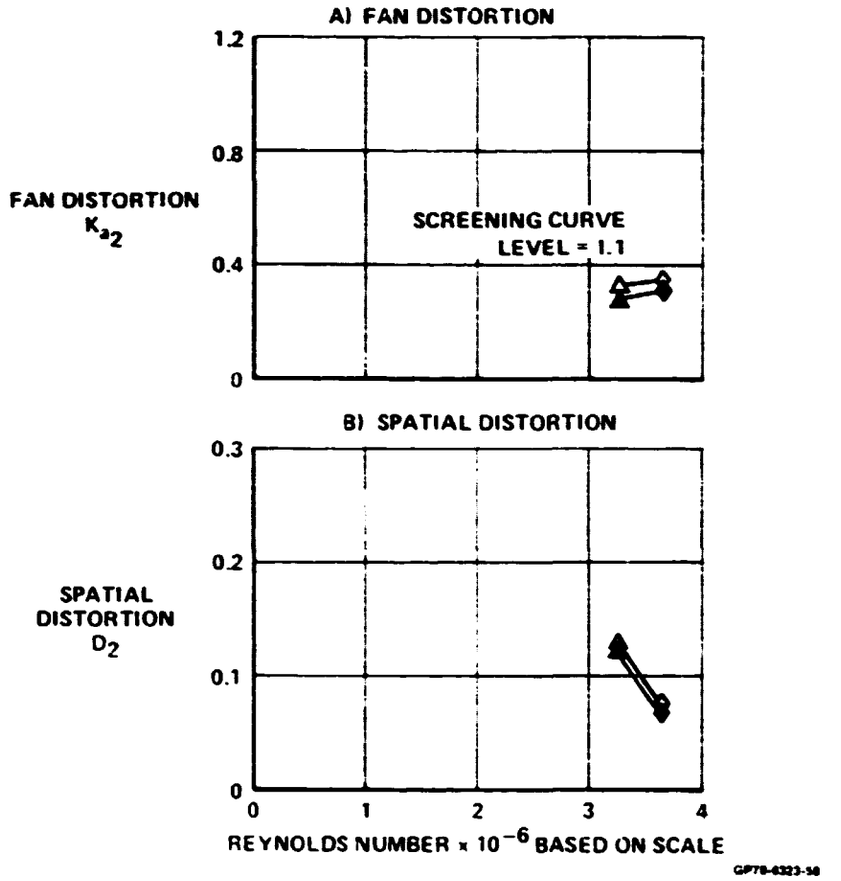

FIGURE 64
EFFECT OF REYNOLDS NUMBER/SCALE ON FAN DISTORTION AND SPATIAL DISTORTION
Mach 0.9 $\alpha = -4$ $\beta = 0$ $\rho = -1$ $\Delta_3 = 8.2$ Bypass = 0.0

REYNOLDS NUMBER/SCALE EFFECTS

Flags indicate interpolated or extrapolated data relative to airflow

Percent WAT2
97.7
77.5

SYM	MODEL	I.D. NUMBER
○	1/6th SCALE	23, 24
□	FSCP	
◇	FSE	25
△	FLT	26-33

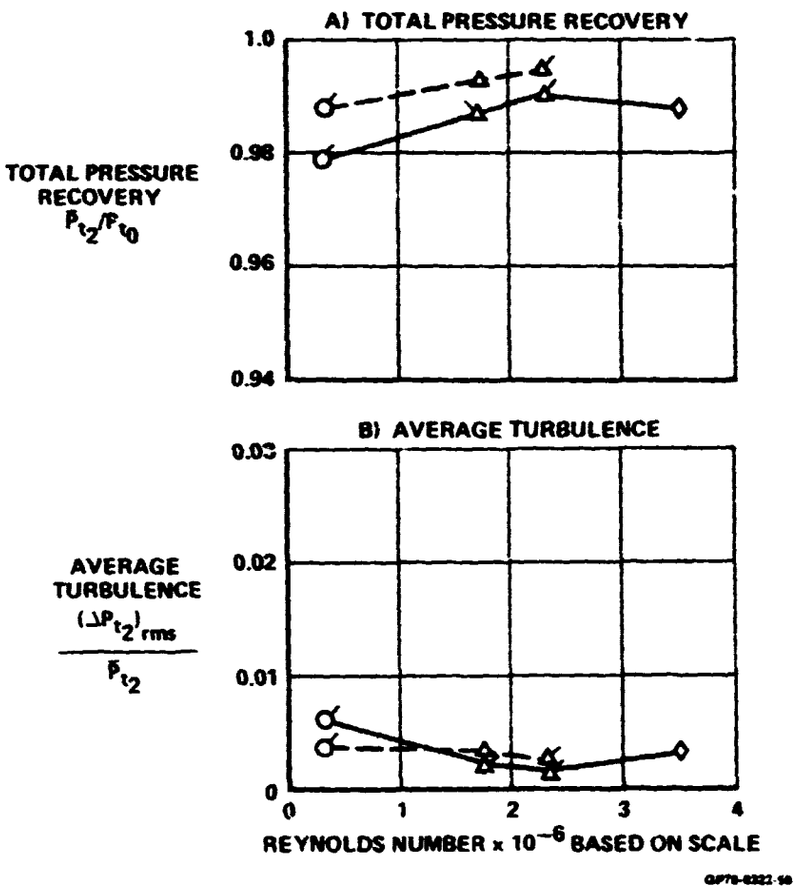

FIGURE 65
EFFECT OF REYNOLDS NUMBER/SCALE ON TOTAL PRESSURE RECOVERY AND TURBULENCE
Mach 0.9 $\alpha = 4$ $\beta = 0$ $\rho = 7$ $\Delta 3 = 10.4$ Bypass = 0.0

REYNOLDS NUMBER/SCALE EFFECTS

Solid symbol - steady state
Open symbol - corresponds to peak time variant fan distortion
Flags indicate interpolated or extrapolated data relative to airflow

Percent WAT2
97.7
77.5

SYM	MODEL	I.D. NUMBER
○	1/6th SCALE	23, 24
□	FSCP	
◇	FSE	25
△	FLT	26-33

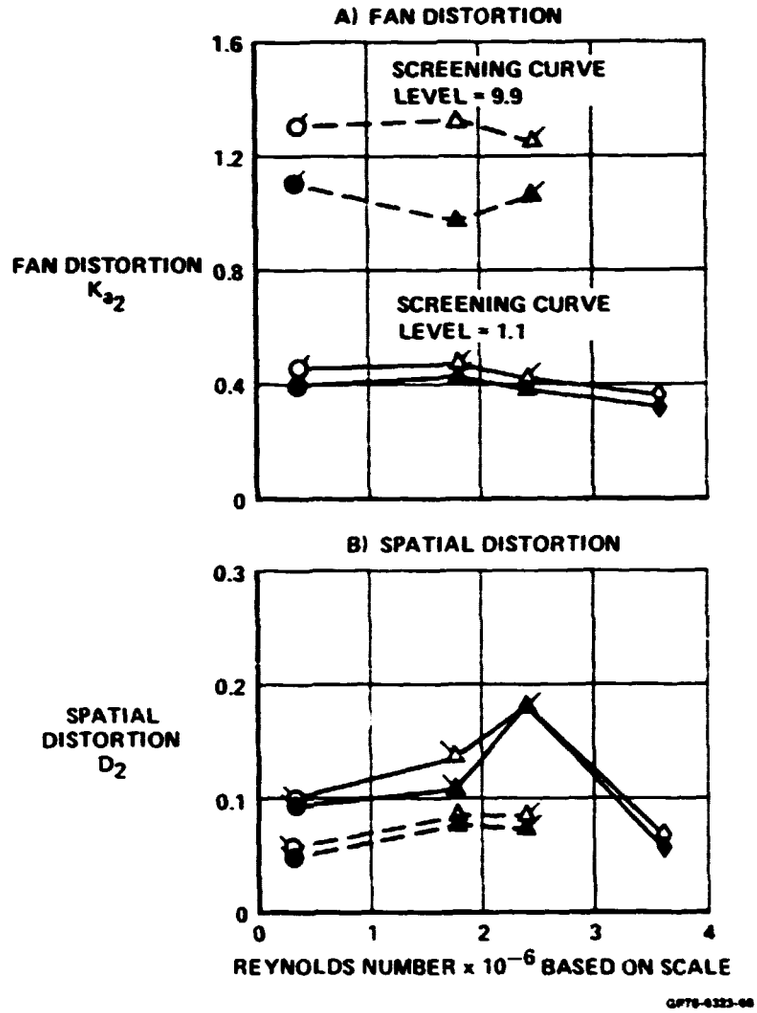

FIGURE 66
EFFECT OF REYNOLDS NUMBER/SCALE ON FAN DISTORTION AND SPATIAL DISTORTION
Mach 0.9 $\alpha = 4$ $\beta = 0$ $\rho = 7$ $\Delta_3 = 10.4$ Bypass = 0.0

REYNOLDS NUMBER/SCALE EFFECTS

Flags indicate interpolated or extrapolated data relative to airflow

Percent WAT2
103.4
76.6

SYM	MODEL	I.D. NUMBER
○	1/6th SCALE	36, 37
□	FSCP	
◇	FSE	
△	FLT	38, 39, 40

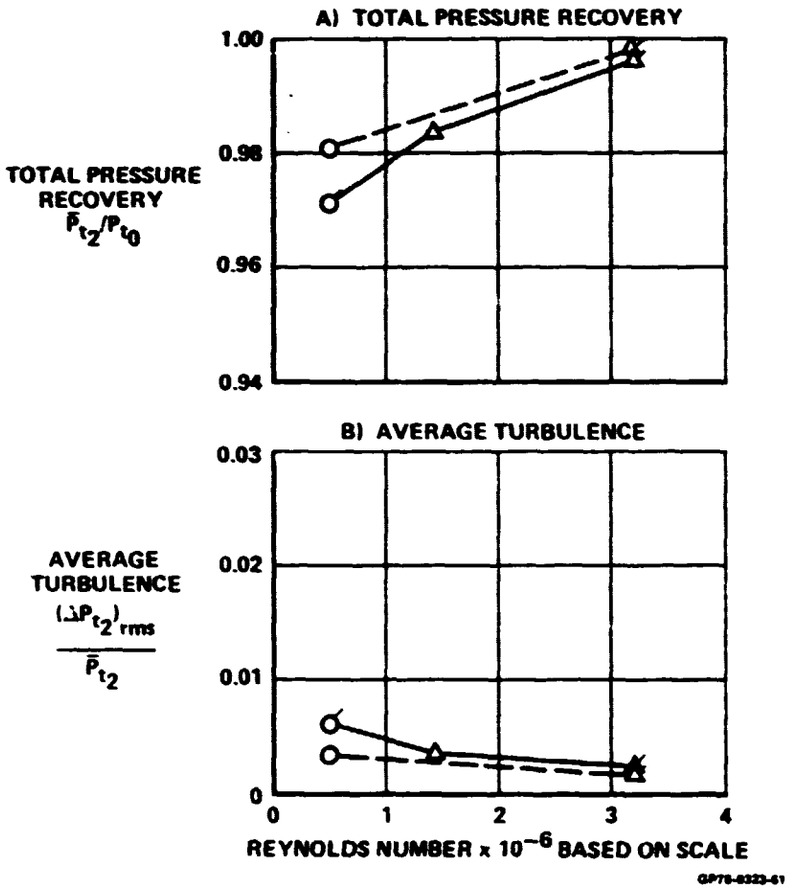

FIGURE 67
EFFECT OF REYNOLDS NUMBER/SCALE ON TOTAL PRESSURE RECOVERY AND TURBULENCE
Mach 1.2 $\alpha = 10$ $\beta = 0$ $\rho = 7$ $\Delta_3 = 10.6$ Bypass = 0.0

REYNOLDS NUMBER/SCALE EFFECTS

Solid symbol - steady state
Open symbol - corresponds to peak time variant fan distortion
Flags indicate interpolated or extrapolated data relative to airflow

Percent WAT2
103.4
76.6

SYM	MODEL	I.D. NUMBER
○	1/6th SCALE	36, 37
□	FSCP	
◇	FSE	
△	FLT	38, 39, 40

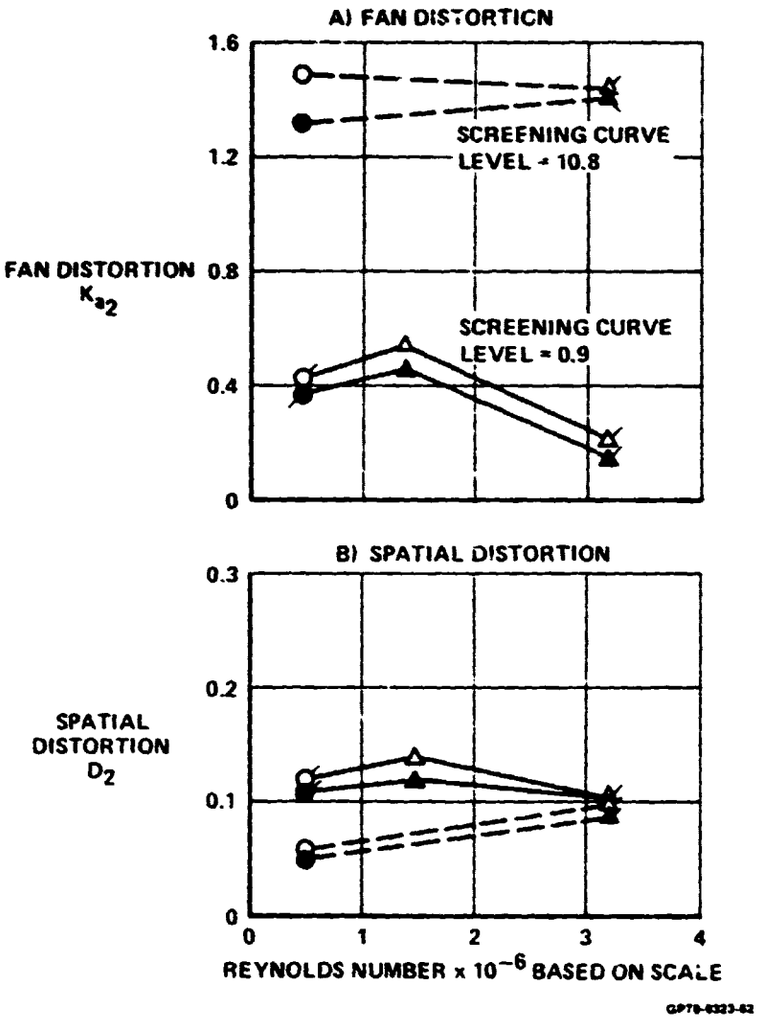

FIGURE 68
EFFECT OF REYNOLDS NUMBER/SCALE ON TOTAL PRESSURE RECOVERY AND TURBULENCE
Mach 1.2 α = 10 β = 0 ρ = 7 Δ_3 = 10.6 Bypass = 0.0

REYNOLDS NUMBER/SCALE EFFECTS

Flags indicate interpolated or extrapolated data relative to airflow

Percent WAT2 89.1

SYM	MODEL	I.D. NUMBER
○	1/6th SCALE	42, 43
□	FSCP	
◇	FSE	
△	FLT	44

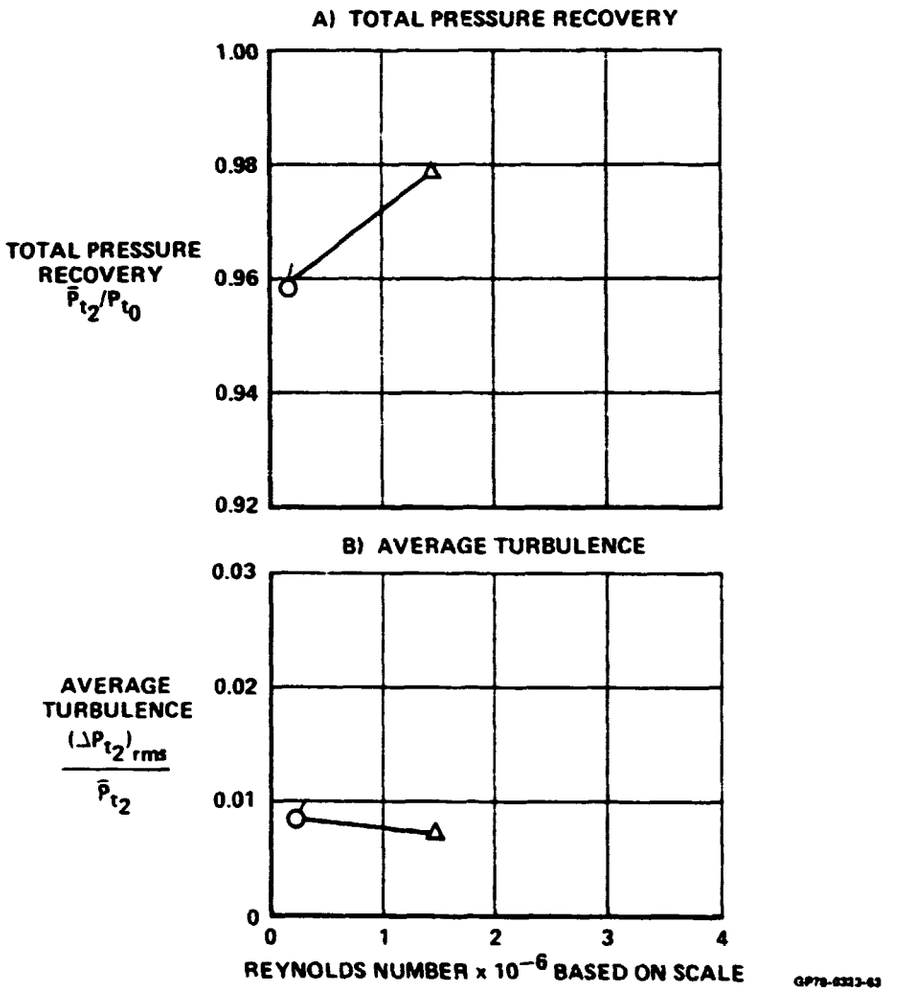

FIGURE 69
EFFECT OF REYNOLDS NUMBER/SCALE ON TOTAL PRESSURE RECOVERY AND TURBULENCE
Mach 1.6 $\alpha = -4$ $\beta = 0$ $\rho = -2$ $\Delta_3 = 13.5$ Bypass = 0.0

REYNOLDS NUMBER/SCALE EFFECTS

Solid symbol - steady state
Open symbol - corresponds to peak time variant fan distortion
Flags indicate interpolated or extrapolated data relative to airflow

Percent
WAT2
89.1

SYM	MODEL	I.D. NUMBER
○	1/6th SCALE	42, 43
□	FSCP	
◇	FSE	
△	FLT	44

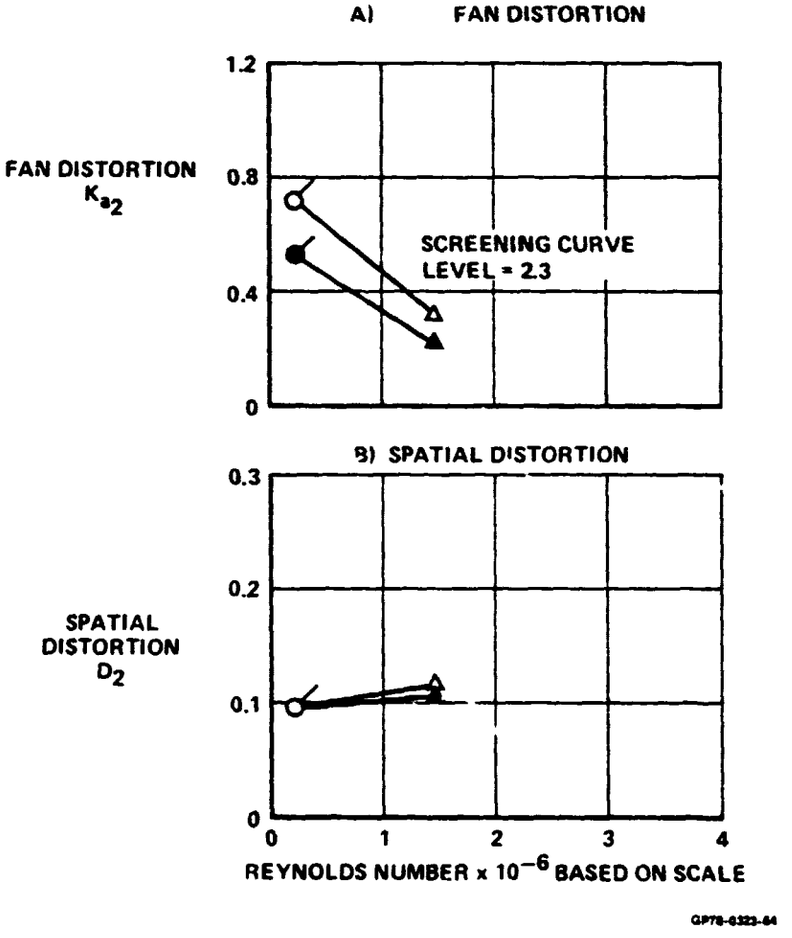

GP78-0323-64

FIGURE 70
EFFECT OF REYNOLDS NUMBER/SCALE ON FAN DISTORTION AND SPATIAL DISTORTION
Mach 1.6 $\alpha = -4$ $\beta = 0$ $\rho = -2$ $\Delta_3 = 13.5$ Bypass = 0.0

REYNOLDS NUMBER/SCALE EFFECTS

Flags indicate interpolated or extrapolated data relative to airflow

Percent WAT2 80.7

SYM	MODEL	I.D. NUMBER
○	1/6th SCALE	45, 46
□	FSCP	
◇	FSE	
△	FLT	47

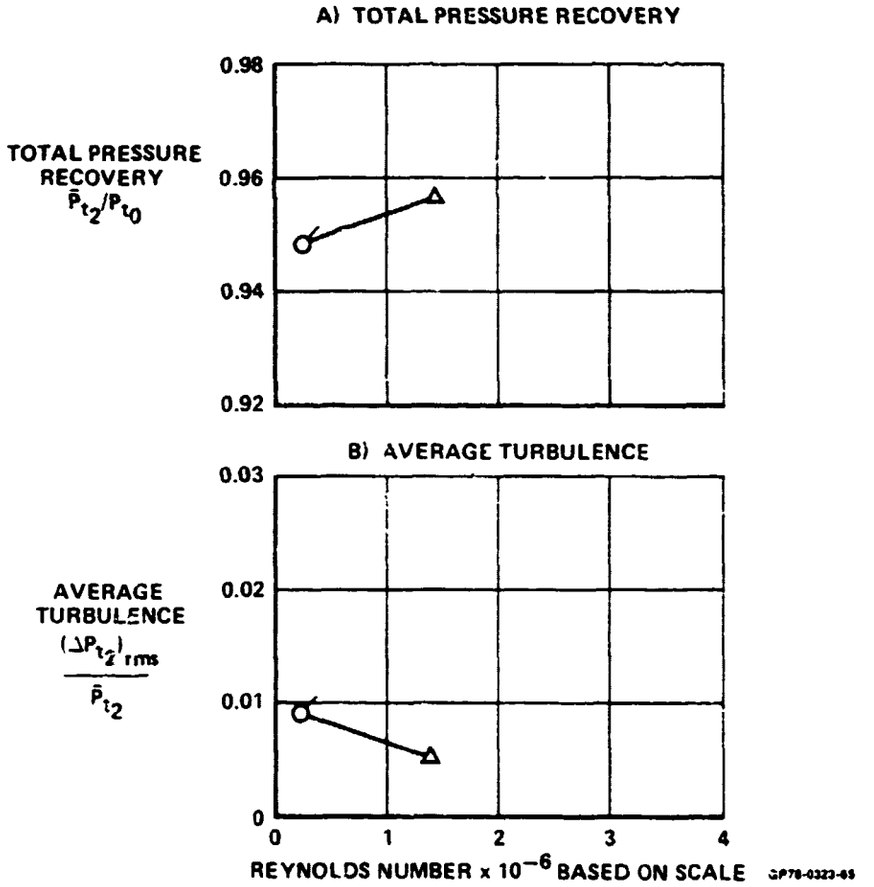

FIGURE 71
EFFECT OF REYNOLDS NUMBER/SCALE ON TOTAL PRESSURE RECOVERY AND TURBULENCE
Mach 1.8 $\alpha = -2$ $\beta = 0$ $\rho = -3$ $\Delta_3 = 17.4$ Bypass 0.0

REYNOLDS NUMBER/SCALE EFFECTS

Solid symbol - steady state
Open symbol - corresponds to peak time variant fan distortion
Flags indicate interpolated or extrapolated data relative to airflow

Percent WAT2
80.7

SYM	MODEL	I.D. NUMBER
○	1/6th SCALE	45, 46
□	FSCP	
◇	FSE	
△	FLT	47

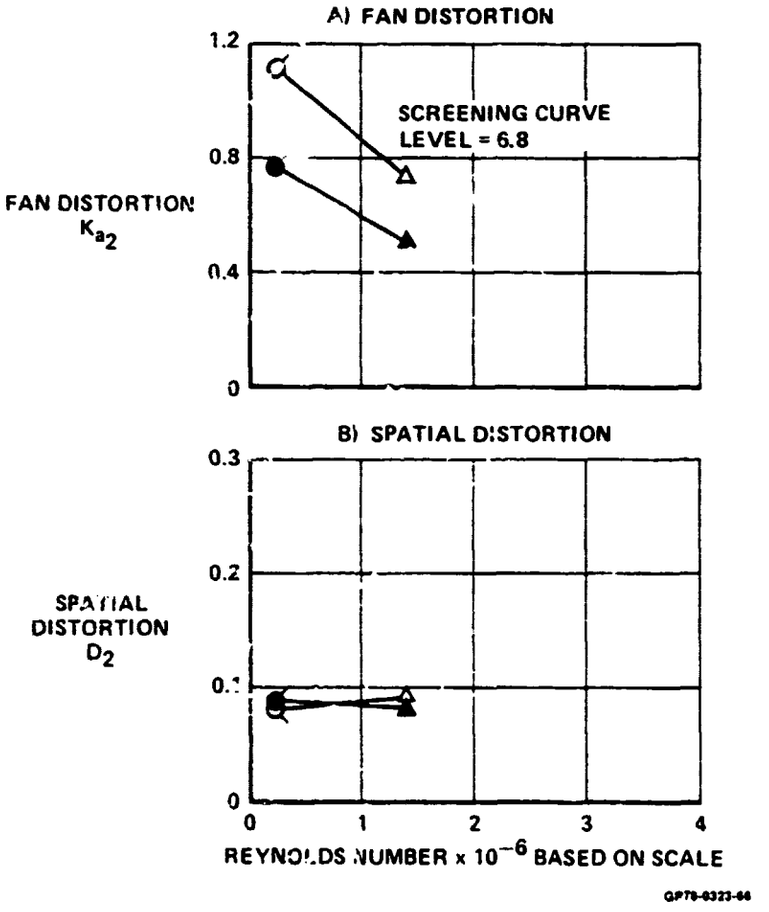

QP78-0323-64

FIGURE 72
EFFECT OF REYNOLDS NUMBER/SCALE ON FAN DISTORTION AND SPATIAL DISTORTION
Mach 1.8 $\alpha = -2$ $\beta = 0$ $\rho = -3$ $\Delta_3 = 17.4$ Bypass = 0.0

REYNOLDS NUMBER/SCALE EFFECTS

Flags indicate interpolated or extrapolated data relative to airflow

Percent WAT2 78.9

SYM	MODEL	I.D. NUMBER
○	1/6th SCALE	
□	FSCP	48, 49
◇	FSE	51, 52
△	FLT	53

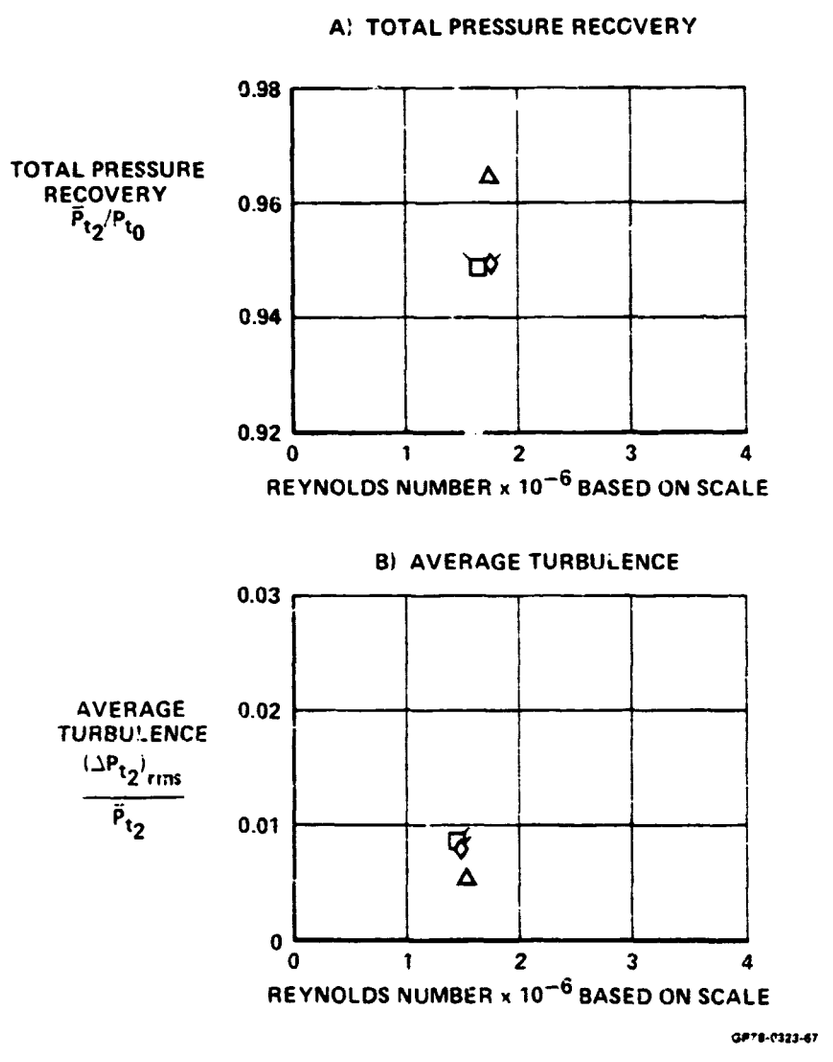

FIGURE 73
EFFECT OF REYNOLDS NUMBER/SCALE ON TOTAL PRESSURE RECOVERY AND TURBULENCE

Mach 1.8 $\alpha = -2$ $\beta = 0$ $\rho = -3$ $\Delta_3 = 18.7$ Bypass = 0.0

REYNOLDS NUMBER SCALE EFFECTS

Solid symbol - steady state
Open symbol - corresponds to peak time variant fan distortion
Flags indicate interpolated or extrapolated data relative to airflow

Percent WAT2
78.9

SYM	MODEL	I.D. NUMBER
○	1/6th SCALE	
□	FSCP	48, 49
◇	FSE	51, 52
△	FLT	53

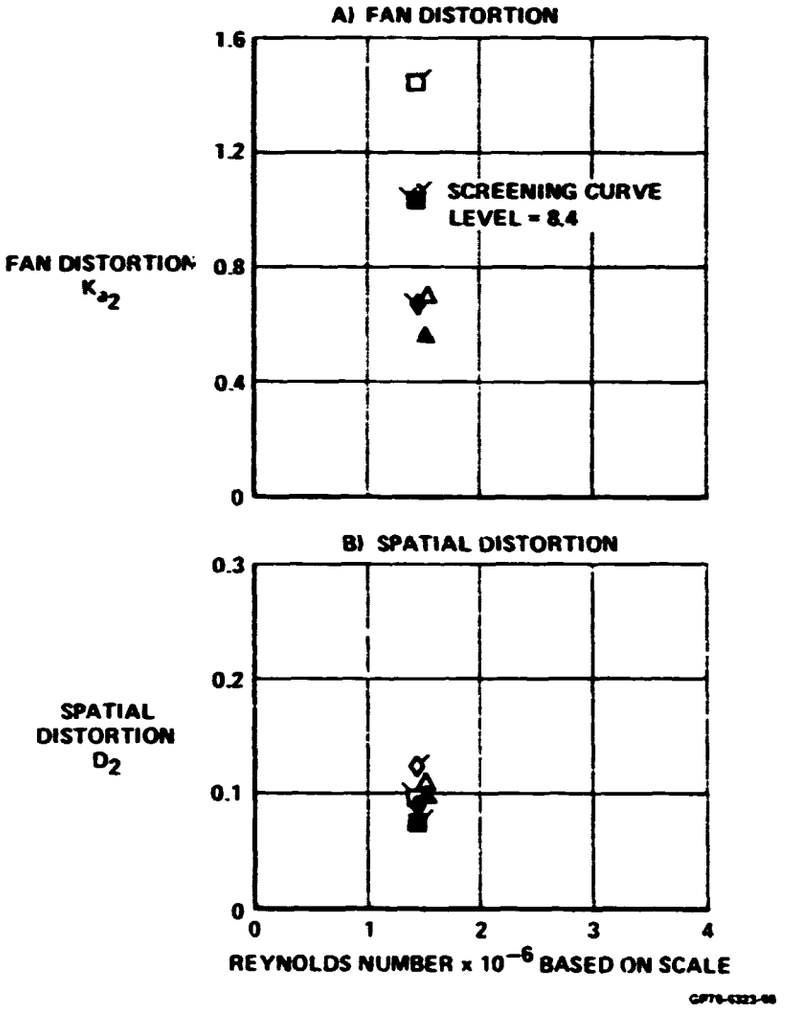

FIGURE 74
EFFECT OF REYNOLDS NUMBER/SCALE ON FAN DISTORTION AND SPATIAL DISTORTION
Mach 1.8 $\alpha = -2$ $\beta = 0$ $\rho = -3$ $\Delta_3 = 18.7$ Bypass = 0.0

REYNOLDS NUMBER/SCALE EFFECTS

Flags indicate interpolated or extrapolated data relative to airflow

Percent WAT2
73.0

SYM	MODEL	I.D. NUMBER
○	1/6th SCALE	66, 67
□	FSCP	
◇	FSE	
△	FLT	70

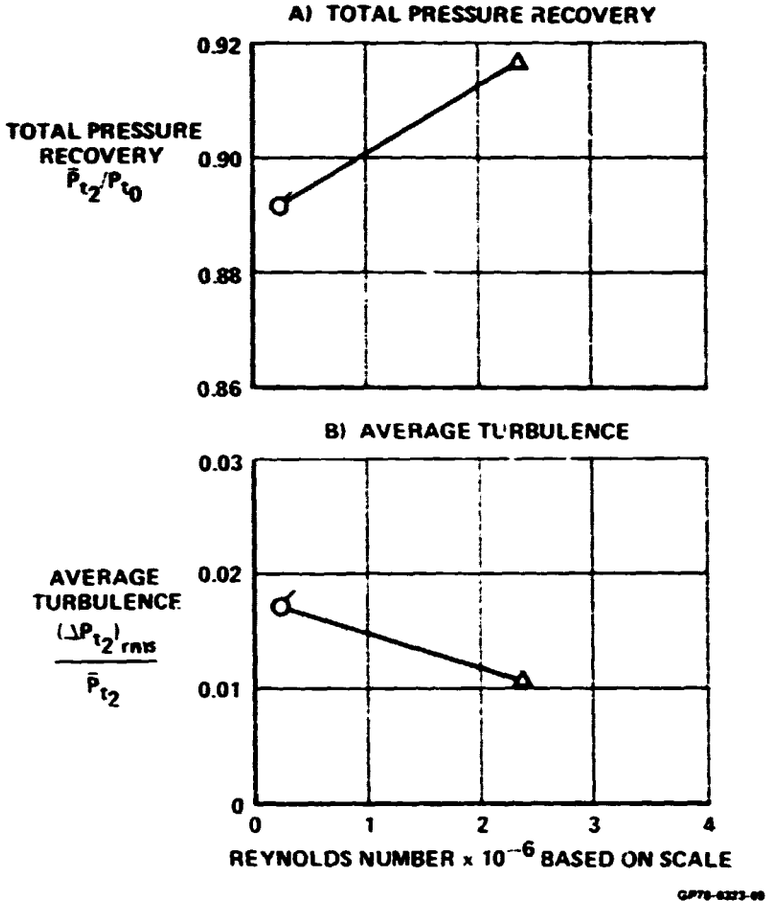

FIGURE 75
EFFECT OF REYNOLDS NUMBER/SCALE ON TOTAL PRESSURE RECOVERY AND TURBULENCE
Mach 2.2 $\alpha = 0$ $\beta = 0$ $\rho = -2$ $\lambda_3 = 22.5$ Bypass = 0.0

REYNOLDS NUMBER/SCALE EFFECTS

Solid symbol - steady state
Open symbol - corresponds to peak time variant fan distortion
Flags indicate interpolated or extrapolated data relative to airflow

Percent WAT2
73.0

SYM	MODEL	I.D. NUMBER
○	1/6th SCALE	66, 67
□	FSCP	
◇	FSE	
△	FLT	70

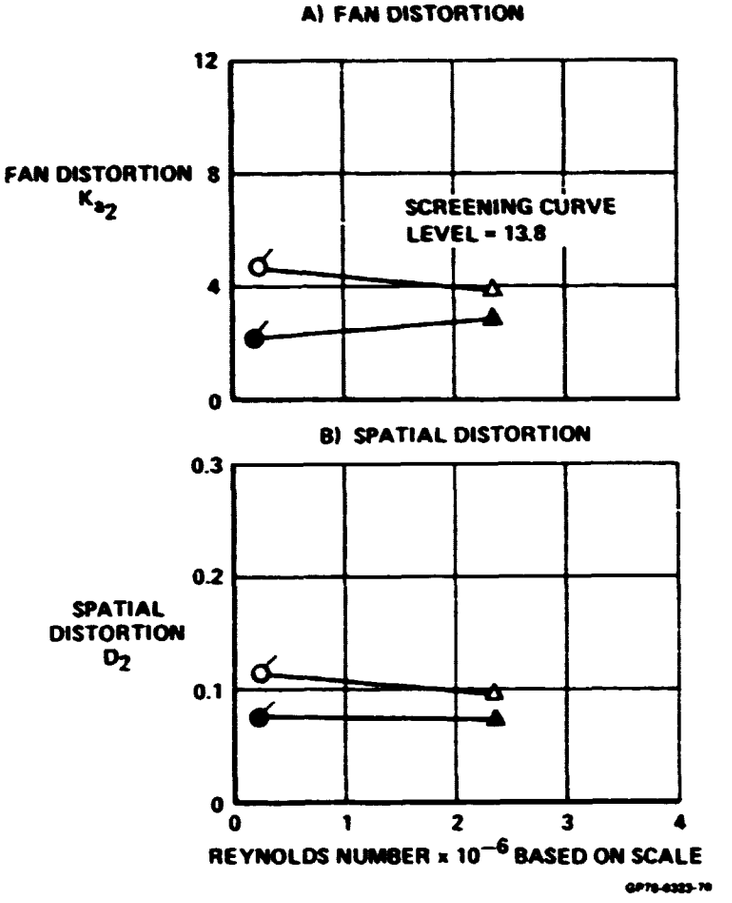

FIGURE 76
EFFECT OF REYNOLDS NUMBER/SCALE ON FAN DISTORTION AND SPATIAL DISTORTION
Mach 2.2 $\alpha = 0$ $\beta = 0$ $\rho = -2$ $\Delta_3 = 22.5$ Bypass = 0.0

REYNOLDS NUMBER SCALE EFFECTS

Flags indicate interpolated or extrapolated data relative to airflow

Percent
WAT2
61.7

SYM	MODEL	I.D. NUMBER
○	1.6th SCALE	60, 61
□	FSCP	62, 63
◇	FSE	
△	FLT	

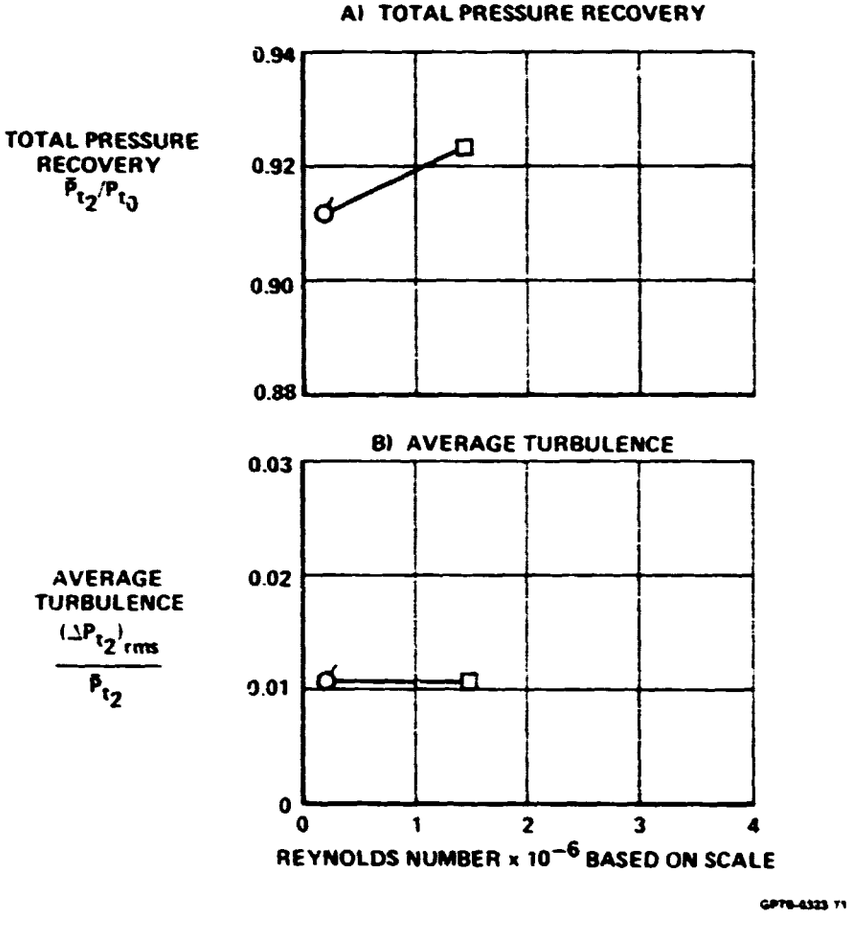

FIGURE 77
EFFECT OF REYNOLDS NUMBER/SCALE ON TOTAL PRESSURE RECOVERY AND TURBULENCE
Mach 2.2 $\alpha = -2$ $\beta = 0$ $\rho = -4$ $\Delta_3 = 25.0$ Bypass 0.071

REYNOLDS NUMBER/SCALE EFFECTS

Solid symbol - steady state
Open symbol - corresponds to peak time variant fan distortion
Flags indicate interpolated or extrapolated data relative to airflow

Percent WAT2
61.7

SYM	MODEL	I.D. NUMBER
○	1/6th SCALE	60, 61
□	FSCP	62, 63
◇	FSE	
△	FLT	

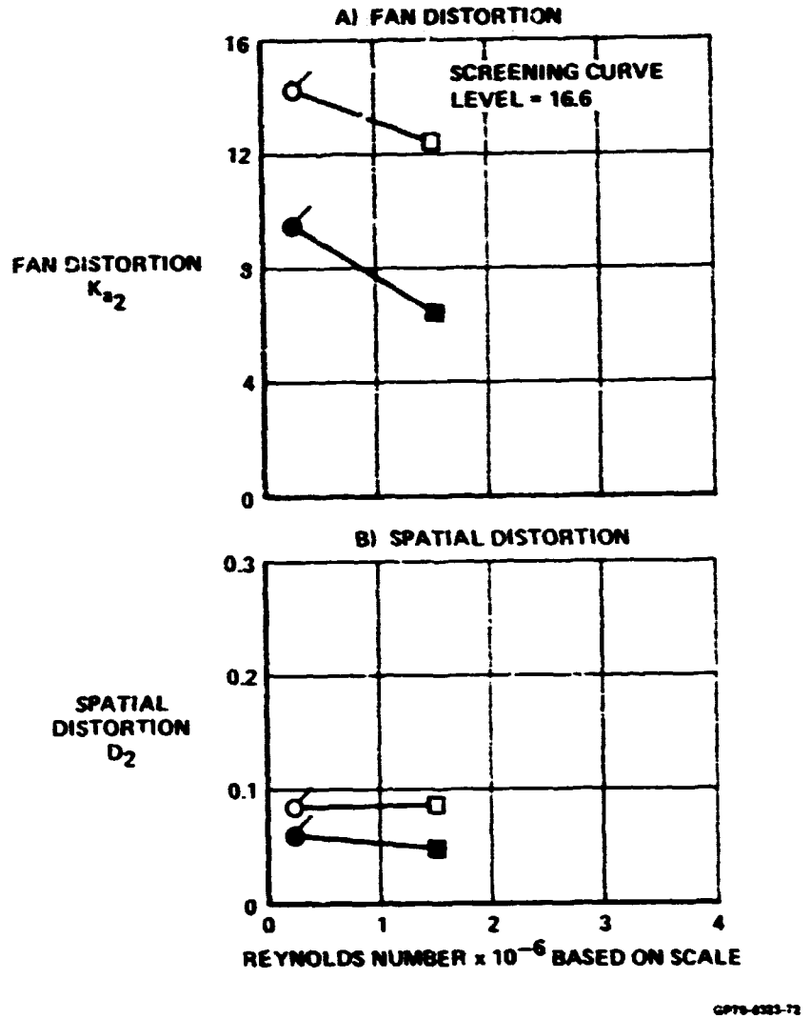

FIGURE 78
EFFECT OF REYNOLDS NUMBER/SCALE ON FAN DISTORTION AND SPATIAL DISTORTION
Mach 2.2 $\alpha = -2$ $\beta = 0$ $\rho = -4$ $\Delta_3 = 25.0$ Bypass = 0.071

REYNOLDS NUMBER/SCALE EFFECTS

Flags indicate interpolated or extrapolated data relative to airflow

Percent WAT2 60.8

SYM	MODEL	I.D. NUMBER
○	1/6th SCALE	74, 75
□	FSCP	76
◇	FSE	77, 78
△	FLT	

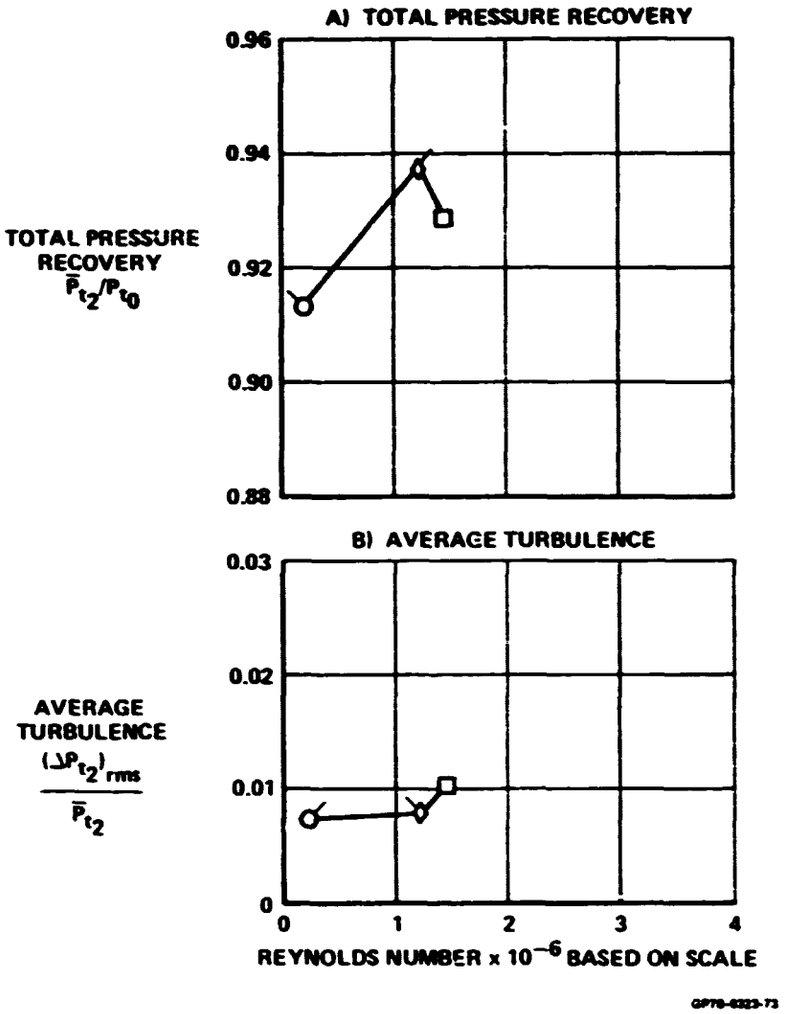

FIGURE 79
EFFECT OF REYNOLDS NUMBER/SCALE ON TOTAL PRESSURE RECOVERY AND TURBULENCE
Mach 2.2 α = 11 β = 0 ρ = 6.8 Λ_3 = 25.0 Bypass = 0.077

REYNOLDS NUMBER SCALE EFFECTS

Solid symbol - steady state
Open symbol - corresponds to peak time variant fan distortion
Flags indicate interpolated or extrapolated data relative to airflow

Percent WAT2
60.8

SYM	MODEL	I.D. NUMBER
○	1/6th SCALE	74, 75
□	FSCP	76
◇	FSE	77, 78
△	FLT	

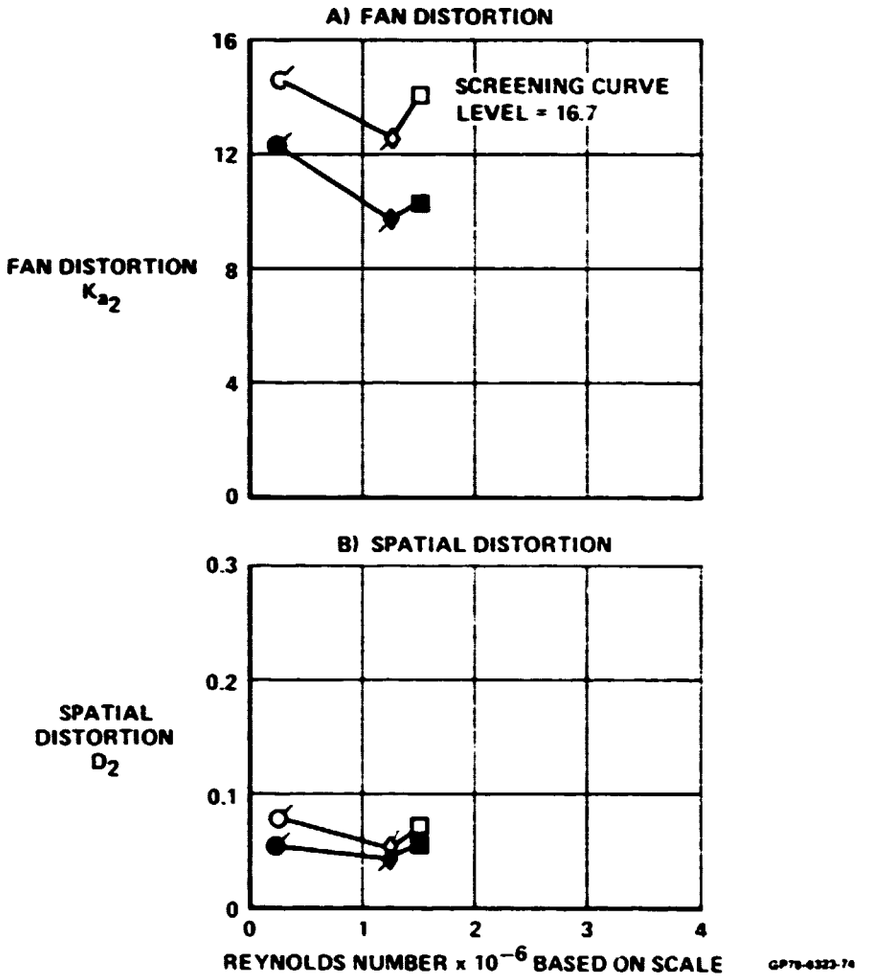

FIGURE 80
EFFECT OF REYNOLDS NUMBER/SCALE ON FAN DISTORTION AND SPATIAL DISTORTION
Mach 2.2 α = 1 β = 0 ρ = 6.8 Δ_3 = 25.0 Bypass = 0.077

REYNOLDS NUMBER/SCALE EFFECTS

Flags indicate interpolated or extrapolated data relative to airflow

Percent
WAT2
63.1

SYM	MODEL	I.D. NUMBER
○	1/6th SCALE	79, 80
□	FSCP	81, 82
◇	FSE	
△	FLT	

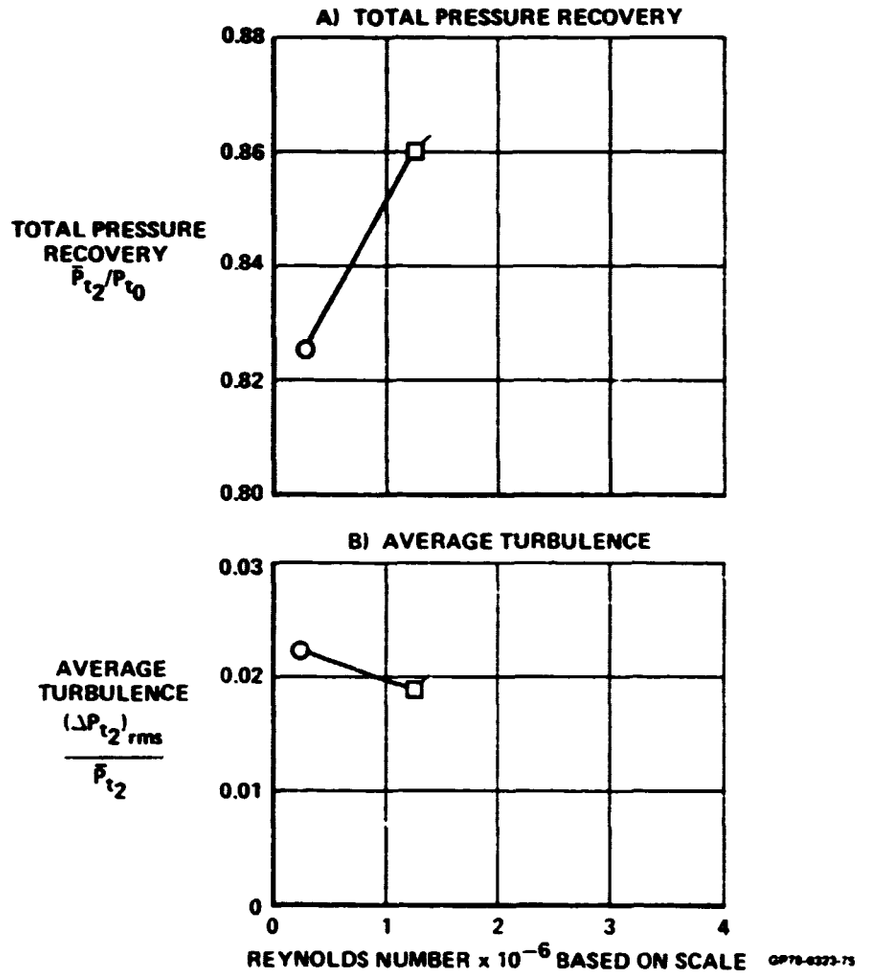

FIGURE 81
EFFECT OF REYNOLDS NUMBER/SCALE ON TOTAL PRESSURE RECOVERY AND TURBULENCE
Mach 2.5 $\alpha = 0$ $\beta = 0$ $\rho = -4$ $\Delta_3 = 26.0$ Bypass = 0.077

FREQUENCY CONTENT EFFECT

Data Point Identification Number										
1/6th Scale	Full Scale Cold Pipe	Full Scale With Engine	Flight Test	M_o	α (deg)	β (deg)	ρ (deg)	Δ_3 (deg)	Bypass*	Percent WAT2
6 5	– –	– –	7	0.6	–10	10	–3	10.6	C	101.2
17 18	– –	– –	19	0.9	–10	10	–3	10.6	C	107.1
42 43	– –	– –	44 –	1.6	–4	0	–2	13.5	C	89.1
–	48,49,50	51, 52	53	1.8	–2	0	–3	18.7	C	78.9
45 46	– –	– –	47	1.8	–2	0	–3	17.4	C	80.7
60, 61	62, 63	64, 65***	–	2.2	–2	0	–4	25.0	O	60.4
66 67	68 69**	– –	70	2.2	0	0	–2	22.5	C	73.0
79 80	81 82	– –	– –	2.5	0	0	–4	26.0	O	63.1

*O = Open bypass, C = Closed bypass, P = Partially open bypass

**These data exhibited harmonic characteristics and are not included in this analysis

***These data have different bypass door positions and are not included in this analysis

GP78-0333-77

FIGURE 83
TEST CONDITIONS FOR
EVALUATING FREQUENCY CONTENT EFFECT

FREQUENCY CONTENT EFFECT

A) POWER SPECTRAL DENSITY PLOT FOR PROBE L8R1

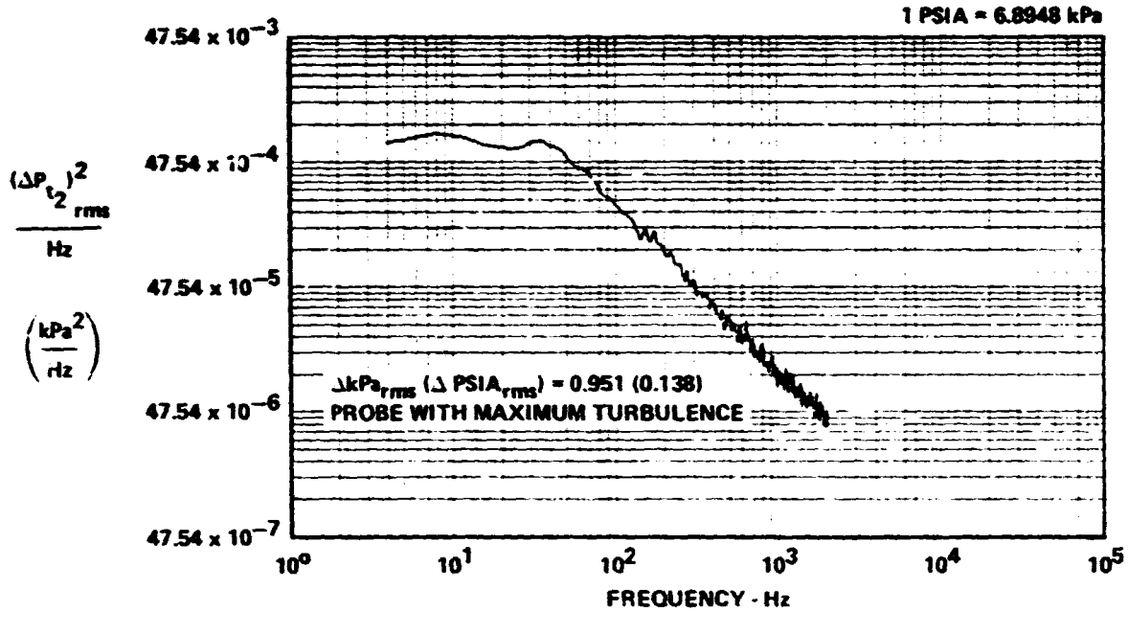

B) DERIVED TURBULENCE vs FILTER CUTOFF FREQUENCY FOR PROBE L8R1

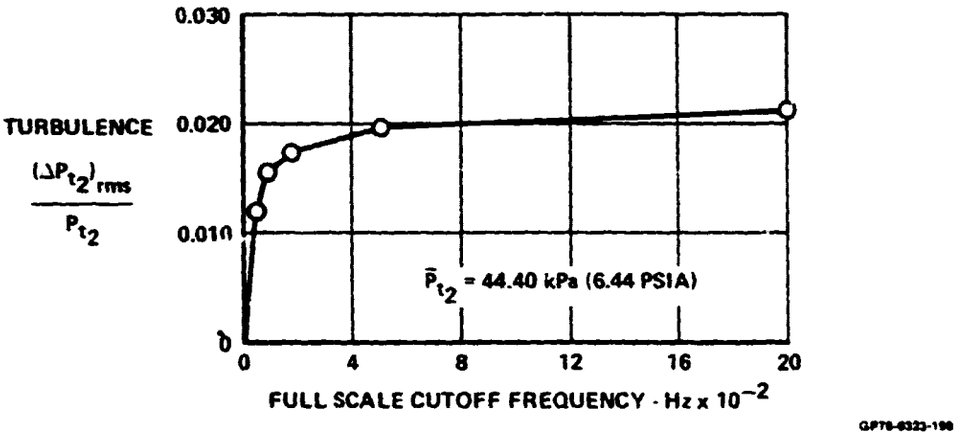

GP76-0323-198

FIGURE 84
INTEGRATION OF THE POWER SPECTRAL DENSITY PLOT TO OBTAIN TURBULENCE AS A FUNCTION OF FILTER CUTOFF FREQUENCY
Mach 2.2 $\alpha = -2$ $\beta = 0$ $\rho = -4$
$\Delta_3 = 25.0$ WAT2 = 61.7% Bypass = 0 I.D. Number = 62

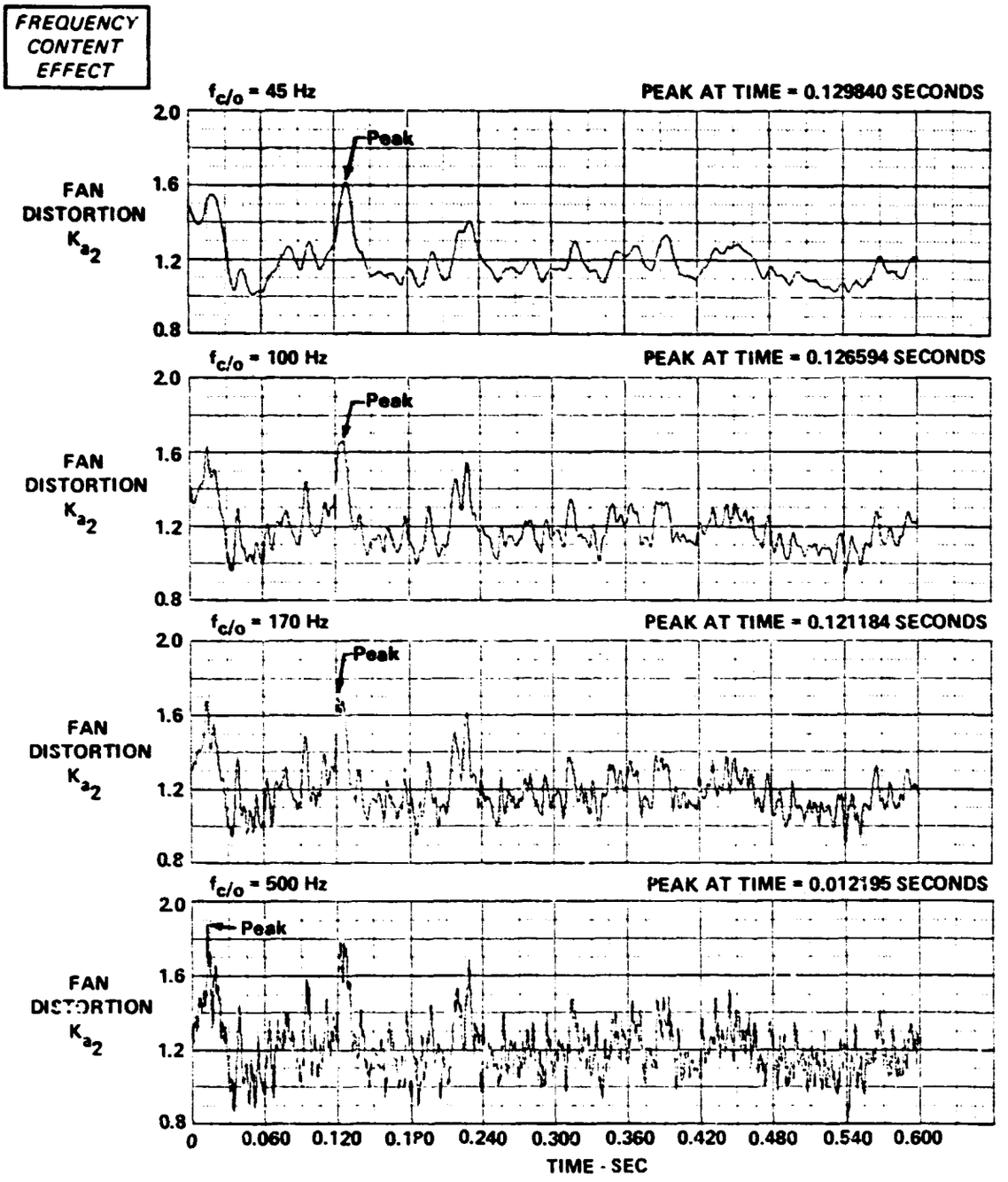

FIGURE 85
COMPARISON OF TIME VARIANT FAN DISTORTION TIME HISTORIES FOR VARIOUS FILTER CUTOFF FREQUENCIES
Mach 1.8 $\alpha = -2$ $\beta = 0.0$ $\rho = -3$
$\Delta_3 = 18.7$ WAT2 = 82.2% Bypass = 0.0 I.D. Number = 49

FREQUENCY CONTENT EFFECT

Solid symbol - steady state
Open symbol - corresponds to peak time variant fan distortion
Flags indicate interpolated or extrapolated data relative to airflow

Percent
WAT2
101.2

SYM	MODEL	I.D. NUMBER
○	1/6th SCALE	5, 6
□	FSCP	
◇	FSE	
△	FLT	7

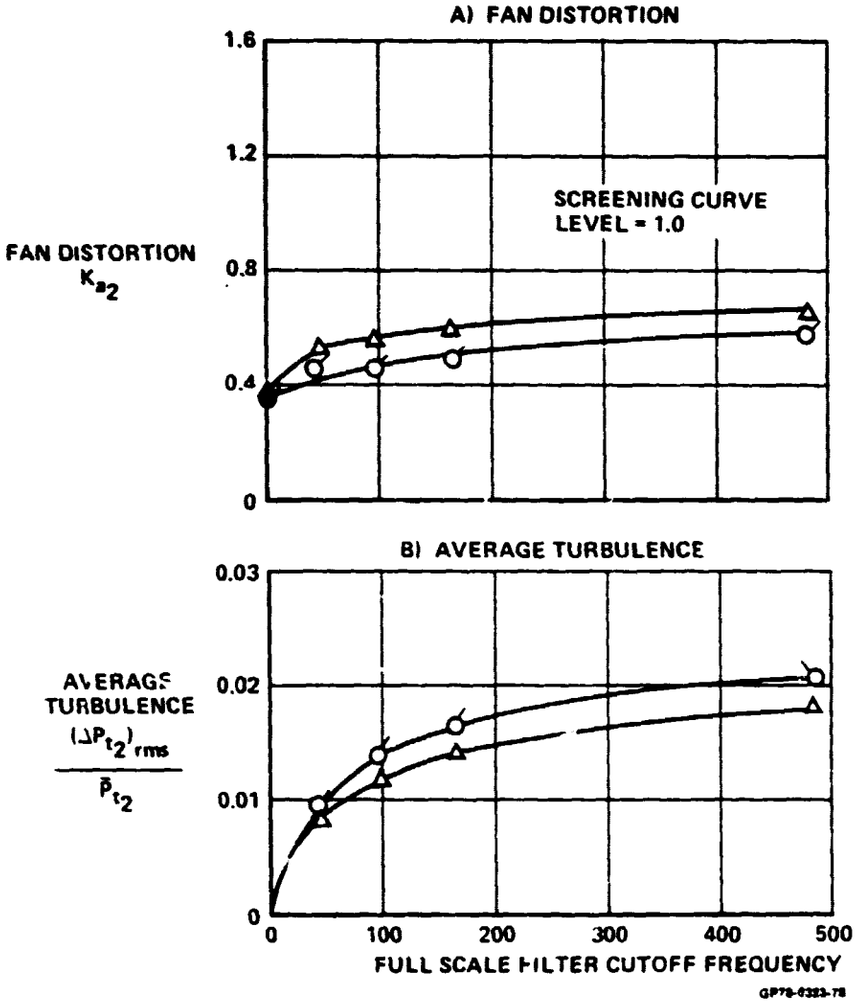

FIGURE 86
EFFECT OF FILTER CUTOFF FREQUENCY ON FAN DISTORTION, TURBULENCE AND SPATIAL DISTORTION
Mach 0.6 $\alpha = -10$ $\beta = 10$ $\rho = -3$ $\Delta_3 = 10.6$ Bypass =0.0

FREQUENCY CONTENT EFFECT

Solid symbol - steady state
Open symbol - corresponds to peak time variant fan distortion
Flags indicate interoolated or extrapolated data relative to airflow

Percent WAT2
101.2

SYM	MODEL	I.D. NUMBER
○	1/6th SCALE	5, 6
□	FSCP	
◇	FSE	
△	FLT	7

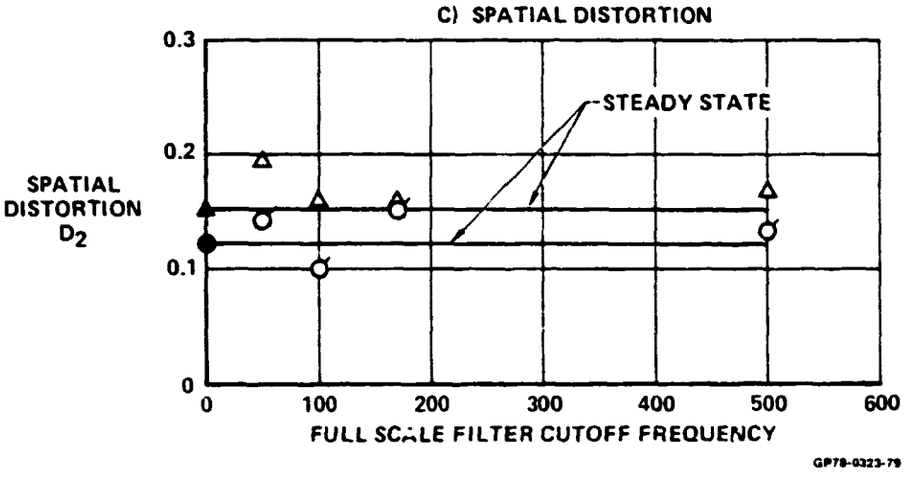

FIGURE 86 (Continued)
EFFECT OF FILTER CUTOFF FREQUENCY ON FAN DISTORTION, TURBULENCE AND SPATIAL DISTORTION
Mach 0.6 $\alpha = -10$ $\beta = 10$ $\rho = -3$ $\Delta 3 = 10.6$ Bypass = 0.0

FREQUENCY CONTENT EFFECT

Solid symbol - steady state
Open symbol - corresponds to peak time variant fan distortion
Flags indicate interpolated or extrapolated data relative to airflow

Percent WAT2
107.1

SYM	MODEL	I.D. NUMBER
○	1/6th SCALE	17, 18
□	FSCP	
◇	FSE	
△	FLT	19

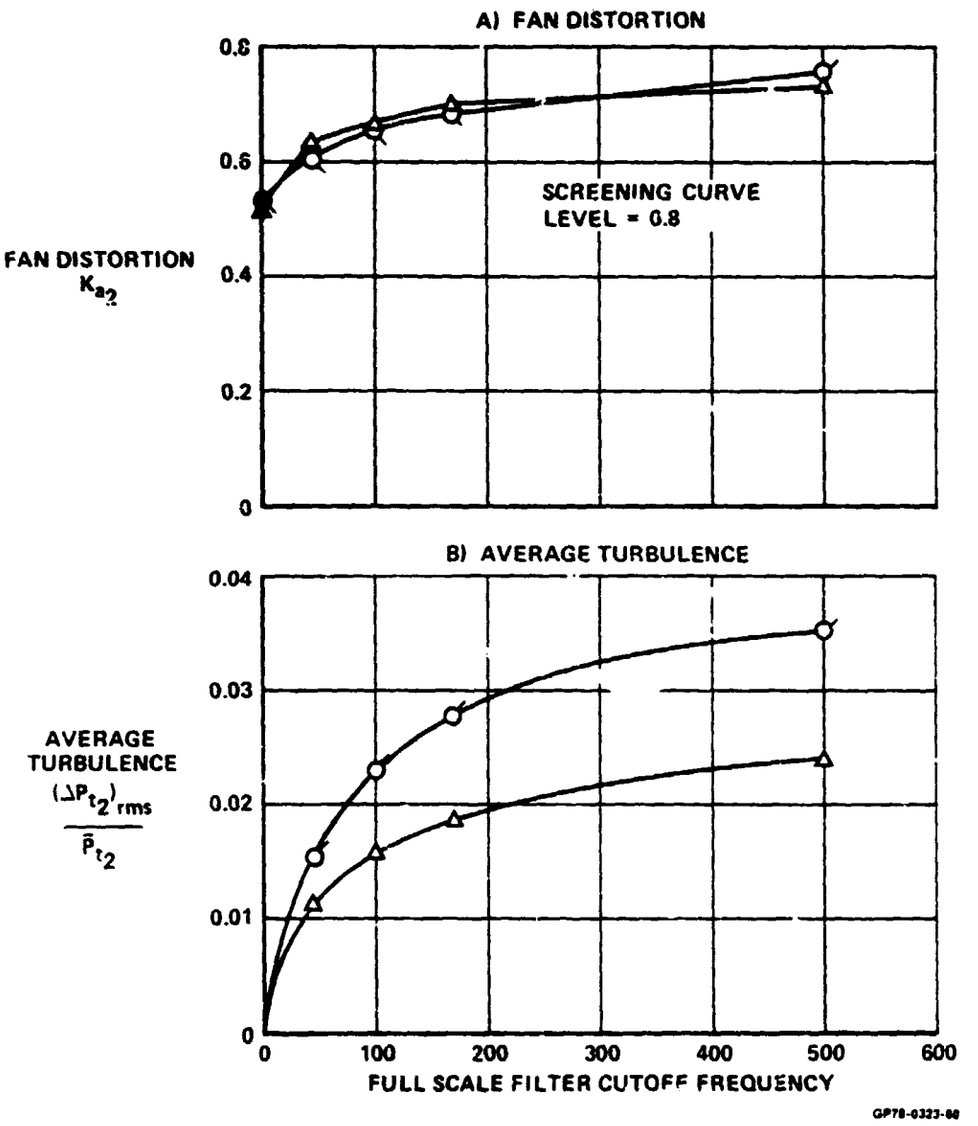

FIGURE 87
EFFECT OF FILTER CUTOFF FREQUENCY ON FAN DISTORTION, TURBULENCE AND SPATIAL DISTORTION
Mach 0.9 $\alpha = -10$ $\beta = 10$ $\rho = -3$ $\lambda_3 = 10.6$ Bypass = 0.0

FREQUENCY CONTENT EFFECT

Solid symbol - steady state
Open symbol - corresponds to peak time variant fan distortion
Flags indicate interpolated or extrapolated data relative to airflow

Percent WAT2
107.1

SYM	MODEL	I.D. NUMBER
O	1/6th SCALE	17, 18
□	FSCP	
◇	FSE	
△	FLT	19

C) SPATIAL DISTORTION

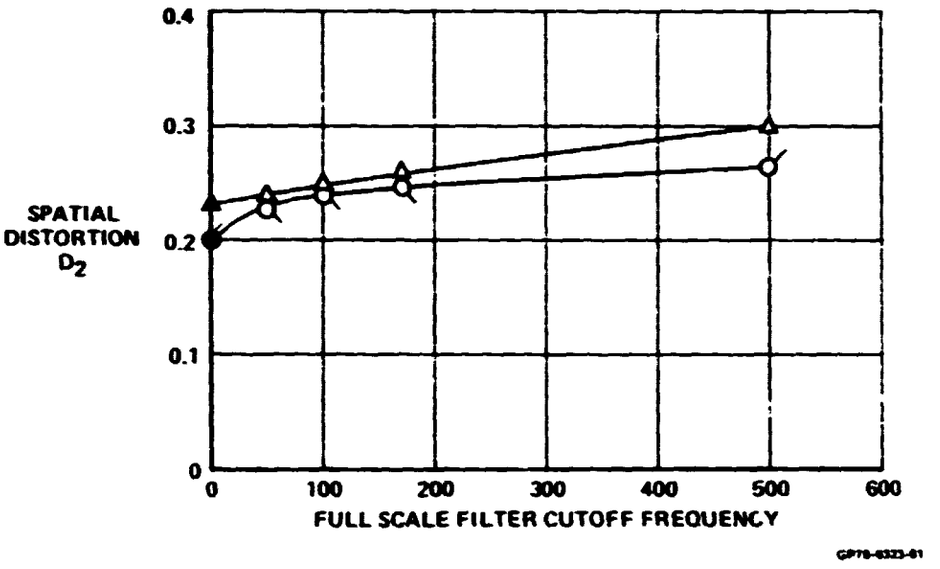

GP78-6323-01

FIGURE 87 (Continued)
EFFECT OF FILTER CUTOFF FREQUENCY ON FAN DISTORTION, TURBULENCE AND SPATIAL DISTORTION
Mach 0.9 $\alpha = -10$ $\beta = 10$ $\rho = -3$ $\Delta_3 = 10.6$ Bypass = 0.0

FREQUENCY CONTENT EFFECT

Solid symbol - steady state
Open symbol - corresponds to peak time variant fan distortion
Flags indicate interpolated or extrapolated data relative to airflow

Percent WAT2
80.7

SYM	MODEL	I.D. NUMBER
○	1/6th SCALE	45, 46
□	FSCP	
◇	FSE	
△	FLT	47

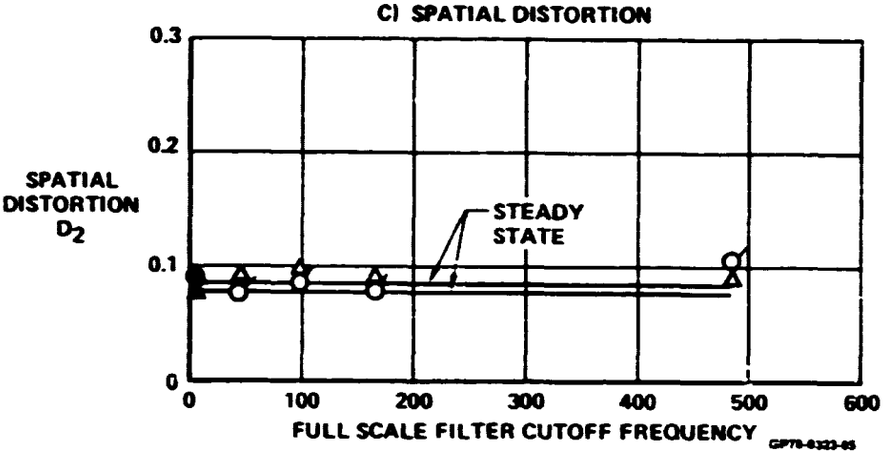

FIGURE 89 (Continued)
EFFECT OF FILTER CUTOFF FREQUENCY ON FAN DISTORTION, TURBULENCE AND SPATIAL DISTORTION
Mach 1.8 $\alpha = -2$ $\beta = 0$ $\rho = -3$ $\lambda_3 = 17.4$ Bypass = 0.0

FREQUENCY CONTENT EFFECT

Solid symbol - steady state
Open symbol - corresponds to peak time variant fan distortion
Flags indicate interpolated or extrapolated data relative to airflow

Percent WAT2
78.5

SYM	MODEL	I.D. NUMBER
○	1/6th SCALE	
□	FSCP	48, 49
◇	FSE	51, 52
△	FLT	53

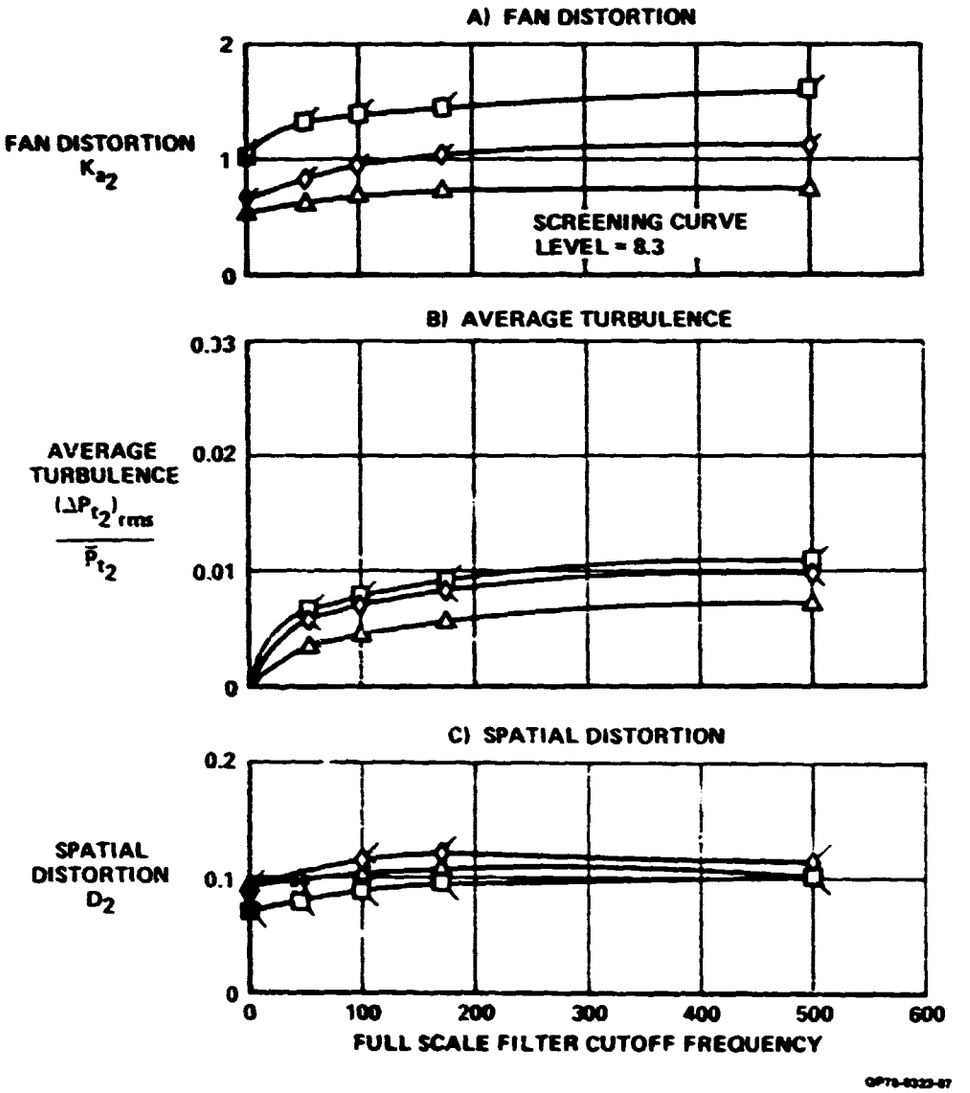

FIGURE 90
EFFECT OF FILTER CUTOFF FREQUENCY ON FAN DISTORTION, TURBULENCE AND SPATIAL DISTORTION
Mach 1.8 $\alpha = -2$ $\beta = 0$ $\rho = -3$ $\Delta_3 = 18.7$ Bypass = 0.0

FREQUENCY CONTENT EFFECT

Solid symbol - steady state
Open symbol - corresponds to peak time variant fan distortion
Flags indicate interpolated or extrapolated data relative to airflow

Percent WAT2
60.4

SYM	MODEL	I.D. NUMBER	BYPASS
○	1/6th SCALE	60, 61	0.0774
□	FSCP	62, 63	0.0774
◇	FSE		
△	FLT		

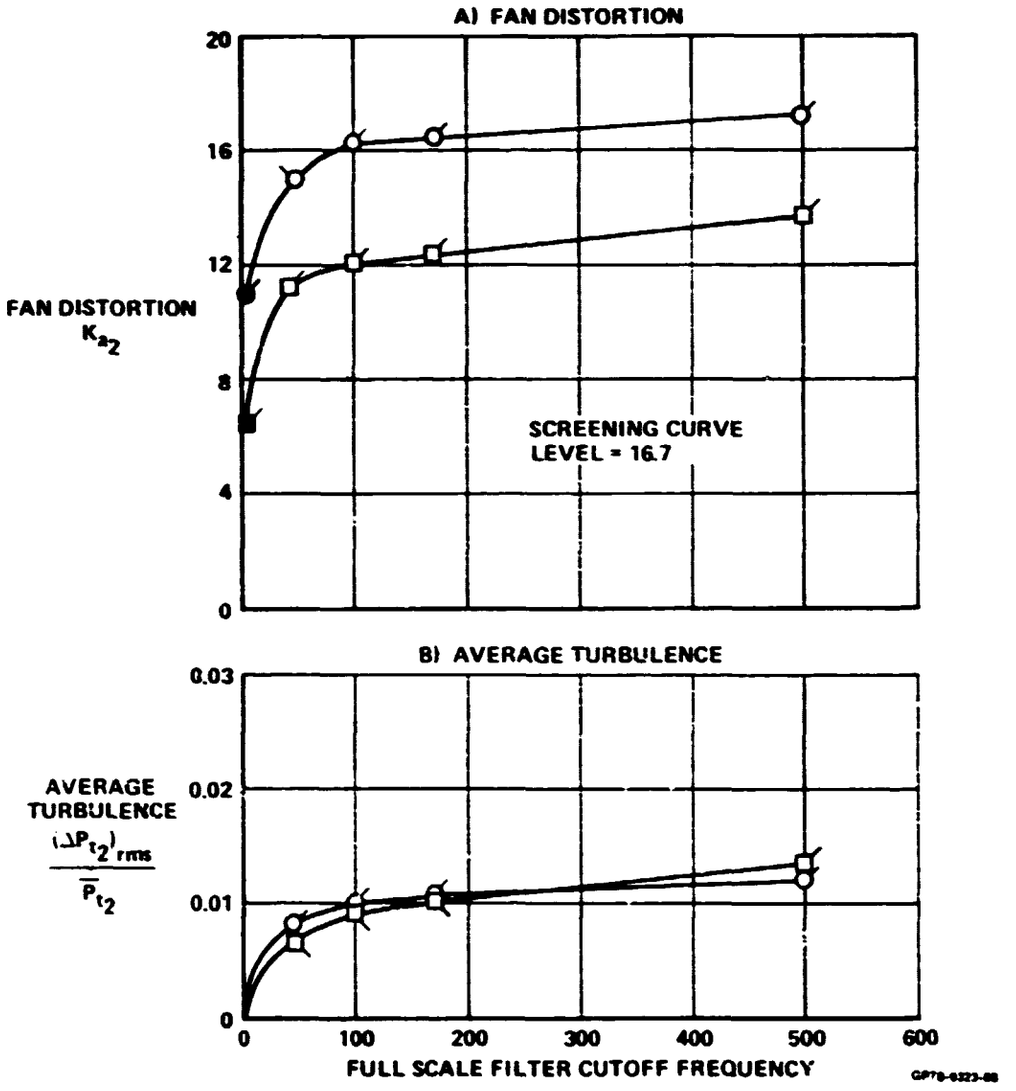

FIGURE 91
EFFECT OF FILTER CUTOFF FREQUENCY ON FAN DISTORTION, TURBULENCE AND SPATIAL DISTORTION
Mach 2.2 $\alpha = -2$ $\beta = 0$ $\rho = -4$ $\Delta_3 = 25$ Bypass = 0.0774

FREQUENCY CONTENT EFFECT

Solid symbol - steady state
Open symbol - corresponds to peak time variant fan distortion
Flags indicate interpolated or extrapolated data relative to airflow

Percent WAT2
73.0

SYM	MODEL	I.D. NUMBER
O	1/6th SCALE	66, 67
□	FSCP	
◇	FSE	
△	FLT	70

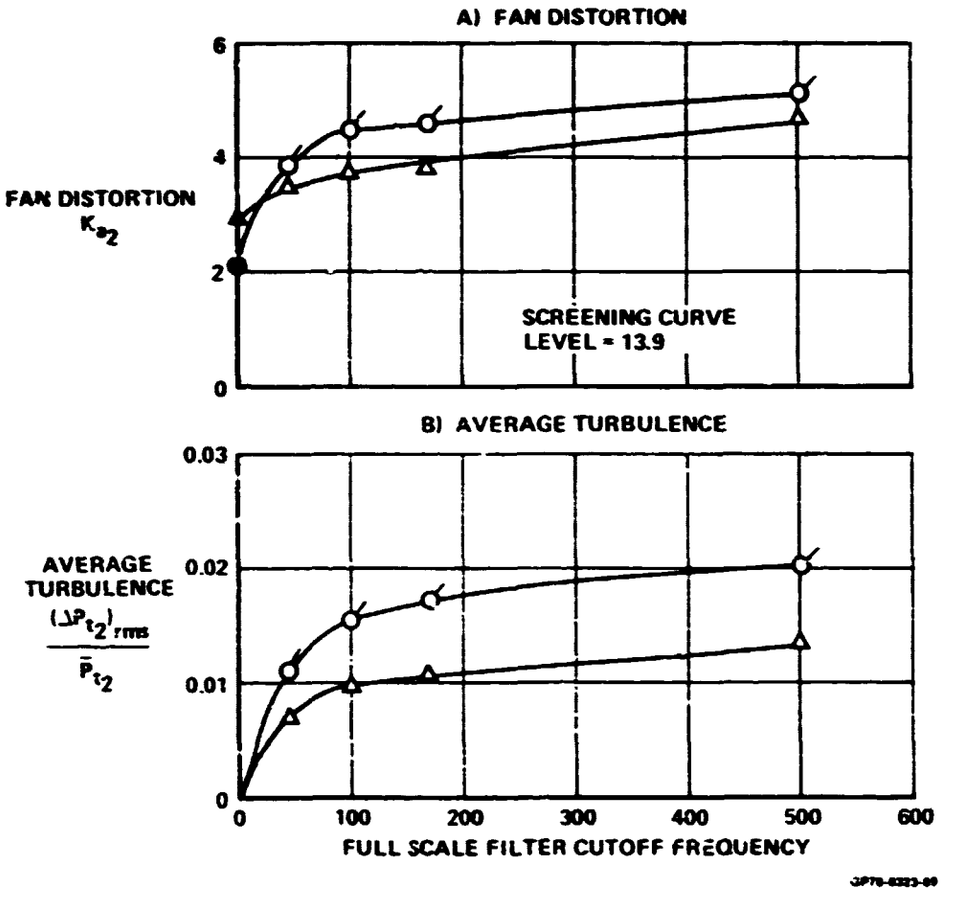

FIGURE 92
EFFECT OF FILTER CUTOFF FREQUENCY ON FAN DISTORTION, TURBULENCE AND SPATIAL DISTORTION
Mach 2.2 $\alpha = 0$ $\beta = 0$ $\nu = -2$ $\Delta_3 = 22.5$ Bypass = 0.0

FREQUENCY CONTENT EFFECT

Solid symbol - steady state

Open symbol - corresponds to peak time variant fan distortion

Flags indicate interpolated or extrapolated data relative to airflow

Percent WAT2 — 73.0

SYM	MODEL	I.D. NUMBER
○	1/6th SCALE	66, 67
□	FSCP	
◇	FSE	
△	FLT	70

C) SPATIAL DISTCRTION

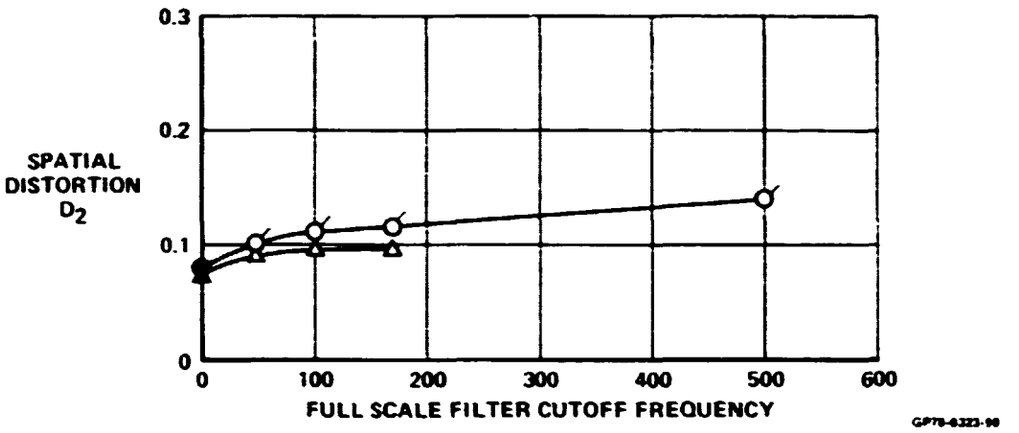

FIGURE 92 (Continued)
EFFECT OF FILTER CUTOFF FREQUENCY ON FAN DISTORTION, TURBULENCE AND SPATIAL DISTORTION
Mach 2.2 $\alpha = 0$ $\beta = 0$ $\rho = -2$ $\Delta_3 = 22.5$ Bypass = 0.0

FREQUENCY CONTENT EFFECT

Solid symbol - steady state
Open symbol - corresponds to peak time variant fan distortion
Flags indicate interpolated or extrapolated data relative to airflow

Percent WAT2
63.1

SYM	MODEL	I.D. NUMBER
O	1/6th SCALE	79
□	FSCP	81, 82
◇	FSE	
△	FLT	

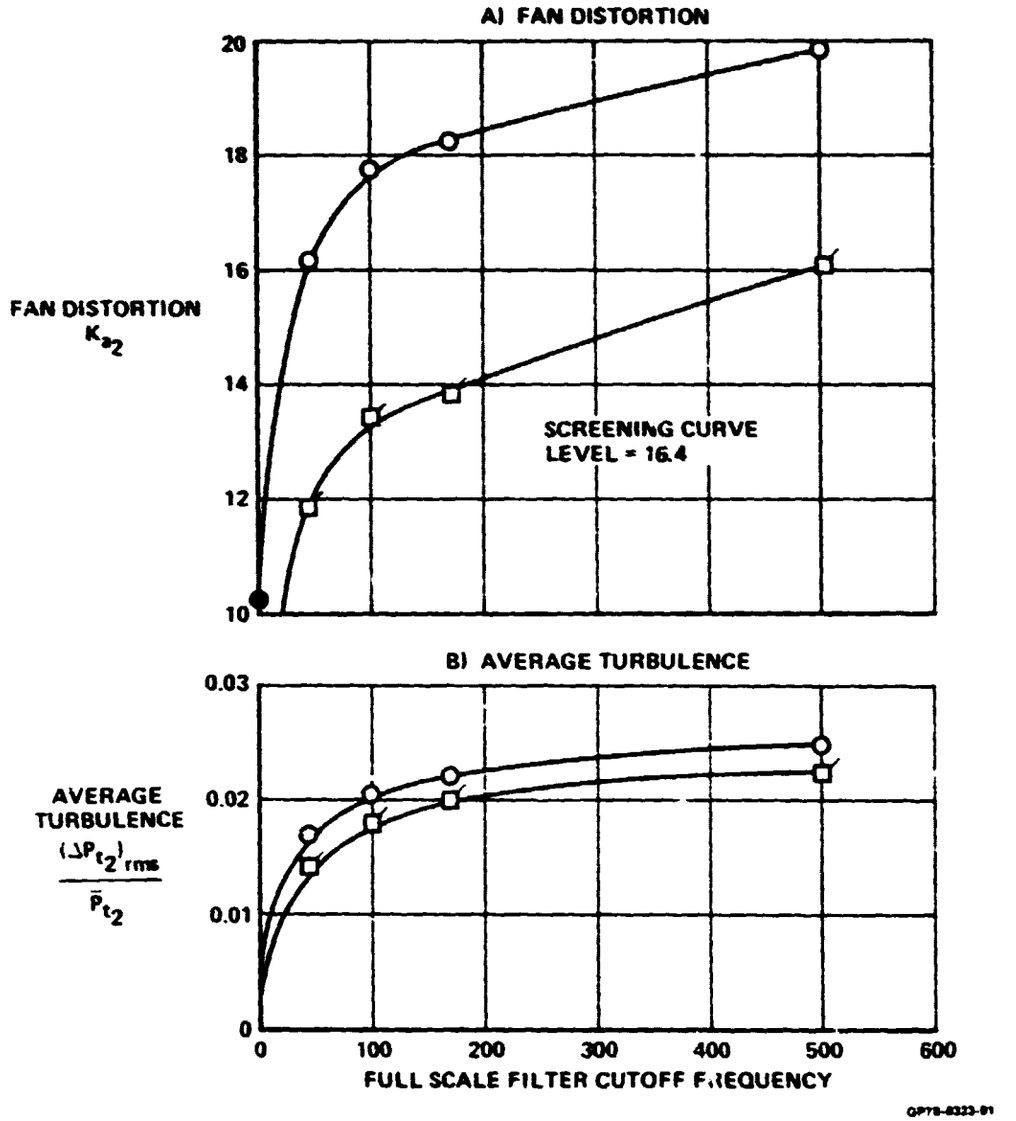

FIGURE 93
EFFECT OF FILTER CUTOFF FREQUENCY ON FAN DISTORTION, TURBULENCE AND SPATIAL DISTORTION
Mach 2.5 $\alpha = 0$ $\beta = 0$ $\rho = -4$ $\Delta_3 = 26$ Bypass = 0.0774

FREQUENCY CONTENT EFFECT

Solid symbol - steady state
Open symbol - corresponds to peak time variant fan distortion
Flags indicate interpolated or extrapolated data relative to airflow

Percent WAT2
63.1

SYM	MODEL	I.D. NUMBER
○	1/6th SCALE	79
□	FSCP	81, 82
◇	FSE	
△	FLT	

C) SPATIAL DISTORTION

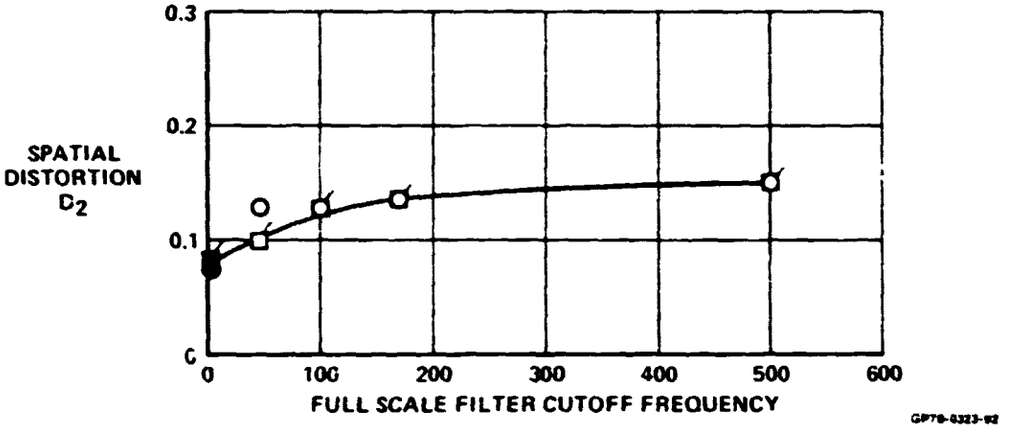

FIGURE 93 (Continued)
EFFECT OF FILTER CUTOFF FREQUENCY ON FAN DISTORTION, TURBULENCE AND SPATIAL DISTORTION
Mach 2.5 $\alpha = 0$ $\beta = 0$ $\rho = -4$ $\Delta_3 = 26$ Bypass = 0.0774

FREQUENCY CONTENT EFFECT

Solid symbol - steady state
Open symbol - corresponds to peak time variant fan distortion
Flags indicate interpolated or extrapolated data relative to airflow

Percent WAT2
101.2

MODEL	I.D. NUMBER	REYNOLDS NUMBER
1/6th SCALE	5, 6	0.4
FSCP		
FSE		
FLT	7	1.4

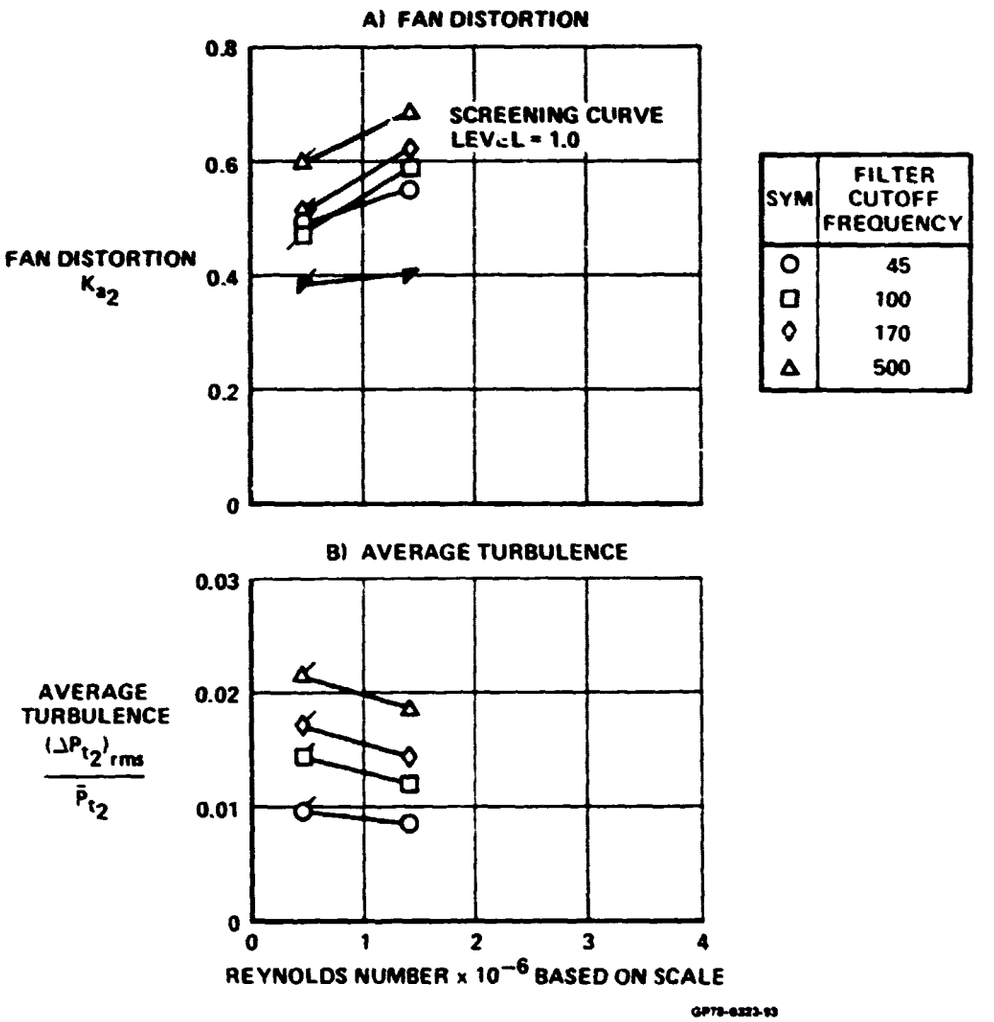

FIGURE 94
EFFECT OF FILTER CUTOFF FREQUENCY AND REYNOLDS NUMBER ON FAN DISTORTION, TURBULENCE AND SPATIAL DISTORTION
Mach 0.6 $\alpha = -10$ $\beta = 10$ $\rho = -3$ $\Delta_3 = 10.6$ Bypass = 0.0

FREQUENCY CONTENT EFFECT

Solid symbol - steady state
Open symbol - corresponds to peak time variant fan distortion
Flags indicate interpolated or extrapolated data relative to airflow

Percent WAT2
101.2

MODEL	I.D. NUMBER	REYNOLDS NUMBER
1/6th SCALE	5, 6	0.4
FSCP		
FSE		
FLT	7	1.4

C) SPATIAL DISTORTION

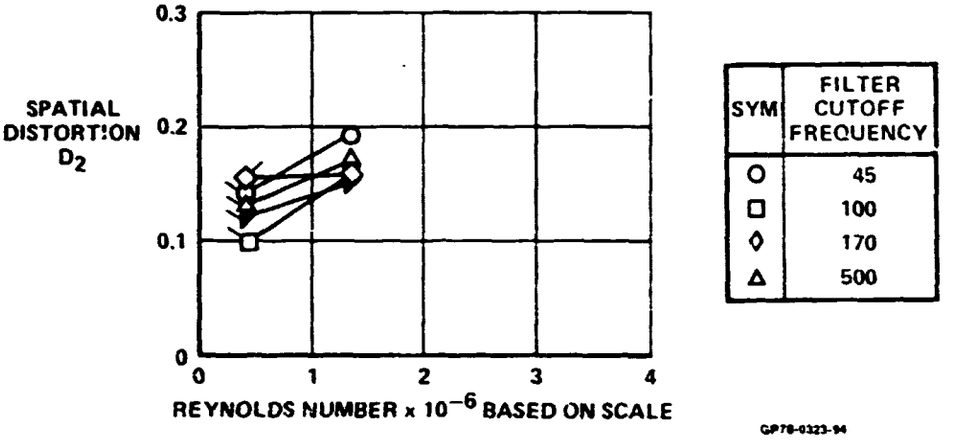

SYM	FILTER CUTOFF FREQUENCY
○	45
□	100
◇	170
△	500

FIGURE 94 (Continued)
EFFECT OF FILTER CUTOFF FREQUENCY AND REYNOLDS NUMBER ON FAN DISTORTION, TURBULENCE AND SPATIAL DISTORTION
Mach 0.6 α =—10 β = 10 ρ = —3 Λ_3 = 10.6 Bypass = 0.0

FREQUENCY CONTENT EFFECT

Solid symbol - steady state
Open symbol - corresponds to peak time variant fan distortion
Flags indicate interpolated or extrapolated data relative to airflow

Percent WAT2
107.1

MODEL	I.D. NUMBER	REYNOLDS NUMBER
1/6th SCALE FSCP FSE	17, 18	0.3
FLT	19	1.6

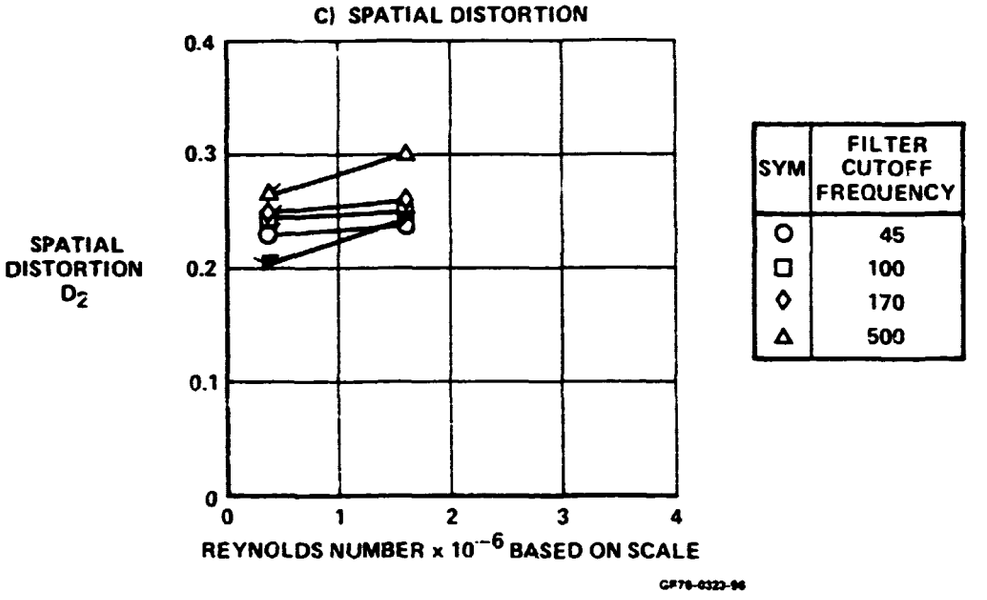

FIGURE 95 (Continued)
EFFECT OF FILTER CUTOFF FREQUENCY AND REYNOLDS NUMBER ON FAN DISTORTION, TURBULENCE AND SPATIAL DISTORTION
Mach 0.9 $\alpha = -10$ $\beta = 10$ $\rho = -3$ $\Delta_3 = 10.6$ Bypass = 0

FREQUENCY CONTENT EFFECT

Solid symbol - steady state
Open symbol - corresponds to peak time variant fan distortion
Flags indicate interpolated or extrapolated data relative to airflow

Percent WAT2
—— 80.1

MODEL	I.D. NUMBER	REYNOLDS NUMBER
1/6th SCALE	42, 43	0.2
FSCP		
FSE		
FLT	44	1.4

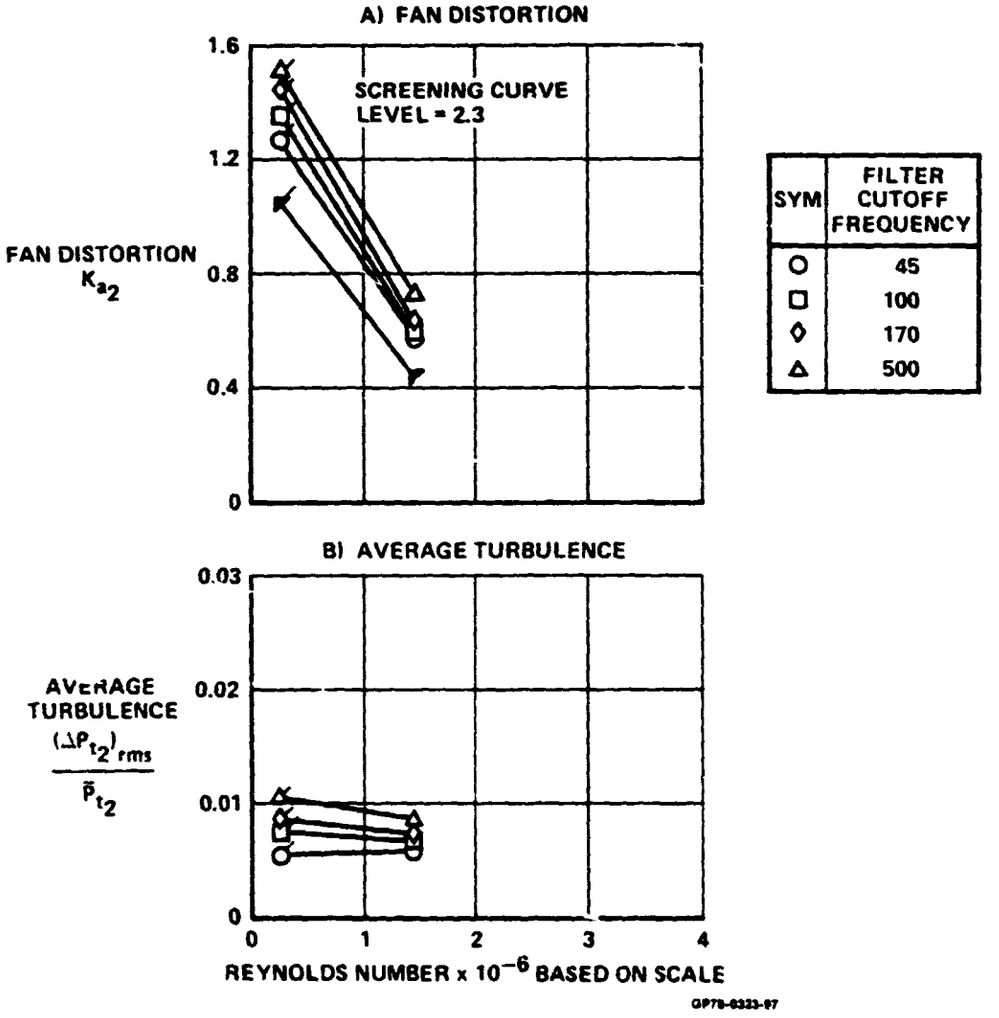

FIGURE 96
EFFECT OF FILTER CUTOFF FREQUENCY AND REYNOLDS NUMBER ON FAN DISTORTION, TURBULENCE AND SPATIAL DISTORTION
Mach 1.6 $\alpha = -4$ $\beta = 0$ $\rho = -2$ $\Delta_3 = 13.5$ Bypass = 0.0

FREQUENCY CONTENT EFFECT

Solid symbol - steady state
Open symbol - corresponds to peak time variant fan distortion
Flags indicate interpolated or extrapolated data relative to airflow

MODEL	I.D. NUMBER	REYNOLDS NUMBER
1/6th SCALE	42, 43	0.2
FSCP		
FSE		
FLT	44	1.4

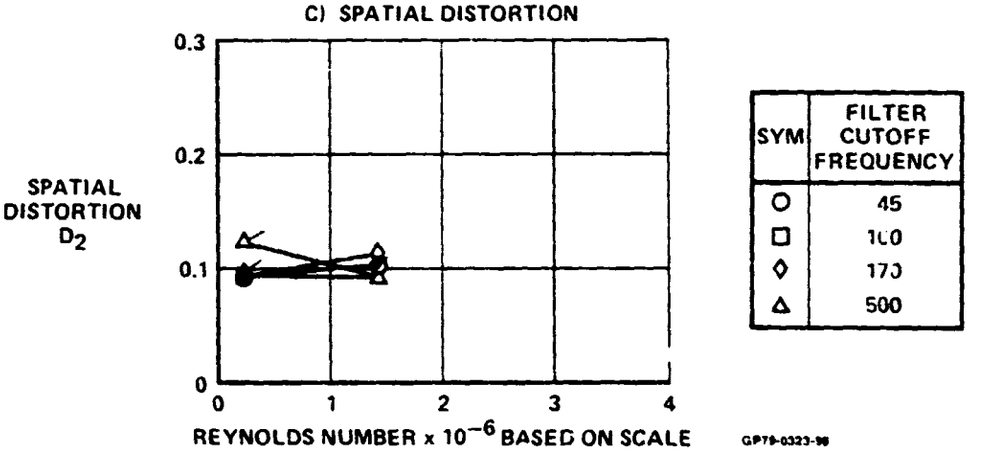

FIGURE 96 (Continued)
EFFECT OF FILTER CUTOFF FREQUENCY AND REYNOLDS NUMBER ON FAN DISTORTION, TURBULENCE AND SPATIAL DISTORTION
Mach 1.6 $\alpha = -4$ $\beta = 0$ $\rho = -2$ $\Delta_3 = 13.5$ Bypass = 0.0

FREQUENCY CONTENT EFFECT

Solid symbol - steady state
Open symbol - corresponds to peak time variant fan distortion
Flags indicate interpolated or extrapolated data relative to airflow

Percent WAT2
80.7

MODEL	I.D. NUMBER	REYNOLDS NUMBER
1/6th SCALE	45, 46	0.2
FSCP		
FSE		
FLT	47	1.4

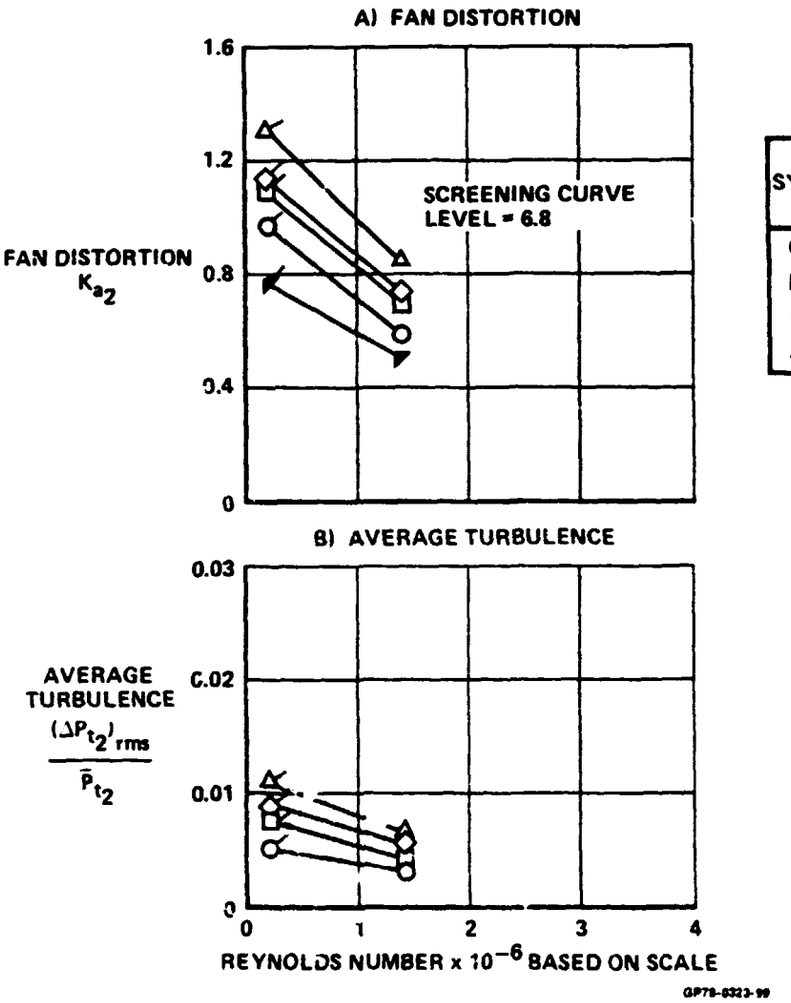

SYM	FILTER CUTOFF FREQUENCY
○	45
□	100
◇	170
△	500

FIGURE 97
EFFECT OF FILTER CUTOFF FREQUENCY AND REYNOLDS NUMBER ON FAN DISTORTION, TURBULENCE AND SPATIAL DISTORTION
Mach 1.8 $\alpha = -2$ $\beta = 0$ $\rho = -3$ $\Delta_3 = 17.4$ Bypass = 0.0

FREQUENCY CONTENT EFFECT

Solid symbol - steady state
Open symbol - corresponds to peak time variant fan distortion
Flags indicate interpolated or extrapolated data relative to airflow

Percent WAT2
80.7

MODEL	I.D. NUMBER	REYNOLDS NUMBER
1/6th SCALE	45, 46	0.2
FSCP		
FSE		
FLT		1.4

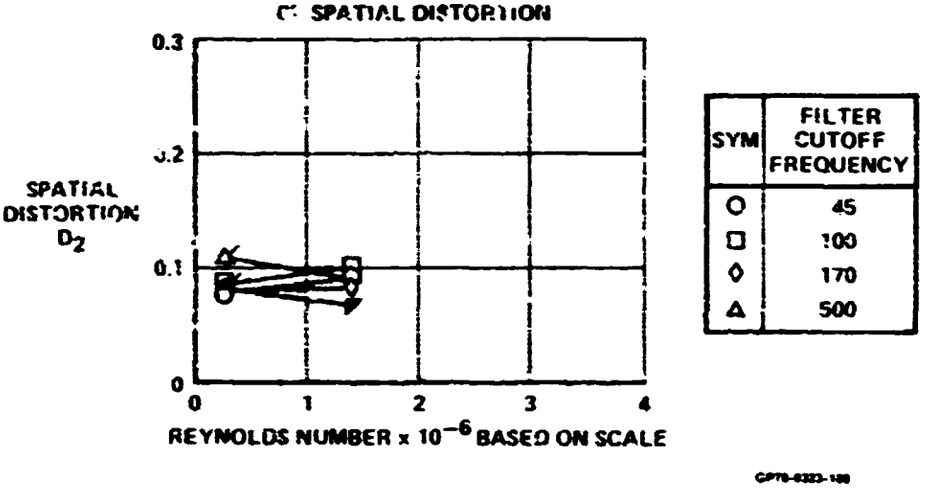

FIGURE 97 (Continued)
EFFECT OF FILTER CUTOFF FREQUENCY AND REYNOLDS NUMBER ON FAN DISTORTION, TURBULENCE AND SPATIAL DISTORTION
Mach 1.8 $\alpha = -2$ $\beta = 0$ $\phi = -3$ $\Delta_2 = 17.4$ Bypass = 0.0

FREQUENCY CONTENT EFFECT

Solid symbol - steady state
Open symbol - corresponds to peak time variant fan distortion
Flags indicate interpolated or extrapolated data relative to airflow

MODEL	I.D. NUMBER	REYNOLDS NUMBER
1/6th SCALE		
FSCP	48, 49	1.45
FSE	51, 52	1.46
FLT	53	1.53

SYM	FILTER CUTOFF FREQUENCY
○	45
□	100
◇	170
△	500

Percent WAT2
78.9

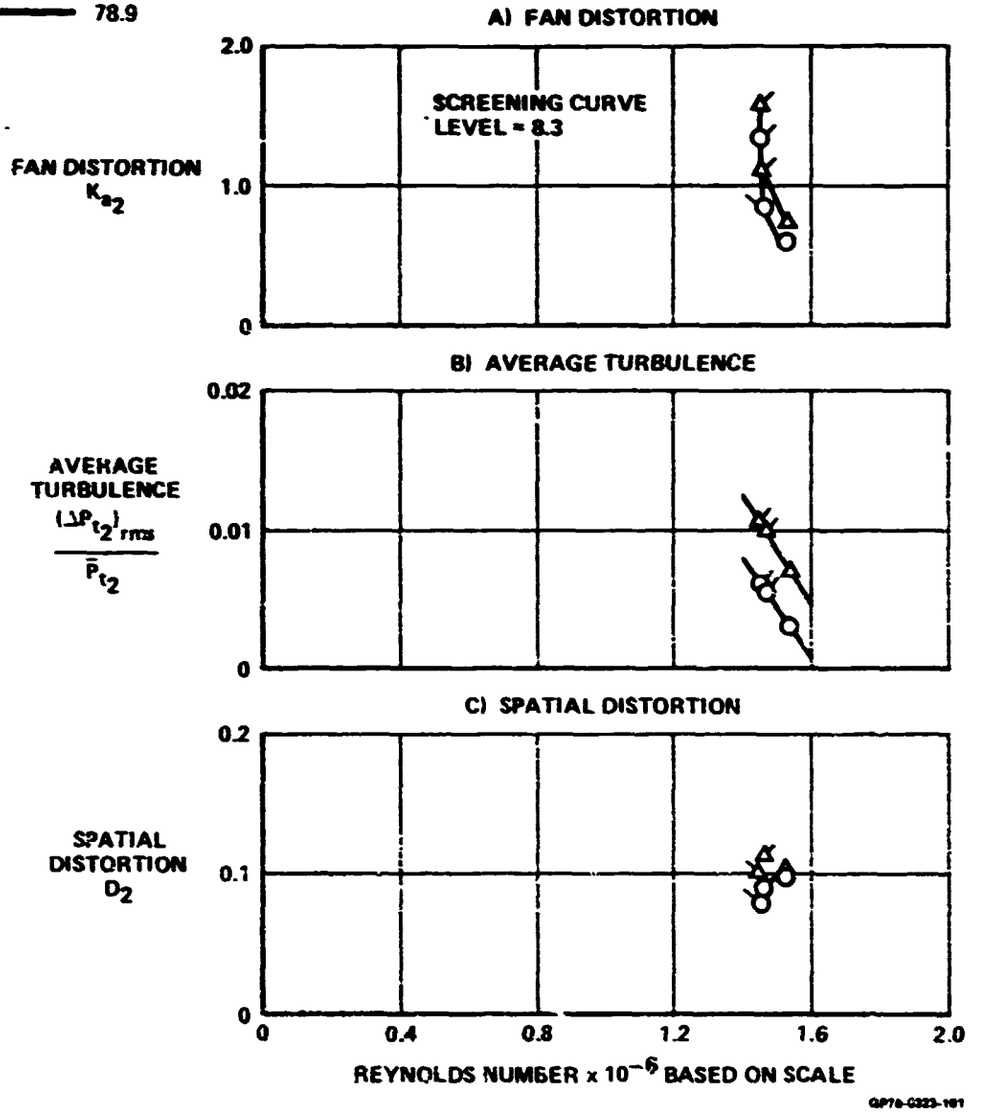

QP76-0323-101

FIGURE 98
EFFECT OF FILTER CUTOFF FREQUENCY AND REYNOLDS NUMBER ON FAN DISTORTION, TURBULENCE AND SPATIAL DISTORTION
Mach 1.8 $\alpha = -2$ $\beta = 0$ $\rho = -3$ $\Delta_3 = 18.7$ Bypass = 0.0

FREQUENCY CONTENT EFFECT

Solid symbol - steady state
Open symbol - corresponds to peak time variant fan distortion
Flags indicate interpolated or extrapolated data relative to airflow

Percent WAT2
60.4

MODEL	I.D. NUMBER	REYNOLDS NUMBER
1/6th SCALE	60, 61	0.2
FSCP	62, 63	1.5
FSE		
FLT		

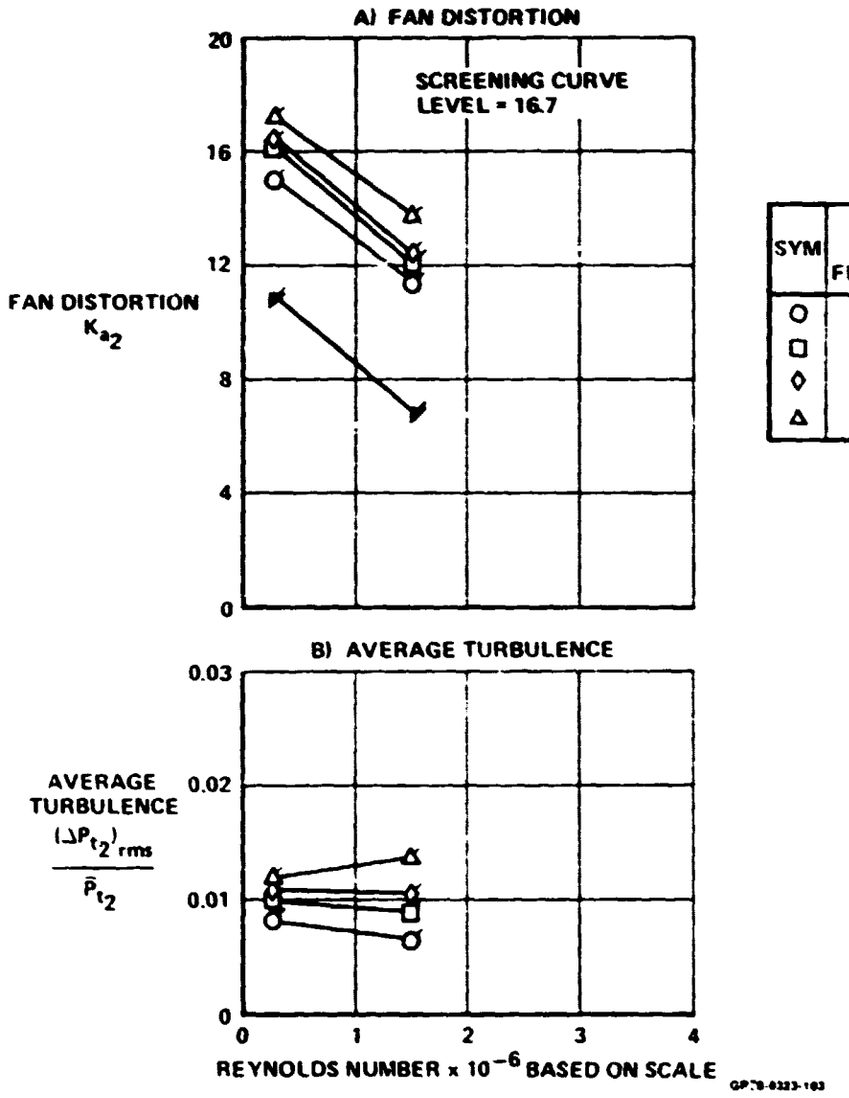

FIGURE 99
EFFECT OF FILTER CUTOFF FREQUENCY AND REYNOLDS NUMBER ON FAN DISTORTION, TURBULENCE AND SPATIAL DISTORTION
Mach 2.2 $\alpha = -2$ $\beta = 0$ $\rho = -4$ $\Delta_3 = 25$ Bypass = 0.0774

FREQUENCY CONTENT EFFECT

Solid symbol - steady state
Open symbol - corresponds to peak time variant fan distortion
Flags indicate interpolated or extrapolated data relative to airflow

Percent WAT2
73.0

MODEL	I.D. NUMBER	REYNOLDS NUMBER
1/6th SCALE	66, 67	0.2
FSCP		
FSE		
FLT	70	2.3

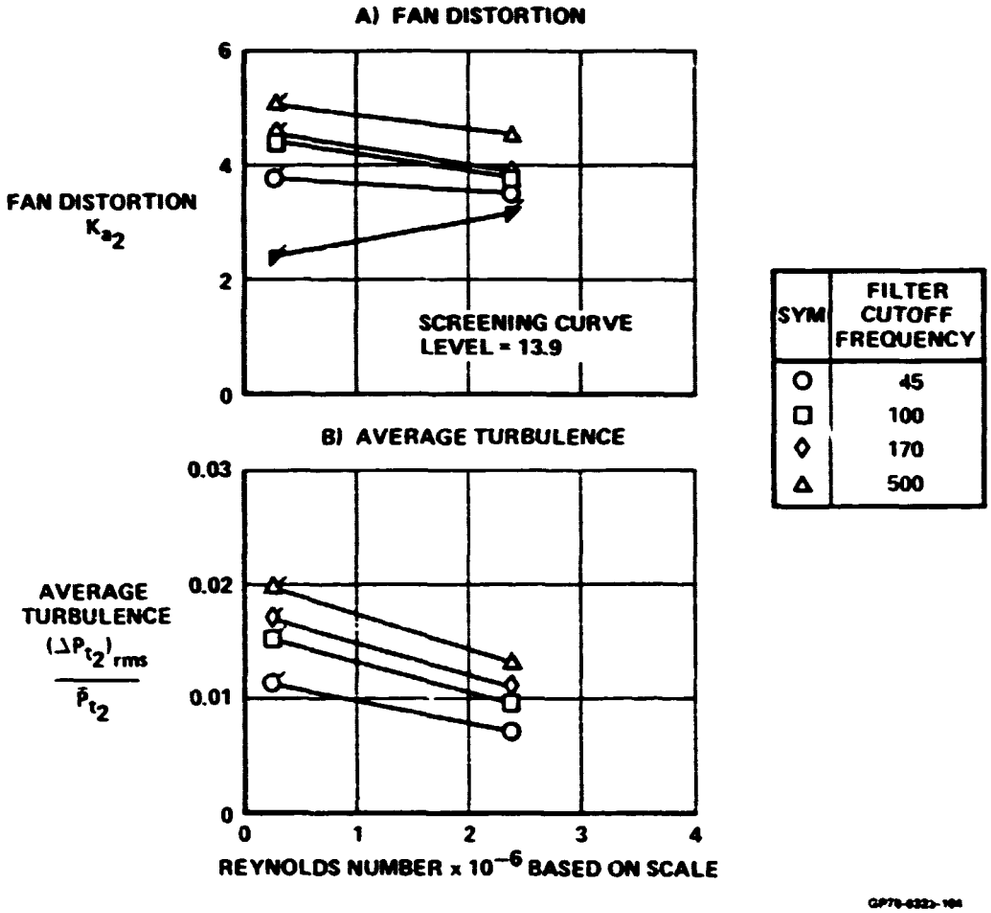

GP78-0322-104

FIGURE 100
EFFECT OF FILTER CUTOFF FREQUENCY AND REYNOLDS NUMBER ON FAN DISTORTION, TURBULENCE AND SPATIAL DISTORTION
Mach 2.2 $\alpha = 0$ $\beta = 0$ $\rho = 2$ $\Delta_3 = 22.5$ Bypass = 0.0

DISTORTION PREDICTION

Data Point Identification Number											
1/6th Scale	Full Scale Cold Pipe	Full Scale With Engine	Flight Test	M_o	α (deg)	β (deg)	ρ (deg)	λ_3 (deg)	Bypass*	Percent WAT2	Turbulence Level
5	–	–	7	0.6	−10	10	−3	10.6	C	97.2,101.2	Nominal
18	–	–	19	0.9	−10	10	−3	10.6	C	106.3,107.1	Nominal
42	–	–	44	1.6	−4	0	−2	13.5	C	87.3,89.1	Nominal
60	63	65	–	2.2	−2	0	−4	25.0	O	65.0,62.3,60.5	Nominal
66	69**	–	70	2.2	0	0	−2	22.5	O	69.3,68.3,73.0	Nominal
79	81	–	–	2.5	0	0	−4	26.0	O	63.1,62.8	Nominal
–	–	–	1	0.4	16.4	−0.8	6.9	27.6	C	104.1	High
–	–	–	2	0.59	13.9	0.9	7.0	26.6	C	102.7	High
–	–	–	3	0.52	10.0	0.7	7.0	27.6	C	107.1	High
–	–	–	4	0.69	11.5	1.0	7.0	26.5	C	104.2	High
–	–	–	15	0.85	8.8	−0.5	7.0	27.6	C	104.2	High
–	–	–	16	0.92	5.6	0.6	7.0	26.6	C	104.5	High
–	–	–	34	1.21	1.5	0	6.0	27.6	C	98.3	High
–	–	–	35	1.24	3.0	0.8	6.7	27.6	C	96.4	High

*O = Open Bypass, C = Closed Bypass

GP78-0323-105

**These data exhibited harmonic characteristics and are not included in this analysis

FIGURE 102
TEST CONDITIONS FOR EVALUATING MELICK'S PROCEDURE

PRECEDING PAGE BLANK NOT FILMED

DISTORTION PREDICTION

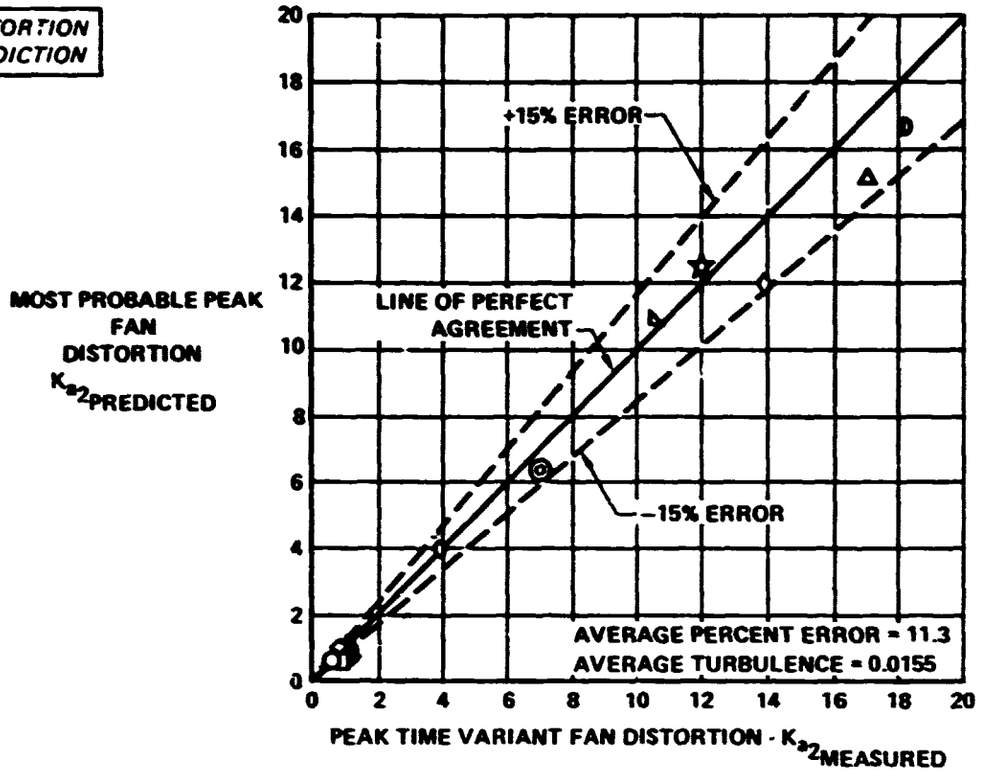

SYM	MACH	α	β	ρ	Δ_3	PERCENT WAT2	SCALE	I.D. NO.	$\overline{RS}$	$\overline{T_3}$	a_0/R_T
○	0.6	−10	10	−3	10.6	97.19	1/6	5	0.4180	0.02493	0.1101
□	0.7	−9	10	1	10.5	101.15	FLT	7	0.2437	0.0260	0.0688
◇	0.9	−10	10	−3	10.6	96.27	1/6	18	0.4529	0.04086	0.1349
◐	0.9	−9	10	1	10.5	100.05	FLT	19	0.2900	0.0307	0.0914
◎	1.6	−4	0	−2	13.5	87.28	1/6	42	0.1163	0.03537	0.0372
⬠	1.6	−4	1	−2	13.7	89.35	FLT	44	0.2837	0.0154	0.0858
◣	2.2	−2	0	−4	25.0	65.02	1/6	60	0.3086	0.02234	0.0534
☆	2.2	−2	0	−4	25.0	62.30	FSCP	63	0.3260	0.02021	0.0536
△	2.2	−2	0	−4	24.8	60.51	FSE	65	0.3823	0.02214	0.0714
◎	2.2	0	0	−2	22.5	69.31	1/6	66	0.4182	0.02617	0.0900
⬯	2.2	0	0	−2	22.9	72.95	FLT	70	0.4235	0.0416	0.1021
◗	2.5	0	0	−4	26.0	63.09	1/6	79	0.5498	0.03021	0.0970
◇	2.5	0	0	−4	26.0	62.76	FSCP	81	0.4528	0.02816	0.0770

GP79-0323-198

FIGURE 103
COMPARISON OF MEASURED AND PREDICTED
PEAK TIME VARIANT DISTORTION VALUES

DISTORTION PREDICTION

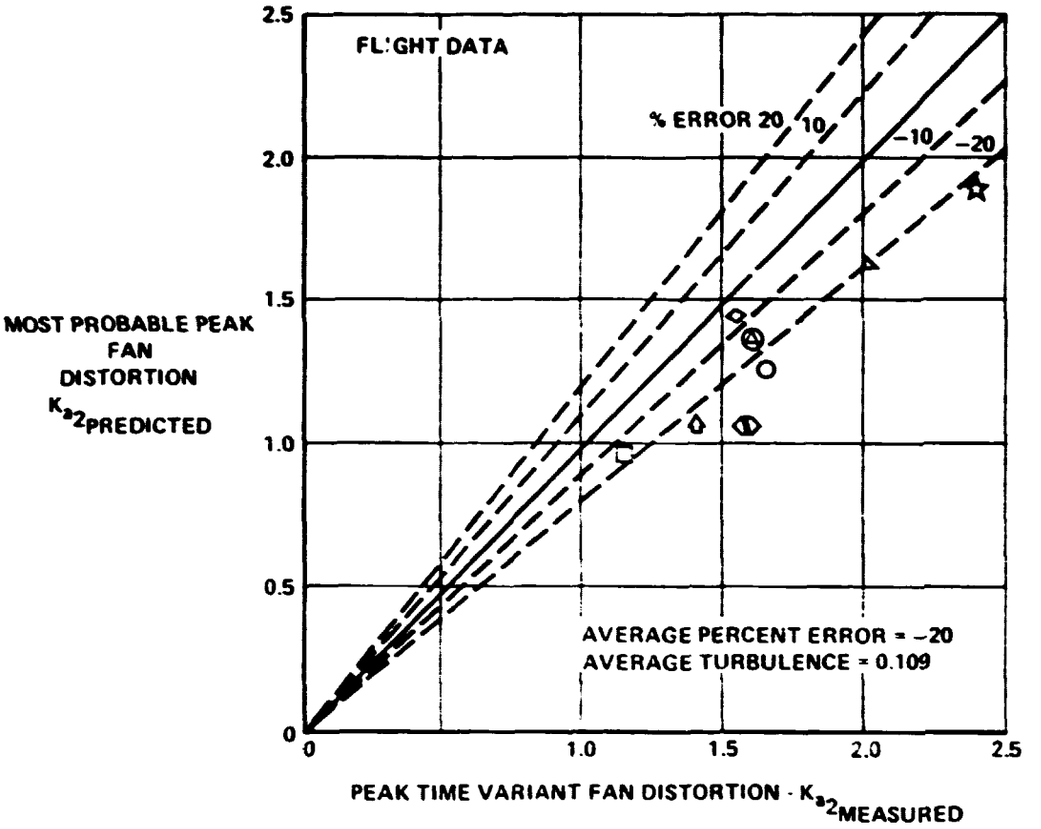

SYM	MACH	α	β	ρ	Δ_3	PERCENT WAT2	SCALE	I.D. NO.	$\overline{RS}$	$\overline{Tu}$	a_0/R_T
○	0.4	16.4	-0.8	6.9	27.6	104.1	FLIGHT	1	0.6971	0.07251	0.0798
□	0.59	13.9	0.9	7.0	26.6	102.7	FLIGHT	2	0.7424	0.05829	0.0870
◇	0.52	10.0	0.7	7.0	27.6	107.1	FLIGHT	3	0.7180	0.08508	0.0811
◫	0.69	11.5	1.0	7.0	26.5	104.2	FLIGHT	4	0.6831	0.06877	0.0761
◎	0.85	8.8	-0.5	7.0	27.6	104.2	FLIGHT	15	0.7508	0.07253	0.0923
⬠	0.92	5.6	0.6	7.0	26.6	104.5	FLIGHT	16	0.701	0.07164	0.0797
◺	1.21	1.5	0	6.0	27.6	98.3	FLIGHT	34	0.7944	0.1022	0.0918
☆	1.24	3.0	0.8	6.7	27.6	96.4	FLIGHT	35	0.7597	0.09451	0.0835

GP78-0323-198

FIGURE 104
COMPARISON OF MEASURED AND PREDICTED PEAK TIME VARIANT DISTORTION VALUES FOR INDUCED ENGINE STALLS

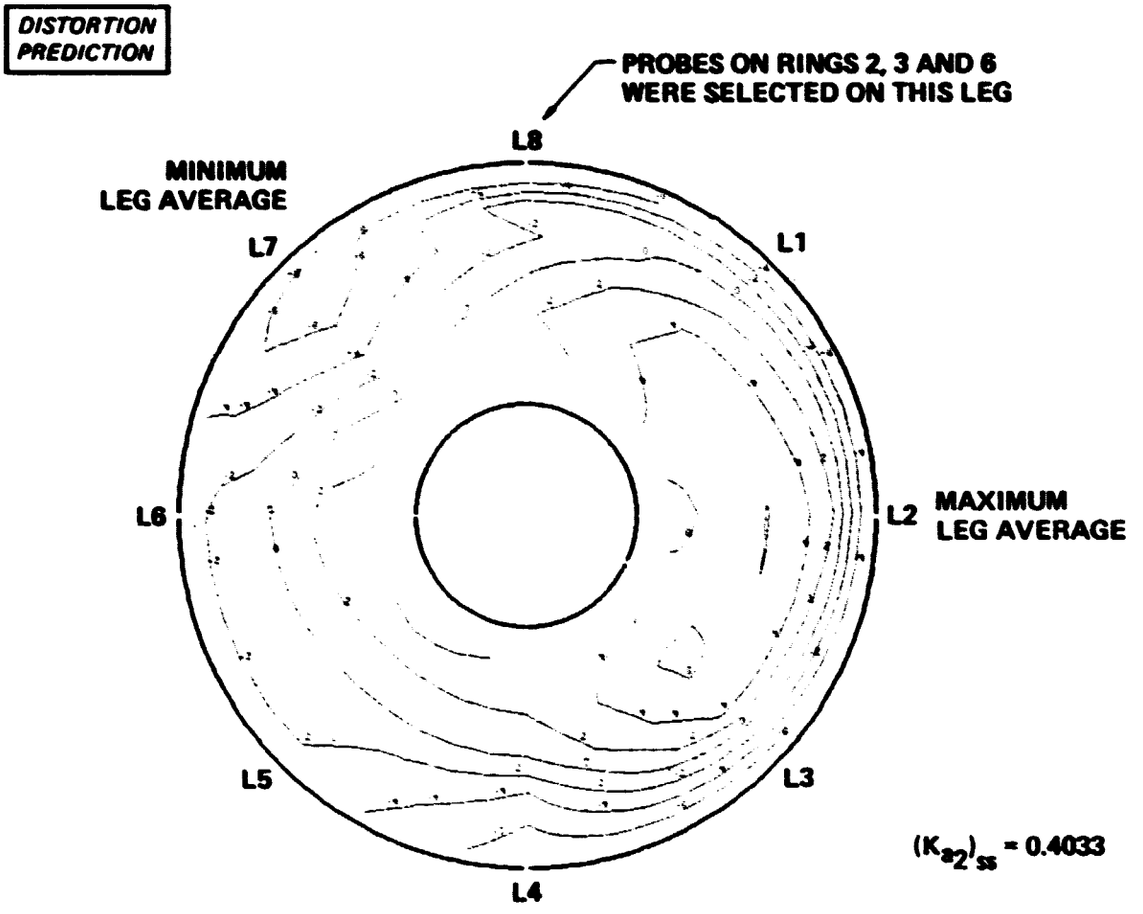

ENGINE FACE PRESSURE PROFILE
LEFT FRONTAL VIEW

Note: Inlet profile in terms of percent deviation from mean face pressure

FIGURE 105
PROBE SELECTION FOR CROSS CORRELATION COEFFICIENT CALCULATIONS
Steady State Pressure Contour
Mach 0.69 α = —8.4 β = 10.6 I.D. Number = 7 Flight 421 Run 10

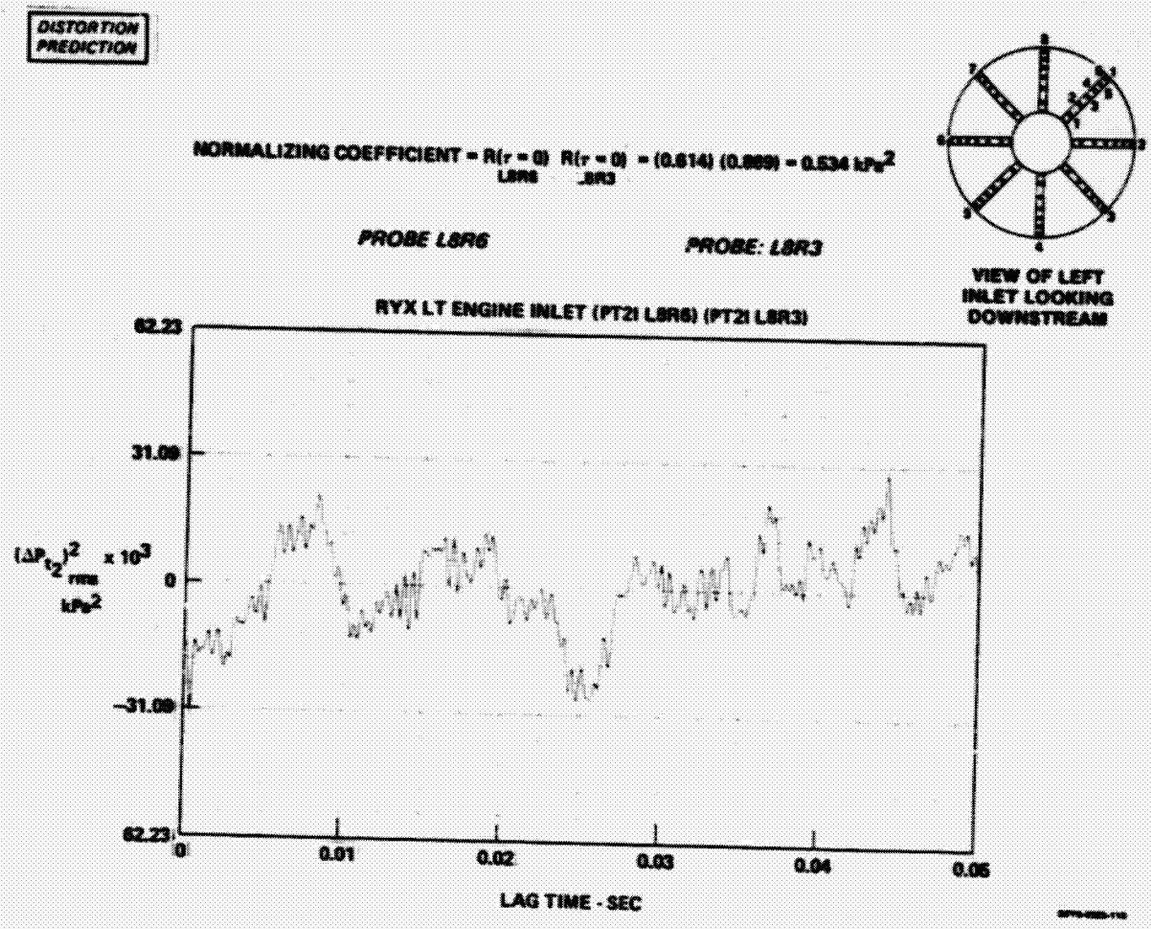

FIGURE 106
CROSS CORRELATION COEFFICIENT

Mach 0.69 α = —8.4 β = 10.6 I.D. Number = 7 Flight 421 Run 10

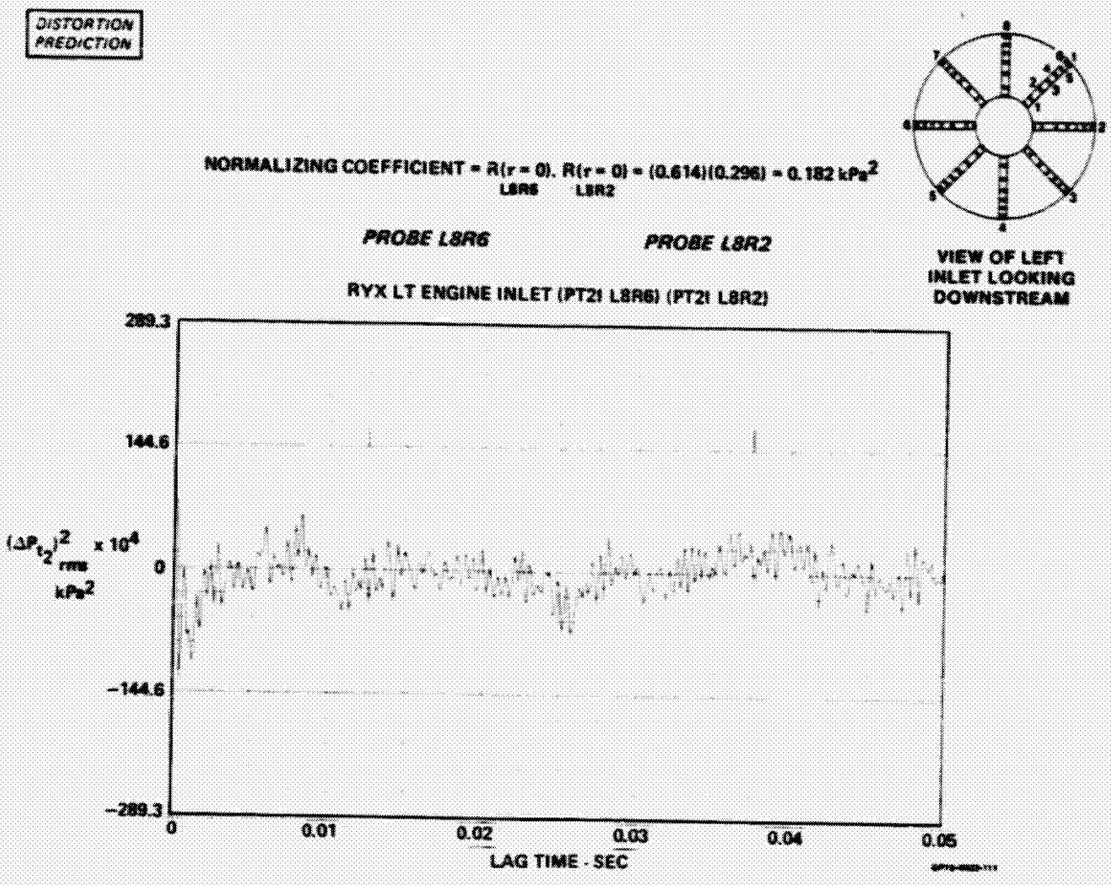

FIGURE 107
CROSS CORRELATION COEFFICIENTS
Mach 0.69 α = −8.4 β = 10.6 I.D. Number = 7 Flight 421 Run 10

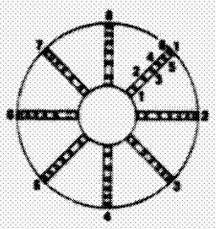

VIEW OF LEFT INLET LOOKING DOWNSTREAM

NORMALIZING COEFFICIENT = $R_{L8R3}(\tau = 0) \cdot R_{L8R2}(\tau = 0) = (0.869)(0.296) = 0.257\ kPa^2$

PROBE L8R3 PROBE L8R2

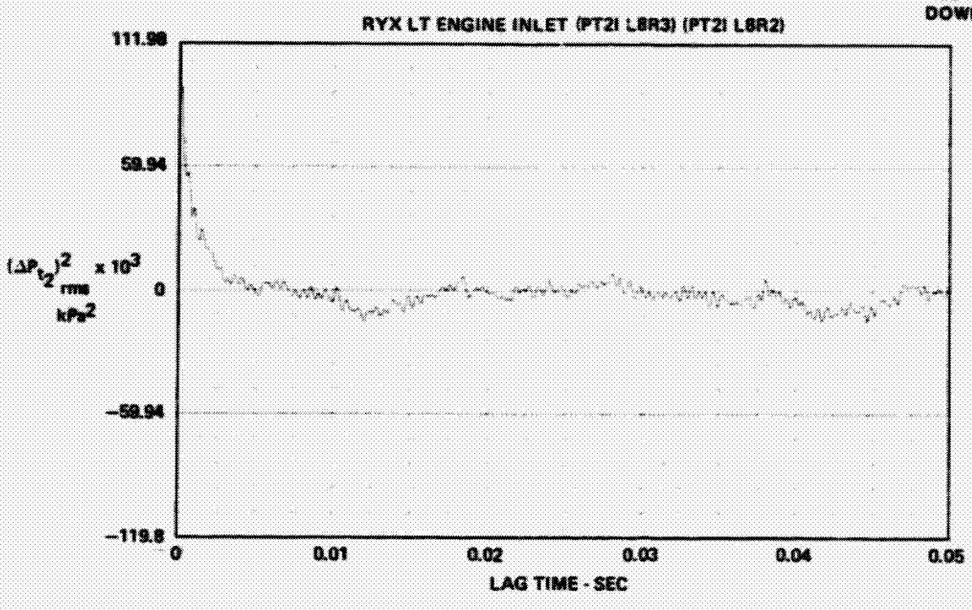

FIGURE 108
CROSS CORRELATION COEFFICIENT
Mach 0.69 α = —8.4 β = 10.6 I.D. Number = 7 Flight 421 Run 10

DISTORTION PREDICTION

PART-POINT	DATA POINT I.D. NO.	M_0	α	β	SCALE	% WAT2	VORTEX RADIUS (CM)	*NORMALIZED CROSS CORRELATION COEFFICIENT	PROBES	**N.F. $\sigma_x \cdot \sigma_y$
164-1	5	0.6	−10	10	1/6th	97.2	4.87	0.9895	L3R2, L3R3	0.3881
								0.7286	L3R2, L3R5	0.2005
								0.5383	L3R3, L3R5	0.3991
421-10	7	0.7	−9	10	FLT	101.2	3.04	0.6177	L8R2, L8R3	0.2576
								0.2107	L8R2, L3R6	0.1819
								0.1637	L8R3, L8R6	0.5331
157-5	18	0.9	−10	10	1/6th	106.3	5.96	0.9793	L3R2, L3R3	1.4784
								0.3571	L3R2, L3R5	0.2855
								0.8318	L3R3, L3R5	1.2504
421-14	19	0.9	−9	10	FLT	107.0	4.04	0.6177	L1R2, L1R3	0.4062
								0.3676	L1R2, L1R6	0.5349
								0.4219	L1R3, L1R6	0.5091
206-9	42	1.6	−4	0	1/6th	87.3	1.64	0.9651	L6R2, L6R3	0.1374
								0.4706	L6R2, L6R6	0.0609
								0.5679	L6R3, L6R6	0.0516
414-2	44	1.6	−4	0	FLT	89.4	3.94	0.6881	L6R2, L6R3	0.2034
								0.4543	L6R2, L6R6	0.2328
								0.3879	L6R3, L6R6	0.2629
249-5	60	2.2	−2	0	1/6th	65.0	2.36	0.9898	L8R2, L8R3	0.2888
								0.7372	L8R2, L8R5	0.1126
								0.9197	L8R3, L8R5	0.1536
385-2	63	2.2	−2	0	FSCP	62.3	2.37	0.9904	L1R2, L1R3	0.3109
								0.5399	L1R2, L1R6	0.0552
								0.3926	L1R3, L1R6	0.0467
543-4	65	2.2	−2	0	FSE	60.5	3.16	0.9836	L8R2, L8R3	0.7174
								0.6923	L8R2, L8R5	0.2347
								0.9542	L8R3, L8R5	0.4716
184-7	66	2.2	0	0	1/6th	69.3	3.49	0.9899	L8R2, L8R3	0.4936
								0.3991	L8R2, L8R5	0.2536
								0.8479	L8R3, L8R5	0.3524
425-1	70	2.2	0	0	FLT	73.0	4.51	0.5846	L1R2, L1R3	3.4855
								0.3035	L1R2, L1R5	3.3396
								0.3953	L1R3, L1R5	3.1147
227-7	79	2.5	0	0	1/6th	63.1	4.29	0.9960	L5R2, L5R3	0.6614
								0.9564	L5R2, L5R5	0.3554
								0.9892	L5R3, L5R5	0.4442
465-8	81	2.5	0	0	FSCP	62.8	3.40	0.9911	L8R2, L8R3	0.4367
								0.6492	L8R2, L8R6	0.1019
								0.9120	L8R3, L8R6	0.1480

GP78-0323-113

*Normalized cross correlation coefficient = $\dfrac{[\sigma_{xy}\,(\tau = 0)]}{\sqrt{\sigma_x \sigma_y}}$

**N.F. = Normalizing Factor

FIGURE 109
COMPARISON OF NORMALIZED VORTEX RADIUS AND CROSS CORRELATION COEFFICIENTS FROM THE ENGINE FACE RAKE PRESSURE PROBES

STABILITY AUDITS

Data Point Identification Number	M_o	Altitude (meters)	α (deg)	β (deg)	μ (deg)	Δ_3 (deg)	Bypass	Airflow	Result	Maneuver
1*	0.4	7,050	–	0	7.0	–	Closed	Max	Stall	5 g wind up turn. While holding turn, step increase Δ_3 on L/H inlet only until engine stalls.
2	0.59	7,610	–	0	7.0	–	Closed	Max	Stall	
3	0.52	10,960	–		7.0	–			A/B Blowout/Relight, Stall	
4*	0.70	16,440	–		7.0	–			A/B Blowout/Relight, Stall	
15	0.85	10,760	–	0	7.0	–	Closed	Max	Stall	
16*	0.92	16,930	–		–	–			A/B Blowout/Relight, Stall	
34	1.2	11,220	–	0	Var	–	Closed	Max	Stall	
35*	1.2	16,210	–	0	Var	–	Closed	Max	Stall	Wind up turn, but sustain M_o, alt. While holding turn, step increase Δ_3 on L/H inlet only until engine stalls.
44	1.6	18,470	–4	0	–2	13.5			No Stall	Pushover
57*	2.0	19,030	–	0	2.5	19	Automatic	Max	No Stall	1 g level flight

*Stability audits are in Appendix K

GP78-0333-116

FIGURE 110
TEST CONDITIONS TO EVALUATE P&WA STABILITY AUDIT PROCEDURE TO PREDICT ENGINE STALL

STABILITY AUDITS

Legend

Surge pressure ratio
- A - Highest available
- A to B - Reynolds no. loss
- B to C - Engine-to-engine variation
- C to D - Distortion loss

Operating pressure ratio
- 1 - Installed match point
- 2 - Distortion rematch
- 3 - Rematch due to augmentor blowout
- 4 - Rematch due to augmentor reignition

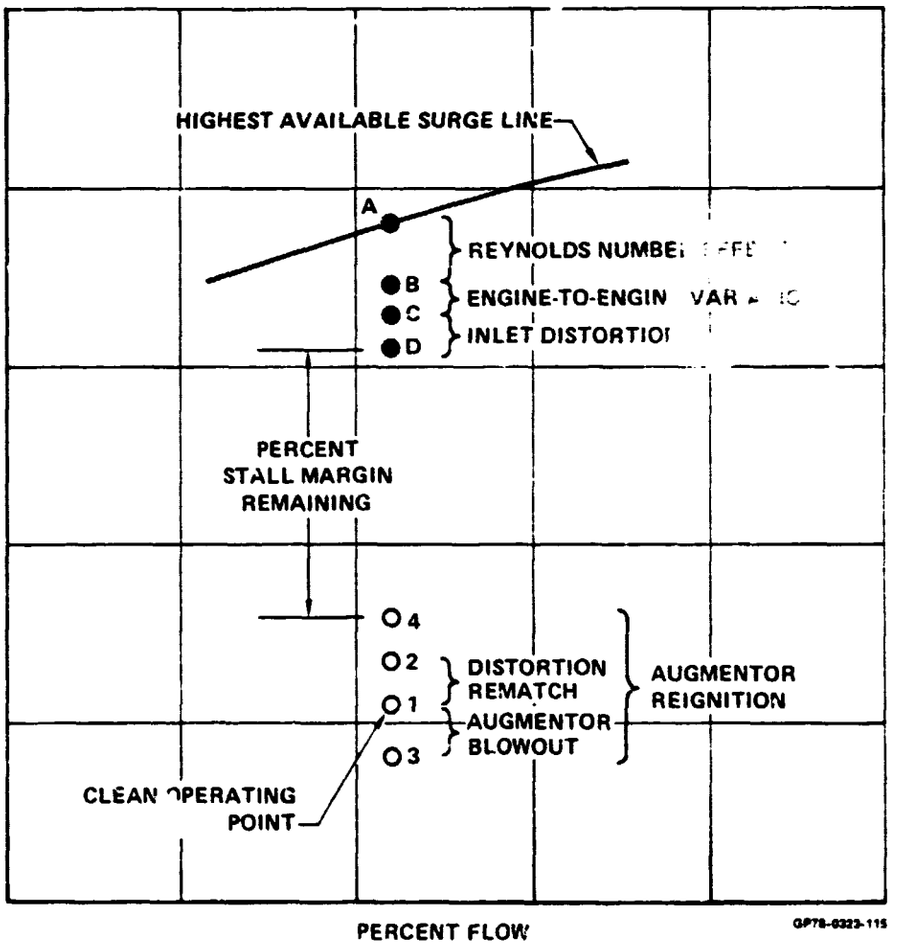

FIGURE 111
STABILITY AUDIT FAN MAP NOMENCLATURE

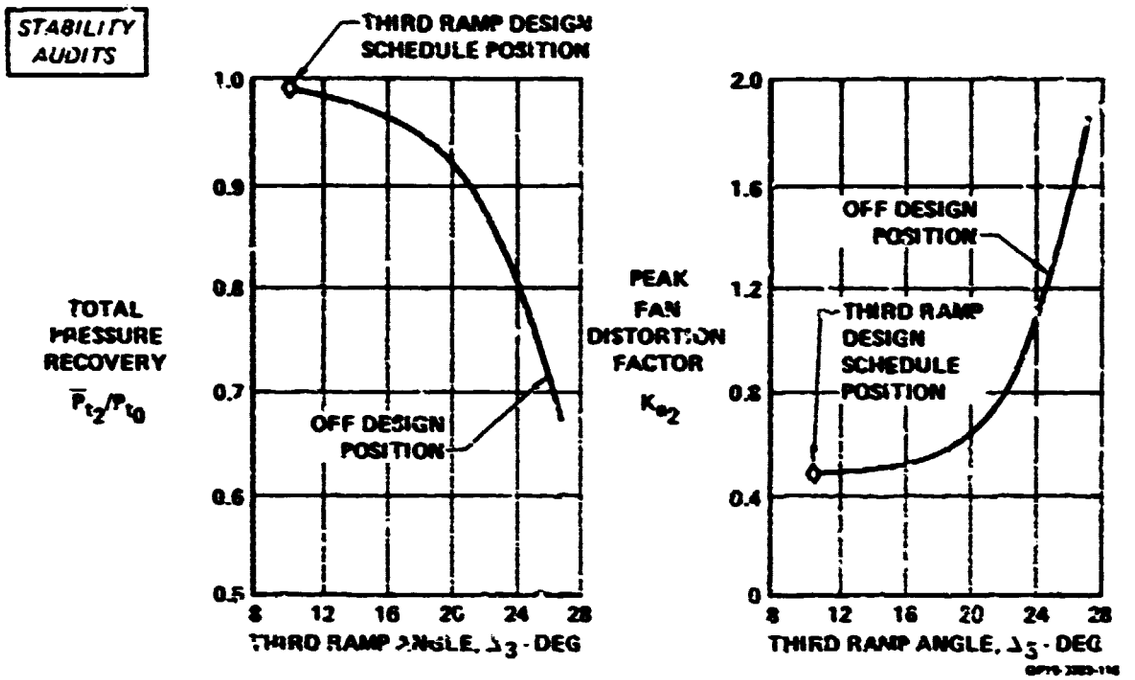

FIGURE 112

EFFECT OF THIRD RAMP ANGLE ON INLET PRESSURE RECOVERY AND FAN DISTORTION

Mach 0.4 α = 16.4 β = —0.8 ρ = 6.9 WAT2 ≅ 104.1 Bypass = 0.0 I.D. Number = 1

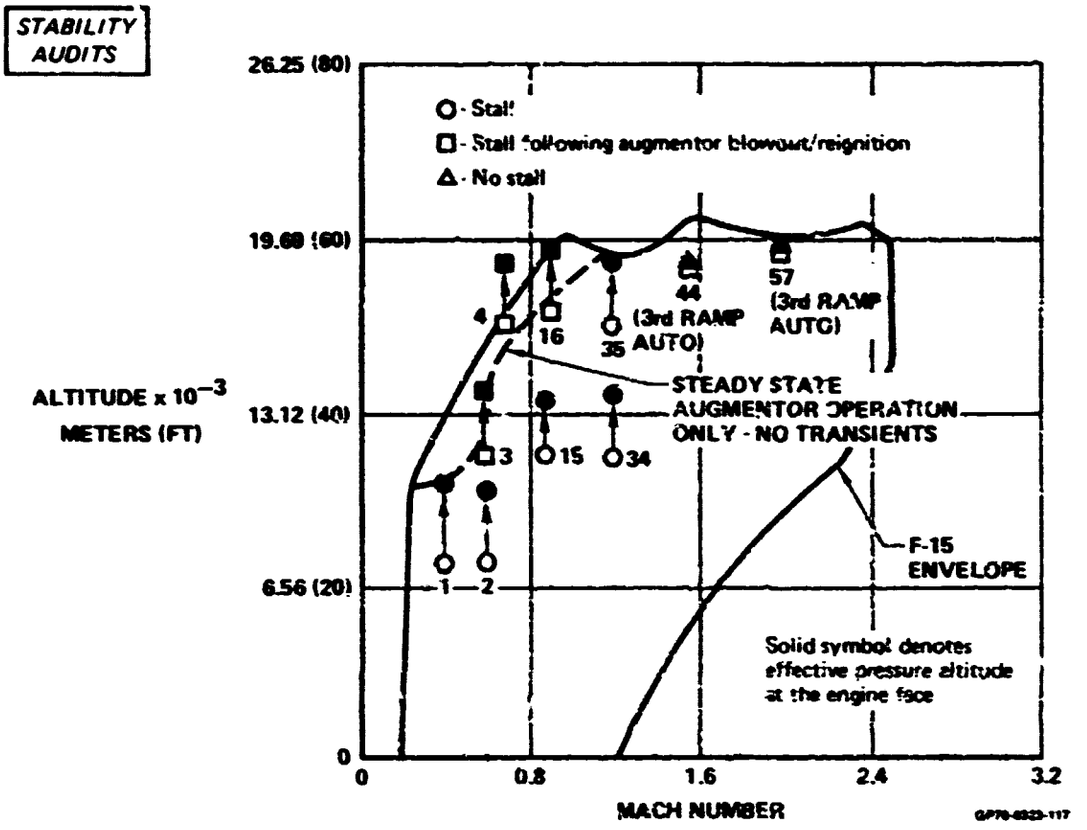

FIGURE 113
COMPARISON OF F-15 FLIGHT ENVELOPE AND TEST CONDITIONS AUDITED

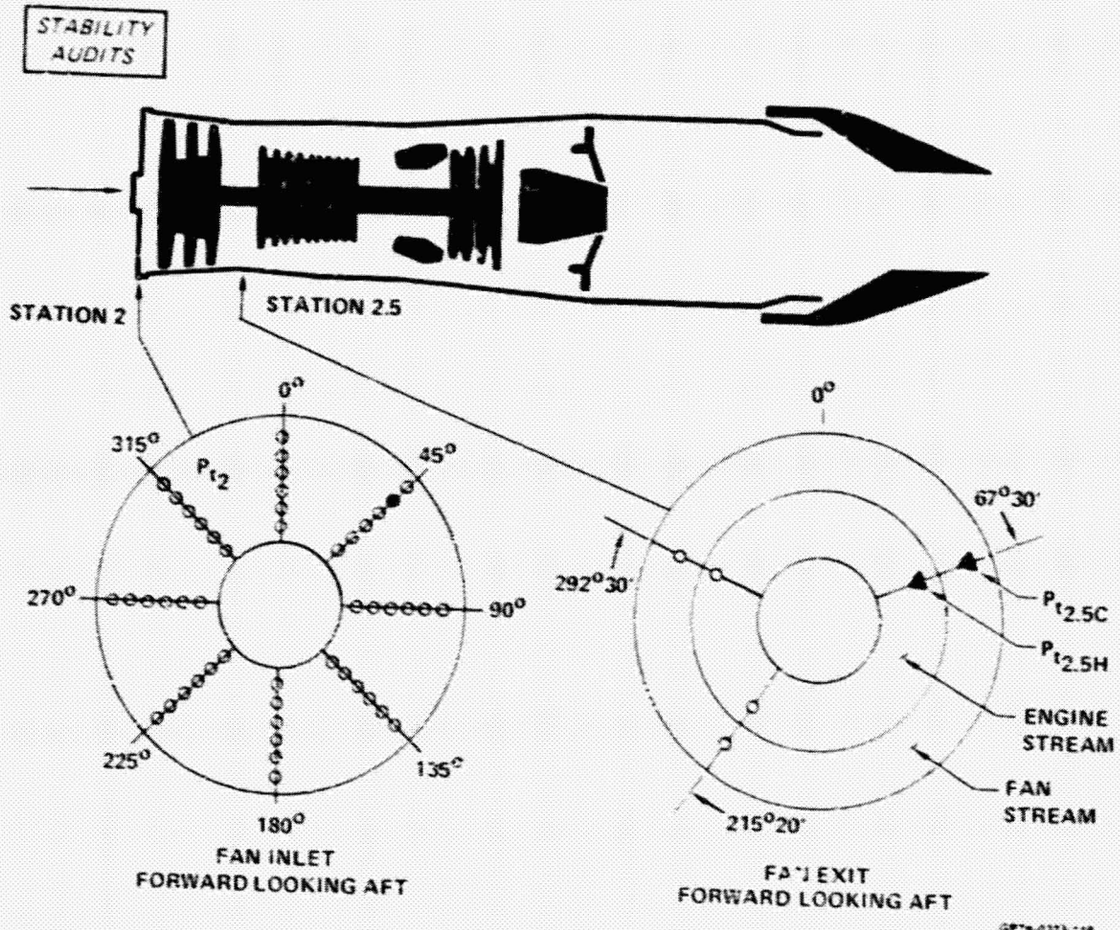

FIGURE 114
F100(2 ea) ENGINE HIGH RESPONSE PRESSURE INSTRUMENTATION

STABILITY AUDITS

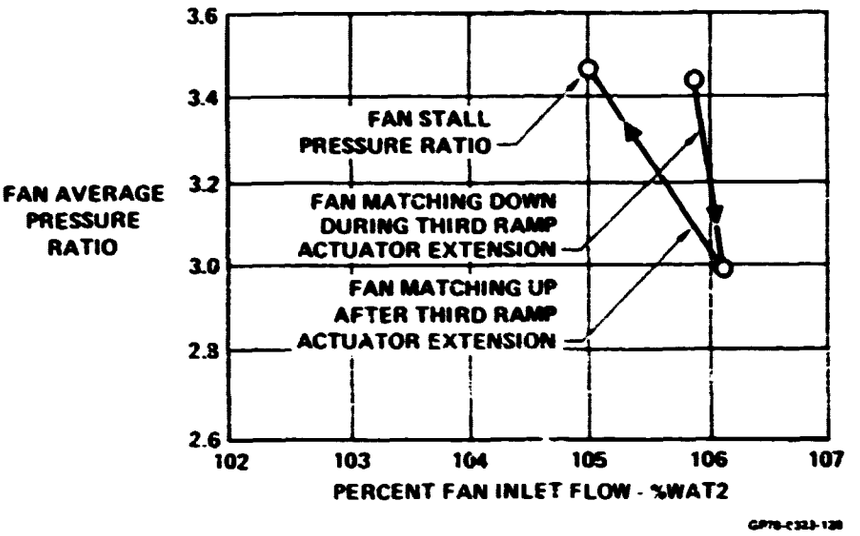

FIGURE 115
FAN PRESSURE RATIO OPERATING POINT EXCURSIONS DURING THIRD RAMP ACTUATOR EXTENSION

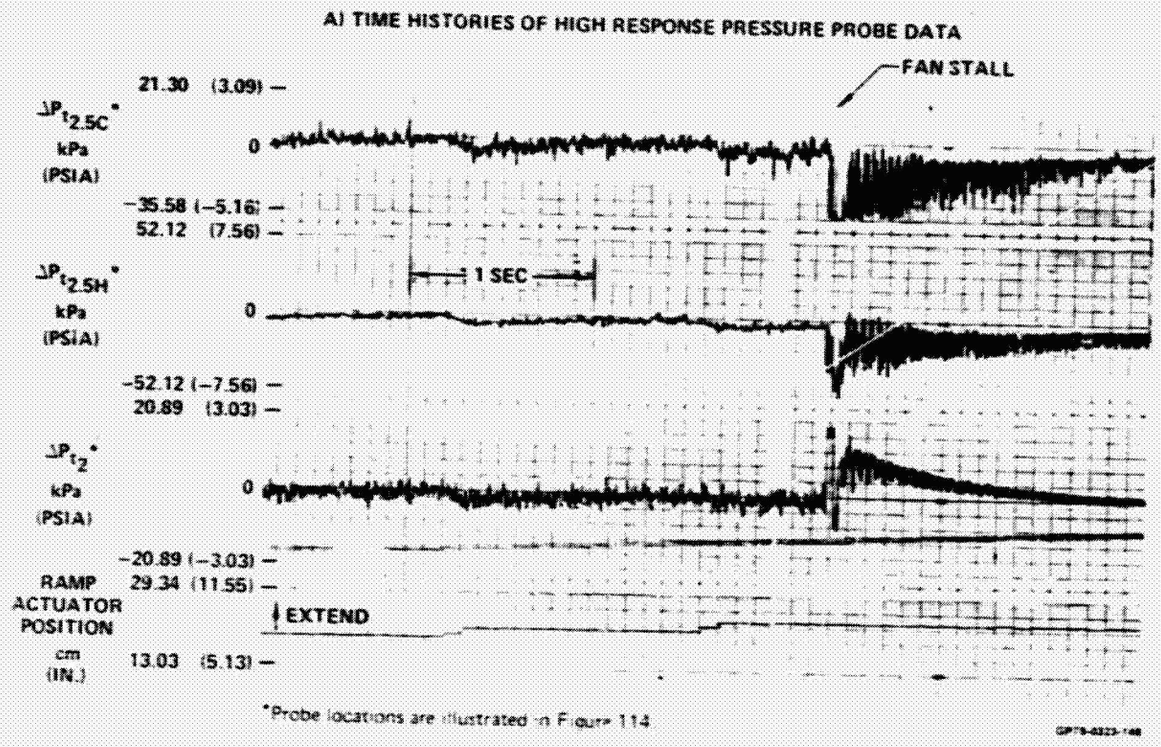

FIGURE 116
STABILITY AUDIT ANALYSIS PLOTS
Mach 0.59 α = 13.9 β = 0.9 ρ = 7.0
Δ_3 = 26.6 WAT2 = 102.7% Bypass = 0 I.D. Number = 2

STABILITY AUDITS

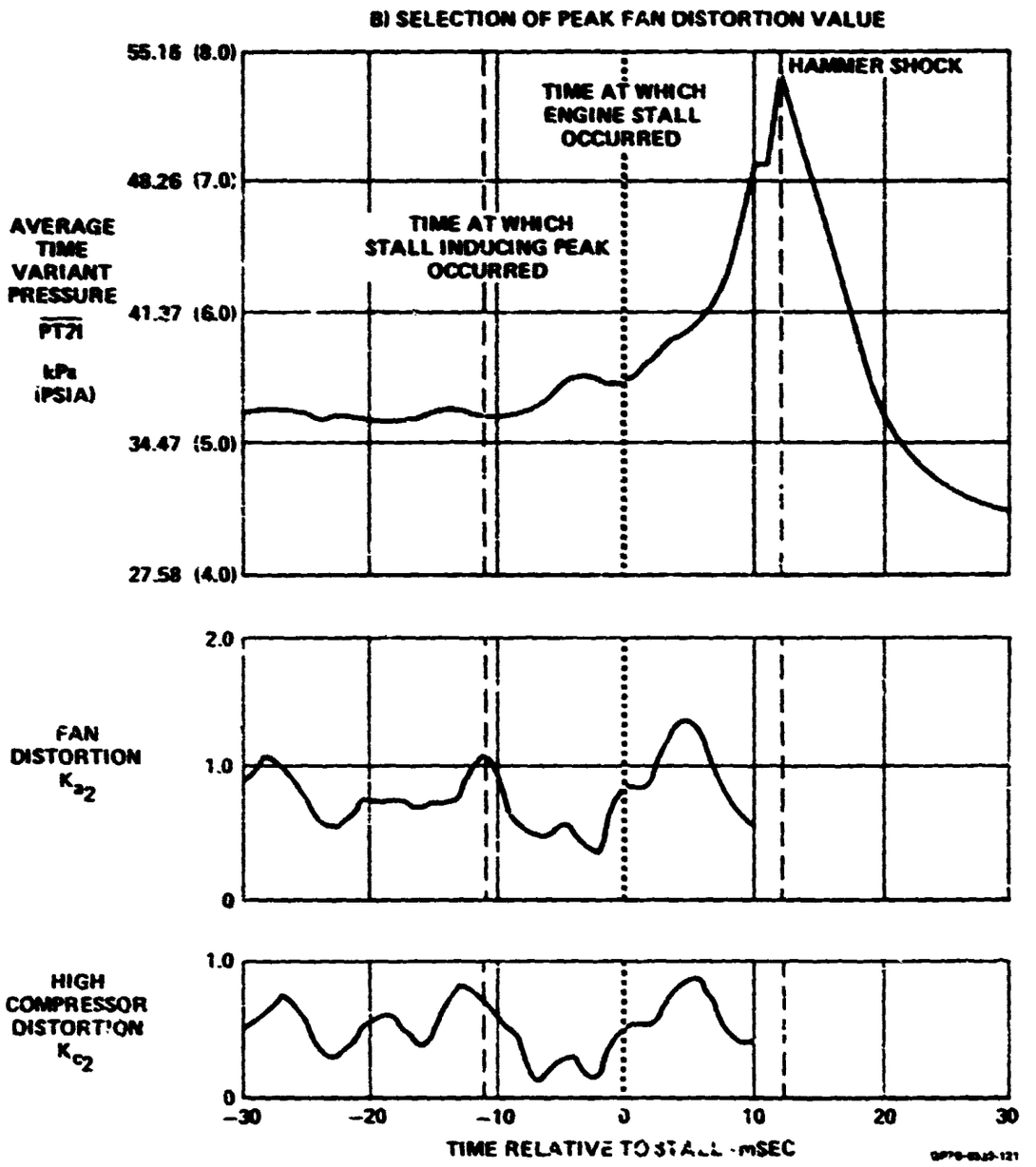

FIGURE 116 (Continued)
STABILITY AUDIT ANALYSIS PLOTS
Mach 0.5° α = 13.9 β = 0.9 ρ = 7.0
Δ_3 = 26.6 WAT 102.7% Bypass = 0 I.D. Number = 2

C) TOTAL PRESSURE CONTOUR AT PEAK FAN DISTORTION

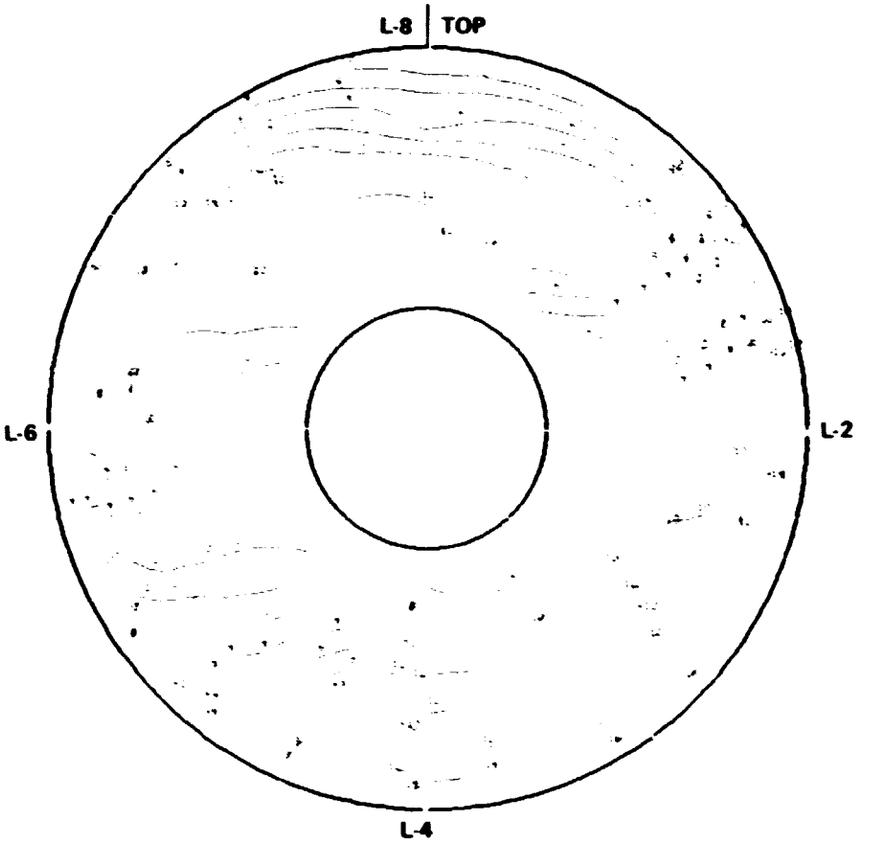

$K_{a_2} = 1.1$

$K_{C_2} = 0.7$

$\frac{\Delta P}{P}\left(\frac{\text{MAX - MIN}}{\text{AVG}}\right) = 38\%$

View of left inlet looking downstream

GP78-8323-122

FIGURE 116 (Continued)
STABILITY AUDIT ANALYSIS PLOTS
Mach 0.59 α = 13.9 β = 0.9 ρ = 7
λ_3 = 26.6 WAT2 = 102.7% Bypass = 0 I.D. Number = 2

STABILITY AUDITS

Legend

Surge Pressure Ratio
- A - Highest available
- A to B - Reynolds number loss
- B to C - Engine-to-engine variation
- C to D - Distortion loss

Operating Pressure Ratio
- 1 - Installed match point
- 2 - Distortion rematch

d) FAN AND COMPRESSOR MAPS FOR THE STABILITY AUDIT

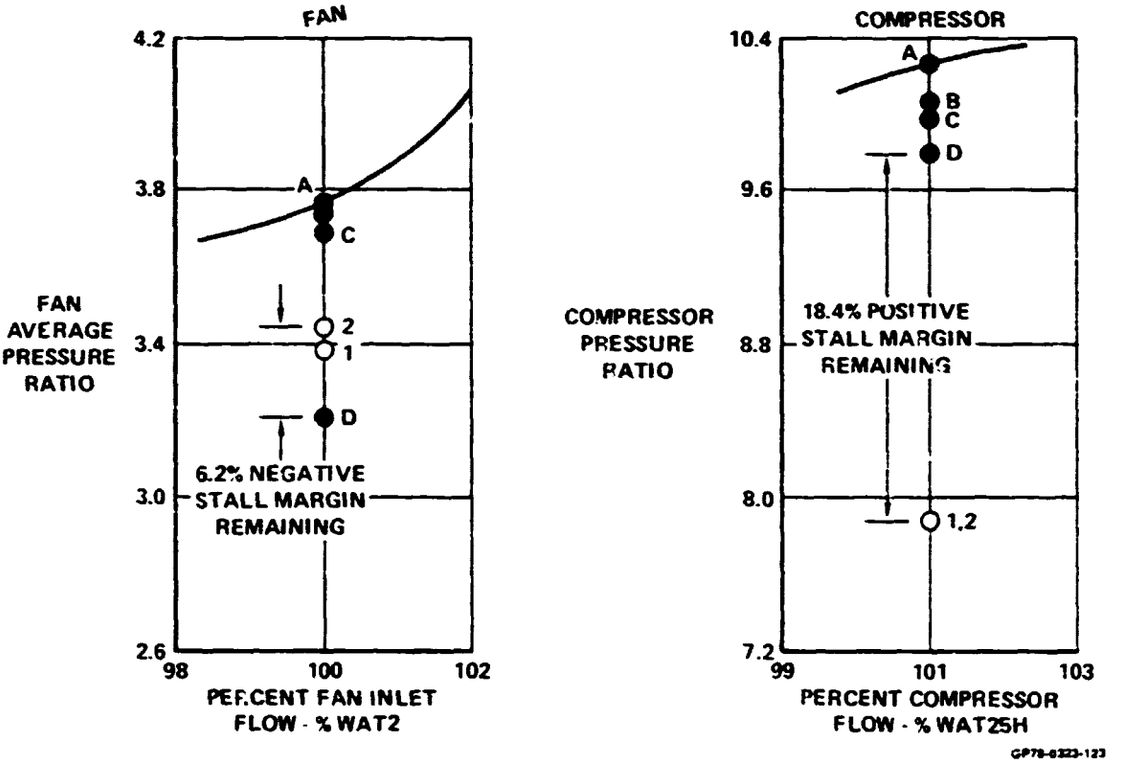

FIGURE 116 (Continued)
STABILITY AUDIT ANALYSIS PLOTS

Mach 0.59 α = 13.9 β = 0.9 ρ = 7.0
Δ_3 = 26.6 WAT2 = 102.7% Bypass = 0 I.D. Number = 2

STABILITY AUDITS

A) TIME HISTORIES OF HIGH RESPONSE PRESSURE PROBE DATA

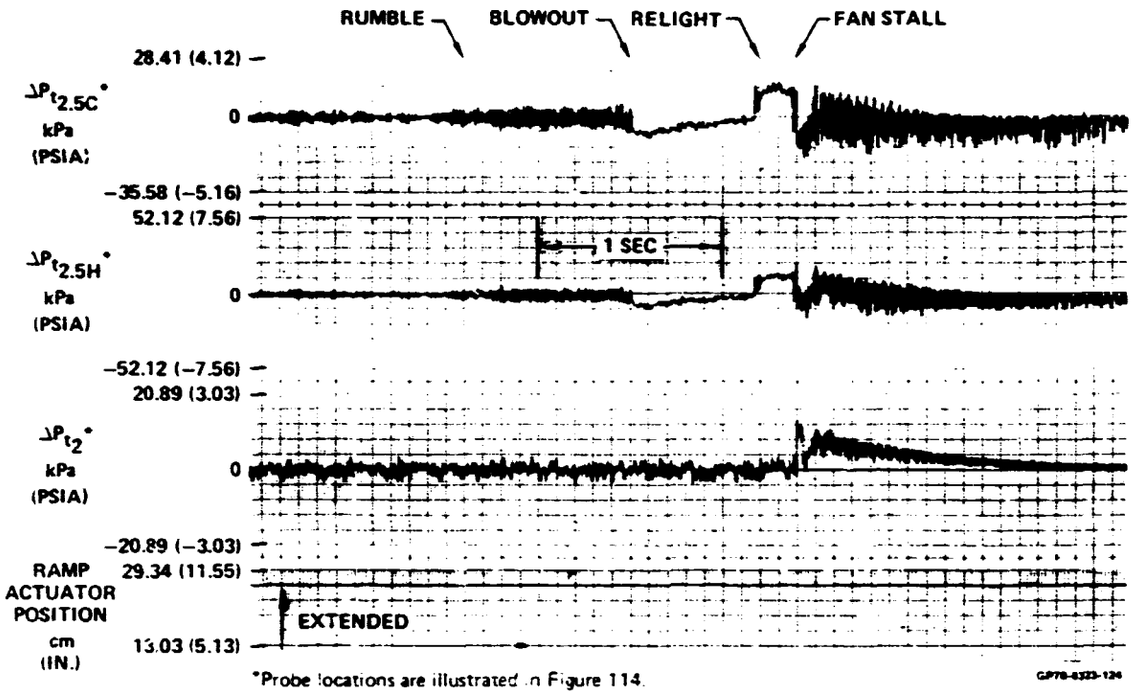

*Probe locations are illustrated in Figure 114.

GP78-0323-124

FIGURE 117
STABILITY AUDIT ANALYSIS PLOTS
Mach 0.52 α = 10.0 β = 0.07 ρ = 7.0
Δ_3 = 27.6 WAT2 = 107.1% Bypass = 0 I.D. Number = 3

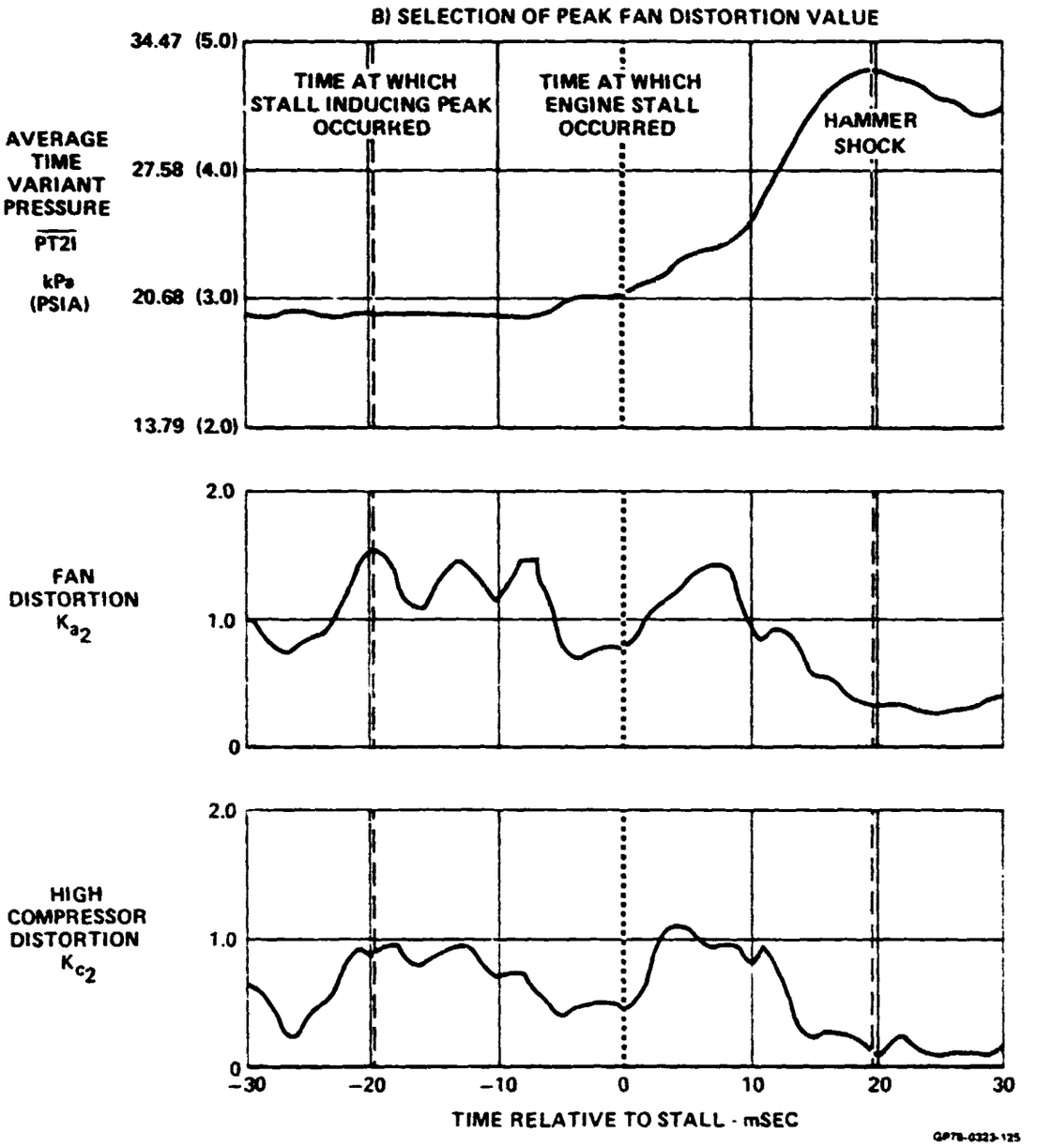

FIGURE 117 (Continued)
STABILITY AUDIT ANALYSIS PLOTS
Mach 0.52 α = 10.0 β = 0.7 ρ = 7.0
Δ_3 = 27.6 WAT2 = 107.1% Bypass = 0 I.D. Number = 3

C) TOTAL PRESSURE CONTOUR AT PEAK FAN DISTORTION

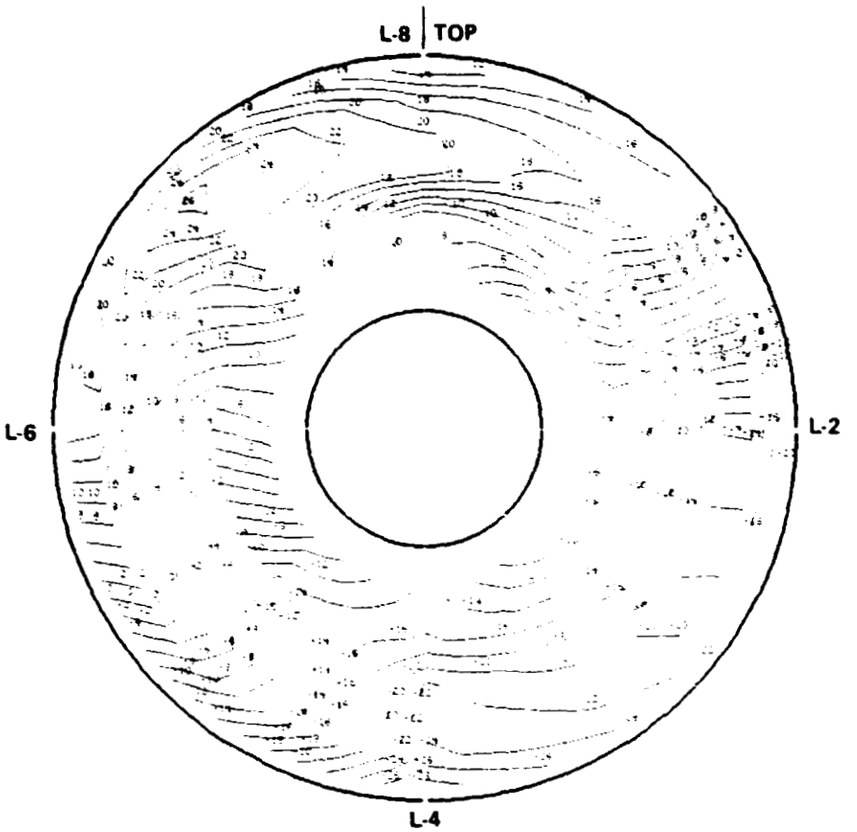

$K_{a_2} = 1.4$

$K_{C_2} = 0.86$

$\frac{\Delta P}{P}\left(\frac{MAX-MIN}{AVG}\right) = 55.6\%$

View of left inlet looking downstream

GP78-0323-126

FIGURE 117 (Continued)
STABILITY AUDIT ANALYSIS PLOTS

Mach 0.52 α = 10.0 β = 0.07 ρ = 7.0
Δ_3 = 27.6 WAT2 = 107.1% Bypass = 0 I.D. Number = 3

STABILITY AUDITS

Legend

Surge pressure ratio
- A - Highest available
- A to B - Reynolds numbe. loss
- B to C - Engine-to-engine variation
- C to D - Distortion loss

Operating pressure ratio
- 1 - Installed match point
- 2 - Distortion rematch
- 3 - Rematch due to augmentor blowout
- 4 - Rematch due to augmentor reignition

D) FAN AND COMPRESSOR MAPS FOR THE STABILITY AUDITS

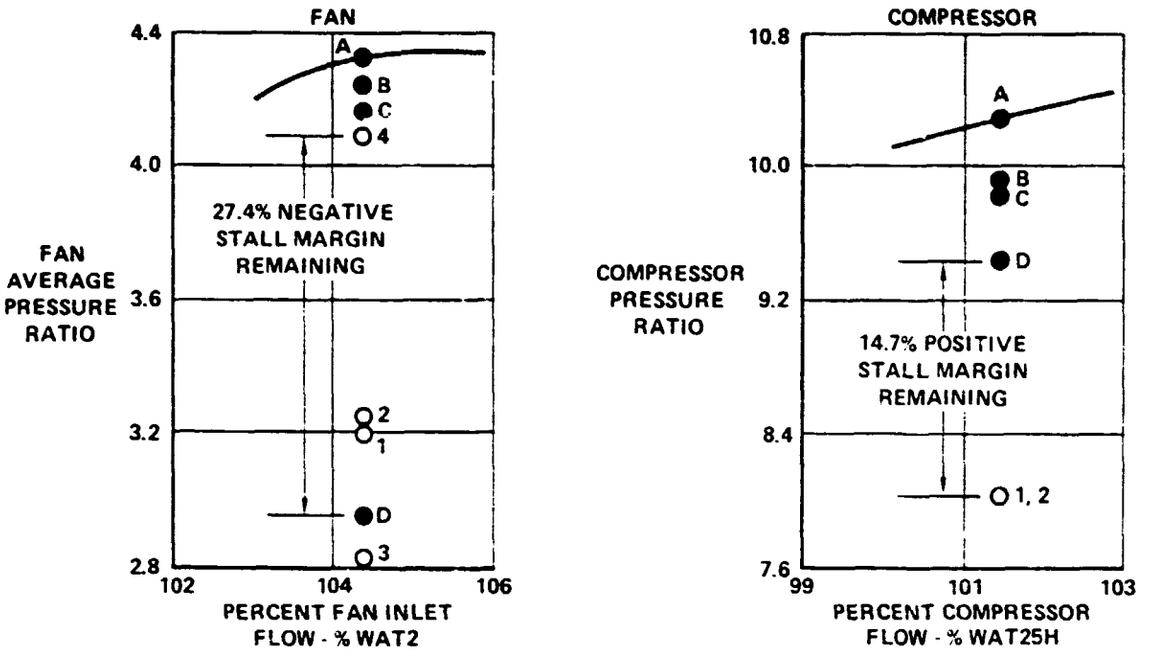

GP78-0323-127

FIGURE 117 (Continued)
STABILITY AUDIT ANALYSIS PLOTS

Mach 0.52 α = 10.0 β = 0.07 ρ = 7.0
Δ_3 = 27.6 WAT2 = 107.1% Bypass = 0 I.D. Number = 3

A) TIME HISTORIES OF HIGH RESPONSE PRESSURE PROBE DATA

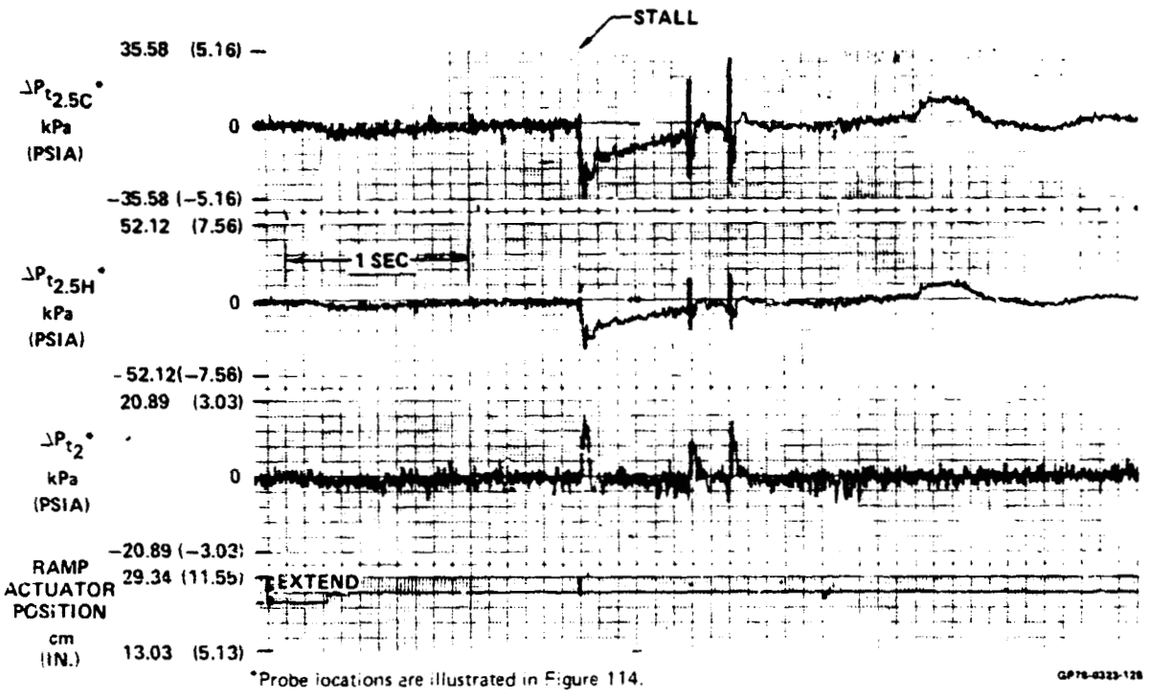

*Probe locations are illustrated in Figure 114.

GP76-0323-126

FIGURE 118
STABILITY AUDIT ANALYSIS PLOTS

Mach 0.85 α = 8.8 β = −0.5 ρ = 7.0
Δ_3 = 27.6 WAT2 = 104.2% Bypass = 0 I.D. Number = 15

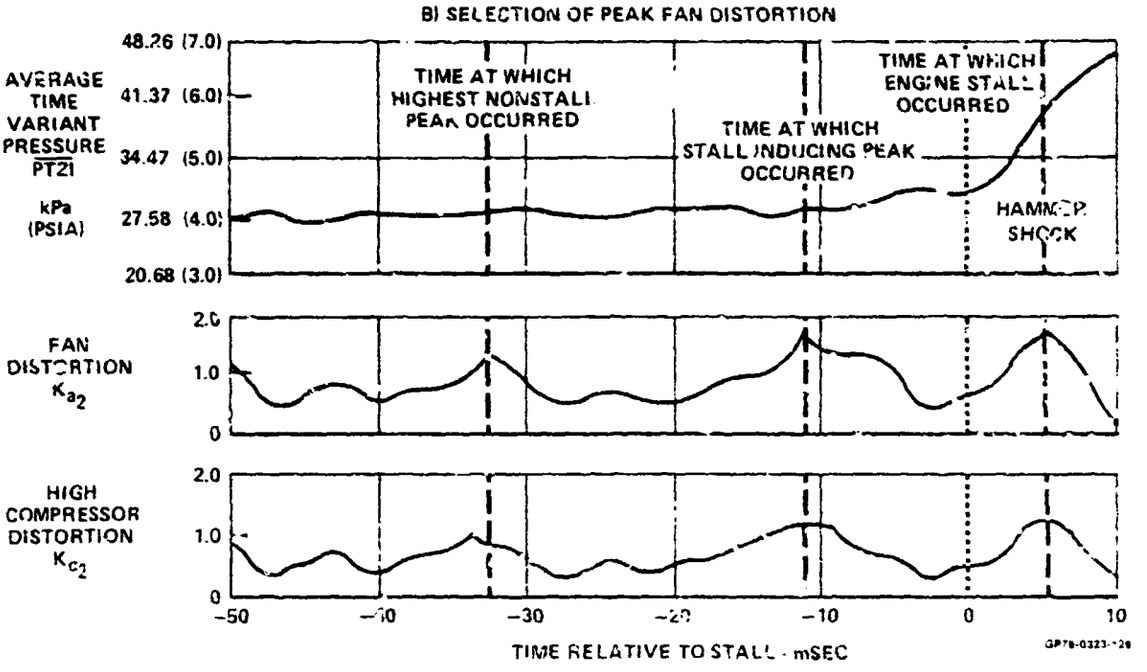

FIGURE 116 (Continued)
STABILITY AUDIT ANALYSIS PLOTS

Mach 0.85 α = 8.8 β = −0.5 ρ = 7.0
Δ_3 = 27.6 WAT2 = 104.2% Bypass = 0 I.D. Number = 15

STABILITY AUDITS

C) TOTAL PRESSURE CONTOUR AT PEAK FAN DISTORTION

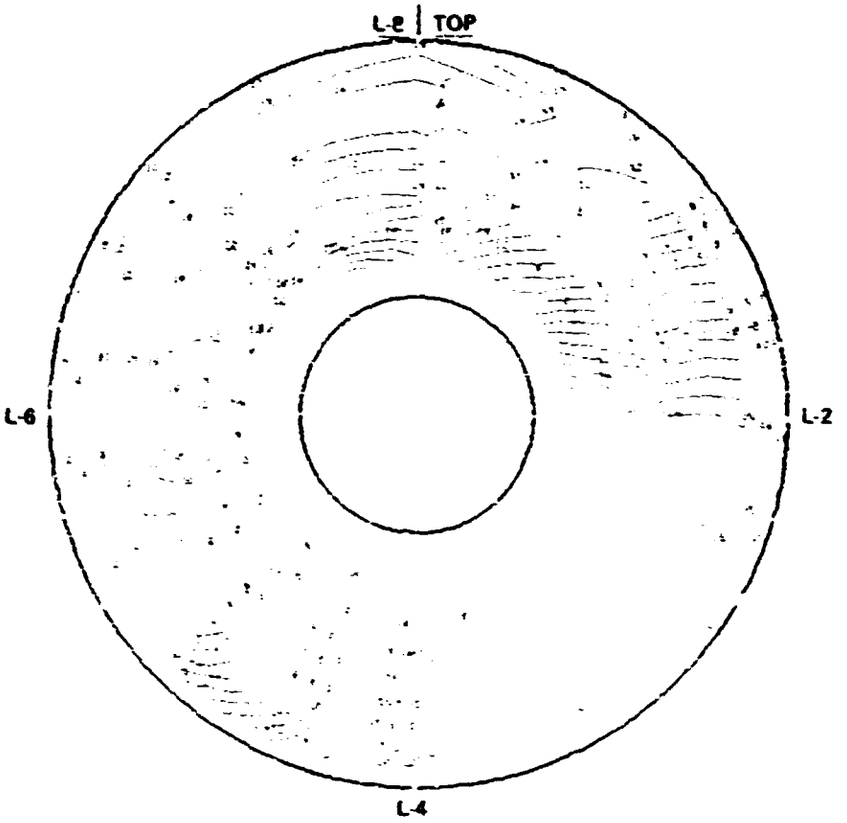

K_{a_2} = 1.6

K_{c_2} = 1.2

$\frac{\Delta P}{P}\left(\frac{MAX-MIN}{AVG}\right)$ = 49.7%

View of left inlet looking downstream

FIGURE 118 (Continued)
STABILITY AUDIT ANALYSIS PLOTS
Mach 0.80 α = 8.8 β = −0.5 ρ = 7.0
Δ_3 = 27.6 WAT2 = 104.2% Bypass = 0 ID Number = 15

Legend

Surge Pressure Ratio
- A - Highest available
- A to B - Reynolds number loss
- B to C - Engine to engine variation
- C to D - Distortion loss

Operating Pressure Ratio
- 1 - Installed match point
- 2 - Distortion rematch
- 3 - Augmentor anomaly

d) COMPARISON OF STALL AND NONSTALL STABILITY AUDIT FAN MAPS

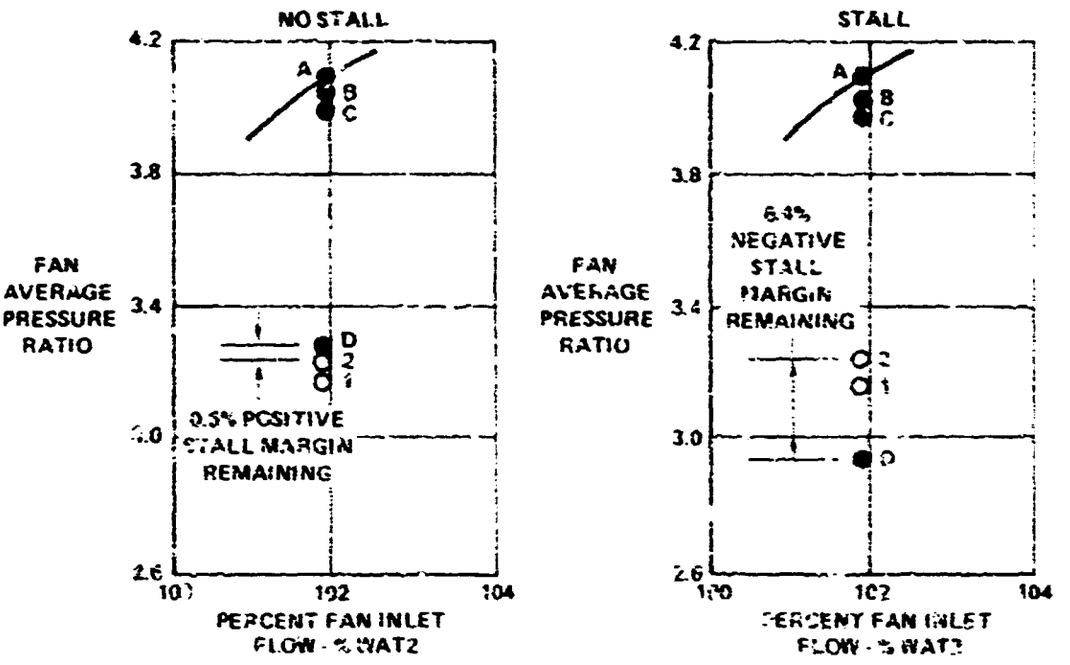

FIGURE 118 (Continued)

STABILITY AUDIT ANALYSIS PLOTS

Mach = 0.85 α = 8.9 β = -0.5 ρ = 7

Δ_3 = 27.6 WAT2 = 104.2% Bypass = 0.0 ID Number = 15

Legend

Surge Pressure Ratio
- A - Highest available
- A to B - Reynolds number loss
- B to C - Engine-to-engine variation
- C to D - Distortion loss

Operating Pressure Ratio
- 1 - Installed match point
- 2 - Distortion rematch
- 3 - Augmentor anomaly

e) FAN AND COMPRESSOR MAPS FOR THE STABILITY AUDIT

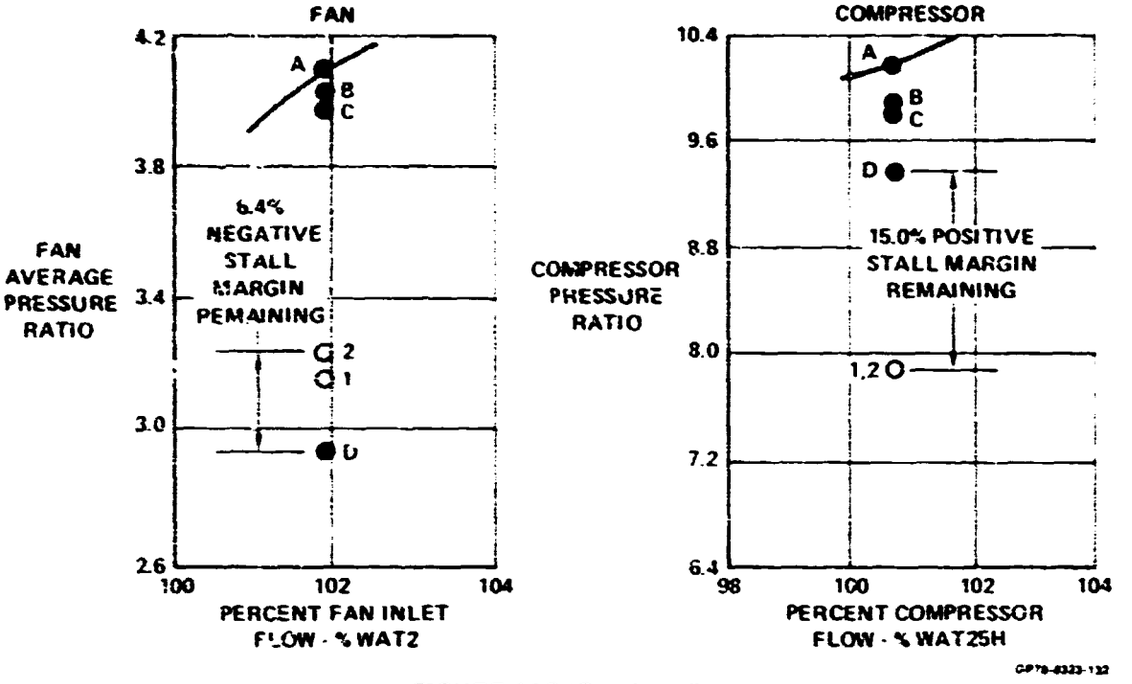

FIGURE 118 (Continued)
STABILITY AUDIT ANALYSIS PLOTS

Mach 0.85 α = 8.8 β = −0.5 ϕ = 27.6
Δ_3 = 27.6 WAT2 = 104.2% Bypass = 0.2 ID Number = 15

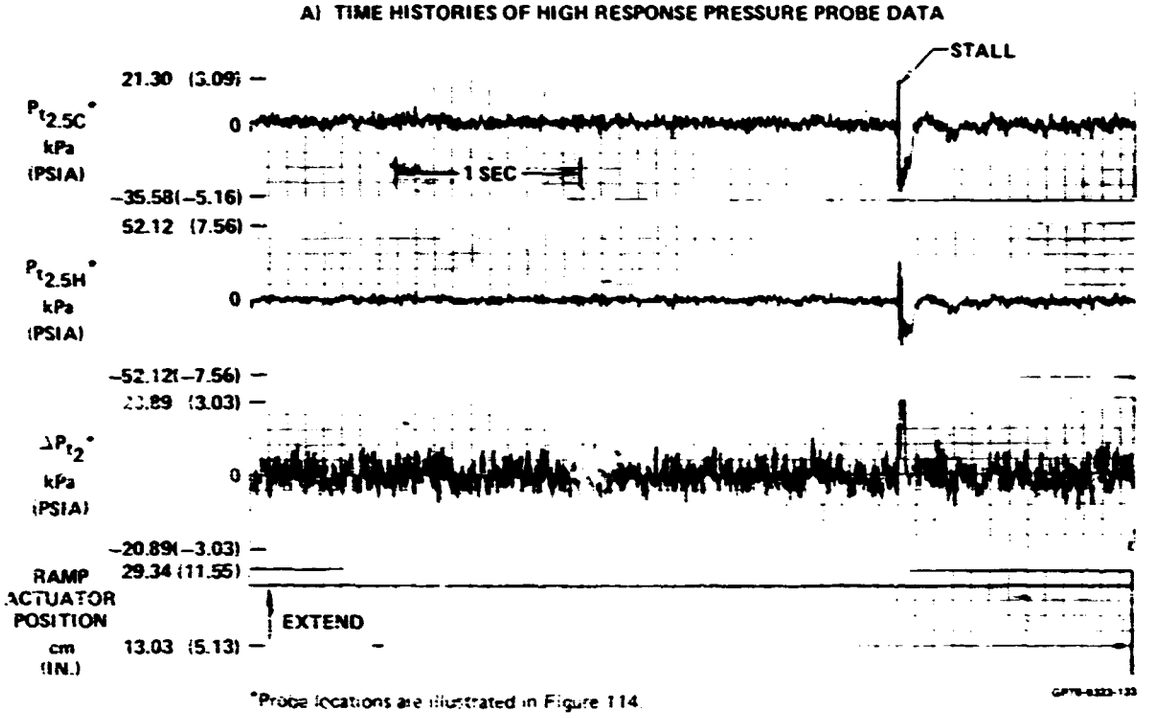

FIGURE 119
STABILITY AUDIT ANALYSIS PLOTS
Mach 1.21 α = 1.5 β = 0 ρ = 6.0
Δ_3 = 27.6 WAT2 = 98.3% Bypass = 0 I.D. Number = 34

B) SELECTION OF PEAK FAN DISTORTION

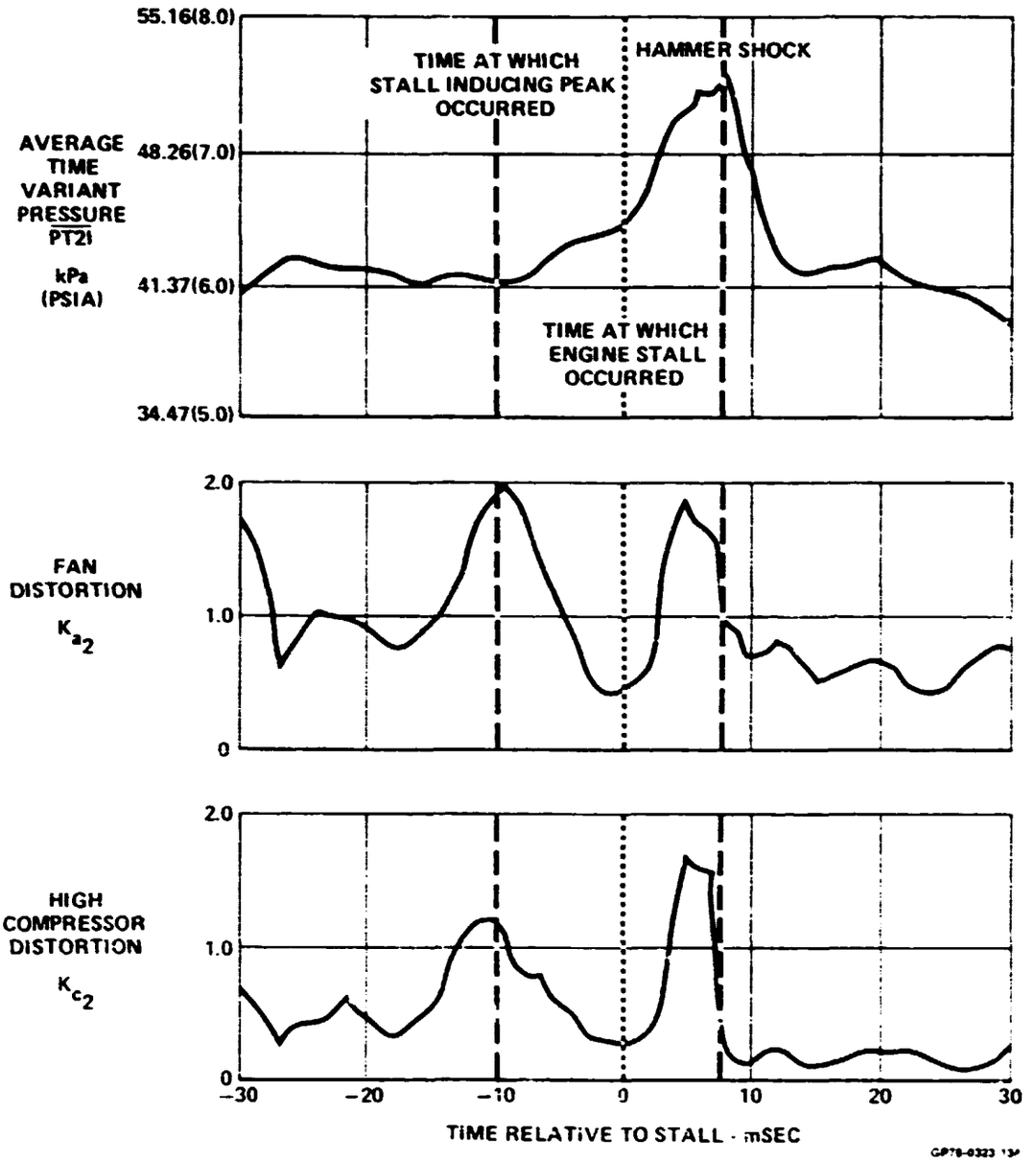

FIGURE 119 (Continued)
STABILITY AUDIT ANALYSIS PLOTS
Mach 1.21 α = 1.5 β = 0 ρ = 6.0
Δ_3 = 27.6 WAT2 = 98.3% Bypass = 0 I.D. Number = 34

STABILITY AUDITS

C) TOTAL PRESSURE CONTOUR AT PEAK FAN DISTORTION

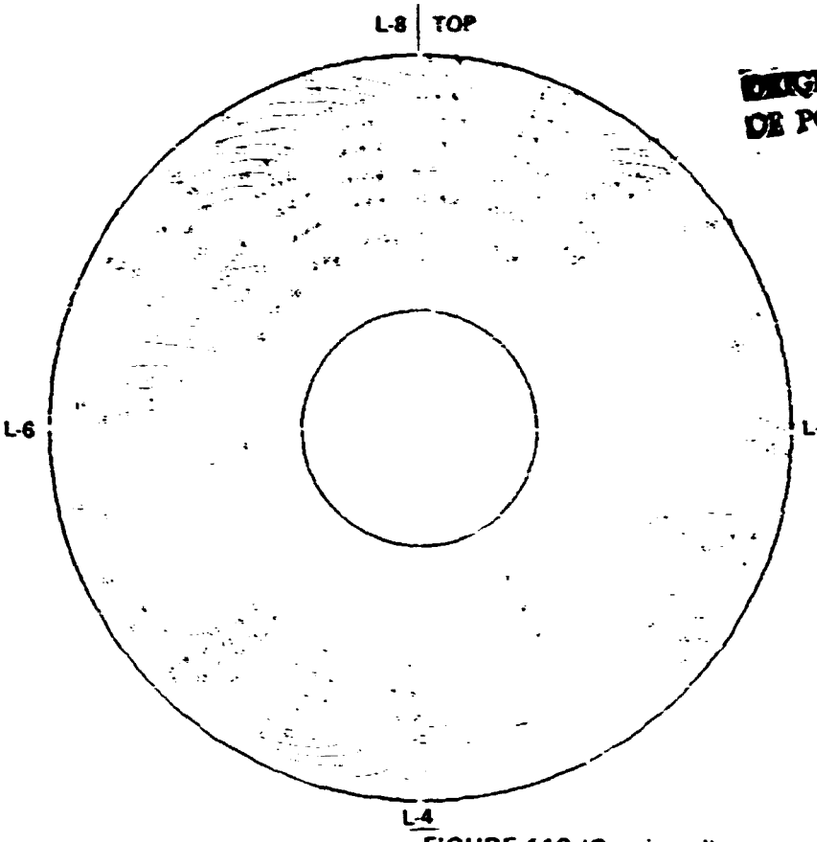

$K_{a_2} = 1.9$

$K_{C_2} = 1.1$

$\frac{\Delta P}{P}\left(\frac{MAX - MIN}{AVG}\right) = 53.4\%$

View of left inlet looking downstream

GP78-6323-135

FIGURE 119 (Continued)
STABILITY AUDIT ANALYSIS PLOTS
Mach 1.21 $\alpha = 1.5$ $\beta = 0$ $\rho = 6.0$
$\Delta_3 = 27.6$ WAT2 = 98.3% Bypass = 0 I.D. Number = 34

STABILITY AUDITS

Legend

Surge Pressure Ratio
- A - Highest available
- A to B - Reynolds number loss
- B to C - Engine-to-engine variation
- C to D - Distortion loss

Operating Pressure Ratio
- 1 - Installed match point
- 2 - Distortion rematch
- 3 - Augmentor anomaly

d) FAN AND COMPRESSOR MAPS FOR THE STABILITY AUDIT

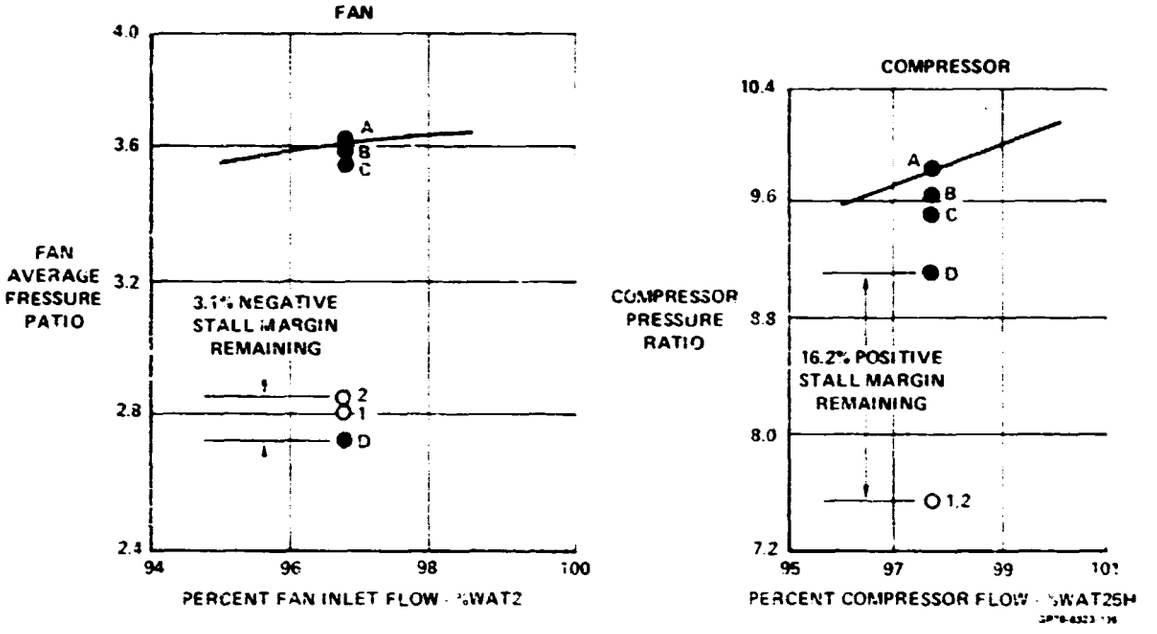

FIGURE 119 (Continued)
STABILITY AUDIT ANALYSIS PLOTS
Mac 1.21 α = 1.5 β = 0.0 ρ = 6.0
Δ_3 = 27.6 WAT2 = 98.3% Bypass = 0.0 I.D. Number = 34

STABILITY AUDITS

A) TIME HISTORIES OF HIGH RESPONSE PROBE DATA

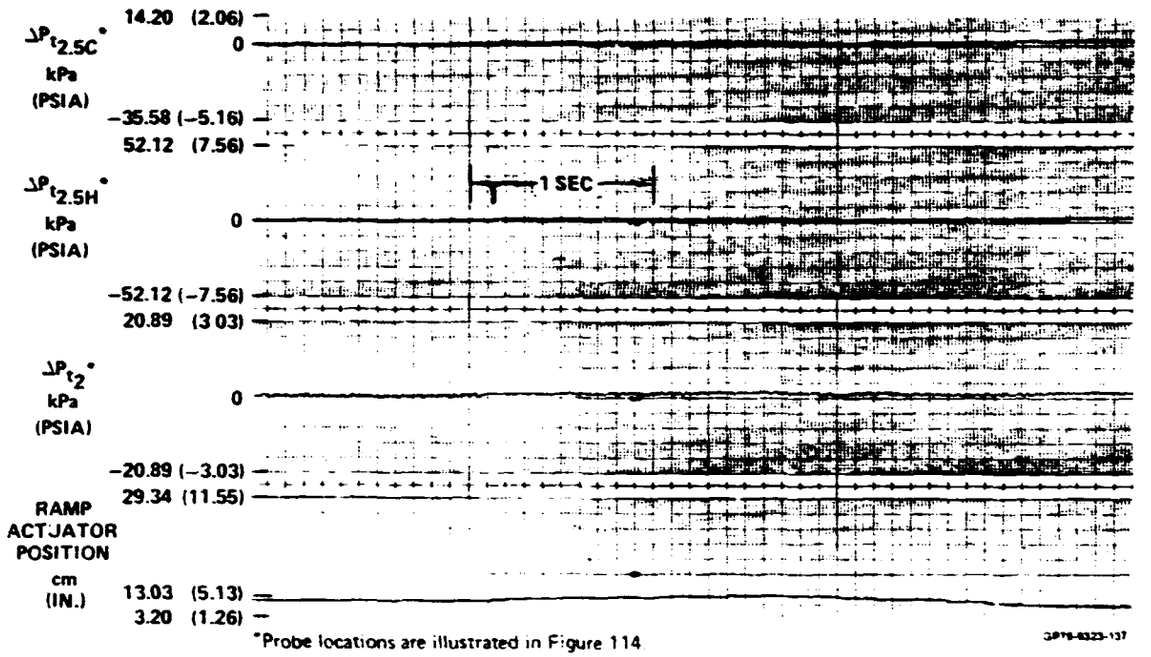

*Probe locations are illustrated in Figure 114

FIGURE 120
STABILITY AUDIT ANALYSIS PLOTS
Mach 1.57 α = -3.6 β = 0.7 ρ = −2.3
Δ_3 = 13.7 WAT2 = 89.3% Bypass = 0 I.D. Number = 44

STABILITY AUDITS

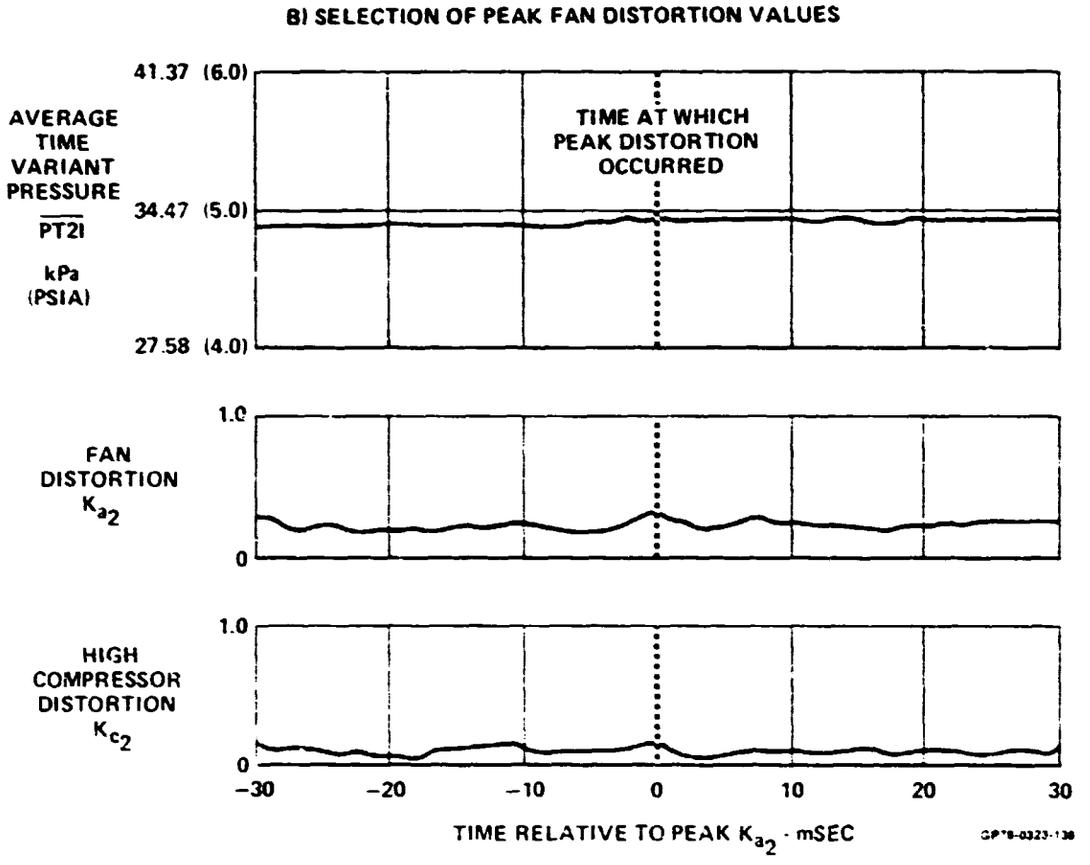

FIGURE 120 (Continued)
STABILITY AUDIT ANALYSIS PLOTS

Mach 1.57 α = −3.6 β = 0.7 ϕ = −2.3 Δ_3 = 13.7

WAT2 = 89.3% Bypass = 0 I.D. Number = 44

C) TOTAL PRESSURE CONTOUR AT PEAK FAN DISTORTION

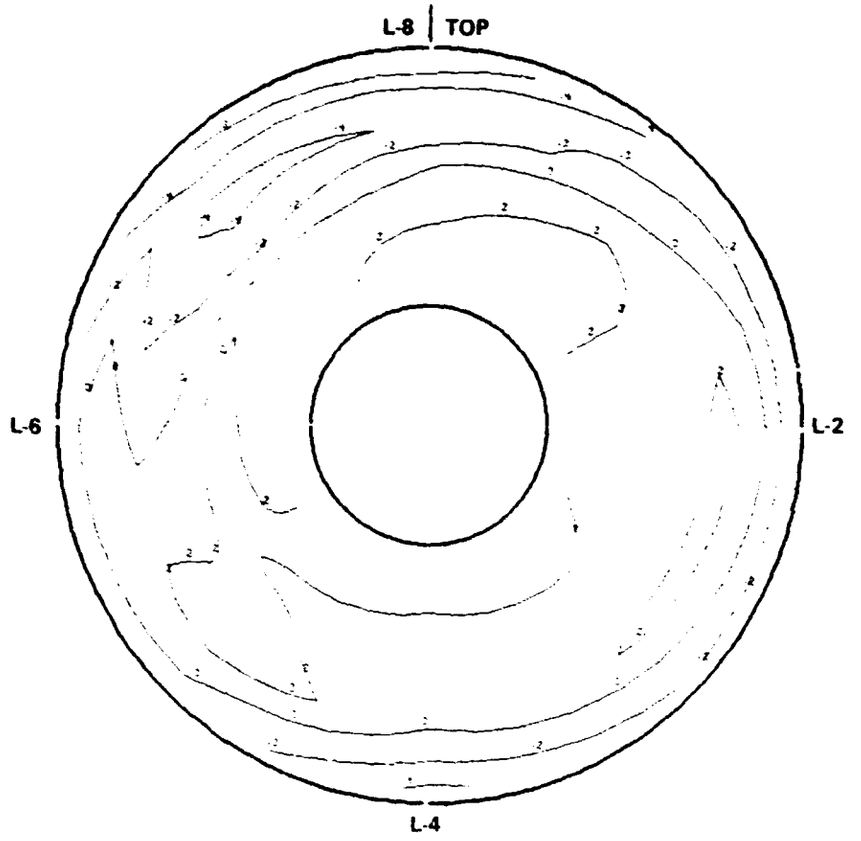

$K_{a_2} = 0.31$

$K_{c_2} = 0.11$

$\frac{\Delta P}{P}\left(\frac{MAX - MIN}{AVG}\right) = 11.4$

View of left inlet looking downstream

GP78-0323-139

FIGURE 120 (Continued)
STABILITY AUDIT ANALYSIS PLOTS

Mach 1.57 $\alpha = -3.6$ $\beta = 0.7$ $\rho = -2.3$

$\Delta_3 = 13.7$ WAT2 = 89.3% Bypass = 0 I.D. Number = 44

Legend

Surge Pressure Ratio
- A - Highest available
- A to B - Reynolds number loss
- B to C - Engine-to-engine variation
- C to D - Distortion loss

Operating Pressure Ratio
- 1 - Installed match point
- 2 - Distortion rematch
- 3 - Augmentor anomaly

d) FAN AND COMPRESSOR MAPS FOR THE STABILITY AUDIT

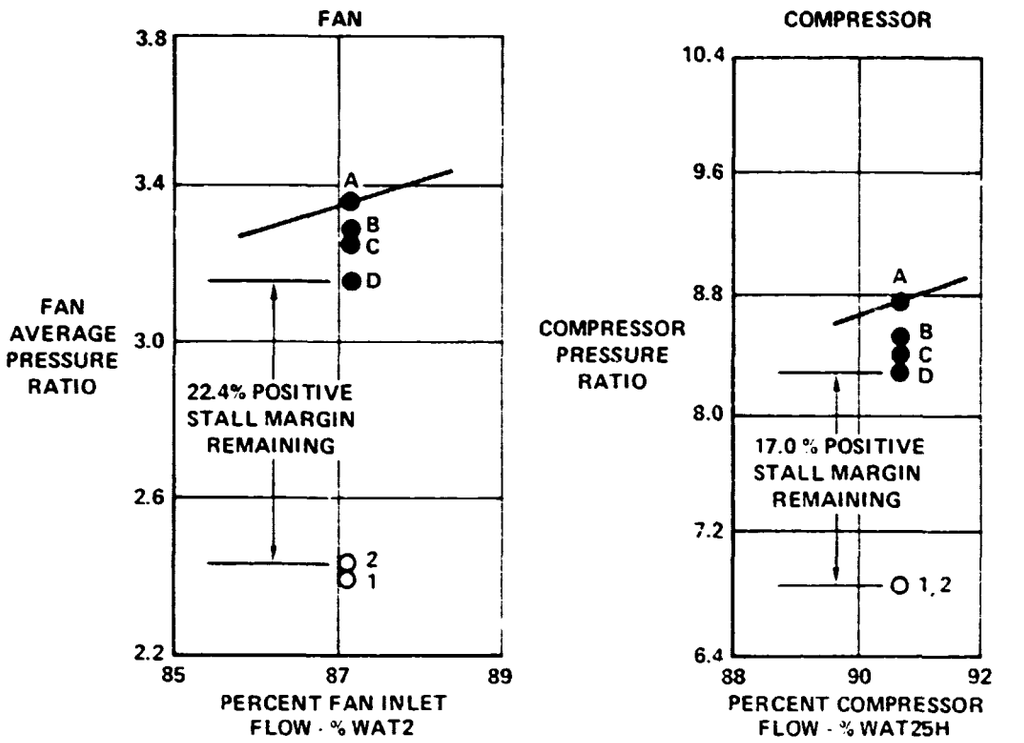

FIGURE 120 (Continued)
STABILITY AUDIT ANALYSIS PLOTS
Mach 1.57 α = —3.6 β = 0.7 ρ = 2.3
Δ_3 = 13.7 WAT2 = 89.3% Bypass = 0 I.D. Number = 44

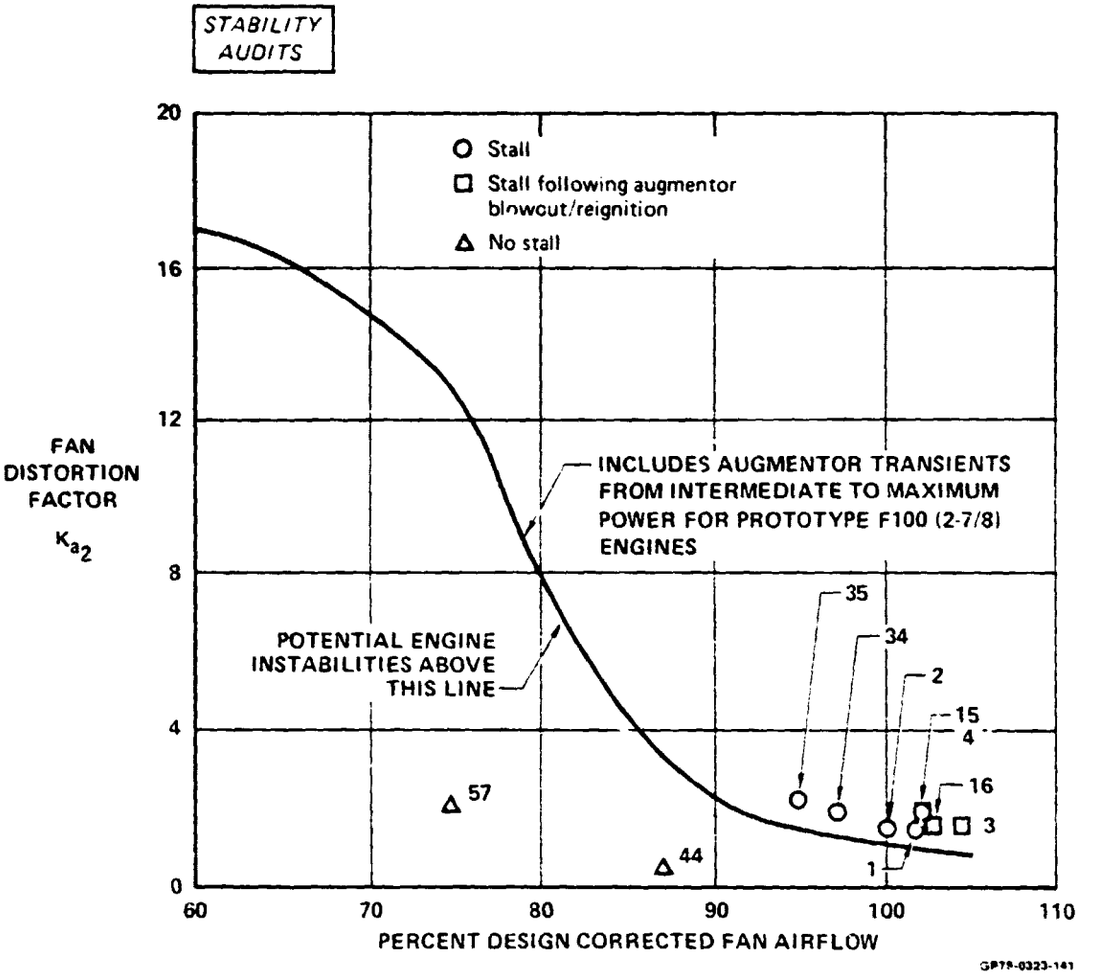

FIGURE 121
COMPARISON OF PEAK DISTORTION VALUES FOR THE AUDITED TEST CONDITIONS AND THE DISTORTION SCREENING CURVE

STABILITY AUDITS

DATA POINT I.D. NO.	FLIGHT	PEAK DISTORTION TIME - HMS**	ENGINE STALL TIME - HMS**	DATA RECORD ELAPSED TIME TO STALL - SEC
1*	422-4	21:12:23.27822	21:12:23.28711	0.63011
2	417-5	17:20:38.78133	17:20:38.81244	0.58344
3	417-4	17:18:28.11367	17:18:28.13700	0.59900
4*	417-2	17:10:21.73233	17:10:21.74567	0.58567
15	417-3	17:14:28.95178	17:14:28.96400	0.61900
16*	417-1	17:04:34.62633	17:04:34.63856	0.60456
34	423-4	21:12:32.31411	21:12:32.32522	0.53122
35*	423-3	21:07:57.09078	21:07:57.10633	0.51233
44	414-2	20:16:47.21722	NO STALL	–
57*	425-2	05:11:14.30756	NO STALL	–

GP78-0323-142

*Stability audits are in Appendix K

**HMS - Hours, Minutes, Seconds

FIGURE 122
EVENTS TIME HISTORY OF STABILITY AUDIT TEST CONDITIONS

APPENDIX A

COMPARISONS OF DIGITIZED AND ANALOG DISTORTION DATA

Presented herein are the comparisons of time history fan distortion values computed by the Analog Distortion Calculator and by the Digital Process of Volume I, Figure 10. A list of illustrations is provided below.

LIST OF ILLUSTRATIONS

LIST OF ILLUSTRATIONS (Continued)

C-2

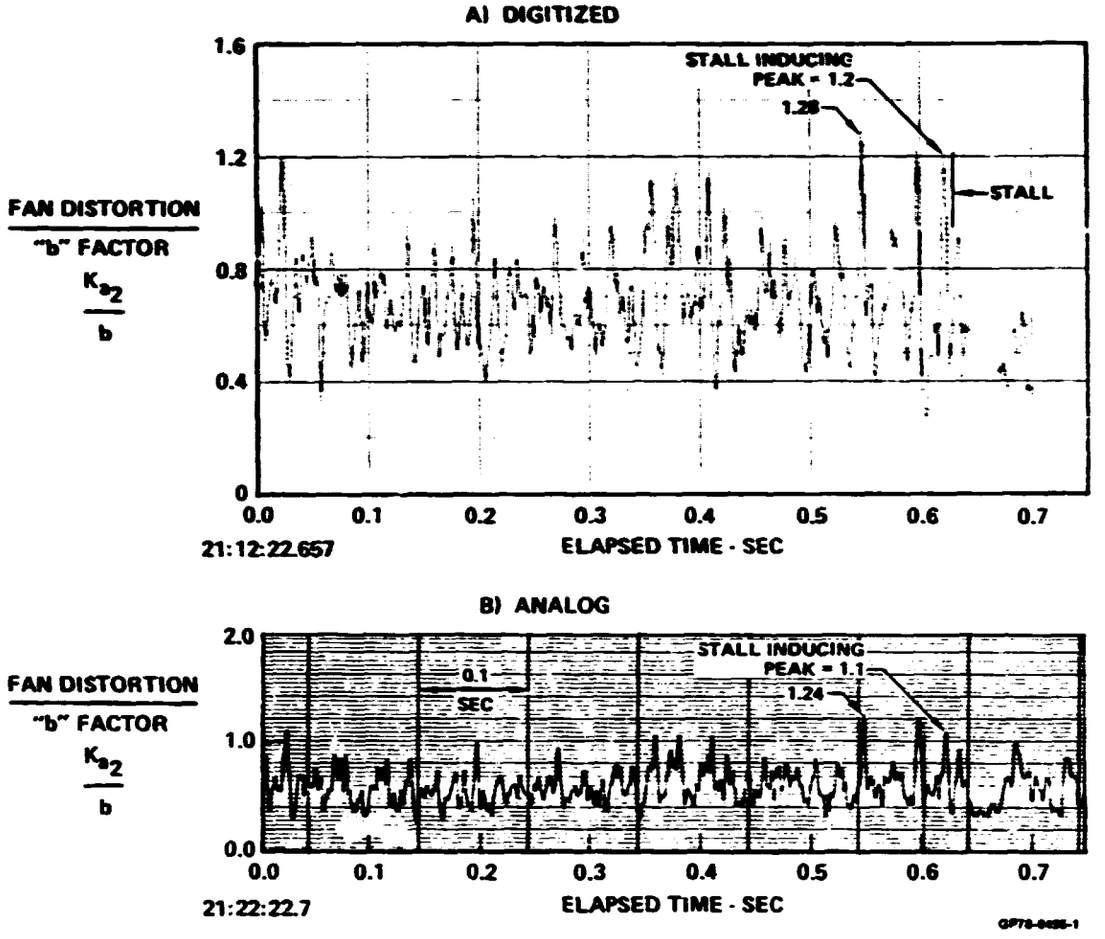

FIGURE A-1
COMPARISONS OF DIGITIZED AND ANALOG DISTORTION DATA
$M_O = 0.4$ $\alpha = 16.4$ $\beta = -0.8$ $\rho = 6.9$
$\Delta_3 = 27.6$ WAT2 = 104.1% Bypass = 0.0
I.D. Number = 1 fc/o = 170

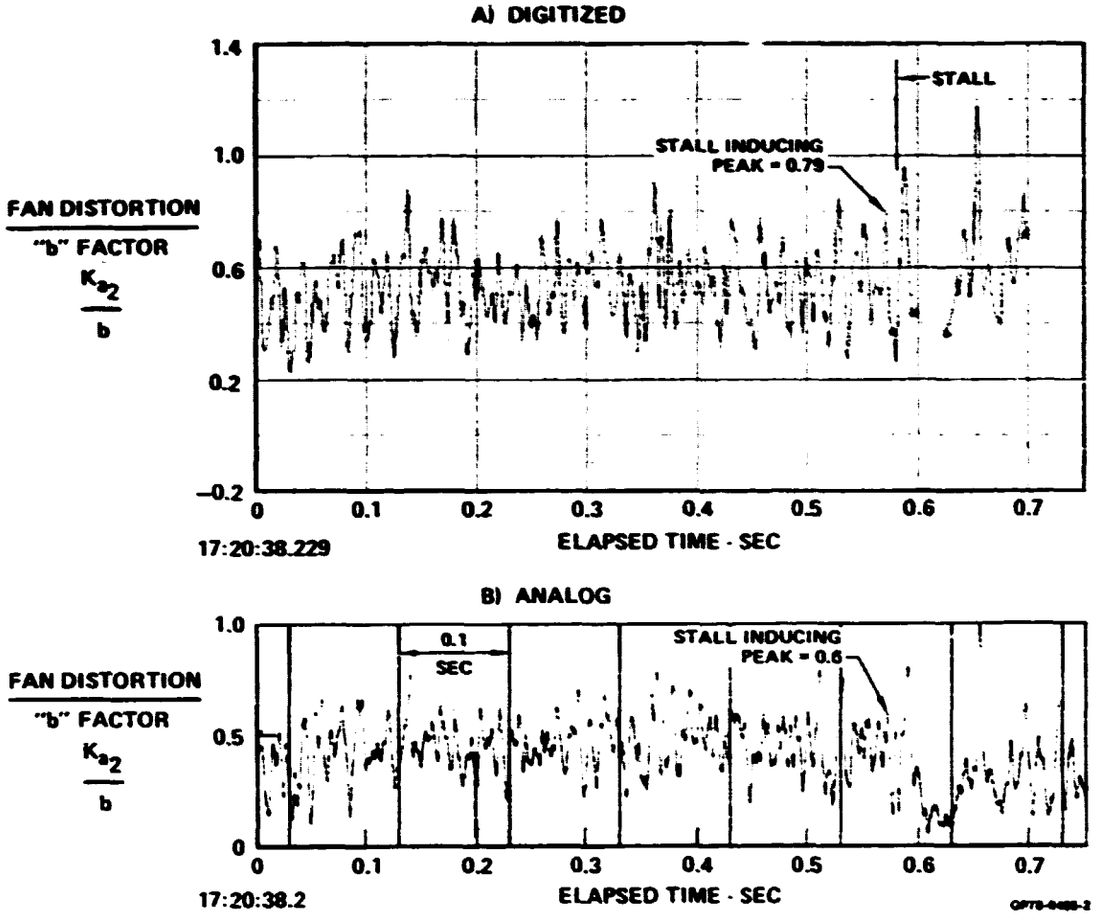

FIGURE A-2
COMPARISONS OF DIGITIZED AND ANALOG DISTORTION DATA
$M_o = 0.59$ $\alpha = 13.9$ $\beta = 0.9$ $\rho = 7.0$
$\Delta_3 = 26.6$ WAT2 = 102.7% Bypass = 0.0
I.D. Number = 2 fc/o = 170

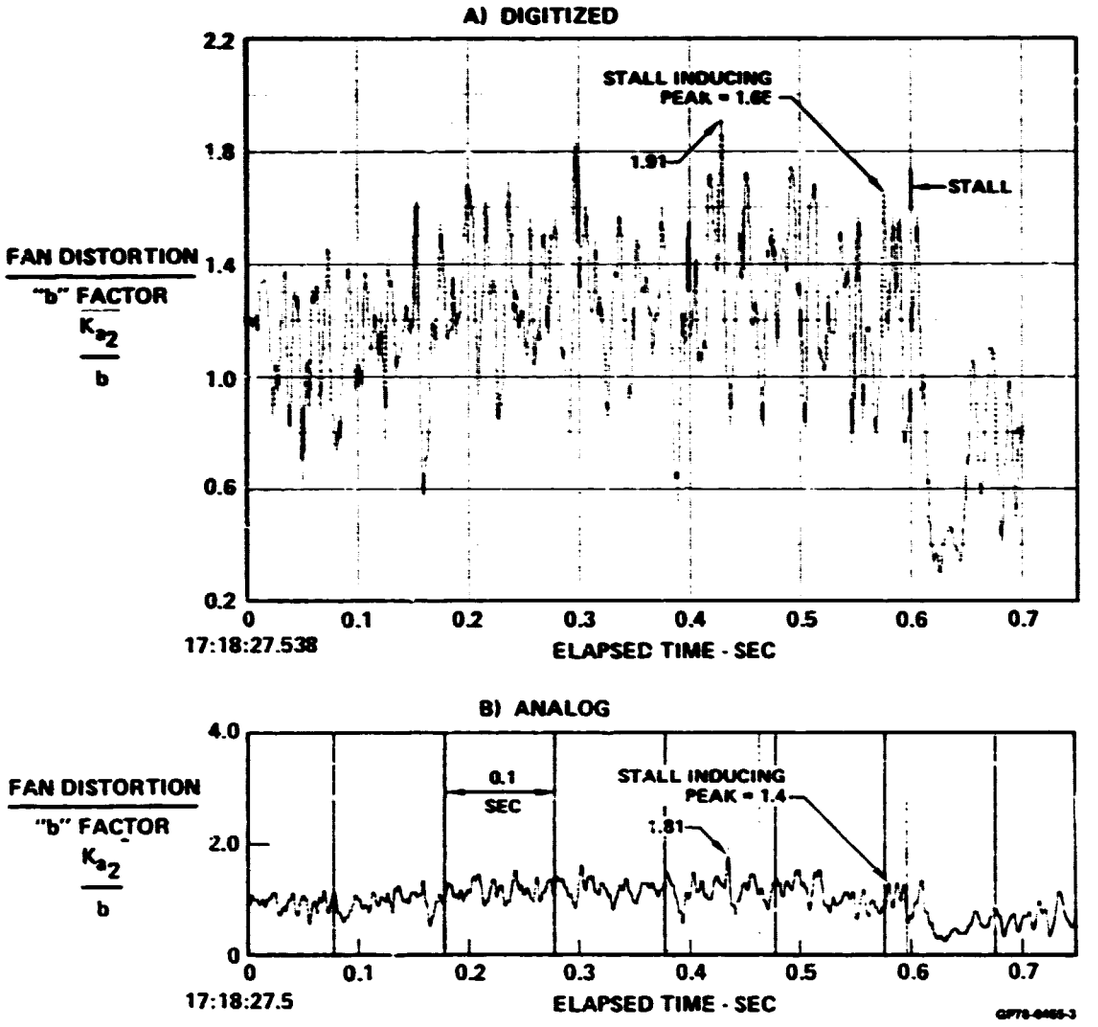

FIGURE A-3
COMPARISONS OF DIGITIZED AND ANALOG DISTORTION DATA
$M_0 = 0.52$ $\alpha = 10.0$ $\beta = 0.7$ $\rho = 7.0$
$\Delta_3 = 27.6$ WAT2 = 107.1% Bypass = 0.0
I.D. Number = 3 fc/o = 170

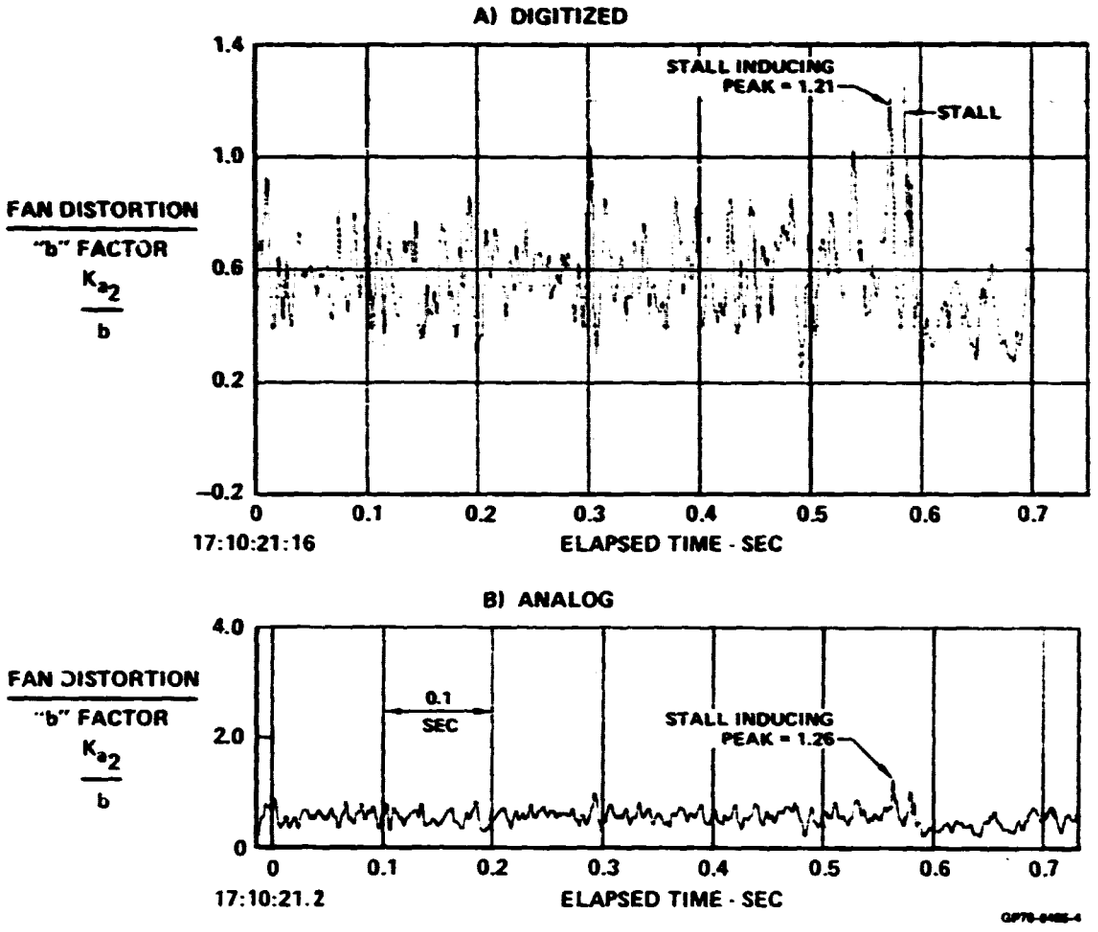

FIGURE A-4
COMPARISONS OF DIGITIZED AND ANALOG DISTORTION DATA
$M_c = 0.69$ $\alpha = 11.5$ $\beta = 1.0$ $\rho = 7.0$
$\Delta_3 = 26.5$ WAT2 = 104.2% Bypass = 0.0
I.D. Number = 4 fc/o = 170

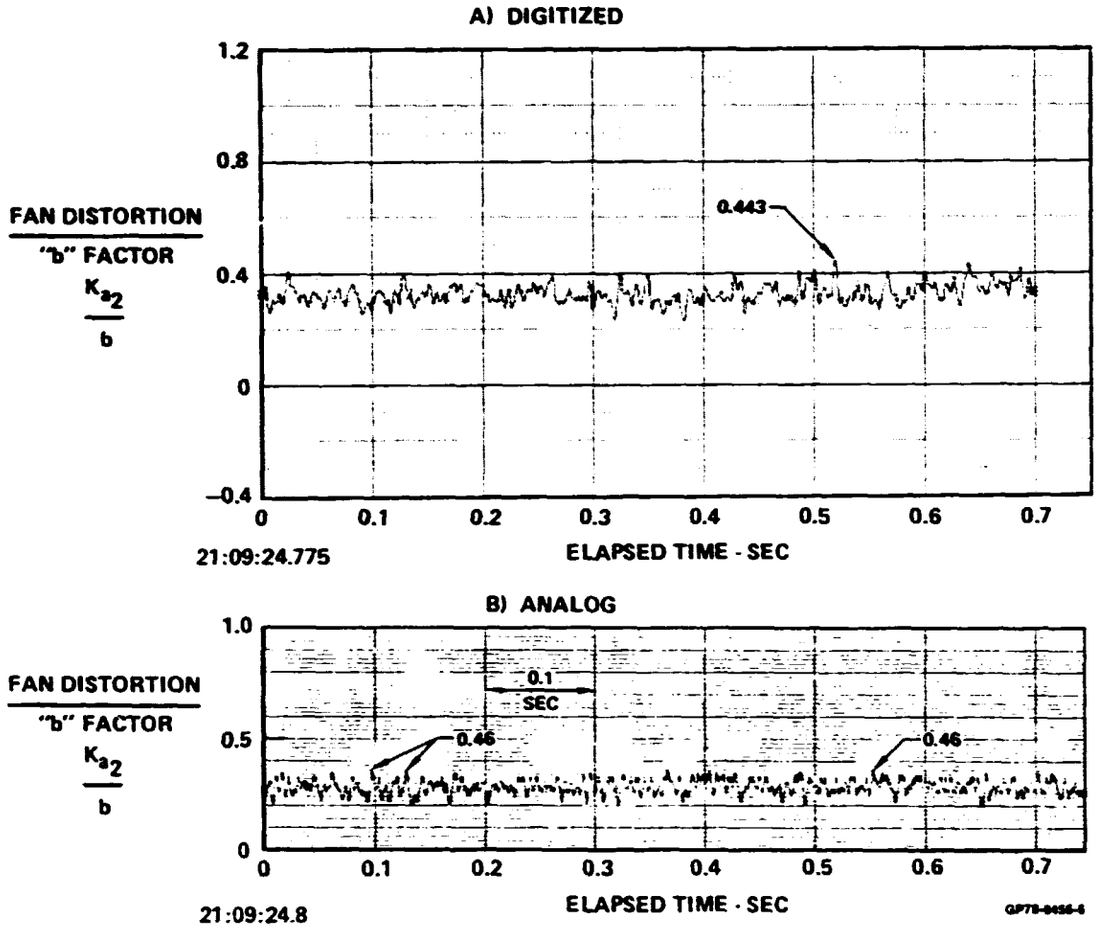

FIGURE A-5
COMPARISONS OF DIGITIZED AND ANALOG DISTORTION DATA
$M_0 = 0.69$ $\alpha = -8.4$ $\beta = 10.6$ $\rho = 0.6$
$\Delta_3 = 10.5$ WAT2 = 101.2% Bypass = 0.0
I.D. Number = 7 fc/o = 170

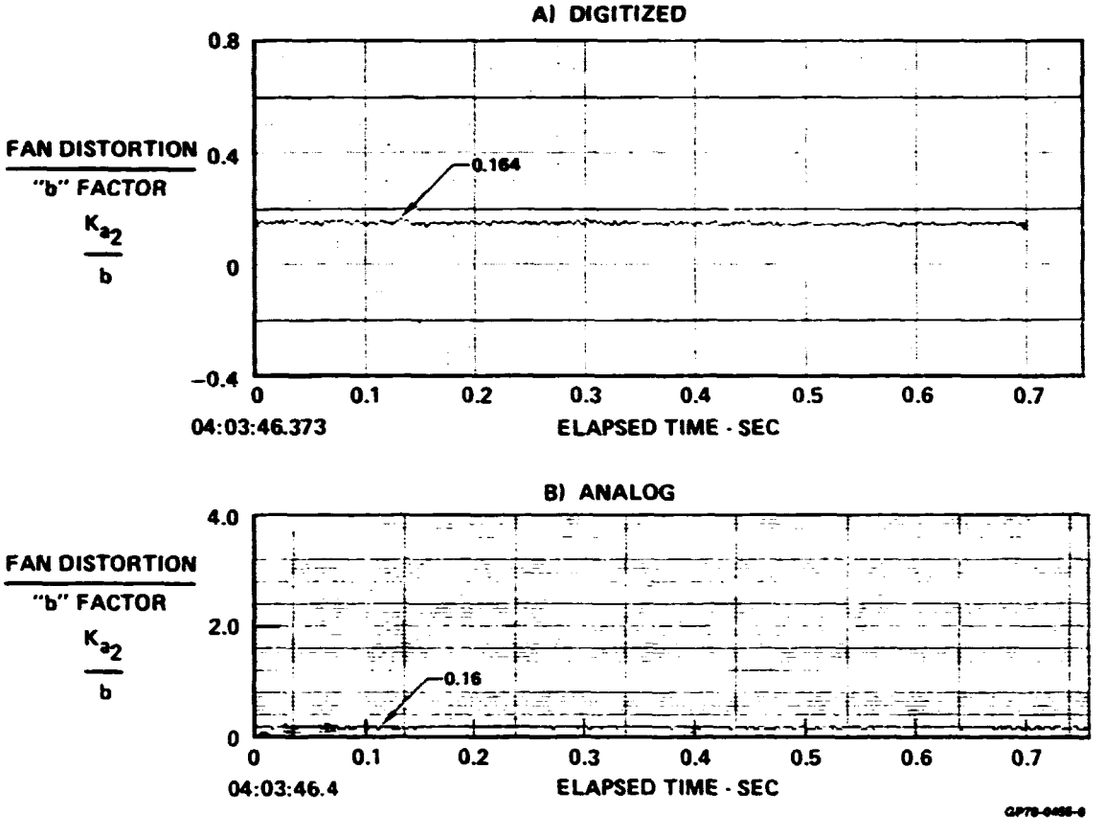

FIGURE A-6
COMPARISONS OF DIGITIZED AND ANALOG DISTORTION DATA
$M_O = 0.67$ $\alpha = 4.3$ $\beta = 0.7$ $\rho = 6.9$
$\Delta_3 = 11.1$ WAT2 = 94.4% Bypass = 0.0
I.D. Number = 11 fc/o = 170

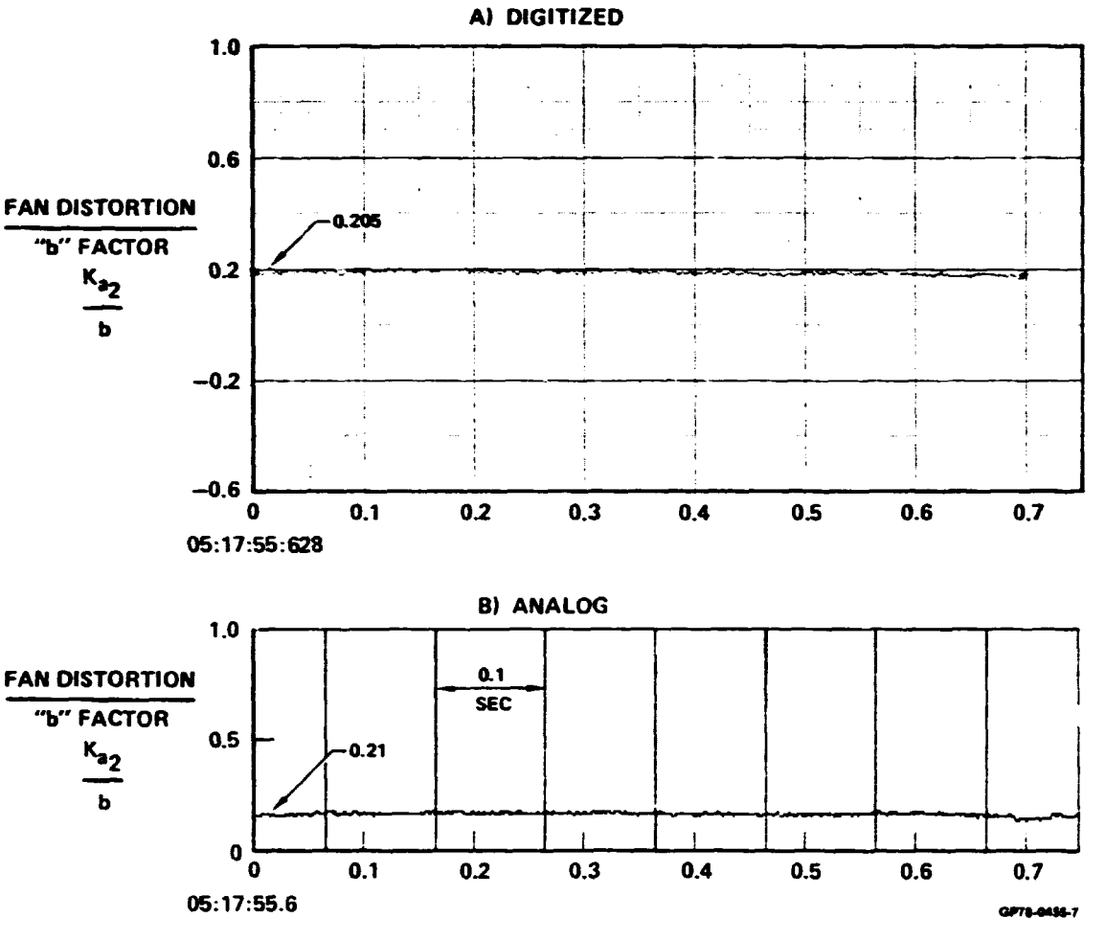

FIGURE A-7
COMPARISONS OF DIGITIZED AND ANALOG DISTORTION DATA
$M_0 = 0.69$ $\alpha = 3.4$ $\beta = 0.7$ $\rho = 6.9$
$\Delta_3 = 11.1$ WAT2 = 74.1% Bypass = 0.0
I.D. Number = 12 fc/o = 170

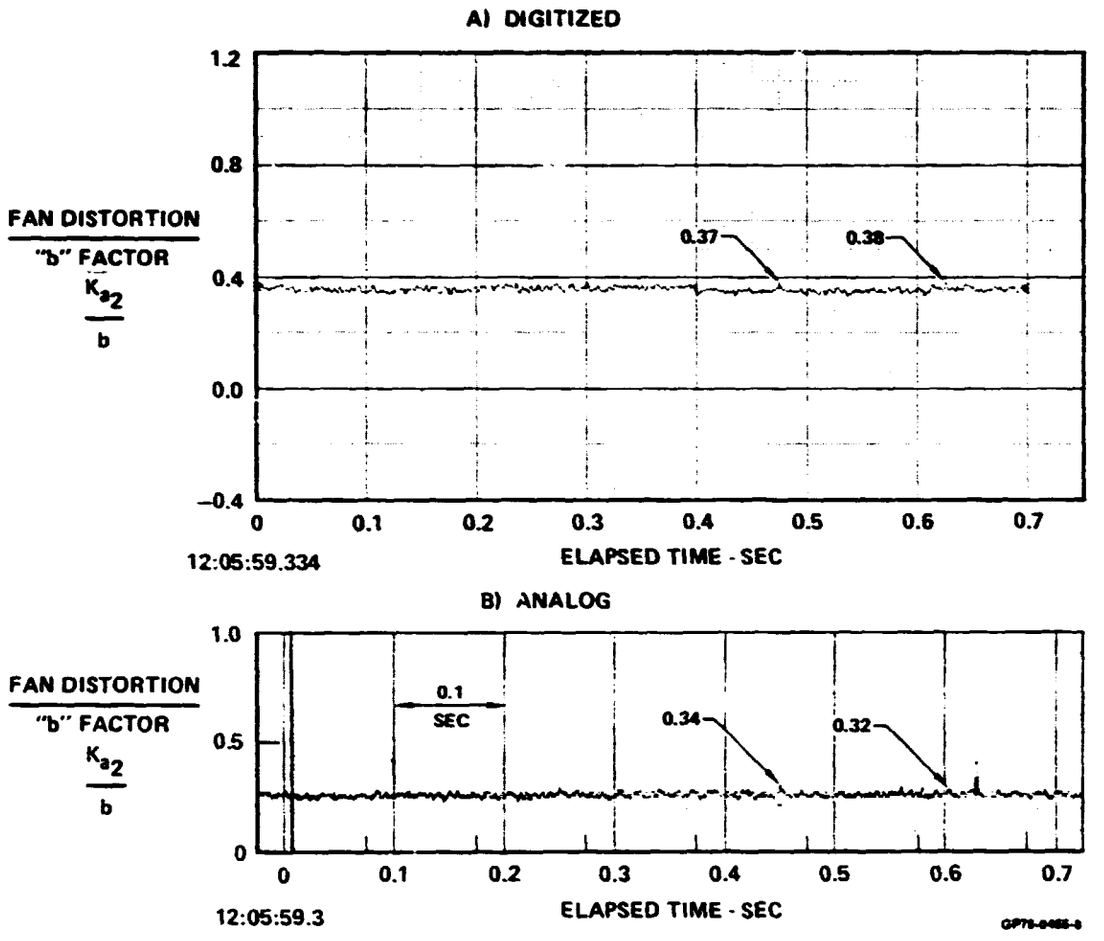

FIGURE A-8
COMPARISONS OF DIGITIZED AND ANALOG DISTORTION DATA
$M_O = 0.59$ $\alpha = 4.6$ $\beta = 1.2$ $\rho = 7.0$
$\Delta_3 = 11.1$ WAT2 = 107.9% Bypass = 0.0
I.D. Number = 13 fc/o = 170

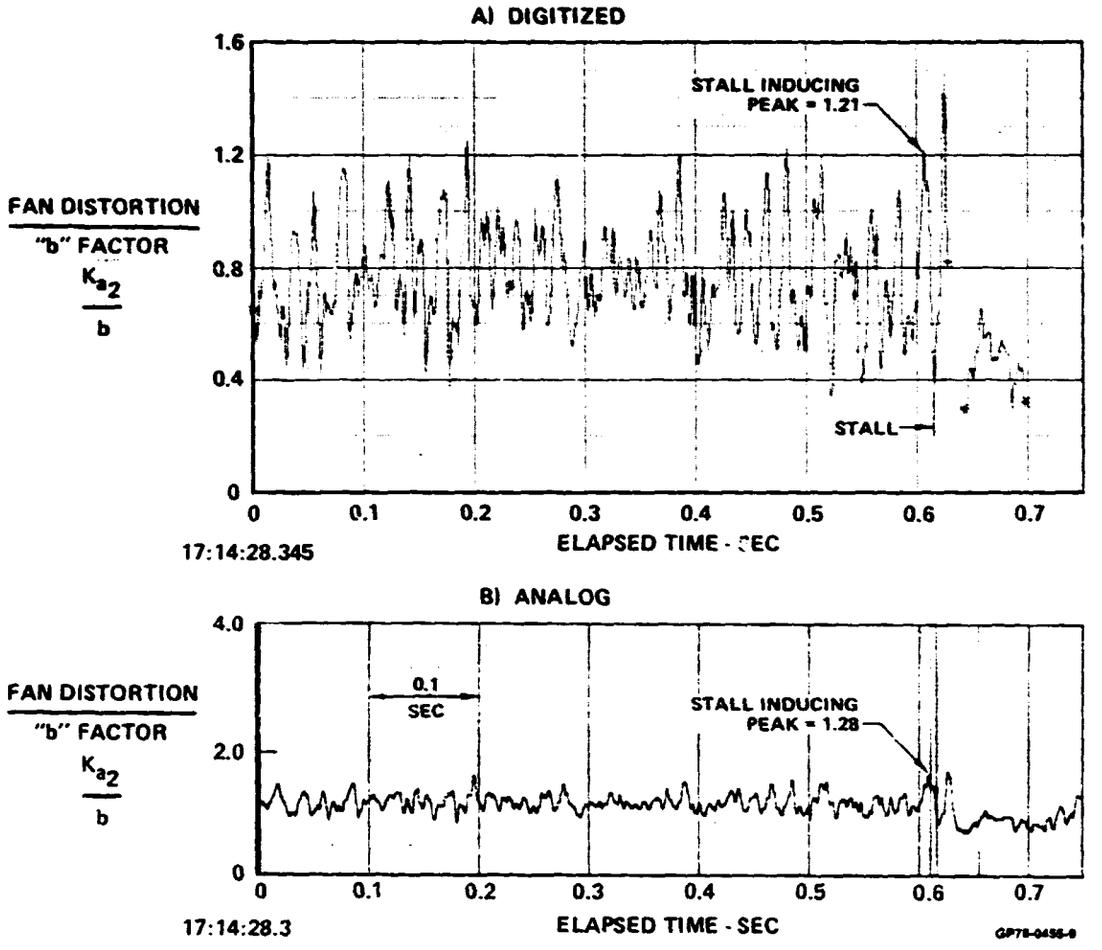

FIGURE A-9
COMPARISONS OF DIGITIZED AND ANALOG DISTORTION DATA
$M_0 = 0.85$ $\alpha = 8.8$ $\beta = -0.5$ $\rho = 7.0$
$\Delta_3 = 27.6$ WAT2 = 104.2% Bypass = 0.0
I.D. Number = 15 fc/o = 170

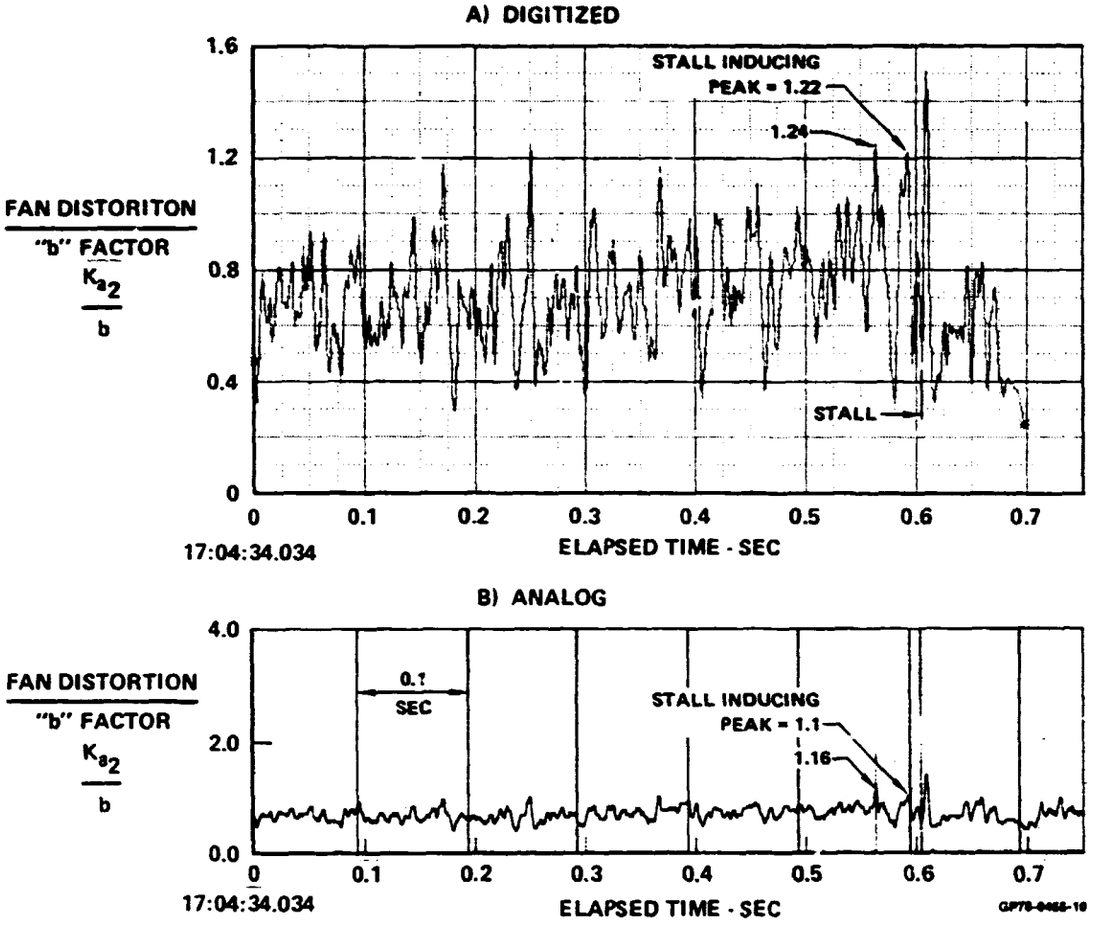

FIGURE A-10
COMPARISONS OF DIGITIZED AND ANALOG DISTORTION DATA
$M_0 = 0.92$ $\alpha = 5.6$ $\beta = 0.6$ $\rho = 7.0$
$\Delta_3 = 26.6$ WAT2 = 104.5% Bypass = 0.0
I.D. Number = 16 fc/o = 170

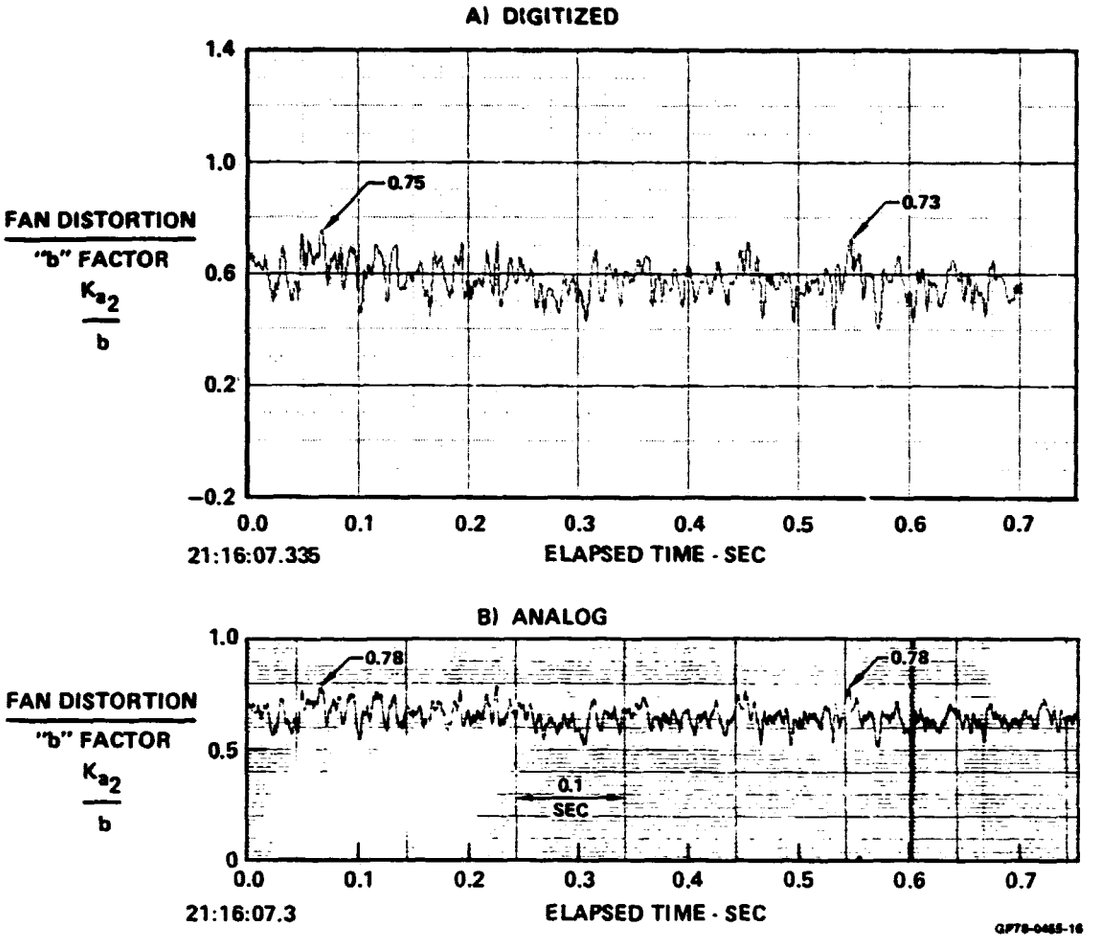

FIGURE A-11
COMPARISONS OF DIGITIZED AND ANALOG DISTORTION DATA
$M_o = 0.94$ $\alpha = -8.9$ $\beta = 10.2$ $\rho = 1.0$
$\Delta_3 = 10.5$ WAT2 = 107.1% Bypass = 0.0
I.D. Number = 19 fc/o = 170

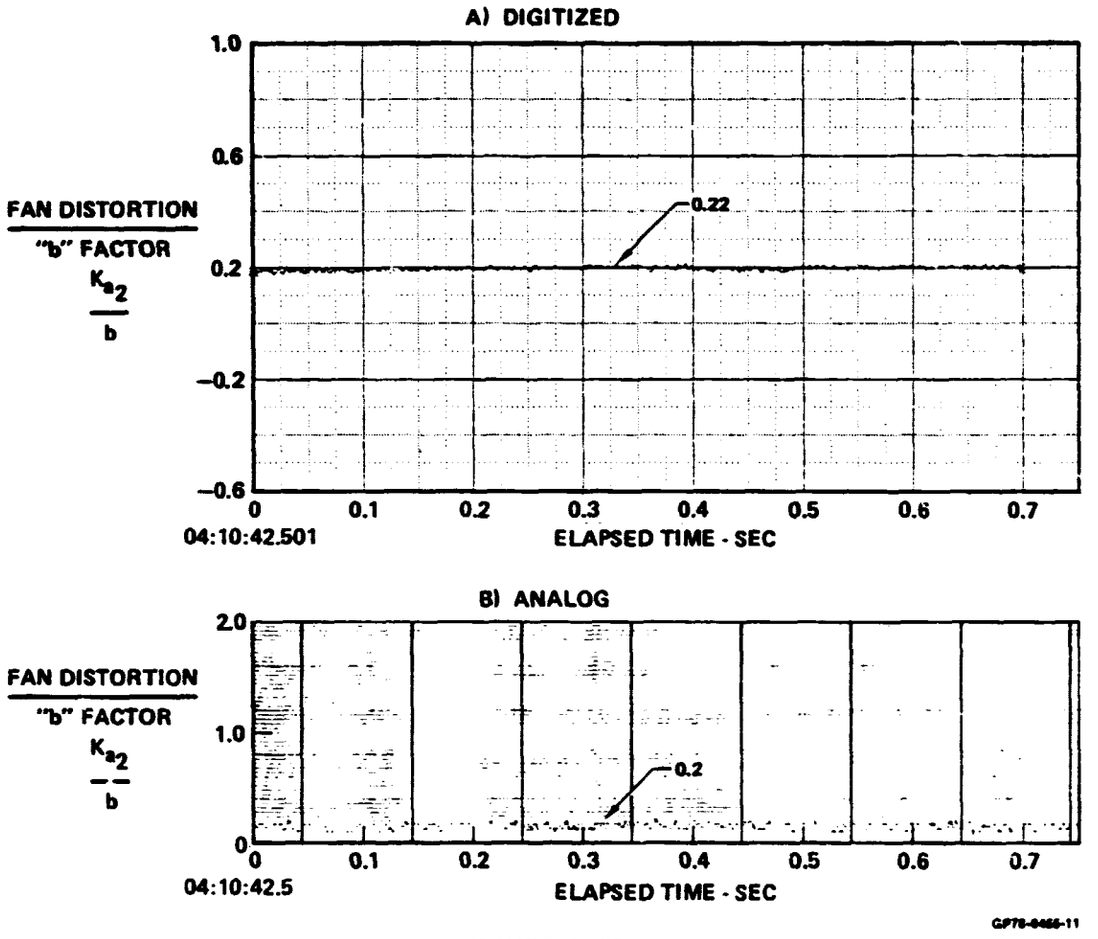

FIGURE A-12
COMPARISONS OF DIGITIZED AND ANALOG DISTORTION DATA
$M_0 = 0.90$ $\alpha = -2.8$ $\beta = -0.2$ $\rho = -1.2$
$\Delta_3 = 8.7$ WAT2 = 97.5% Bypass = 0.0
I.D. Number = 21 fc/o = 170

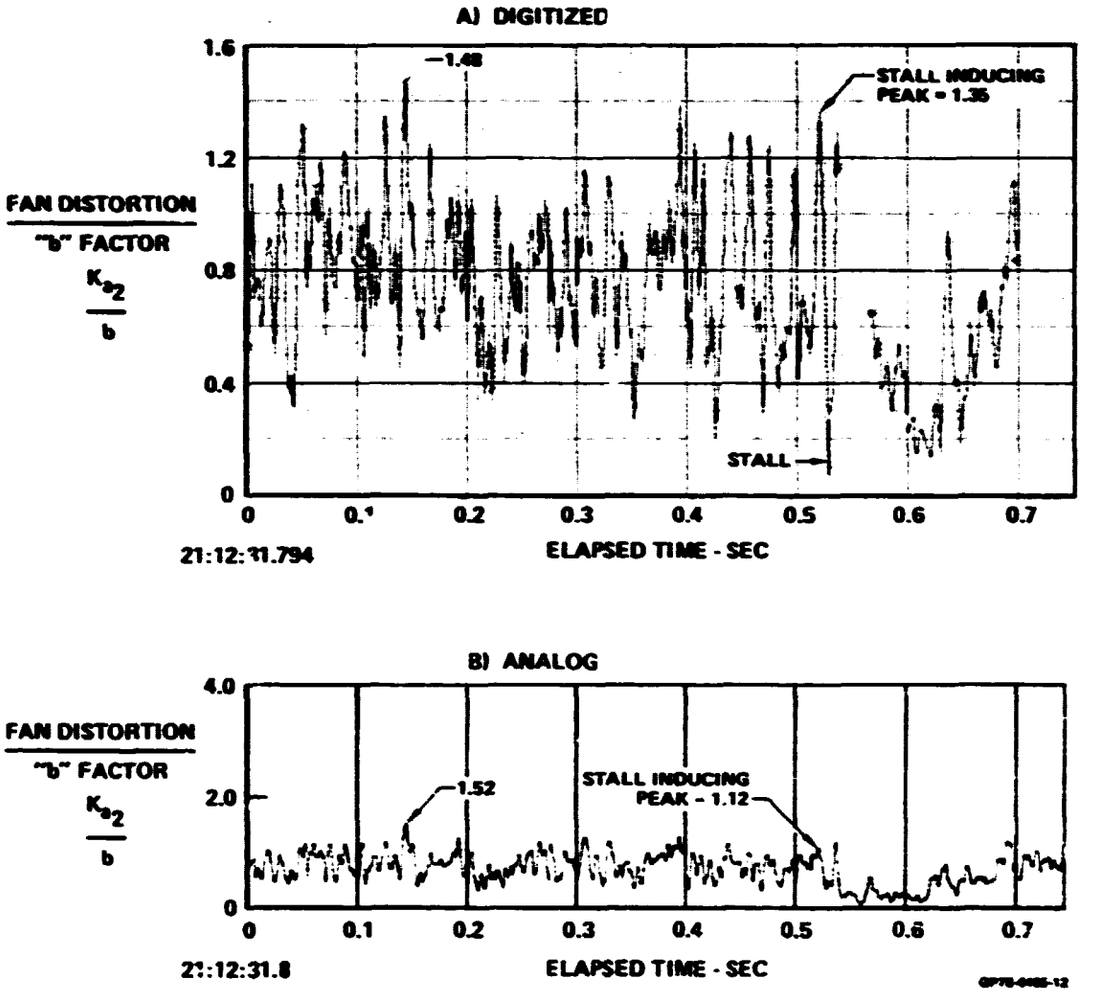

FIGURE A-13
COMPARISONS OF DIGITIZED AND ANALOG DISTORTION DATA
$M_0 = 1.21$ $\alpha = 1.5$ $\beta = 0.0$ $\rho = 6.0$
$\Delta_3 = 27.6$ WAT2 = 98.3% Bypass = 0.0
I.D. Number = 34 fc/o = 170

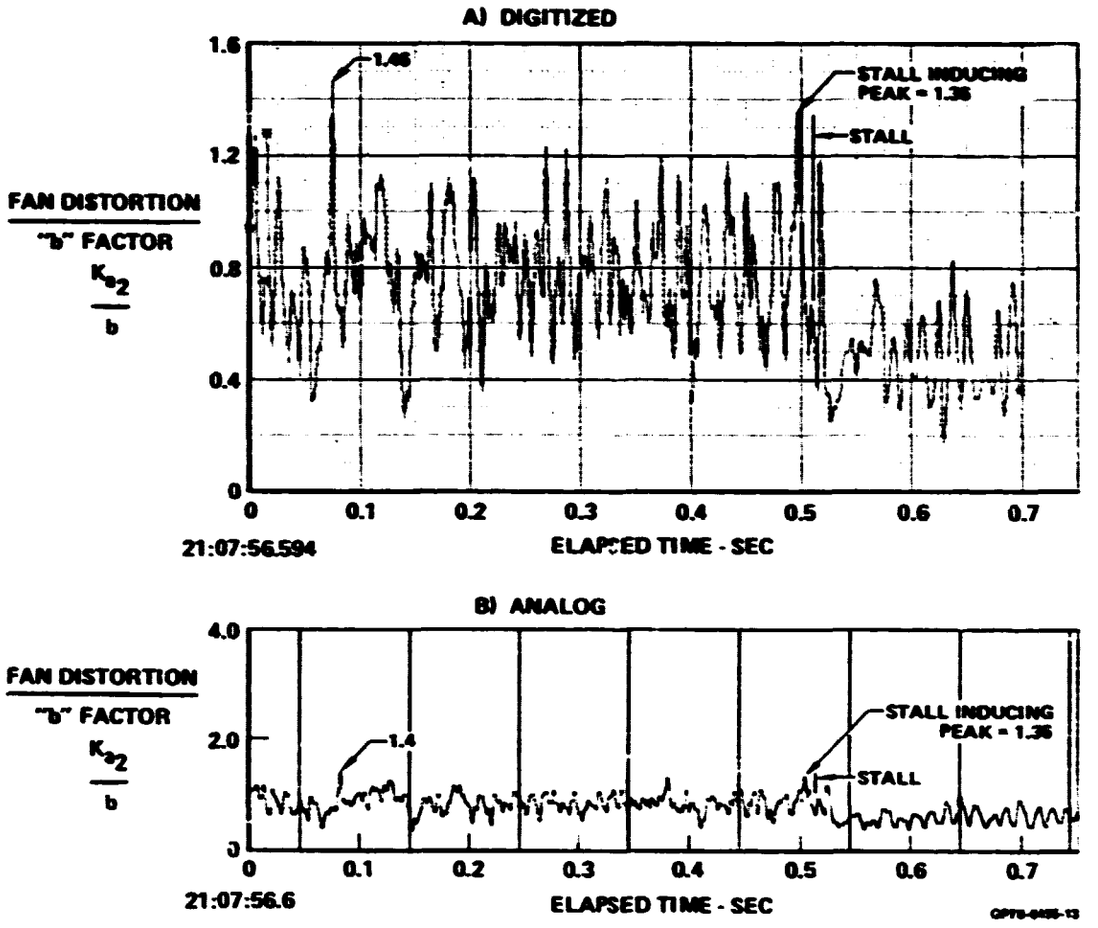

FIGURE A-14
COMPARISONS OF DIGITIZED AND ANALOG DISTORTION DATA
$M_o = 1.24$ $\alpha = 3.0$ $\beta = 0.8$ $\rho = 6.7$
$\Delta_3 = 27.6$ WAT= 96.4% Bypass = 0.0
I.D. Number = 35 $f_r/o = 170$

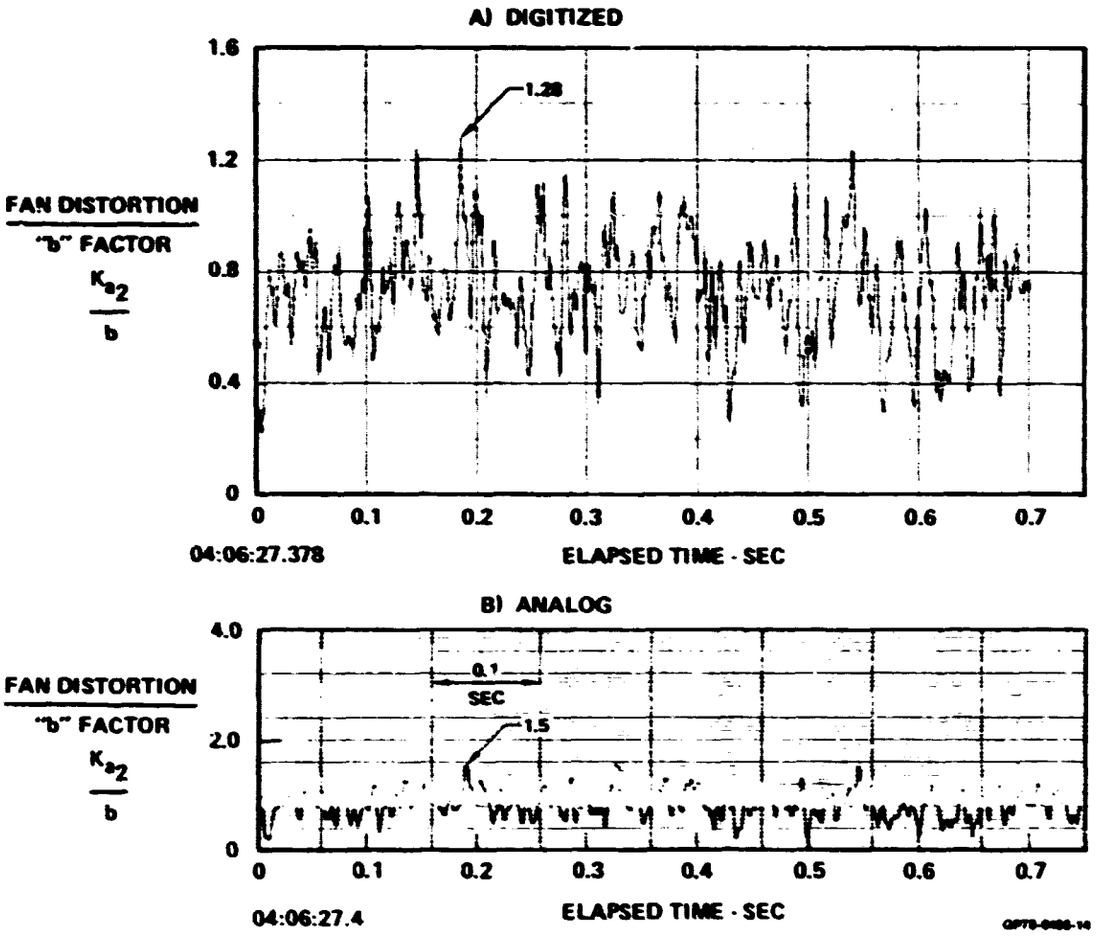

FIGURE A-15
COMPARISONS OF DIGITIZED AND ANALOG DISTORTION DATA
$M_0 = 1.54$ $\alpha = 1.5$ $\beta = 0.0$ $\rho = -1.4$
$\Delta_3 = 27.0$ WAT2 = 95.4% Bypass = 0.0
I.D. Number = 41 fc/o = 170

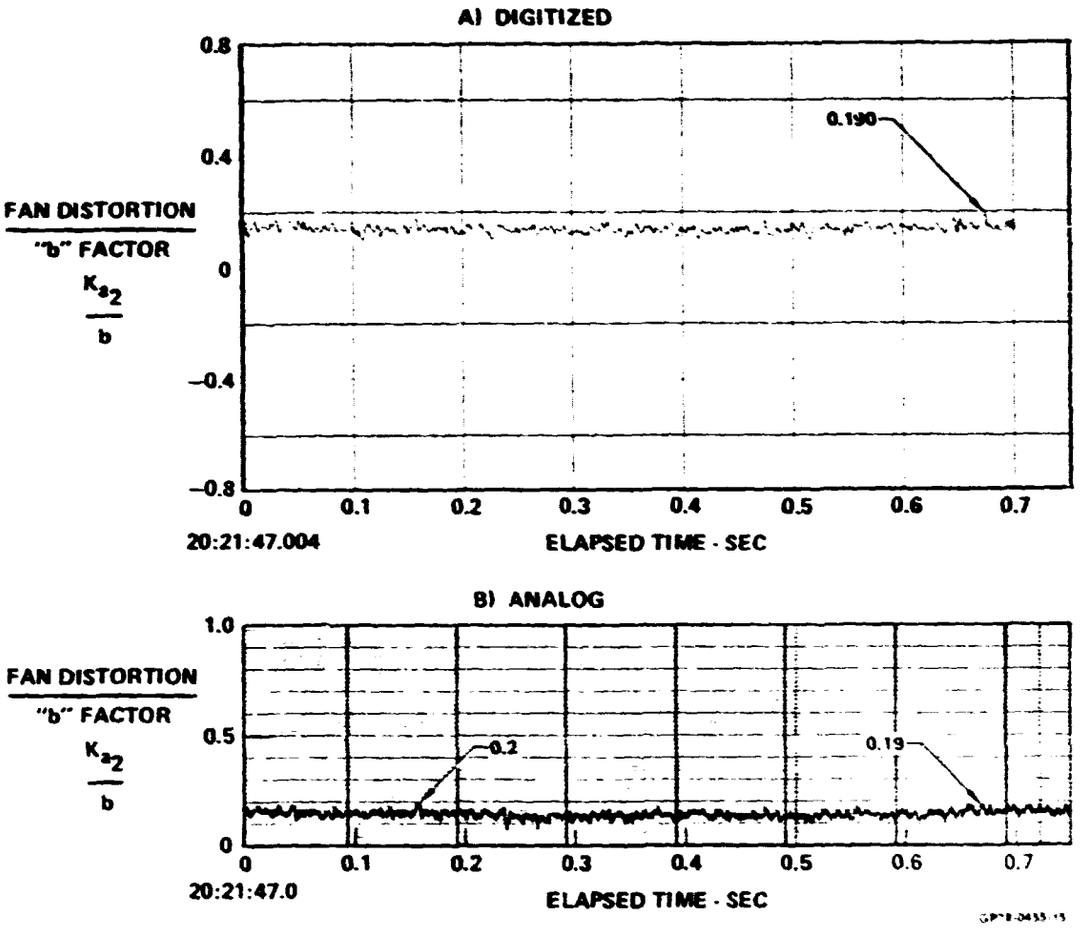

FIGURE A-16
COMPARISONS OF DIGITIZED AND ANALOG DISTORTION DATA
$M_0 = 1.75$ $\alpha = -2.6$ $\beta = 0.4$ $\rho = -2.2$
$\Delta_3 = 16.7$ WAT2 = 80.7% Bypass = 0.0
I.D. Number = 47 fc/υ = 170

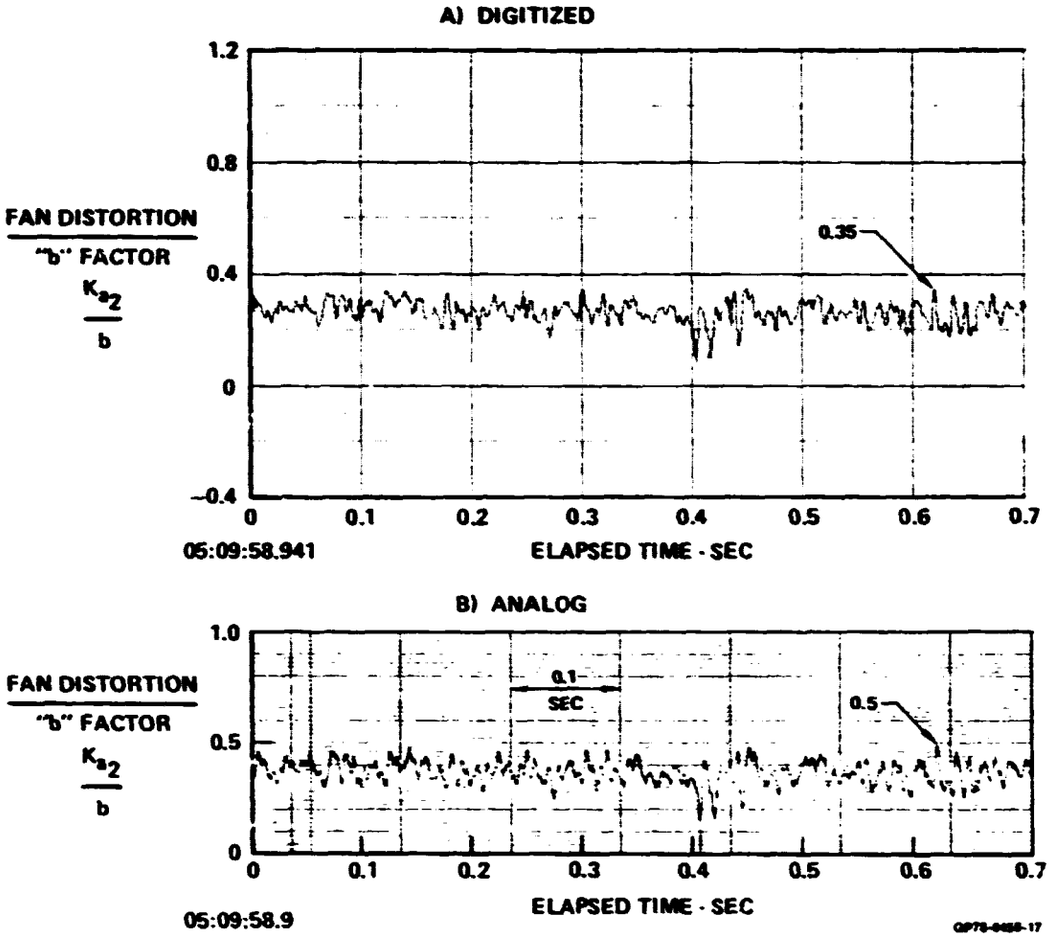

FIGURE A-17
COMPARISONS OF DIGITIZED AND ANALOG DISTORTION DATA
$M_O = 2.2$ $\alpha = 0.3$ $\beta = 0.2$ $\rho = -2.2$
$\Delta_3 = 22.9$ WAT2 = 73.0% Bypass = 0.0
I.D. Number = 70 fc/o = 170

APPENDIX B

DISTORTION DESCRIPTOR EQUATIONS AND SAMPLE CALCULATION

Presented herein are the details of the distortion descriptor equations, of the distortion descriptor calculation procedure, of a sample calculation and of the distortion descriptor reference radial profile and radial distortion weighting factor that are used in this study. These topics are separated into sections as follows.

LIST OF ILLUSTRATIONS

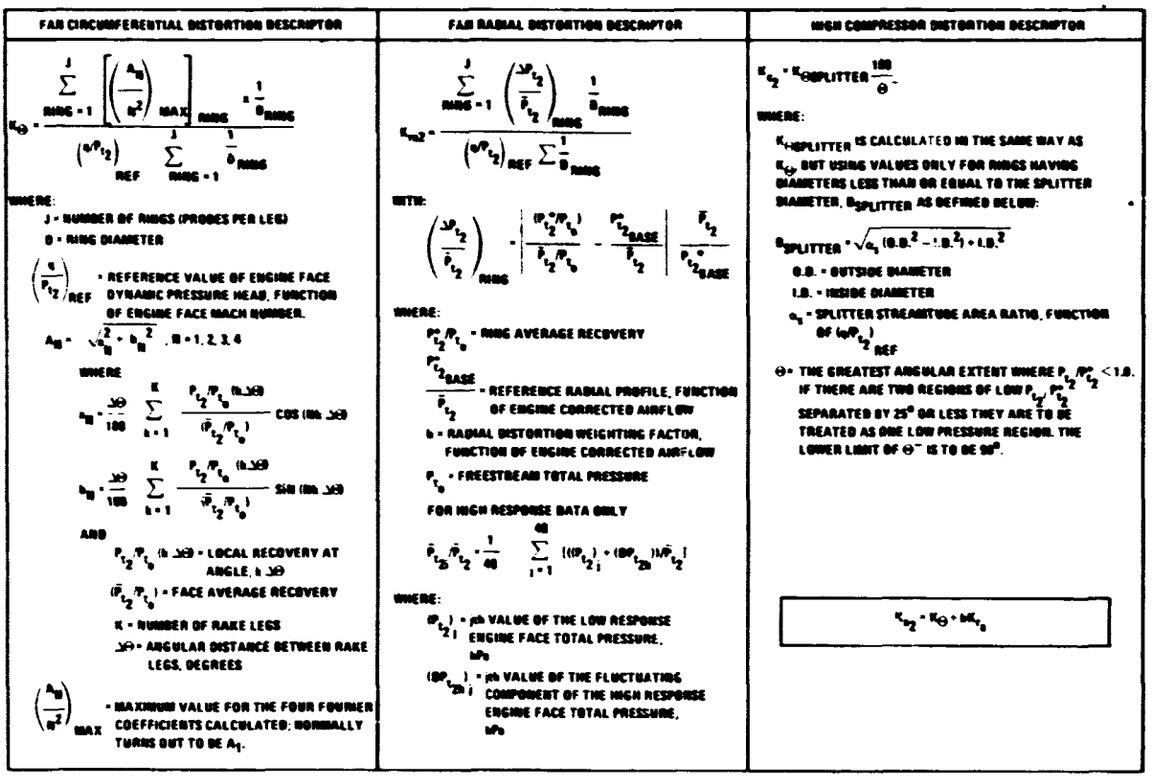

GP78-0323-158

FIGURE B-1
SUMMARY OF DISTORTION DESCRIPTOR EQUATIONS FOR THE NASA/F-15 DISTORTION METHODOLOGIES STUDY

ORIGINAL PAGE IS
OF POOR QUALITY

CALCULATION PROCEDURE FOR K_{a_2} AND K_{c_2} FOR INLET TIME VARIANT PRESSURE DATA

1. Select the recorded inlet pressure pattern for the operating condition under consideration.

2. This pattern is obtained from total pressure data measured at equidistant circumferential stations, θ_1, θ_2, θ_3...etc., and at the mean of J annular rings, d_1, d_2, d_3...etc., counting from the hub to the tip.

3. Consider the ring d_1 and list the total pressure ratio P_{t2}/P_{to} for each angle of θ.

4. For each angle θ obtain the sine and cosine of the angle and the product (P_{t2}/P_{to}) sine θ and (P_{t2}/P_{to}) cosine θ.

5. Sum the values of P_{t2}/P_{to} sine θ and P_{t2}/P_{to} cosine θ for all angles of θ to give

$$\sum_{-\pi}^{\pi} P_{t2}/P_{to} \text{ sine } \theta \text{ and } \sum_{-\pi}^{\pi} P_{t2}/P_{to} \text{ cosine } \theta$$

6. From the sum computed in step (5) and the value $(\Delta\theta/\pi)$, obtain the product

$$\frac{1}{\pi} \sum_{\pi}^{\pi} P_{t2}/P_{to} \text{ sine } \theta\Delta\theta \text{ and } \frac{1}{\pi} \sum_{\pi}^{\pi} P_{t2}/P_{to} \text{ cosine } \theta\Delta\theta$$

These values are respectively equal to a_1/P_{to} and b_1/P_{to}

7. The Fourier coefficient parameter A_1/P_{to} is then obtained

$$A_1/P_{to} = \sqrt{(a_1/P_{to})^2 + (b_1/P_{to})^2}$$

8. The value of the Fourier coefficient is determined for ten values of N where N (i.e., θ, 2θ, 3θ, ...10θ) is substituted for θ in steps 4-7 and the largest value of

$$\frac{1}{P_{to}} \frac{A_N}{N^2} \text{ is obtained.}$$

9. Find the ring average value of pressure, P_{t2*}/P_{to}

$$P_{t2*}/P_{to} = 1/N_\theta \sum_{1}^{N\theta} P_{t2}/P_{to}$$

where N_θ is the number of circumferential location.

10. Repeat steps 3-9 for each ring.

11. Multiply the values of $1/P_{to}$ (A_N/N^2) maximum obtained in step 8 by the weighting function 1/D and sum for all rings to obtain

$$\sum_{1}^{J} 1/P_{to} \ (A_N/N^2)\text{maximum } 1/D$$

Where J is the number of diameters.

12. Obtain the sum of the weighting factors 1/D

$$\sum_{1}^{J} 1/D$$

13. Obtain $\overline{P}_{t2}/P_{to}$, the arithmetic average value of P_{t2*}/P_{to}, from step 9

$$P_{t2}/P_{to} = \quad) \sum_{1}^{J} P_{t2*}/P_{to}$$

14. Obtain Q/P_{t2}, where Q/P_{t2} is defined as a function of percent total engine air flow corrected to the engine face.

15. Obtain K_θ from the results of steps 11, 12, 13 and 14.

$$K_\theta = \frac{\left\{ \sum_{1}^{J} \frac{1}{P_{to}} \left[\frac{A_N}{N^2} \right]_{max} \quad \frac{1}{D} \right\}}{\left(\frac{P_{t2}}{P_{to}} \right)_{avg} \quad \left(\frac{Q}{P_{t2}} \right)_{avg} \quad \sum_{1}^{J} \frac{1}{D}}$$

16. Obtain αs from Q/P_{t2} (step 14) and Figure B-2.

17. Compute Splitter Diameter

$$D_{SPLITTER} = \sqrt{\alpha s \ (OD^2 - ID^2) + ID^2}$$

18. Computer $K_{\theta \ SPLITTER}$ as in step 15, but using values only for rings having diameter smaller than or equal to splitter diameter.

19. Compute $\left(\frac{P_{t2}}{P_{t2*}} \right)_{inst}$

$$\left(\frac{P_{t2}}{P_{t2*}} \right)_{inst} = \left(\frac{P_{t2}}{P_{to}} \right)_{inst} \Big/ \left(\frac{P_{t2*}}{P_{to}} \right)_{inst}$$

20. Plot $\left(\frac{P_{t2}}{P_{t2^*}}\right)_{inst}$ vs θ for ring diameters smaller than or equal to splitter diameter.

21. Obtain $\bar{\theta}$ where $\bar{\theta}$ is equal to the greatest circumferential extent where $P_{t2}/P_{t2^*} < 1.0$. If there are two regions of low P_{t2}/P_{t2^*} by 25 deg or less, they are to be treated as one low pressure region. The lower limit of $\bar{\theta}$ is to be 90 deg.

22. Compute K_{c_2}

$$K_{c_2} = K_{\theta splitter} \left(\frac{180}{\bar{\theta}}\right)$$

23. Compute $\left(P_{t2^*}/\bar{P}_{t2}\right)_{inst} = \left(\frac{\bar{P}_{t2^*}}{P_{to}}\right)_{inst} \Big/ \left(\frac{\bar{P}_{t2}}{P_{to}}\right)_{inst}$

24. Select appropriate reference radial profile.

25. For each ring, compute $\frac{P_{t2^*} - P_{t2^* base}}{\bar{P}_{t2}}$

$$\frac{P_{t2^*} - P_{t2^* base}}{P_{t2}} = \left.\frac{P_{t2^*}}{P_{t2}}\right|_{inst \ \ (step\ 23)} - \left.\frac{P_{t2^*}}{P_{t2}}\right|_{base}$$

26. Compute $\frac{1}{D}$ for each ring.

27. Compute K_{ra_2}

$$\frac{\sum_{1}^{J} \left|\frac{P_{t2^*} - P_{t2^* base}}{\bar{P}_{t2}}\right| \left(\frac{1}{P_{t2^* base}/P_{t2}}\right)\left(\frac{1}{D}\right)}{\left(\frac{Q}{\bar{P}_{t2}}\right)_{avg} \sum_{1}^{J} \left(\frac{1}{D}\right)}$$

28. Select appropriate radial distortion weighting factor

29. Compute K_{a_2}

$$K_{a_2} = K_\theta + b\, K_{ra_2}$$

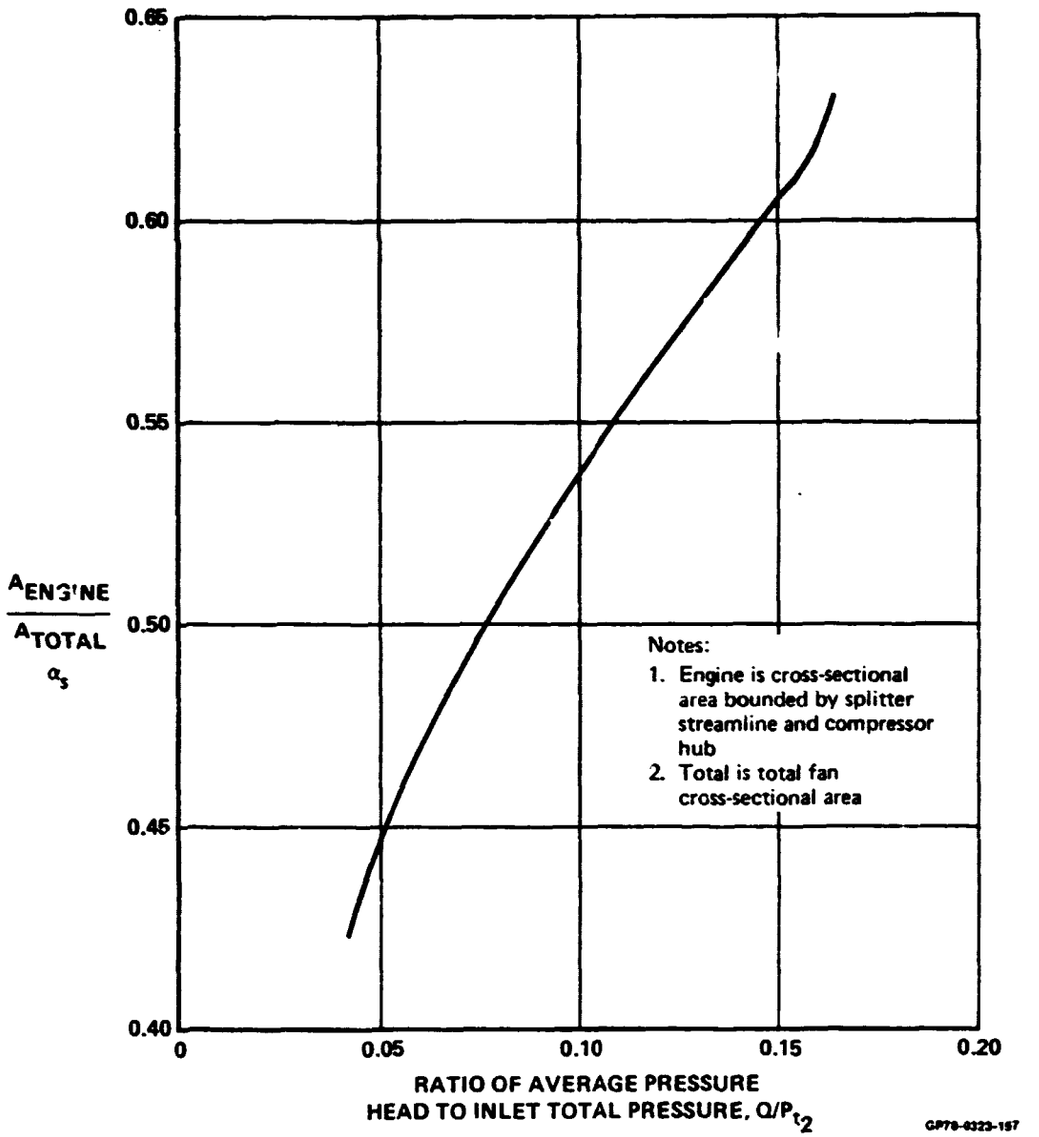

FIGURE 8-2
F100-PW-100 TURBOFAN ENGINE NOMINAL αS AS A FUNCTION OF THE RATIO OF AVERAGE DYNAMIC PRESSURE HEAD TO INLET TOTAL PRESSURE

Sample Calculation of K_{a2} and K_{c2} Distortion Descriptors

Given Values:

Ring	Diameter	Reference Radial Profile	"b" factor	
1	14.64036	.9622	12.50	
2	19.91952	.9783		
3	24.03636	1.0016		See following page for probe pressure values
4	27.54072	1.0166		
5	30.64836	1.0191		
6	33.48108	1.0185		

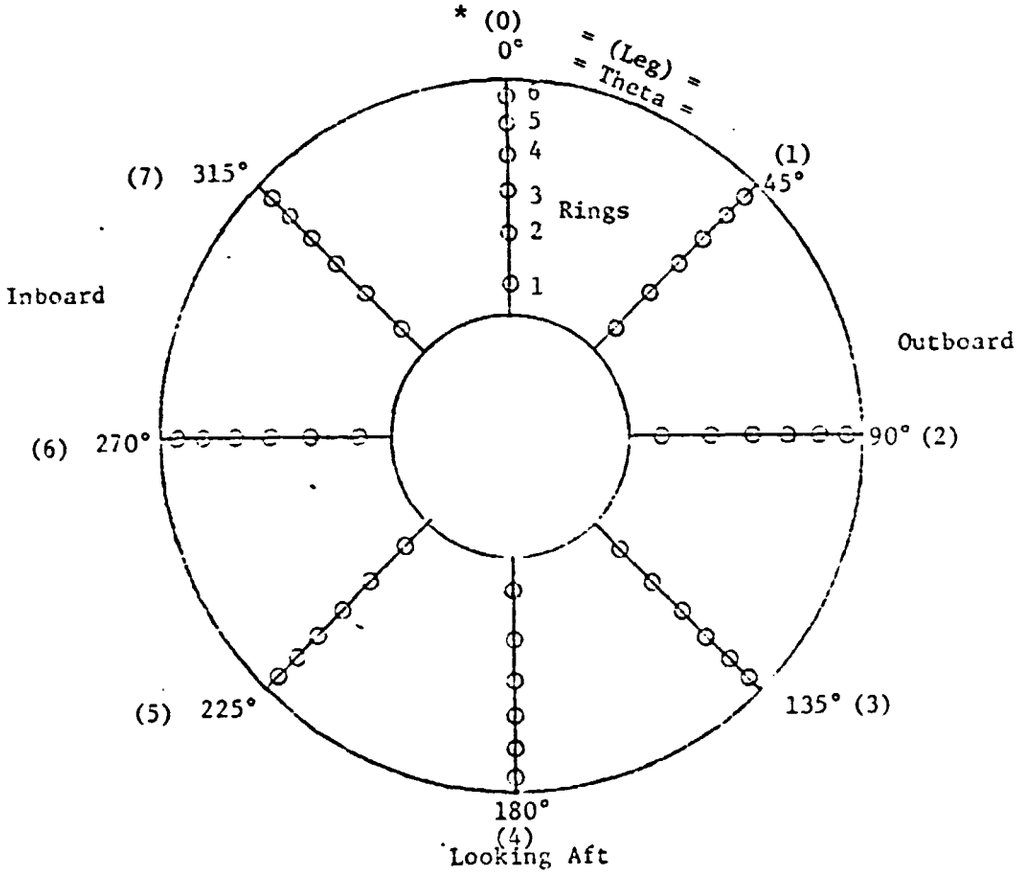

* This leg is generally labeled (8). The distortion value computed with (8) is identical to this calculation.

Calculation of $\bar{P}_{T_2}$

Diameter \ θ	0	45	90	135	180	225	220	315
14.64036	10.799600	10.848300	10.89.399	10.907100	10.808999	10.461499	10.586100	10.506100
19.91952	10.423499	10.484099	10.729799	10.96999	10.979699	10.379700	10.44100	10.260699
24.03636	10.183800	10.232400	10.777900	10.690599	10.733899	10.368899	10.239799	10.143800
27.54072	10.099500	10.231199	10.868299	10.629399	10.550099	10.279999	10.511700	9.9966993
30.64836	10.104600	10.179600	10.79400	10.535399	10.484200	10.382.00	10.176900	9.9592991
33.48108	10.063200	10.274799	10.676900	10.375600	10.519099	10.286799	10.333400	9.9924994

$$\sum_{i=1}^{48} \frac{(P_{t_2})_i}{48} = 10.46148$$

Calculation of Maximum A_N/N^2 and K_θ

where

$$\frac{A_N}{N^2} = \frac{1}{N^2} \sqrt{a_1^2 + b_1^2}$$

$$= \frac{1}{N^2} \sqrt{\left[\frac{\Delta\theta}{180} \Sigma \frac{P_{t_2}}{\bar{P}_{t_2}} \cos (KN\Delta\theta)\right]^2 \left[\frac{\Delta\theta}{180} \Sigma \frac{P_{t_2}}{\bar{P}_{t_2}} \sin (KN\Delta\theta)\right]^2}$$

Calculation of $(a_1)_{Ring} \times \bar{P}_{t_2}$

$\Delta\theta = 45°$; N=1

Ring	P_{t_2}	$\frac{\Delta\theta}{180} \cos(Nk\Delta\theta)$	$(P_{t_2})_{ring} \times \frac{\Delta\theta}{180} \cos(Nk\Delta\theta)$ Ring #1	Ring #2	Ring #3	Ring #4	Ring #5	Ring #6	Leg (k)
1	10.7996	.250000	2.6999						0
2	10.4235			2.605875					
3	10.1838				2.54595				
4	10.0995					2.524875			
5	10.1046						2.52615		
6	10.0632							2.5158	
1	10.8483	.1767767	1.91774						1
2	10.4841			1.85336					
3	10.2324				1.80886				
4	10.2312					1.80865			
5	10.1796						1.79953		
6	10.2748							1.81636	
1	10.8919	0.0000	0.0						2
2	10.7298			0.0					
3	10.7779				0.0				
4	10.8683					0.0			
5	10.7940						0.0		
6	10.6769							0.0	
1	10.9071	-0.1767777	-1.92813						3
2	10.9700			-1.93925					
3	10.6906				-1.88986				
4	10.6294					-1.87904			
5	10.5354						-1.86242		
6	10.3756							-1.83417	
1	10.8090	-0.250000	-2.70225						4
2	10.9797			-2.74492					
3	10.7339				-2.68348				
4	10.5501					-2.63752			
5	10.4842						-2.62105		
6	10.5191							-2.62978	
1	10.4615	-0.176777	-1.84936						5
2	10.3797			-1.83490					
3	10.3698				-1.83315				
4	10.2760					-1.81657			
5	10.3827						-1.83543		
6	10.2868							-1.81848	
1	10.5861	0.0	0.0						6
2	10.4410			0.0					
3	10.2398				0.0				
4	10.5117					0.0			
5	10.1769						0.0		
6	10.3334							0.0	
1	10.5061	0.1767777	1.85724						7
2	10.1607			1.81386					
3	10.1438				1.79320				
4	9.9957					1.76719			
5	9.9593						1.76058		
6	9.9925							1.76645	
$\left[\Sigma \frac{\Delta\theta}{180} P_{t_2} \cos(k\Delta\theta)\right]_{Ring}$ =			-.00486	-.24598	-.25848	-.23242	-.23264	-.18382	$(b_1)_{Ring} \times \bar{P}_{t_2}$

Calculation of $(a_2)_{Ring} \times \bar{P}_{t_2}$

$\Delta\theta = 45°$; $k=2$

Ring	P_{t_2}	$\frac{\Delta\theta}{180} \cos(2k\Delta\theta)$	$(P_{t_2})_{Ring} \times \frac{\Delta\theta}{180} \cos(2k\Delta\theta)$						Leg (k)
			Ring #1	Ring #2	Ring #3	Ring #4	Ring #5	Ring #6	
1	10.7996	.25000	2.6999	2.6059	2.5460	2.5249	2.5262	2.5158	0
2	10.4235								
3	10.1838								
4	10.0995								
5	10.1046								
6	10.0632								
1	10.8483	0.0000	0.0	0.0	0.0	0.0	0.0	0.0	1
2	10.4841								
3	10.2324								
4	10.1312								
5	10.1796								
6	10.2748								
1	10.9919	-.2500	-2.7230	-2.6824	-2.6945	-2.7174	-2.6985	-2.6692	2
2	10.7298								
3	10.7779								
4	10.8683								
5	10.7946								
6	10.6769								
1	10.9871	0.0000	0.0	0.0	0.0	0.0	0.0	0.0	3
2	10.9700								
3	10.6906								
4	10.6294								
5	10.5354								
6	10.3756								
1	10.8090	.2500	2.7022	2.7449	2.6835	2.6375	2.6210	2.6298	4
2	10.9797								
3	10.7339								
4	10.5501								
5	10.4842								
6	10.5191								
1	10.4615	0.0000	0.0	0.0	0.0	0.0	0.0	0.0	5
2	10.3797								
3	10.3698								
4	10.2760								
5	10.3827								
6	10.2868								
1	10.5861	-.2500	-2.6465	-2.6102	-2.5600	-2.6279	-2.5442	-2.5834	6
2	10.4410								
3	10.2398								
4	10.5117								
5	10.1769								
6	10.3334								
1	10.5061	0.000	0.0	0.0	0.0	0.0	0.0	0.0	7
2	10.2667								
3	10.1438								
4	9.9967								
5	9.9593								
6	9.9925								
$\left[\sum \frac{\Delta\theta}{180} P_{t_2} \cos(2k\Delta\theta)\right]_{Ring}$ =			.0326	.0582	-.075	-.1826	-.0955	-.107	$= (a_2)_{Ring} \times \bar{P}_{t_2}$

Calculation of $(a_3)_{Ring} \times \bar{P}_{c_2}$

$\Delta\theta = 45°$; $k=3$

Ring	P_{c_2}	$\frac{\Delta\theta}{180}\cos(3k\Delta\theta)$	$(P_{c_2})_{Ring} \times \frac{\Delta\theta}{180}\cos(3k\Delta\theta)$						
			Ring #1	Ring #2	Ring #3	Ring #4	Ring #5	Ring #6	Leg (k)
1	10.7996	.25000	2.6999	2.6059	2.5463	2.5249	2.5262	2.5158	0
2	10.4235								
3	10.1838								
4	10.0995								
5	10.1046								
6	10.0632								
1	10.8483	-.1767777	-1.9177	-1.8533	-1.8089	-1.8086	-1.7995	-1.8163	1
2	10.4861								
3	10.2324								
4	10.2312								
5	10.1796								
6	10.2748								
1	10.8919	0.0	0.0	0.0	0.0	0.0	0.0	0.0	2
2	10.7298								
3	10.7779								
4	10.8683								
5	10.7940								
6	10.6769								
1	10.9071	.1767777	1.9291	1.9392	1.8899	1.8790	1.8624	1.8342	3
2	10.9700								
3	10.6906								
4	10.6294								
5	10.5354								
6	10.3756								
1	10.9090	-.2500	-2.7022	-2.7[illegible]9	-2.6835	-2.6375	-2.6210	-2.6298	4
2	10.9797								
3	10.7339								
4	10.5501								
5	10.4842								
6	10.5191								
1	10.4615	.1767777	1.8494	1.8349	1.8331	1.8166	1.8354	1.8185	5
2	10.3797								
3	10.3698								
4	10.2760								
5	10.3827								
6	10.2868								
1	10.5861	0.000	0.0	0.0	0.0	0.0	0.0	0.0	6
2	10.4410								
3	10.2398								
4	10.5117								
5	10.1769								
6	10.3334								
1	10.5061	-.1767777	-1.8572	-1.8139	-1.7932	-1.7672	-1.7606	-1.7664	7
2	10.2607								
3	10.1438								
4	9.9967								
5	9.9593								
6	9.9925								
$\left[\Sigma \frac{\Delta\theta}{180} P_{c_2} \cos(3k\Delta\theta)\right]_{Ring}$ =			.0004	-.0321	-.0166	.0072	.0429	-.044	$= (a_3)_{Ring} \times \bar{P}_{c_2}$

Calculation of $(a_k)_{Ring} \times \bar{P}_{t_2}$

	$\Delta\theta = 45°$; $m=4$		$(P_{t_2})_{Ring} \times \frac{\Delta\theta}{180} \cos(mk\Delta\theta)$						
Ring	P_{t_2}	$\frac{\Delta\theta}{180} \cos(mk\Delta\theta)$	Ring #1	Ring #2	Ring #3	Ring #4	Ring #5	Ring #6	Leg (k)
1	10.7996	.2500	2.6999	2.6059	2.5460	2.5249	2.5262	2.5158	0
2	10.4235								
3	10.1838								
4	10.0995								
5	10.1366								
6	10.0632								
1	10.8483	-.2500	-2.7121	-2.6219	-2.5581	-2.5578	-2.5449	-2.5687	1
2	10.4842								
3	10.2324								
4	10.2312								
5	10.1796								
6	10.2748								
1	10.8919	.2500	2.7230	2.6824	2.6045	2.7171	2.6985	2.6692	2
2	10.7298								
3	10.7779								
4	10.8683								
5	10.7940								
6	10.6769								
1	10.9071	-.2500	-2.7268	-2.7425	-2.6726	-2.6574	-2.6338	-2.5939	3
2	10.9700								
3	10.8906								
4	10.8294								
5	10.5354								
6	10.3756								
1	10.8090	.2500	2.7022	2.7449	2.6835	2.6375	2.6210	2.6298	4
2	10.4797								
3	10.7339								
4	10.5501								
5	10.4842								
6	10.5191								
1	10.4615	-.2500	-.26154	-2.5949	-2.5924	-2.5690	-2.5957	-2.5717	5
2	10.3747								
3	10.3698								
4	10.2760								
5	10.3827								
6	10.2868								
1	10.5861	.2500	2.6465	2.6102	2.5470	2.6279	2.5442	2.5834	6
2	10.4410								
3	10.2398								
4	10.5117								
5	10.1769								
6	10.3334								
1	10.5061	-.2500	-2.6265	-2.6052	-2.5360	-2.4992	-2.4898	-2.4981	7
2	10.2607								
3	10.1438								
4	9.9967								
5	9.9593								
6	9.9925								
$\left[\sum \frac{\Delta\theta}{180} P_{t_2} \cos(4k\Delta\theta)\right]_{Ring}$			.0878	.1198	.1249	.224	.1257	.1638	$= (a_k)_{Ring} \times \bar{P}_{t_2}$

Calculation of $(b_1)_{Ring} \times \bar{P}_{t_2}$

$\Delta\theta = 45°$; M=1

Ring	P_{t_2}	$\frac{\Delta\theta}{180} \sin(k\Delta\theta)$	$(P_{t_2})_{Ring} \times \frac{\Delta\theta}{180} \sin(k\Delta\theta)$ Ring #1	Ring #2	Ring #3	Ring #4	Ring #5	Ring #6	Leg (k)
1	10.7996	0.0	0.0						0
2	10.4235			0.0					
3	10.1838				0.0				
4	10.0995					0.0			
5	10.1046						0.0		
6	10.0632							0.0	
1	10.8483	.1767777	1.91774						1
2	10.4841			1.85336					
3	10.2324				1.80886				
4	10.2312					1.80865			
5	10.1796						1.79953		
6	10.2748							1.81636	
1	10.8919	.250000	2.72298						2
2	10.7298			2.68245					
3	10.7779				2.69448				
4	10.8683					2.71708			
5	10.7940						2.6985		
6	10.6769							2.66922	
1	10.9071	.1767777	1.92813						3
2	10.9700			1.93925					
3	10.6906				1.88986				
4	10.6294					1.87904			
5	10.5354						1.86242		
6	10.3756							1.83417	
1	10.8090	0.0	0.0						4
2	10.9797			0.0					
3	10.7339				0.0				
4	10.5501					0.0			
5	10.4842						0.0		
6	10.5191							0.0	
1	10.4615	-0.1767777	-1.84936						5
2	10.3797			-1.83490					
3	10.3698				-1.83315				
4	10.2760					-1.81657			
5	10.3827						-1.83543		
6	10.2868							-1.31848	
1	10.5861	-0.25000	-2.64652						6
2	10.4410			-2.61025					
3	10.2398				-2.55995				
4	10.5117					-2.62792			
5	10.1769						-2.54422		
6	10.3334							-2.58335	
1	10.5061	-0.1767777	-1.85724						7
2	10.2607			-1.81386					
3	10.1438				-1.79320				
4	9.9967					-1.76719			
5	9.9593						-1.76058		
6	9.9925							-1.76645	
$\left[\sum \frac{\Delta\theta}{180} P_{t_2} \sin(k\Delta\theta)\right]_{Ring}$ =			.21573	.21605	.2069	.19310	.22022	.15147	$= (b_1)_{Ring} \times \bar{P}_{t_2}$

Calculation of $(b_2)_{Ring} \times \bar{P}_{c_2}$

$\Delta\theta = 45°$; $N=2$

Ring	P_{c_2}	$\frac{\Delta\theta}{180}$ sin (NkΔθ)	$(P_{c_2})_{Ring} \times \frac{\Delta\theta}{180}$ sin (NkΔθ) Ring #1	Ring #2	Ring #3	Ring #4	Ring #5	Ring #6	Leg (k)
1	10.7996	0.0000	0.0						0
2	10.4235			0.0					
3	10.1838				0.0				
4	10.0995					0.0			
5	10.1046						0.0		
6	10.0632							0.0	
1	10.8483	.2500	2.7121						1
2	10.4841			2.6210					
3	10.2324				2.5581				
4	10.2312					2.5578			
5	10.1796						2.5449		
6	10.2748							2.5687	
1	10.8919	0.0000	0.0						2
2	10.7298			0.0					
3	10.7779				0.0				
4	10.8683					0.0			
5	10.7940						0.0		
6	10.6769							0.0	
1	10.9071	-.2500	-2.7268						3
2	10.9700			-2.7425					
3	10.6906				-2.6726				
4	10.6294					-2.6574			
5	10.5354						-2.6338		
6	10.3756							2.5939	
1	10.8090	0.0000	0.0						4
2	10.9797			0.0					
3	10.7339				0.0				
4	10.5501					0.0			
5	10.4842						0.0		
6	10.5191							0.0	
1	10.4615	.2500	2.6154						5
2	10.3797			2.5945					
3	10.3698				2.5924				
4	10.2760					2.569			
5	10.3827						2.5957		
6	10.2868							2.5717	
1	10.5861	0.0000	0.0						6
2	10.4410			0.0					
3	10.2398				0.0				
4	10.5117					0.0			
5	10.1769						0.0		
6	10.3334							0.0	
1	10.5061	-.2500	-2.6265						7
2	10.2607			-2.5652					
3	10.1438				-2.5360				
4	9.9967					-2.4992			
5	9.9593						-2.4898		
6	9.9925							-2.4981	
$\left[\Sigma \frac{\Delta\theta}{180} P_{c_2} \sin (2k\Delta\theta)\right]_{Ring}$ =			-.0258	-.0918	-.0581	-.0298	.017	.0484	$= (b_2)_{Ring} \times \bar{P}_{c_2}$

Calculation of $(b_3)_{Ring} \times \bar{P}_{t_2}$

	$\Delta\theta = 45°$; $3k=3$		$(P_{t_2})_{Ring} \times \frac{\Delta\theta}{180} \sin(3k\Delta\theta)$						
Ring	P_{t_2}	$\frac{\Delta\theta}{180} \sin(3k\Delta\theta)$	Ring #1	Ring #2	Ring #3	Ring #4	Ring #5	Ring #6	Lag (k)
1	10.7996	0.000	0.0						0
2	10.4235			0.0					
3	10.1838				0.0				
4	10.0995					0.0			
5	10.1046						0.0		
6	10.0632							0.0	
1	10.8483	.176777	1.9177						1
2	10.4841			1.8533					
3	10.2324				1.8089				
4	10.2312					1.8086			
5	10.1796						1.7995		
6	10.2748							1.8163	
1	10.8919	-.2500	-2.7250						2
2	10.7298			-2.6824					
3	10.7779				-2.6945				
4	10.8683					-2.7171			
5	10.7940						-2.6985		
6	10.6769							-2.6692	
1	10.9071	.176777	1.9280						3
2	10.9700			1.9392					
3	10.6906				1.8898				
4	10.6294					1.8790			
5	10.5354						1.8623		
6	10.3756							1.8341	
1	10.8090	0.000	0.0						4
2	10.9797			0.0					
3	10.7339				0.0				
4	10.5501					0.0			
5	10.4842						0.0		
6	10.5191							0.0	
1	10.4615	-.176777	-1.8494						5
2	10.3797			-1.8349					
3	10.3698				-1.8331				
4	10.2760					-1.8166			
5	10.3827						-1.8354		
6	10.2868							-1.8185	
1	10.5861	0.2500	2.6465						6
2	10.4410			2.6102					
3	10.7398				2.5600				
4	10.5117					2.6279			
5	10.1769						2.5442		
6	10.3334							2.5834	
1	10.5061	-.176777	-1.8572						7
2	10.2607			-1.8139					
3	10.1438				-1.7932				
4	9.9967					-1.7672			
5	9.9593						-1.7606		
6	9.9925							-1.7664	
$\left[\Delta \frac{\Delta\theta}{180} P_{t_2} \sin(3k\Delta\theta)\right]_{Ring}$			.0626	.0715	-.0621	.0146	-.0885	-.0203	$= (b_3)_{Ring} \times \bar{P}_{t_2}$

Calculation of $(b_4)_{Ring} \times \bar{P}_{c_2}$

$\Delta\theta = 45°$; M=4			$(P_{c_2})_{Ring} \times \frac{\Delta\theta}{180} \sin(Mk\Delta\theta)$						
Ring	P_{c_2}	$\frac{\Delta\theta}{180} \sin(Mk\Delta\theta)$	Ring #1	Ring #2	Ring #3	Ring #4	Ring #5	Ring #6	Leg (k)
1	10.7996	0.000	0.0						0
2	10.4235			0.0					
3	10.1838				0.0				
4	10.0995					0.0			
5	10.1046						0.0		
6	10.0632							0.0	
1	10.8483	0.000	0.0						1
2	10.4841			0.0					
3	10.2326				0.0				
4	10.2312					0.0			
5	10.1796						0.0		
6	10.2748							0.0	
1	10.8919	0.000	0.0						2
2	10.7298			0.0					
3	10.7779				0.0				
4	10.8683					0.0			
5	10.7940						0.0		
6	10.6769							0.0	
1	10.9071	0.000	0.0						3
2	10.9700			0.0					
3	10.6906				0.0				
4	10.6294					0.0			
5	10.5354						0.0		
6	10.3756							0.0	
1	10.8090	0.000	0.0						4
2	10.9797			0.0					
3	10.7339				0.0				
4	10.5501					0.0			
5	10.4842						0.0		
6	10.5191							0.0	
1	10.4615	0.000	0.0						5
2	10.3797			0.0					
3	10.3698				0.0				
4	10.2760					0.0			
5	10.3827						0.0		
6	10.2868							0.0	
1	10.5861	0.000	0.0						6
2	10.4410			0.0					
3	10.2398				0.0				
4	10.5117					0.0			
5	10.1769						0.0		
6	10.3334							0.0	
1	10.5061	0.000	0.0						7
2	10.2607			0.0					
3	10.1438				0.0				
4	9.9967					0.0			
5	9.9593						0.0		
6	9.9925							0.0	
$\left[\Sigma \frac{\Delta\theta}{180} P_{c_2} \sin(Mk\Delta\theta)\right]_{Ring}$ =			0.0	0.0	0.0	0.0	0.0	0.0	$= (b_4)_{Ring} \times \bar{P}_{c_2}$

Summary of A_N/N^2

Ring / Calculation	1	2	3	4	5	6	N	
$\Sigma \frac{\Delta\theta}{180} P_{t_2} \cos(NK\Delta\theta)$	-.00486	-.24598	-.25848	-.23242	-.23264	-.18382	1	$(a_1)_{ring} \cdot \bar{P}_{t_2}$
$\Sigma \frac{\Delta\theta}{180} P_{t_2} \sin(NK\Delta\theta)$	.21573	.21605	.2069	.19310	.22022	.15147	1	$(b_1)_{ring} \cdot \bar{P}_{t_2}$
$\Sigma \frac{\Delta\theta}{180} P_{t_2} \sqrt{\cos^2(NK\Delta\theta)+\sin^2(NK\Delta\theta)}$	.21578	.32739	.33109	.30217	.32034	.23819	1	$A_1 \cdot \bar{P}_{t_2}$
*	.21578	.32739	.33109	.30217	.32034	.23819	1	$A_1 \cdot \bar{P}_{t_2}/N^2$
$\Sigma \frac{\Delta\theta}{180} P_{t_2} \cos(NK\Delta\theta)$	.0326	.0582	-.0250	-.1826	-.0955	-.1070	2	$(a_2)_{ring} \cdot \bar{P}_{t_2}$
$\Sigma \frac{\Delta\theta}{180} P_{t_2} \sin(NK\Delta\theta)$	-.0258	-.0918	-.0581	-.0298	.017	.0484	2	$(b_2)_{ring} \cdot \bar{P}_{t_2}$
$\Sigma \frac{\Delta\theta}{180} P_{t_2} \sqrt{\cos^2(NK\Delta\theta)+\sin^2(NK\Delta\theta)}$	.04157	.1087	.06325	.1850	.0970	.1174	2	$A_2 \cdot \bar{P}_{t_2}$
	.01039	.02717	.01581	.04625	.02425	.02936	2	$A_2 \cdot \bar{P}_{t_2}/N^2$
$\Sigma \frac{\Delta\theta}{180} P_{t_2} \cos(NK\Delta\theta)$	.0004	-.0321	-.0166	.0072	.0429	-.044	3	$(a_3)_{ring} \cdot \bar{P}_{t_2}$
$\Sigma \frac{\Delta\theta}{180} P_{t_2} \sin(NK\Delta\theta)$	.0626	.0715	-.0621	.0146	-.0885	-.0203	3	$(b_3)_{ring} \cdot \bar{P}_{t_2}$
$\Sigma \frac{\Delta\theta}{180} P_{t_2} \sqrt{\cos^2(NK\Delta\theta)+\sin^2(NK\Delta\theta)}$	.0626	.0784	.06428	.01628	.09835	.04846	3	$A_3 \cdot \bar{P}_{t_2}$
	.00696	.00871	.00714	.00181	.01093	.00538	3	$A_3 \cdot \bar{P}_{t_2}/N^2$
$\Sigma \frac{\Delta\theta}{180} P_{t_2} \cos(NK\Delta\theta)$	.0878	.1198	.1249	.2240	.1257	.1658	4	$(a_4)_{ring} \cdot \bar{P}_{t_2}$
$\Sigma \frac{\Delta\theta}{180} P_{t_2} \sin(NK\Delta\theta)$	0.0	0.0	0.0	0.0	0.0	0.0	4	$(b_4)_{ring} \cdot \bar{P}_{t_2}$
$\Sigma \frac{\Delta\theta}{180} P_{t_2} \sqrt{\cos^2(NK\Delta\theta)+\sin^2(NK\Delta\theta)}$	.0878	.1198	.1249	.2240	.1257	.1658	4	$A_4 \cdot \bar{P}_{t_2}$
	.00549	.00749	.00781	.014	.00786	.0104	4	$A_4 \cdot \bar{P}_{t_2}/N^2$

* Maximum A_N/N^2 Values

Calculation of K_θ

$$K_\theta = \frac{\sum_{Ring=1}^{6} \left[\left(\frac{A_N}{N^2}\right)_{max}\right]_{Ring} \times \frac{1}{D_{Ring}}}{\left[(q/\bar{P}_{t_2})\right] \sum_{Ring=1}^{6} \frac{1}{D_{Ring}}} = \frac{\frac{1}{\bar{P}_{t_2}} \sum_{Ring=1}^{6} \left[\left(\frac{A_N \cdot \bar{P}_{t_2}}{N^2}\right)_{max}\right]_{Ring} \times \frac{1}{D_{Ring}}}{\left[(q/\bar{P}_{t_2})\right] \sum_{Ring=1}^{6} \frac{1}{D_{Ring}}}$$

$$= \frac{\frac{1}{10.46148}\left(\frac{.21578}{14.64036} + \frac{.32739}{19.91952} + \frac{.33109}{24.03636} + \frac{.30217}{27.54072} + \frac{.32034}{30.64836} + \frac{.23819}{33.48108}\right)}{.061522\ (.2589156)}$$

$K_\theta = .44099$

Calculation of $K_{r_{a_2}}$

Ring \ θ	0°	45°	90°	135°	180°	225°	270°	315°	Ring Average
1	10.7996	10.8483	10.8919	10.9071	10.8090	10.4615	10.5861	10.5061	10.7261875
2	10.42350	10.4841	10.7298	10.9700	10.9797	10.3797	10.4410	10.2607	10.5835625
3	10.1838	10.2324	10.7779	10.6906	10.7339	10.3689	10.2398	10.1438	10.4213875
4	10.09950	10.2312	10.8683	10.6294	10.5501	10.2760	10.5117	9.9967	10.3953625
5	10.10460	10.17960	10.7940	10.5354	10.4842	10.3827	10.1769	9.9593	10.3270875
6	10.06320	10.2748	10.6769	10.3756	10.5191	10.2868	10.3334	9.9925	10.3152875

Avg $\bar{P}_{t_2}$ = 10.46148

	①	②	③ ①/②	④ Base Radial Profile	⑤ ③-④	⑥ ⑤/④
Ring	$P_{t_2}{}^*$	$\bar{P}_{t_2}$	$\frac{P_{t_2}{}^*/P_{t_0}}{\bar{P}_{t_2}/P_{t_0}}$	$(P_{t_2}{}^*)_{Base}/\bar{P}_{t_2}$	$\left\lvert\frac{\Delta P}{\bar{P}_{t_2}}\right\rvert$	$\frac{\Delta P_{t_2}}{\bar{P}_{t_2}}_{Ring}$
1	10.7261875	10.46148	1.0253031	.9622	.0631031	.0655821
2	10.5835625	↓	1.0116697	.9783	.0333697	.0341099
3	10.4213875		.9961676	1.0016	.00543239	.00542371
4	10.3953624		.9936799	1.0165	.02292009	.02254583
5	10.3270875		.9871535	1.0191	.03194641	.03134767
6	10.3152875		.9860256	1.0185	.03247436	.03188450

$$K_{r_{a_2}} = \frac{\sum_{Ring=1}^{6} \left(\frac{\Delta P_{t_2}}{\bar{P}_{t_2}}\right)_{Ring} \frac{1}{D_{Ring}}}{[(q/\bar{P}_{t_2})] \sum_{Ring=1}^{6} \frac{1}{D_{Ring}}}$$

$$K_{r_{a_2}} = \frac{\frac{.0655821}{14.64036} + \frac{.0341099}{19.91952} + \frac{.00542371}{24.03636} + \frac{.02254583}{27.54072} + \frac{.03134767}{30.64836} + \frac{.03188450}{33.48108}}{.061522\ (.2589156)}$$

$$= .57827$$

Calculation of K_{a_2}

$$K_{a_2} = K_\theta + b \cdot K_{r_{a_2}}$$

$$= .44099 + (12.50)\ (.57827)$$

$$K_{a_2} = 7.6694$$

Calculation of K_{c_2}

$$D_{Splitter}^{*} = \sqrt{\alpha_s\ (OD^2 - ID^2) + ID^2} \qquad \alpha_s = .47 \text{ from Figure B-2}$$

$$= \sqrt{.47\ (33.48108^2 \cdot 14.64036^2) + 14.64036^2}$$

$$D_{Splitter} = 25.30735$$

$$\bar{\theta} = 218 \text{ from Figure B-4}$$

$$K_{c_2} = K_{\theta_{Splitter}} \times \frac{180}{\bar{\theta}}$$

$$K_{\theta_{Splitter}} = \frac{\sum_{Ring=1}^{3}\left[\left(\frac{A_N}{N^2}\right)_{max}\right]_{ring} \times \frac{1}{D_{Ring}}}{\left[(q/\bar{P}_{t_2})\right]\sum_{Ring=1}^{3}\frac{1}{D_{Ring}}} = \frac{\left(\frac{1}{\bar{P}_{t_2}}\right)_{Rings\ 1,2,3} \cdot \sum_{Ring=1}^{3}\left[\left(\frac{A_N \cdot \bar{P}_{t_2}}{N^2}\right)_{max}\right]_{Ring} \times \frac{1}{D_{Ring}}}{\left[(q/\bar{P}_{t_2})\right]\sum_{Ring=1}^{3}\frac{1}{D_{Ring}}}$$

$$K_{c_2} = \frac{\frac{1}{10.57705}\left(\frac{.21578}{14.64036} + \frac{.32739}{19.91952} + \frac{.33109}{24.03636}\right)}{.061522\left(\frac{1}{14.64036} + \frac{1}{19.91952} + \frac{1}{24.03636}\right)} \times \frac{180}{218}$$

$$K_{c_2} = .43143 \times \frac{180}{218} = .35622$$

$$K_{c_2} = .35622$$

*This value usually computes so as to use the inner three rings.

Determination of $\bar{\theta}$

Maximum value of $\bar{\theta}$ occurs in Ring 2, which can be determined by examining the Ring 1 through Ring 6 Circumferential Pressure Contours that are shown in Figures B-3 through B-8. In addition, the Fourier Series curve fit of Ring 2 Circumferential Pressure contour is plotted on the graph and the equation is shown below. The fit has less than .6% error throughout the entire contour.

$$P_2(\theta) = 10.5836 - .24598 \cos(45K) + .21605 \sin(45K)$$
$$+ .0582 \cos(90K) - .0918 \sin(90K)$$
$$- .0321 \cos(135K) + .0715 \sin(135K)$$
$$+ .1198 \cos(180K)$$
$$K = 0, 1, 2, 3, 4, 5, 6, 7$$

$\bar{\theta} = 218°$ on Ring 2, Figure B-4

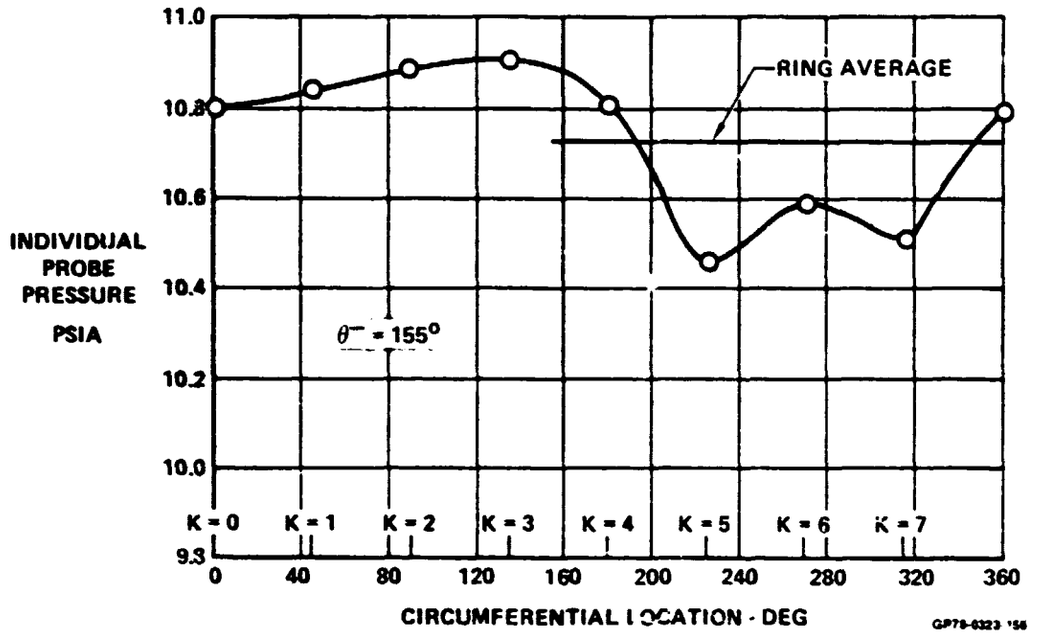

FIGURE B-3
RING 1 CIRCUMFERENTIAL PRESSURE CONTOUR

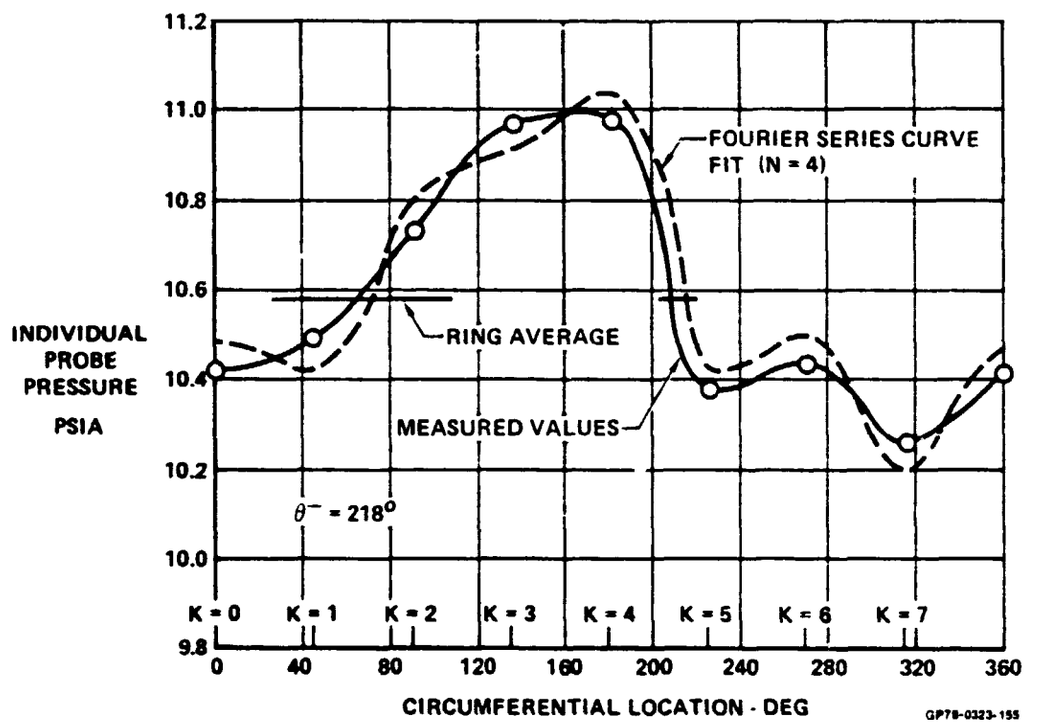

FIGURE B-4
RING 2 CIRCUMFERENTIAL PRESSURE CONTOUR

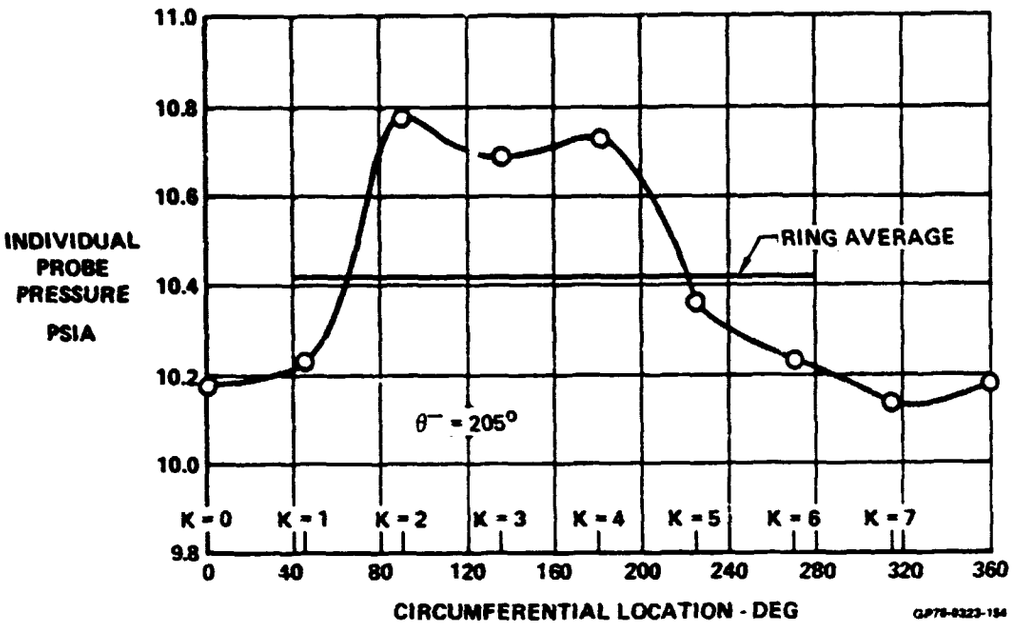

FIGURE B-5
RING 3 CIRCUMFERENTIAL PRESSURE CONTOUR

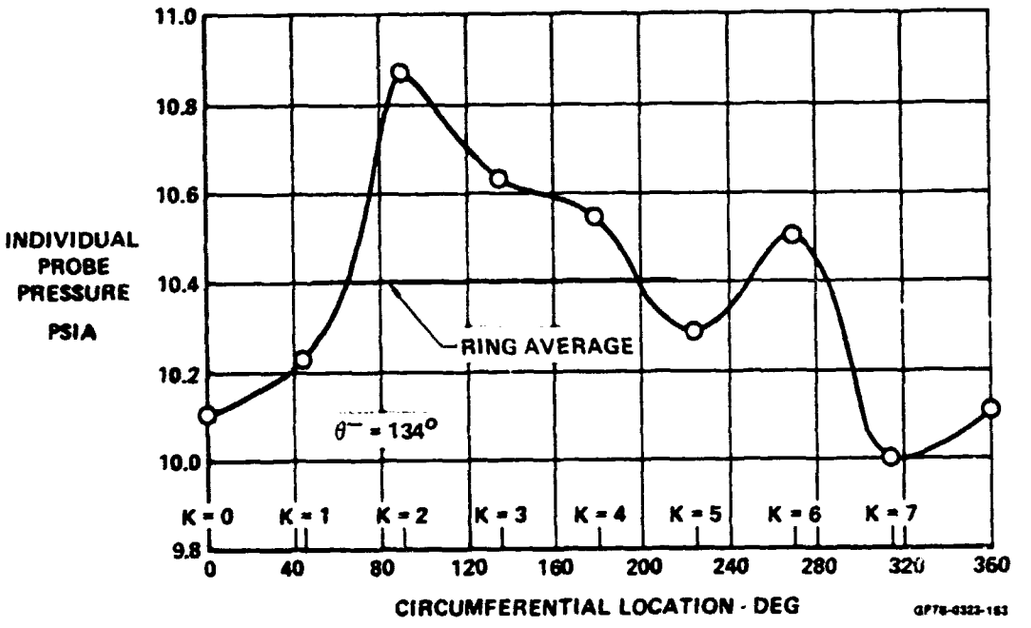

FIGURE B-6
RING 4 CIRCUMFERENTIAL PRESSURE CONTOUR

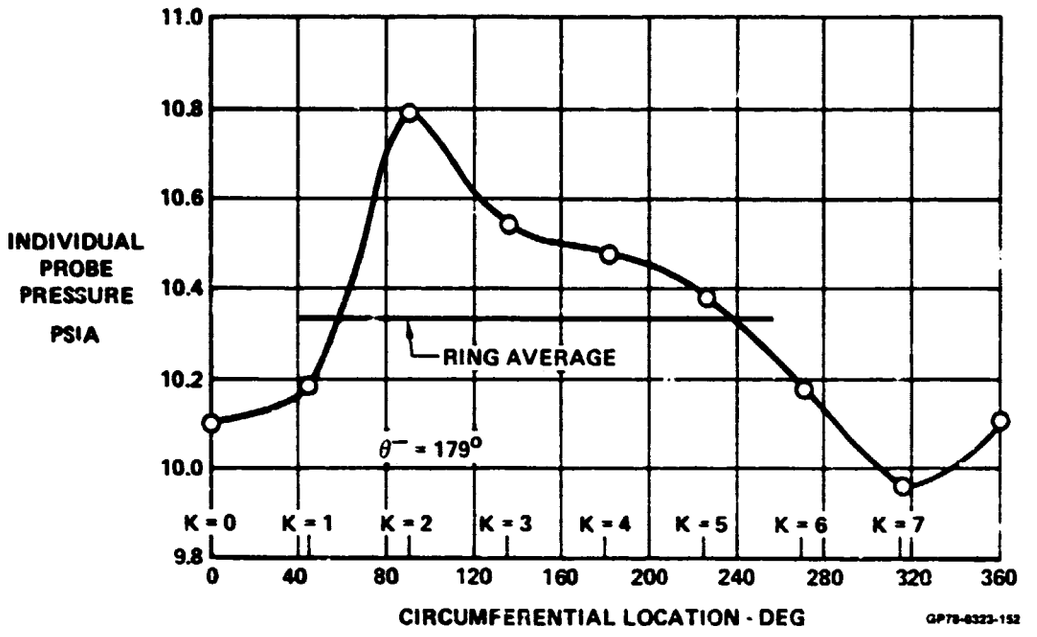

FIGURE B-7
RING 5 CIRCUMFERENTIAL PRESSURE CONTOUR

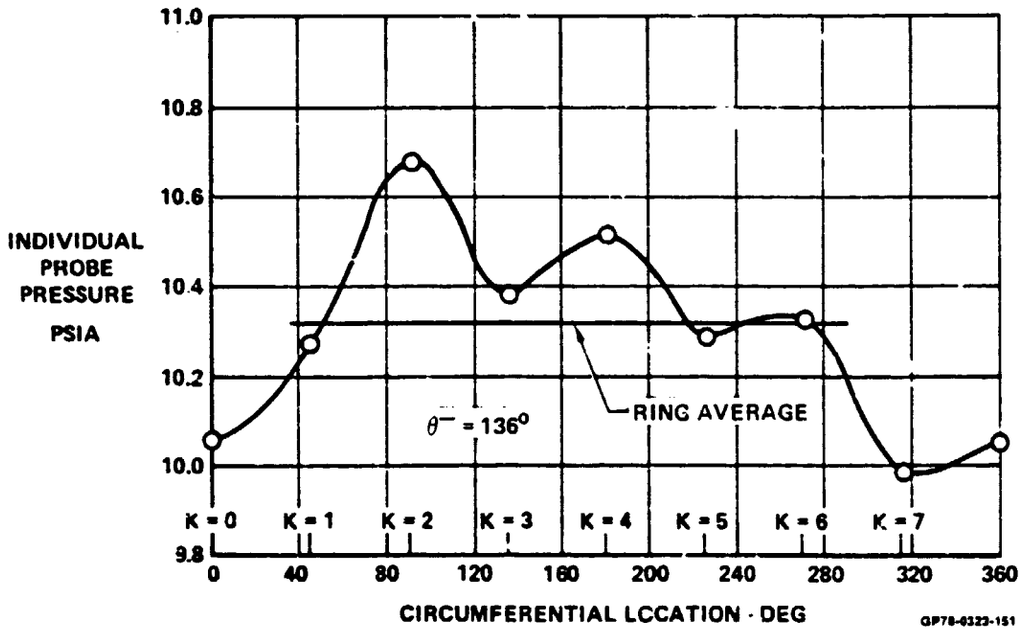

FIGURE B-8
RING 6 CIRCUMFERENTIAL PRESSURE CONTOUR

% WAT2	$r_i/r_{O.D.}$ / "b" FACTOR	REFERENCE RADIAL PROFILE					
		0.4207	0.5724	0.6907	0.7914	0.8807	0.9621
55.0	23.42	0.9806	0.9894	1.0033	1.0111	1.0099	1.0060
60.0	29.26	0.9824	0.9907	1.0034	1.0103	1.0090	1.0054
60.5	28.77	0.9823	0.9905	1.0033	1.0104	1.0091	1.0054
62.3	24.49	0.9820	0.9901	1.0033	1.0106	1.0092	1.0054
62.8	23.79	0.9819	0.9901	1.0033	1.0106	1.0091	1.0054
63.1	23.37	0.9818	0.9901	1.0033	1.0106	1.0091	1.0054
65.0	20.72	0.9813	0.9900	1.0033	1.0106	1.0091	1.0053
66.0	19.33	0.9811	0.9899	1.0033	1.0106	1.0091	1.0052
68.0	16.71	0.9806	0.9899	1.0033	1.0105	1.0090	1.0051
68.4	16.23	0.9807	0.9900	1.0034	1.0105	1.0090	1.0050
69.3	15.13	0.9808	0.9901	1.0035	1.0106	1.0088	1.0048
70.0	14.27	0.9810	0.9903	1.0036	1.0106	1.0087	1.0046
72.0	11.99	0.9813	0.9909	1.0036	1.0102	1.0085	1.0041
72.9	11.04	0.9814	0.9913	1.0037	1.0101	1.0083	1.0040
73.0	10.92	0.9811	0.9911	1.0037	1.0102	1.0085	1.0043
74.0	9.95	0.9812	0.9914	1.0038	1.0101	1.0084	1.0046
75.0	8.99	0.9832	0.9926	1.0038	1.0094	1.0076	1.0030
76.0	8.06	0.9852	0.9938	1.0037	1.0088	1.0069	1.0015
77.0	6.50	0.9857	0.9941	1.0037	1.0084	1.0064	1.0012
78.0	5.43	0.9863	0.9944	1.0037	1.0081	1.0060	1.0010
79.0	4.47	0.9897	0.9983	1.0065	1.0071	1.0005	0.9938
80.0	3.86	1.0150	1.0217	1.0217	1.0064	0.9760	0.9469
82.0	6.29	1.0298	1.0304	1.0284	1.0031	0.9637	0.9410
82.5	4.00	1.0288	1.0296	1.0276	1.0031	0.9648	0.9426
85.0	2.20	1.0242	1.0258	1.0243	1.0031	0.9699	0.9496
87.3	2.32	1.0216	1.0239	1.0226	1.0032	0.9726	0.9531
87.5	2.32	1.0215	1.0238	1.0225	1.0032	0.9727	0.9533
89.4	2.38	1.0222	1.0246	1.0230	1.0031	0.9720	0.9520
90.0	2.34	1.0210	1.0239	1.0225	1.0033	0.9731	0.9534
92.5	2.19	1.0211	1.0242	1.0227	1.0034	0.9729	0.9527
95.0	2.00	1.0262	1.0281	1.0247	1.0020	0.9678	0.9453
97.0	1.71	1.0392	1.0341	1.0255	0.9985	0.9612	0.9371
97.2	1.67	1.0409	1.0348	1.0256	0.9982	0.9606	0.9363
97.5	1.66	1.0429	1.0360	1.0261	0.9981	0.9598	0.9344
99.0	1.57	1.0551	1.0421	1.0292	0.9963	0.9525	0.9264
100.0	1.53	1.0630	1.0473	1.0333	0.9947	0.9432	0.9169
101.2	1.40	1.0701	1.0485	1.0306	0.9910	0.9418	0.9173
102.5	1.82	1.0736	1.0514	1.0354	0.9932	0.9367	0.9084
105.0	1.08	1.0811	1.0477	1.0324	0.9924	0.9364	0.9115
106.3	0.94	1.0811	1.0477	1.0324	0.9925	0.9364	0.9115
107.0	0.93	1.0811	1.0477	1.0324	0.9924	0.9364	0.9115
107.1	0.93	1.0811	1.0477	1.0324	0.9924	0.9364	0.9115

*Prototype F100 (2 7 8) Engine

GP78-0[illegible]-158

FIGURE B-9
REFERENCE RADIAL PROFILES AND RADIAL WEIGHTING FACTORS FOR THE NASA/F-15 DISTORTION METHODOLOGIES STUDY*

SYMBOLS, SUPERSCRIPTS, AND SUBSCRIPTS

Symbol	Quantity
$\frac{a_N}{P_{to}}$	= N^{th} coefficient of the sine term in a Fourier expansion of the P_{t2}/P_{to} vs θ curve for one ring.
$\frac{A_N}{P_{to}}$	= $\sqrt{\left(\frac{a_N}{P_{to}}\right)^2 + \left(\frac{b_N}{P_{to}}\right)^2}$
$\frac{1}{P_{to}} \left(\frac{A_N}{N^2}\right)_{Max}$	= maximum value of $\left(\frac{A_N}{P_{to}}\right)\sqrt{N^2}$
$\frac{b_N}{P_{to}}$	= N^{th} coefficient of the cosine term in a Fourier expansion of the P_{t2}/P_{to} vs θ curve for one ring.
d_i	= ring at diameter D_i
D	= diameter of ring - any units
f/f_n	= normalized frequency ratio
ID	= Inside Diameter
J	= Number of diameters
K	= distortion factor
N	= order of Fourier coefficient (number of waves per circumference)
N_θ	= number of circumferential locations
OD	= Outside Diameter
P_t	= total or stagnation pressure - lb/ft^2
b	= radial distrotion weight factor
$\bar{q}$, q	= average dynamic pressure heat at compressor face - lb/ft^2
$\Delta\theta$	= angular increment between two adjacent circumferential points. (This quantity must be the same for all points.) - radians

ΔP_t	= circumferential location - radians
θ	= circumferential extent of distortion (largest region of pressure less than the average)
π	= 3.14159

Superscripts

$(\overline{})$	= overall average
$(\ )^*$	= ring average

Subscripts

a	= applies to fan
avg	= refers to time averaged value
c	= applies to high pressure compressor
i	= index of any ring counting from hub to tip
inst	= refers to instantaneous average value
N	= order of Fourier coefficient (number of waves per circumference)
o	= reference
ra	= radial part applies to fan
t	= total or stagnation
2	= refers to engine inlet plane